ISSN 2587-1366

TUJE

TURKISH JOURNAL OF ENGINEERING

VOLUME 6 ISSUE 2 APRIL 2022

Dr. Ghazi DROUBI
Robert Gordon University Engineering Faculty
Scotland, UK

JOURNAL SECRETARY

Nida DEMİRTAŞ
nidademirtas@mersin.edu.tr

TURKISH JOURNAL OF ENGINEERING (TUJE)

Turkish Journal of Engineering (TUJE) is a multi-disciplinary journal. The Turkish Journal of Engineering (TUJE) publishes the articles in English and is being published 4 times (January, April, July and October) a year. The Journal is a multidisciplinary journal and covers all fields of basic science and engineering. It is the main purpose of the Journal that to convey the latest development on the science and technology towards the related scientists and to the readers. The Journal is also involved in both experimental and theoretical studies on the subject area of basic science and engineering. Submission of an article implies that the work described has not been published previously and it is not under consideration for publication elsewhere. The copyright release form must be signed by the corresponding author on behalf of all authors. All the responsibilities for the article belongs to the authors. The publications of papers are selected through double peer reviewed to ensure originality, relevance and readability.

AIM AND SCOPE

The Journal publishes both experimental and theoretical studies which are reviewed by at least two scientists and researchers for the subject area of basic science and engineering in the fields listed below:

Aerospace Engineering
Environmental Engineering
Civil Engineering
Geomatic Engineering
Mechanical Engineering
Geology Science and Engineering
Mining Engineering
Chemical Engineering
Metallurgical and Materials Engineering
Electrical and Electronics Engineering
Mathematical Applications in Engineering
Computer Engineering
Food Engineering

PEER REVIEW PROCESS

All submissions will be scanned by iThenticate® to prevent plagiarism. Author(s) of the present study and the article about the ethical responsibilities that fit PUBLICATION ETHICS agree. Each author is responsible for the content of the article. Articles submitted for publication are priorly controlled via iThenticate ® (Professional Plagiarism Prevention) program. If articles that are controlled by iThenticate® program identified as plagiarism or self-plagiarism with more than 25% manuscript will return to the author for appropriate citation and correction. All submitted manuscripts are read by the editorial staff. To save time for authors and peer-reviewers, only those papers that seem most likely to meet our editorial criteria are sent for formal review. Reviewer selection is critical to the publication process, and we base our choice on many factors, including expertise, reputation, specific recommendations and our own previous experience of a reviewer's characteristics. For instance, we avoid using people who are slow, careless or do not provide reasoning for their views, whether harsh or lenient. All submissions will be double blind peer reviewed. All papers are expected to have original content. They should not have been previously published and it should not be under review. Prior to the sending out to referees, editors check that the paper aim and scope of the journal. The journal seeks minimum three independent referees. All submissions are subject to a double blind peer review; if two of referees gives a negative feedback on a paper, the paper is being rejected. If two of referees gives a positive feedback on a paper and one referee negative, the editor can decide whether accept or reject. All submitted papers and referee reports are archived by journal Submissions whether they are published or not are not returned. Authors who want to give up publishing their paper in TUJE after the submission have to apply to the editorial board in written. Authors are responsible from the writing quality of their papers. TUJE journal will not pay any copyright fee to authors. A signed Copyright Assignment Form has to be submitted together with the paper.

PUBLICATION ETHICS

Our publication ethics and publication malpractice statement is mainly based on the Code of Conduct and Best-Practice Guidelines for Journal Editors. Committee on Publication Ethics (COPE). (2011, March 7). Code of Conduct and Best-Practice Guidelines for Journal Editors. Retrieved from http://publicationethics.org/files/Code%20of%20Conduct_2.pdf

PUBLICATION FREQUENCY

The TUJE accepts the articles in English and is being published 4 times (January, April, July and October) a year.

CORRESPONDENCE ADDRESS

Journal Contact: tuje@mersin.edu.tr

CONTENTS

Volume 6 – Issue 2

ARTICLES

Turkish Journal of Engineering

https://dergipark.org.tr/en/pub/tuje

e-ISSN 2587-1366

A statistical investigation to determine dominant frequency of layered soil profiles

Ahmet Güllü[*1], **Serkan Hasanoğlu** [2]

[1] *Istanbul Gedik University, Faculty of Engineering, Department of Civil Engineering, Istanbul, Turkey*
[2] *Kocaeli University, Faculty of Engineering, Department of Civil Engineering, Kocaeli, Turkey*

Keywords
Energy based seismic design
Layered soil profile
Fundamental period
Resonance

ABSTRACT

Energy based seismic design getting attraction since it accounts for all structural (hysteretic behavior of structural members), earthquake (amplitude, duration and frequency content) and soil (bearing capacity, frequency content) characteristics. To develop an efficient energy based seismic design procedure, accurate determination of the fundamental periods of the soil deposits is crucial. Hence, several analytical, numerical and approximate methods were suggested in the literature to find out fundamental periods of layered soil profiles. However, practitioners tend to use the simplest and the roughest methods, generally. In this particular research, a statistical study was performed to find out the best fit coefficient for the total travel time having minimum standard deviation. In the analyses, the calculated fundamental periods of 459 different soil profiles are compared with the results of almost exact analytical equations. Resultantly, the equation generally preferred by the practitioners is improved. It is proved that the improved equation has higher accuracy with lowest standard deviation and higher correlation. Therefore, using the improved equation to determine fundamental period of the layered soil profiles is highly suggested.

1. INTRODUCTION

Energy-based seismic design is a promising procedure in structural and earthquake engineering since it accounts for all soil, structure and earthquake characteristics, (Güllü et al. 2019). Moreover, energy is a scalar quantity, which makes modal combinations easier. To develop an efficient energy-based design procedure, determining the dominant frequencies of soil deposits is crucial. It is also well-known for conventional design procedures that local geological conditions (especially near surface soil deposits) has a direct effect on vulnerability of structures against strong ground motions (Sextos et al. 2018). Greater input energy will be imparted to the structures having similar frequencies with the soil layers i.e. the structure will be exposed to resonance. As an example, it was reported that low- and mid-rise buildings in the Katmandu Valley almost unaffected by great 2015 Gorkha, Nepal earthquake since long period nature of the earthquake (Goda et al. 2015).

Characteristics of seismic waves (e.g. amplitude, frequency content) alter during the propagation of the wave through heterogeneous soil deposits. This phenomenon is primarily dependent on modal characteristics of the layered soil profiles. Particularly, amplification is dominant in the vicinity of the fundamental frequency of the soil deposit (Vijayendra et al. 2014).

Even though investigating the strong ground motion records is an easier and suitable way to determine the fundamental period of a soil site, finding data for any place is not possible. Hence, different procedures have been proposed in the literature for this purpose (Dobry et al.,1976; Gazetas, 1982; Zhao, 1996, 1997; Hadjian 2002; Vijayendra et al. 2014; Urzua et al., 2017; Wang et al.,2018).

Dobry et al. (1976) evaluated several numerical and approximate procedures to determine fundamental periods of layered soil profiles. The numerical method, namely Rayleigh method, provide almost exact results comparing to measured fundamental periods. However, it is fairly complex for more than two layers. Hence, a simplified version of the method was proposed by supposing constant soil density for the layers. In this method, single iteration is sufficient to catch modal shape and fundamental period of the soil profiles, Eqs. (1a-c).

* **Corresponding Author**

* (ahmet.gullu@gedik.edu.tr) ORCID ID 0000-0001-6678-9372
(serkan.hasanoglu@kocaeli.edu.tr) ORCID ID 0000-0002-7018-0479

Cite this article

Gullu A & Hasanoglu S (2022). A statistical investigation to determine dominant frequency of layered soil profiles. Turkish Journal of Engineering, 6(2), 95-105

Research Article / DOI: 10.31127/tuje.818539

Received: 30/10/2020; Accepted: 01/03/2021

$$X(i+1) = X(i) + \frac{H - H_{mi}}{V_i^2} H_i \quad (1a)$$

$$\omega^2 = 4 \frac{\frac{\sum [H - H_{mi}]^2}{V_i^2} H_i}{\sum [X(i) + X(i+1)]^2 H_i} \quad (1b)$$

$$T = \frac{2\pi}{\omega} \quad (1c)$$

In the equations, H is total depth to engineering bedrock, H_i and H_{mi} are height and the mid-depth of the i^{th} layer. Additionally, $X(i)$ and $X(i+1)$ are the first-mode shape at the top and bottom of the i^{th} soil layer.

A simple approximate method for two-layer soil which yields acceptable results was also suggested by Madera (1970). Dobry et al. (1976), improved this analytical and graphical solution considering constant density for multilayer soil profiles. Combined fundamental period for a two-layer profile, $T_{a\text{-}b}$, can be calculated by Eq. (2). In the equation ρ and h are stand for soil density and height, respectively. T_a and T_b are the fundamental periods of each soil layers.

$$\tan\left(\frac{\pi}{2}\frac{T_a}{T_{a-b}}\right)\tan\left(\frac{\pi}{2}\frac{T_b}{T_{a-b}}\right) = \frac{\rho_b h_b T_a}{\rho_a h_a T_b} \quad (2)$$

where $T_a = 4\frac{H_a}{V_a}$ and $T_b = 4\frac{H_b}{V_b}$.

For the application of the method to a multi-layered soil, firstly T_{a-b}^{1-2} of the top two layers should be calculated. Then, the combined fundamental period of the top three layers ($T_{a-b}^{1,2-3}$) can be calculated by considering the top two layers as a single layer with efficient fundamental period of T_{a-b}^{1-2}. Fundamental period of the multi-layered soil profile ($T_{a-b}^{1,2-n}$) can be obtained easily by repeating the process till the bottommost soil layer. Hadjian (2002) improved the Madera's method (Madera 1970) applying some algebraic manipulations on Eq. (2) and proposed a non-graphical solution.

Although the numerical methods provide accurate results, employing them is a tedious and time-consuming task for practitioners. Thus, several simple and rough methods were generated by researchers. Many practitioners preferred using Eq. (3) to determine fundamental periods of the soil profiles due to its simplicity. In the equation, H is height of soil column on the engineering bedrock, V_{avg} is weighted average shear wave velocity of the soil layers.

$$T = 4\frac{H}{V_{avg}} \quad (3)$$

Increasing the accuracy of Eq. (3) through a statistical study is the rational of this paper. To serve this purpose 459 layered soil profile data is analyzed. Since the *Simplified Rayleigh method* has a remarkable accuracy (Dobry et al. 1976), results of the method were considered as "*true*" values. A novel and simple equation with lower standard deviation and higher correlation is suggested.

2. Materials and Method

The data provided by KiK-net of Japan is utilized here as the material. In the method, *true* dominant frequencies of the soil profiles, which is calculated by Eqs. (1a-b), compared with the results of varied coefficients of Eq. (3). Consequently, the coefficient having the smallest standard deviation is proposed for the quick and robust determination of the fundamental periods of the soil profiles. Details of the data set and analyzing procedures are described in the following sub-sections.

2.1. Data set

Since reaching a soil data set of Istanbul could not be possible after many attempts those were made to related division of the municipality, the detailed layered soil profile data provided by KiK-net (Kiban Kyoshin Network) of Japan (National Research Institute for Earth Science and Disaster Resilience) were utilized. KiK-net has 698 stations, and uniformly cover Japan with an average station-to-station distance of about 20 km.

Generally, fundamental periods of layer soil profiles were calculated by considering the engineering bedrock has a shear wave velocity of 760 m/sec (Ghofrani et al. 2013, Zhao et al. 2015, Wang et al. 2018) or 700 m/sec (Zhao et al., 2006; Zhao and Xu, 2013). In this study, bedrock is considered to be the depth where shear wave velocity reaches to 760 m/sec.

The data set was filtered according to following conditions in line with Wang et al. (2018);

- The data should be obtained by drilling up to engineering bedrock
- There should be at least two soil layers within the soil depth.
- Minimum shear wave velocity is accepted as 100 m/sec since low values of shear wave velocity may occur due to instrumental errors.

After filtering the data set, 459 KiK-net soil profiles were chosen to utilize in the analyses. The layered soil profiles which are *not* utilized in this study are listed in Appendix-1.

2.2. True determination of fundamental periods

Assuming constant density for the soil layers is an important characteristic of the Simplified Rayleigh method. The assumption considerably simplify the problem and it is possible to reach almost exact results by just one single iteration. According to Dobry et al. (1976), Simplified Rayleigh method differs only a few percent from the correct value. Thus, the results of the method can be accepted as true values for fundamental period calculations of layered soil profiles.

The parameters of the method (V_i, H_i, H and H_{mi}) are considered layer by layer starting from the bottom of the soil profile. At the lower boundary of the bottommost layer, X_i is taken as zero i.e., $X_i = X_1 = 0$. Once all X_i values are computed by Eq. (1a), fundamental circular frequencies of the soil profile can be calculated by Eq. (1b). Then, it can be converted to the period, easily. Fundamental period calculation of the soil profiles ABSH03 and CHBH06 by means of Simplified Rayleigh method, are given in Table 1. In the third column of the table, total depths (H) of the soil profiles are given. The fourth and fifth columns are the depth of each layer (H_i) and depth of center of each layer (H_{mi}). The seventh column is the measured shear wave velocity of the layers. Other columns are calculated by using the data given in these columns.

Table 1. Fundamental period calculation examples by simplified Rayleigh method.

Sta. ID	Layer #	H (m)	H_i (m)	H_{mi} (m)	$H-H_{mi}$ (m)	$V_{s,i}$ (m/s)	X_i (×10^{-4})	$(X_i+X_{i+1})^2\times H_i$ (×10^{-7})	$(H-H_{mi})^2\times H_i/V_{s,i}^2$ (×10^{-4})
ABSH03	1	12	6	3	9.00	640	1.318	1.042	11.865
	2		4	8	4.00	310	2.983	7.402	6.659
	3		2	11	1.00	100	4.983	12.693	2
							Σ=	21.13781	20.52496
								ω (Hz)=	*62.321*
								T (sec)=	*0.101*
Sta. ID	Layer #	H (m)	H_i (m)	H_{mi} (m)	$H-H_{mi}$ (m)	$V_{s,i}$ (m/s)	X_i (×10^{-2})	$(X_i+X_{i+1})^2\times H_i$ (×10^{-1})	$(H-H_{mi})^2\times H_i/V_{s,i}^2$ (×10^{0})
CHBH06	1	165	35.00	17.50	147.50	460	2.44	0.208	3.599
	2		38.00	54.00	111.00	440	4.619	1.893	2.418
	3		38.00	92.00	73.00	400	6.352	4.574	1.266
	4		36.00	129.00	36.00	360	7.352	6.761	0.36
	5		13.00	153.50	11.50	200	7.726	2.956	0.043
	6		5.00	162.50	2.50	180	776.45	1.2	0.001
							Σ=	17.592	7.687
								ω (Hz)=	*4.181*
								T (sec)=	*1.503*

2.3. Statistical Study

Fundamental period values of 459 KiK-net stations are calculated by a fully-automatic MATLAB code which was developed in this study. The fully automatic algorithm calculates the *true* fundamental periods based on Simplified Rayleigh method, initially. Secondly, the predicted fundamental periods for each i^{th} total travel time coefficient of average shear wave velocity are calculated. The difference of the true and predicted periods is nominated as the residuals. Henceforth, standard deviations of the residuals of 459 KiK-net data are calculated for each coefficient between 2.0 to 5.0 with 0.01 increments. The coefficient having the minimum standard deviation for residuals with highest correlation coefficients is considered to be the best-fit coefficient. Totally, 459×301=138159 calculations are performed in the content of this study. It is worth to note that in the mostly preferred equation by practitioners, the coefficient of the total travel time of shear wave was 4, see Eq. (3).

Hereafter, relative difference (*Rel. Dif.*) for each data is calculated by Eq. (4) where $T_{calculated}$ and T_{true} correspond to determined fundamental periods of the soil layers by different coefficients of Eq. (3) and Simplified Rayleigh method, Eq. (1c), respectively.

$$\text{Rel. Dif.} = \frac{\left|T_{calculated} - T_{true}\right|}{T_{true}} \tag{4}$$

Relative differences and their mean values of the original and proposed equations are also compared in the study.

3. RESULTS

Variation of the standard deviations of residuals with the coefficients for travel time of average shear wave (from bedrock to surface) is depicted in Figure 1.

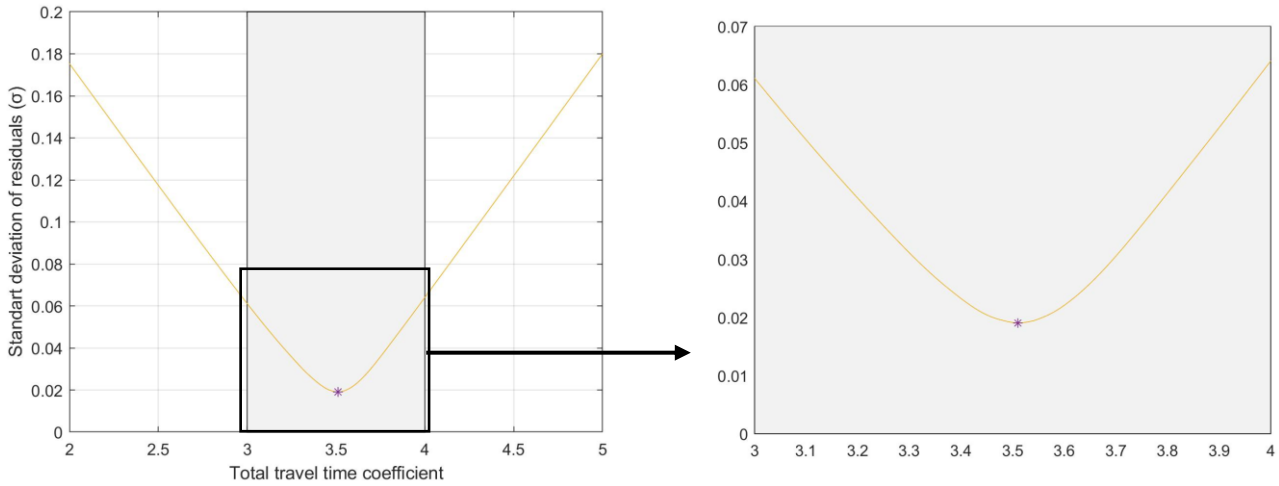

Figure 1. Variation of the standard deviation of the residuals for diverse total travel time coefficients of V_{avg}

The minimum standard deviation is obtained to be 0.019 for the coefficient of 3.51. Changing the coefficient of the equation simply with 3.51 will yield significantly lower standard deviation (~%336) and increase the reliability of the equation.

Mean value and standard deviation of the residuals are given in Table 2 for the coefficients of 3.51 and the original value of 4.00.

Table 2. Mean value and standard deviations of the residuals obtained by the proposed and original coefficients.

Equation	Mean value	Standard deviation
3.51 H/V_s	0.0147	0.0191
4.00 H/V_s	0.0487	0.0641

The correlation coefficient calculated for the *true* periods and the periods determined for the case of total travel time of shear velocity coefficient of 3.51 was found to be 0.998. The obtained correlation coefficient between the two series is extremely high. Therefore, Eq. (5) is proposed to determine fundamental periods of the layered soil profiles.

$$T = 3.51\frac{H}{V_{avg}} \quad (5)$$

In the second step, absolute residuals of each data point are plotted for the coefficients of 3.51 and 4.00 in Figures 2a-b. In the figures, mean value ± one standard deviation ranges are also depicted with gray color. Using the coefficient of 3.51 instead of 4.00, considerably reduced the scattering area of the residuals. Additionally, highest absolute residuals are obtained as 0.12 for the proposed coefficient and 0.54 for the original coefficient of 4.00.

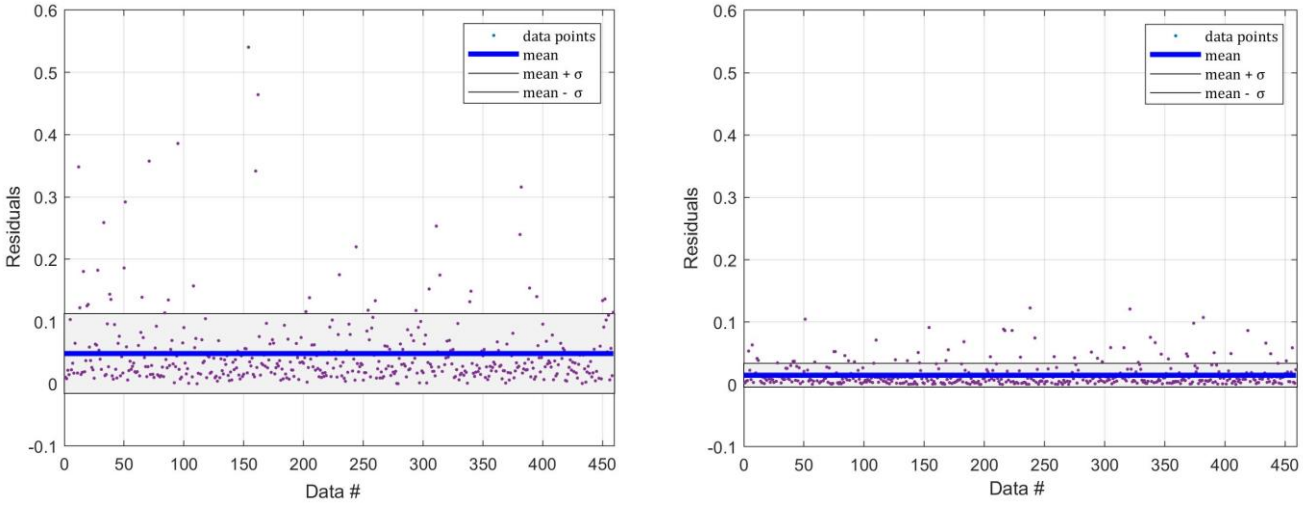

a- for Eq. (3) b- for Eq. (5)

Figure 2. Calculated absolute residuals

These statistical results show that the newly proposed equation, Eq. (5), provides better correlation with the true results. To be able to show the difference of proposed formula and the original one, relative differences of Eqs. (3) and (5) with respect to Simplified Rayleigh method are illustrated for the all stations considered in this study, Figure 3. Average relative

difference is reduced to almost 5% from 15% by using Eq. (5).

Finally, the predicted dominant periods are compared with the true ones in Figure 4. As it was expected, soft soils have longer fundamental periods while the value is quite shorter for stiff soils. It is clear that the proposed equation has superior performance to capture *true* dominant period.

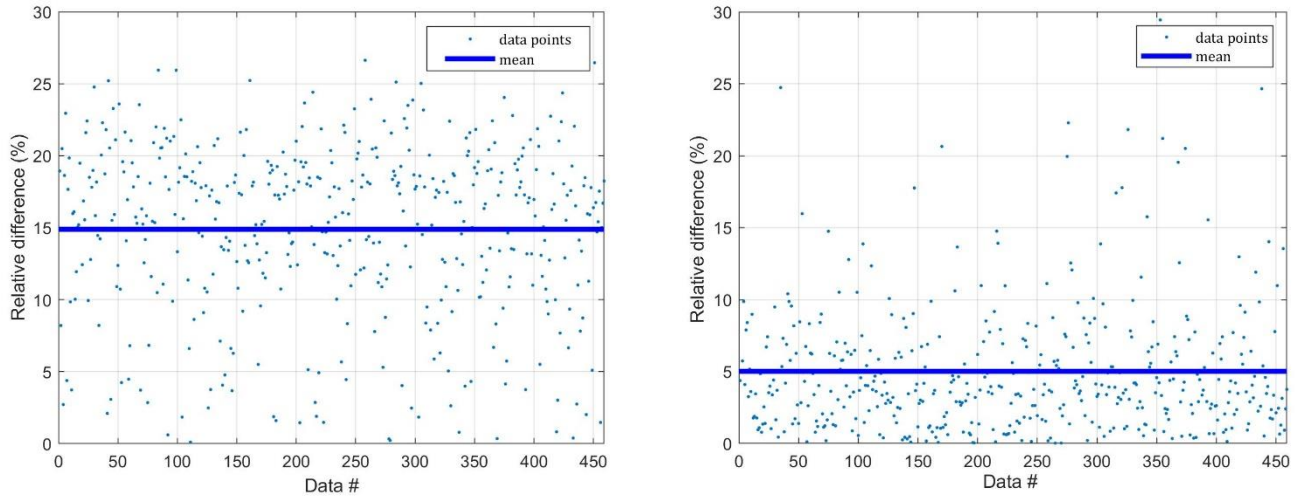

a- for Eq. (3) b- for Eq. (5)

Figure 3. Calculated relative differences

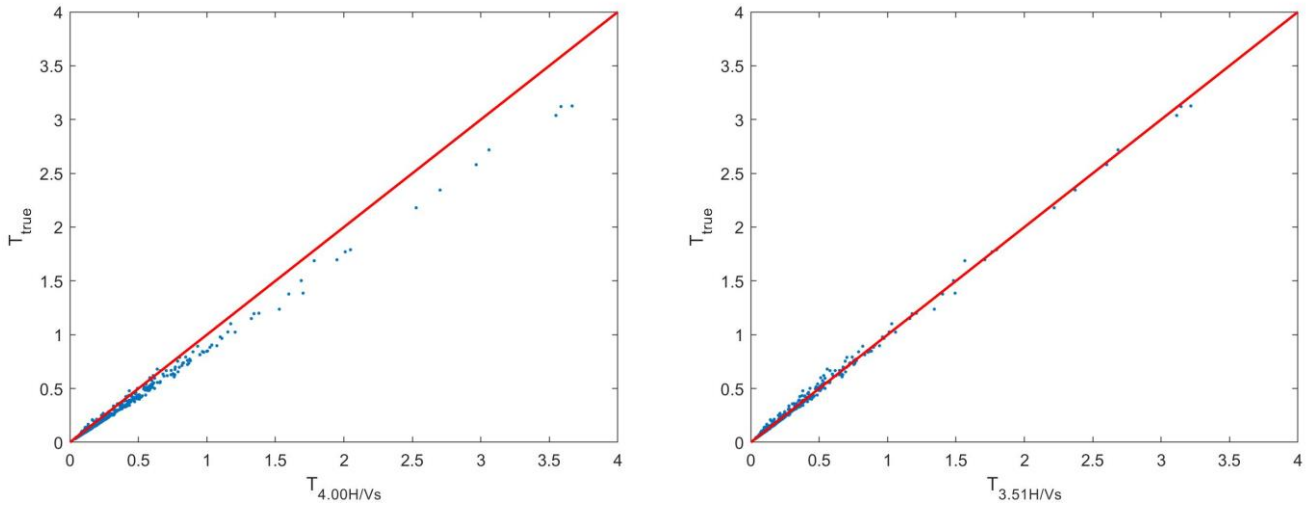

a- for Eq. (3) b- for Eq. (5)

Figure 4. Comparisons of the previous and the proposed equations with *true* period

Based on the performed statistical analyses, it can be said that the proposed equation, Eq. (5), yields more concrete results with similar simplicity.

4. CONCLUSION

Fundamental period of the layer soil profiles is a crucial parameter for the earthquake resistant design of structures and energy based seismic design. Due to the difficulty of applying numerical methods to the calculation of fundamental periods of soils, many simple formulas exist in the literature for practitioners. The roughest and the simplest equation, Eq. (3), is mostly preferred by the practitioners. Although this formula may give adequate results for some specific cases, it has a great standard deviation and approximately 15% error in average. In this study, a statistical study is applied to find out a better coefficient for total travel time (H/V_{avg}) by utilizing the KiK-net database of Japan. The proposed formula gives better results with smaller standard deviation, higher correlation coefficient and it has only 5% mean relative difference with respect to true results. Moreover, the proposed equation has the same simplicity with the existing equation. Hence, using the proposed equation instead of the existing one is highly suggested. It is worth to remind that the study based on solely the KiK-net data. So, an amount of discrepancy may arise for some specific soil profiles which is not represented in this data set.

ACKNOWLEDGEMENT

The authors are so grateful to National Research Institute for Earth Science and Disaster Resilience (NIED)for providing the free access to KiK-net data.

APPENDIX Soil data which is not utilized in the study

Site Code	Site Name	Latitude	Longitude	Altitude (m)	Depth (m)	Prefecture	Seismo-graph	Notes
ABSH02	OKOPPE-W	44.4234	143.0264	38	113	HOKKAIDO	KiK-net06	
ABSH04	TAKINOUE-N	44.192	143.0767	134	200	HOKKAIDO	KiK-net06	
ABSH11	MEMAMBETSU	43.9144	144.1913	40	122	HOKKAIDO	KiK-net11B	
ABSH12	KOSHIMIZU	43.8566	144.4574	25	120	HOKKAIDO	KiK-net06	
AICH05	TOKONAME	34.8886	136.8763	50	401	AICHIKEN	---	suspension
AICH13	KIYOSU	35.2177	136.8509	5	741	AICHIKEN	KiK-net06	
AICH15	ASUKE	35.1392	137.3359	150	120	AICHIKEN	KiK-net11B	
AKTH02	NISHIKI-S	39.6634	140.5721	95	100	AKITAKEN	KiK-net06	
AKTH03	YAJIMA	39.2223	140.1283	145	103	AKITAKEN	KiK-net11A	
AKTH05	CHOKAI	39.0718	140.3185	275	200	AKITAKEN	KiK-net06	
AKTH07	KOSAKA	40.4563	140.8395	405	105	AKITAKEN	KiK-net06	
AKTH09	TASHIRO	40.2755	140.4596	45	101	AKITAKEN	KiK-net06	
AKTH10	ODATE	40.3002	140.5812	85	100	AKITAKEN	KiK-net06	
AKTH16	NISHISEMBOKU	39.545	140.3481	20	154	AKITAKEN	KiK-net06	
AKTH18	OMORI	39.3548	140.3869	65	100	AKITAKEN	KiK-net06	
AOMH01	OMA	41.5273	140.9127	10	100	AOMORIKEN	KiK-net06	
AOMH03	KAWAUCHI	41.234	140.9896	20	100	AOMORIKEN	KiK-net11C	
AOMH04	AOMORI	40.8524	140.6759	10	307	AOMORIKEN	KiK-net06	
AOMH08	AJIGASAWA	40.7618	140.3121	50	160	AOMORIKEN	KiK-net06	
AOMH11	TOWADAKO-W	40.58	140.995	240	100	AOMORIKEN	KiK-net06	
AOMH12	TOWADAKO-E	40.5846	141.1547	85	100	AOMORIKEN	KiK-net06	
AOMH13	HACHINOHE	40.5794	141.4451	10	150	AOMORIKEN	KiK-net11C	
AOMH16	SHINGO	40.4624	141.0923	315	150	AOMORIKEN	KiK-net06	
CHBH04	SHIMOSA	35.7966	140.0206	23	2300	CHIBAKEN	KiK-net06	
CHBH10	CHIBA	35.5458	140.2417	65	2000	CHIBAKEN	KiK-net06	
CHBH11	YORO	35.2867	140.1529	80	2000	CHIBAKEN	KiK-net06	
CHBH12	FUTTSU	35.3445	139.8554	3	2000	CHIBAKEN	KiK-net11C	
CHBH13	NARITA	35.8307	140.298	12	1300	CHIBAKEN	KiK-net06	
CHBH14	CHOSHI-C	35.7342	140.823	2	525	CHIBAKEN	KiK-net11A	
CHBH15	TATEYAMA-W	34.9591	139.7885	30	500	CHIBAKEN	KiK-net11A	
CHBH19	HASUNUMA	35.5943	140.5107	1	1630	CHIBAKEN	KiK-net06	
CHBH20	KAMOGAWA-S	35.0882	140.0997	28	306	CHIBAKEN	KiK-net11B	
EHMH01	TSUSHIMA	33.0556	132.5552	375	100	EHIMEKEN	KiK-net11A	
EHMH04	TAMBARA	33.9023	133.0658	15	200	EHIMEKEN	KiK-net11A	
EHMH12	UWA	33.427	132.5055	250	150	EHIMEKEN	KiK-net11B	
EHMH13	MISAKI	33.3719	132.1157	10	222	EHIMEKEN	KiK-net18	
FKIH01	EIHEIJI	36.0955	136.3617	65	100	FUKUIKEN	KiK-net06	
FKOH04	KAHO	33.5512	130.7451	60	100	FUKUOKAKEN	KiK-net18	
FKOH05	SAIGAWA	33.5293	130.9503	370	100	FUKUOKAKEN	KiK-net18	
FKOH06	BUZEN	33.5925	131.1348	35	303	FUKUOKAKEN	KiK-net11C	
FKOH10	UKIHA	33.2891	130.817	190	200	FUKUOKAKEN	KiK-net11B	
FKSH15	INAWASHIRO	37.6461	140.1735	757	100	FUKUSHIMAKEN	KiK-net06	
FKSH16	FUKUSHIMA	37.7643	140.3766	135	300	FUKUSHIMAKEN	KiK-net11A	
FKSH17	KAWAMATA	37.6636	140.5974	205	100	FUKUSHIMAKEN	KiK-net06	
FKSH20	NAMIE	37.4911	140.9871	12	109	FUKUSHIMAKEN	KiK-net06	
GIFH04	FURUKAWA	36.2448	137.1983	572	100	GIFUKEN	KiK-net11A	
GIFH05	SHOKAWA	36.0654	136.9479	839	100	GIFUKEN	KiK-net11A	
GIFH14	KAMITAKARA	36.2493	137.5174	810	100	GIFUKEN	KiK-net18	

GIFH16	ASAHI-N	36.094	137.3438	790	100	GIFUKEN	KiK-net18
GIFH18	MAZE	35.8991	137.1495	570	107	GIFUKEN	KiK-net11A
GIFH20	GERO-N	35.7991	137.2531	355	128	GIFUKEN	KiK-net18
GIFH21	MINAMI	35.6665	136.9618	170	200	GIFUKEN	KiK-net18
GIFH22	KANAYAMA	35.6682	137.1054	435	100	GIFUKEN	KiK-net18
GNMH05	ISESAKI	36.3143	139.1847	57	2000	GUNMAKEN	KiK-net11A
GNMH06	TATEBAYASHI	36.2441	139.5443	20	1203	GUNMAKEN	KiK-net06
GNMH07	TONE	36.6998	139.2104	646	200	GUNMAKEN	KiK-net11B
GNMH14	MIDORI	36.4931	139.3219	360	200	GUNMAKEN	KiK-net11A
HDKH03	MOMBETSU-E	42.5934	142.3521	160	106	HOKKAIDO	KiK-net06
HRSH03	MITSUGI	34.5183	133.1375	160	200	HIROSHIMAKEN	KiK-net11A
HRSH04	NUMAKUMA	34.3785	133.3493	25	200	HIROSHIMAKEN	KiK-net11A
HRSH12	HIROSHIMA	34.581	132.4295	360	150	HIROSHIMAKEN	KiK-net11C
HRSH17	TOGOUCHI	34.5716	132.2326	265	102	HIROSHIMAKEN	KiK-net11C
IBRH06	KITAIBARAKI2	36.8809	140.6545	395	100	IBARAKIKEN	KiK-net11
IBRH07	EDOSAKI	35.9521	140.3301	3	1200	IBARAKIKEN	KiK-net11A
IBRH08	TAIYO	36.1188	140.5621	40	1200	IBARAKIKEN	KiK-net06
IBRH09	JOHOKU	36.439	140.3559	50	106	IBARAKIKEN	KiK-net11C
IBRH15	GOZENYAMA	36.5566	140.3013	45	107	IBARAKIKEN	KiK-net11B
IBRH19	TSUKUBA	36.2137	140.0893	175	210	IBARAKIKEN	KiK-net06
IBRH21	TSUKUBA-S	35.9814	140.105	22	929	IBARAKIKEN	KiK-net06
IBUH03	ATSUMA	42.6486	141.8641	10	153	HOKKAIDO	KiK-net06
IKRH02	SHINSHINOTSU	43.2204	141.6523	10	127	HOKKAIDO	KiK-net06
ISKH01	SUZU	37.5266	137.2844	48	200	ISHIKAWAKEN	KiK-net06
ISKH02	YANAGIDA	37.3644	137.0413	121	102	ISHIKAWAKEN	KiK-net11C
ISKH06	SHIKA	37.0533	136.8206	20	200	ISHIKAWAKEN	KiK-net11A
IWTH03	IWAIZUMI	39.802	141.652	310	100	IWATEKEN	KiK-net11C
IWTH06	NINOHE-W	40.2611	141.1709	225	100	IWATEKEN	KiK-net06
IWTH07	KARUMAI	40.2705	141.5709	260	120	IWATEKEN	KiK-net06
IWTH09	KUJI-S	40.0861	141.712	240	100	IWATEKEN	KiK-net06
IWTH15	YAHABA	39.6148	141.0929	195	122	IWATEKEN	KiK-net06
IWTH17	KAWAI-N	39.6442	141.5977	305	103	IWATEKEN	KiK-net11C
IWTH20	HANAMAKI-S	39.3434	141.0473	106	156	IWATEKEN	KiK-net11C
IWTH24	KANEGASAKI	39.1979	141.0118	200	150	IWATEKEN	KiK-net11C
IWTH26	ICHINOSEKI-E	38.969	141.0013	125	108	IWATEKEN	KiK-net11C
IWTH27	RIKUZENTAKATA	39.0307	141.532	80	100	IWATEKEN	KiK-net11C
KGSH03	MIYANOJO	31.9812	130.4438	110	100	KAGOSHIMAKEN	KiK-net06
KGSH04	SENDAI	31.8374	130.3602	14	100	KAGOSHIMAKEN	KiK-net11C
KGSH05	KEDOIN	31.8699	130.4958	73	107	KAGOSHIMAKEN	KiK-net06
KGSH06	KORIYAMA	31.6988	130.4594	131	203	KAGOSHIMAKEN	KiK-net06
KGSH07	AIRA	31.714	130.6149	6	302	KAGOSHIMAKEN	KiK-net11C
KGSH08	OHSUMI	31.5618	130.9969	97	150	KAGOSHIMAKEN	KiK-net06
KGSH13	KANOYA	31.4005	130.8541	40	101	KAGOSHIMAKEN	KiK-net06
KGWH03	MIKI	34.27	134.1482	50	100	KAGAWAKEN	KiK-net11A
KGWH05	UCHINOMI	34.4572	134.3241	20	433	KAGAWAKEN	KiK-net11B
KKWH01	BIFUKA-N	44.5973	142.3036	61	111	HOKKAIDO	KiK-net06
KKWH03	BIFUKA-W	44.4732	142.2725	100	100	HOKKAIDO	KiK-net06
KKWH04	NAYORO	44.4376	142.4056	84	100	HOKKAIDO	KiK-net06
KKWH05	SHIMOKAWA-W	44.2921	142.6303	160	300	HOKKAIDO	KiK-net06
KKWH06	SHIMOKAWA-E	44.3207	142.7656	200	100	HOKKAIDO	KiK-net06
KKWH12	BIEI-E	43.5038	142.6006	450	207	HOKKAIDO	KiK-net11B

KMMH04	ASO	32.9514	131.0199	475	127	KUMAMOTOKEN	---	suspension
KMMH07	MISUMI	32.6234	130.5584	22	300	KUMAMOTOKEN	KiK-net11B	
KMMH11	ASHIKITA	32.2918	130.5777	100	300	KUMAMOTOKEN	KiK-net11B	
KMMH17	TAMANA	32.9873	130.5608	55	100	KUMAMOTOKEN	KiK-net11B	
KMMH18	ASO2	33.0031	131.0071	932	78	KUMAMOTOKEN	KiK-net11B	
KNGH10	YOKOHAMA	35.4991	139.5195	62	2000	KANAGAWAKEN	KiK-net06	
KNGH11	ATSUGI	35.404	139.3539	12	1800	KANAGAWAKEN	KiK-net06	
KNGH21	KIYOKAWA	35.4628	139.2146	455	210	KANAGAWAKEN	KiK-net11A	
KOCH02	GOHOKU	33.7079	133.3641	590	100	KOCHIKEN	KiK-net11A	
KOCH04	OTSUKI	32.8414	132.7066	55	100	KOCHIKEN	KiK-net11A	
KOCH05	IKEKAWA	33.6472	133.1444	260	100	KOCHIKEN	KiK-net11A	
KOCH06	NAKAMURA	33.0754	132.9524	31	100	KOCHIKEN	KiK-net11A	
KOCH09	KAHOKU	33.6748	133.8243	190	100	KOCHIKEN	KiK-net11B	
KOCH11	MUROTO	33.2866	134.1603	90	300	KOCHIKEN	KiK-net11B	
KSRH01	AKAN-N	43.4361	144.0844	431	106	HOKKAIDO	KiK-net11B	
KSRH02	AKAN-S	43.1142	144.123	30	105	HOKKAIDO	KiK-net06	
KSRH03	SHIBECHA-N	43.3848	144.6279	83	107	HOKKAIDO	KiK-net06	
KSRH04	SHIBECHA-S	43.2139	144.6804	30	240	HOKKAIDO	KiK-net11A	
KSRH06	TSURUI-E	43.22	144.4285	30	237	HOKKAIDO	KiK-net06	
KSRH07	TSURUI-S	43.1359	144.3274	38	222	HOKKAIDO	KiK-net11B	
KSRH08	SHIRANUKA-N	43.1603	143.8936	174	100	HOKKAIDO	KiK-net06	
KSRH09	SHIRANUKA-S	42.9856	143.9841	27	100	HOKKAIDO	KiK-net06	
KSRH10	HAMANAKA	43.2084	145.1168	31	255	HOKKAIDO	KiK-net11B	
KYTH04	MIYAMA	35.2685	135.5508	190	100	KYOTOFU	KiK-net18	
KYTH07	KUMIYAMA	34.8983	135.7461	11	800	KYOTOFU	KiK-net18	
MIEH08	MATSUSAKA	34.5424	136.5033	35	150	MIEKEN	KiK-net11B	
MYGH04	TOWA	38.786	141.3254	35	100	MIYAGIKEN	KiK-net06	
MYGH07	KAWASAKI	38.1802	140.6405	186	142	MIYAGIKEN	KiK-net11	
MYGH08	IWANUMA	38.1133	140.8441	10	100	MIYAGIKEN	KiK-net11C	
MYGH12	SHIZUGAWA	38.6416	141.4428	18	102	MIYAGIKEN	---	suspension
MYGH14	RIFU	38.34	140.9551	48	1034	MIYAGIKEN	KiK-net11	
MYZH05	NANGO	32.347	131.2668	353	100	MIYAZAKIKEN	KiK-net06	
MYZH06	TOGO	32.3607	131.4643	100	100	MIYAZAKIKEN	KiK-net11C	
MYZH09	SUKI	32.0421	131.0618	335	100	MIYAZAKIKEN	KiK-net11C	
MYZH16	NOBEOKA	32.506	131.6958	2	100	MIYAZAKIKEN	KiK-net06	
NARH02	TOTSUKAWA-E	33.9692	135.8574	480	100	NARAKEN	KiK-net11A	
NARH06	YAMAZOE	34.6413	136.0512	277	101	NARAKEN	KiK-net11A	
NGNH07	NAKANO	36.7434	138.376	378	200	NAGANOKEN	KiK-net06	
NGNH09	TAKESHI	36.2859	138.2491	605	100	NAGANOKEN	KiK-net06	
NGNH12	MINAMIMAKI	35.9696	138.4797	1320	206	NAGANOKEN	KiK-net06	
NGNH22	HASE	35.7946	138.0824	820	100	NAGANOKEN	KiK-net06	
NGNH27	SHINSHUSHIN	36.577	138.0479	505	102	NAGANOKEN	KiK-net06	
NGNH34	OHMACHI-C	36.5327	137.8201	825	106	NAGANOKEN	KiK-net06	
NGNH54	IIDA	35.4489	138.0058	1168	104	NAGANOKEN	KiK-net06	
NGSH02	SASEBO-N	33.2122	129.7652	140	112	NAGASAKIKEN	KiK-net18	
NGSH06	NAGASAKI	32.6999	129.8625	155	200	NAGASAKIKEN	KiK-net18	
NIGH01	NAGAOKA	37.4272	138.8876	85	100	NIIGATAKEN	KiK-net11A	
NIGH02	ASAHI	38.2799	139.5486	34	104	NIIGATAKEN	KiK-net06	
NIGH03	ARAKAWA	38.1327	139.4289	6	221	NIIGATAKEN	KiK-net06	
NIGH04	SEKIKAWA	38.1313	139.5428	78	100	NIIGATAKEN	KiK-net06	
NIGH05	SEIRO	37.9759	139.2788	7	147	NIIGATAKEN	KiK-net06	

NIGH06	KAMO	37.6527	139.0676	30	100	NIIGATAKEN	KiK-net06
NIGH15	MUIKA	37.0533	138.9951	358	100	NIIGATAKEN	KiK-net06
NIGH19	YUZAWA	36.8114	138.7849	985	100	NIIGATAKEN	KiK-net11C
NMRH03	NAKASHIBETSU	43.5508	144.9665	30	228	HOKKAIDO	KiK-net11B
NMRH04	BEKKAI-E	43.3978	145.1224	30	216	HOKKAIDO	KiK-net11A
NMRH05	BEKKAI-W	43.39	144.8021	92	220	HOKKAIDO	KiK-net06
OITH01	YAMAGUNI	33.4122	131.0326	249	200	OITAKEN	KiK-net11B
OITH02	YAMAGA	33.4581	131.4429	165	100	OITAKEN	KiK-net11B
OITH05	NOTSUHARA	33.1525	131.542	160	100	OITAKEN	KiK-net11B
OITH06	TAKETA	32.9726	131.3984	260	103	OITAKEN	KiK-net11B
OITH09	UME-E	32.8486	131.6786	190	100	OITAKEN	KiK-net06
OKYH02	SETO	34.7501	134.0702	30	200	OKAYAMAKEN	KiK-net11A
OKYH07	SHINGO	35.0493	133.3169	564	100	OKAYAMAKEN	KiK-net18
OKYH10	KAMISAIBARA	35.2826	133.9263	495	200	OKAYAMAKEN	KiK-net11A
OKYH11	SHOO	35.0732	134.1162	129	200	OKAYAMAKEN	KiK-net11A
OKYH12	OHARA	35.0999	134.319	280	200	OKAYAMAKEN	KiK-net11A
OKYH13	HINASE	34.7283	134.2744	3	103	OKAYAMAKEN	KiK-net18
OKYH14	HOKUBO	34.9363	133.6205	218	100	OKAYAMAKEN	KiK-net18
OSKH01	TAJIRI	34.3977	135.2836	5	1505	OSAKAFU	KiK-net06
OSKH02	KONOHANA	34.6628	135.3896	7	2008	OSAKAFU	KiK-net11A
RMIH01	HORONOBE	45.0167	142.0795	30	100	HOKKAIDO	KiK-net06
RMIH02	TESHIO	44.8948	141.9251	10	107	HOKKAIDO	KiK-net06
RMIH03	EMBETSU	44.6359	141.8187	20	209	HOKKAIDO	KiK-net06
SAGH05	SHIROISHI	33.1806	130.1046	18	203	SAGAKEN	KiK-net18
SBSH01	FURUBIRA	43.2341	140.6228	28	100	HOKKAIDO	KiK-net06
SBSH02	TOMARI	43.0527	140.5017	25	100	HOKKAIDO	KiK-net06
SBSH03	AKAIGAWA	43.0842	140.8199	145	220	HOKKAIDO	KiK-net11B
SBSH04	KYOWA	42.9758	140.6219	20	200	HOKKAIDO	KiK-net06
SBSH05	KUCCHAN	42.95	140.8223	240	100	HOKKAIDO	KiK-net06
SBSH06	RANKOSHI	42.8309	140.4831	39	130	HOKKAIDO	KiK-net06
SBSH07	MAKKARI	42.763	140.8084	228	100	HOKKAIDO	KiK-net06
SBSH10	SHIMAMAKI	42.7797	140.1557	32	100	HOKKAIDO	KiK-net11B
SIGH01	TAGA	35.2383	136.3599	610	100	SHIGAKEN	KiK-net06
SIGH02	OHTSU	35.2482	135.8671	305	100	SHIGAKEN	KiK-net11A
SITH01	IWATSUKI	35.929	139.7349	8	3510	SAITAMAKEN	KiK-net11A
SITH03	HIDAKA	35.899	139.3843	51	1800	SAITAMAKEN	KiK-net06
SITH04	TOKOROZAWA	35.8028	139.5353	30	2000	SAITAMAKEN	KiK-net06
SITH05	KAMIIZUMI	36.1509	139.0504	150	100	SAITAMAKEN	KiK-net11A
SMNH10	MIHONOSEKI	35.5579	133.3004	9	200	SHIMANEKEN	KiK-net06
SMNH12	YOSHIDA	35.1634	132.8558	380	101	SHIMANEKEN	KiK-net06
SMNH14	MUIKAMACHI	34.3904	131.8925	249	100	SHIMANEKEN	KiK-net06
SOYH02	SARUFUTSU-S	45.2163	142.2254	5	100	HOKKAIDO	KiK-net06
SOYH03	WAKKANAI-W	45.2531	141.6334	8	137	HOKKAIDO	KiK-net06
SOYH04	WAKKANAI-E	45.2303	141.8806	30	203	HOKKAIDO	KiK-net06
SOYH06	TOYOTOMI	45.1019	141.7834	15	135	HOKKAIDO	KiK-net11A
SRCH03	HOROKANAI-S	43.9994	142.1258	155	100	HOKKAIDO	KiK-net06
SRCH04	NUMATA	43.8203	141.9397	100	105	HOKKAIDO	KiK-net06
SRCH08	SUNAGAWA	43.5138	141.909	30	122	HOKKAIDO	KiK-net06
SRCH09	KURIYAMA	43.0587	141.8063	30	122	HOKKAIDO	KiK-net06
SRCH10	YUBARI	42.993	142.0085	195	200	HOKKAIDO	KiK-net06
SZOH24	INASA	34.8343	137.6616	19	300	SHIZUOKAKEN	KiK-net11B

SZOH26	FUKUROI	34.7948	137.9034	23	450	SHIZUOKAKEN	KiK-net06
SZOH41	MINAMIIZU	34.6749	138.834	60	109	SHIZUOKAKEN	KiK-net06
SZOH53	KAKEGAWA3	34.8768	138.0174	182	100	SHIZUOKA KEN	KiK-net11B
SZOH54	HATSUSHIMA2	35.0417	139.1685	20	110	SHIZUOKA KEN	KiK-net06
TCGH06	MOKA	36.4458	139.9509	70	1648	TOCHIGIKEN	KiK-net06
TCGH08	KURIYAMA-E	36.8828	139.6459	702	203	TOCHIGIKEN	KiK-net11A
TCGH11	IMAICHI	36.7084	139.7694	290	200	TOCHIGIKEN	KiK-net11A
TCGH13	BATO	36.7342	140.1781	135	140	TOCHIGIKEN	KiK-net11C
TCGH16	HAGA	36.548	140.0751	105	112	TOCHIGIKEN	KiK-net11A
TCGH17	FUJIHARA2	36.9853	139.6922	635	104	TOCHIGIKEN	KiK-net06
TKCH06	MEMURO	42.892	143.0603	97	227	HOKKAIDO	KiK-net06
TKCH07	TOYOKORO	42.8114	143.5203	9	100	HOKKAIDO	KiK-net06
TKSH02	SADAMITSU	34.0112	134.0918	190	100	TOKUSHIMAKEN	KiK-net11A
TKSH03	KOYADAIRA	33.8778	134.1294	640	201	TOKUSHIMAKEN	KiK-net11A
TKYH02	FUCHU	35.6539	139.4704	45	2753	TOKYOTO	KiK-net06
TKYH11	KOTO	35.6114	139.8125	6	3000	TOKYOTO	KiK-net11A
TKYH13	HINOHARA-S	35.7017	139.1275	360	100	TOKYOTO	KiK-net11B
TYMH02	DAIMON	36.7142	137.0378	5	212	TOYAMAKEN	KiK-net06
TYMH03	TOYAMA	36.7294	137.2627	8	580	TOYAMAKEN	KiK-net06
TYMH04	UOZU	36.7914	137.4689	154	100	TOYAMAKEN	KiK-net06
TYMH06	YATSUO	36.5711	137.1595	110	200	TOYAMAKEN	KiK-net06
WKYH04	SUSAMI	33.5559	135.5454	130	100	WAKAYAMAKEN	KiK-net11A
WKYH06	OTO	33.6948	135.5953	218	100	WAKAYAMAKEN	KiK-net11A
YMGH01	HOFU	34.0494	131.5618	35	200	YAMAGUCHIKEN	KiK-net11A
YMGH06	UBE	33.9893	131.3012	80	200	YAMAGUCHIKEN	KiK-net11A
YMGH12	MITO	34.2176	131.3597	150	102	YAMAGUCHIKEN	KiK-net06
YMGH16	KAMINOSEKI	33.826	132.104	65	106	YAMAGUCHIKEN	KiK-net06
YMNH08	NISHINOHARA	35.6895	138.734	375	1206	YAMANASHIKEN	KiK-net06
YMNH10	HAYAKAWA-N	35.5351	138.3087	695	107	YAMANASHIKEN	KiK-net11A
YMNH13	MINOBU	35.3509	138.4203	255	204	YAMANASHIKEN	KiK-net11A
YMNH14	TSURU-S	35.5115	138.9675	1010	250	YAMANASHIKEN	KiK-net11A
YMNH15	KAMIKUISHIKI	35.5323	138.6045	525	116	YAMANASHIKEN	KiK-net11A
YMNH16	KOFU2	35.7421	138.5653	595	256	YAMANASHIKEN	KiK-net06
YMTH01	TENDO	38.3841	140.3805	113	207	YAMAGATAKEN	KiK-net11A
YMTH02	YAMAGATA	38.2693	140.2583	130	150	YAMAGATAKEN	KiK-net11A
YMTH03	NANYO	38.1035	140.1553	278	114	YAMAGATAKEN	KiK-net11A
YMTH08	YAWATA	38.9701	140.0333	115	106	YAMAGATAKEN	KiK-net11A
YMTH14	NISHIKAWA-W	38.386	139.9916	465	103	YAMAGATAKEN	KiK-net11C

Author Contributions

Serkan Hasanoğlu: Development and application of MATLAB codes, writing, editing; **Ahmet Güllü**: Conceptualize, development of algorithms, evaluating the results, writing, editing.

Conflict of interest

The authors declare that there is no known conflict of interest.

REFERENCES

Dobry R, Oweis I & Urzua A (1976). Simplified procedures for estimating the fundamental period of a soil profile. Bulletin of Seismological Society of America 66:1293–1321.

Gazetas G (1982). Vibrational characteristics of soil deposits with variable wave velocity. Int. J. Numer. Anal. Methods Geomech. 6, 1–20, doi:10.1002/nag.1610060103.

Ghofrani H, Atkinson G M, & Goda K (2013). Implications of the 2011 M9.0 Tohoku Japan earthquake for the treatment of site effects in large earthquakes. Bull. Seismol. Soc. Am. 11, 171–203, doi:10.1007/s10518-012-9413-4.

Goda K, Kiyota T, Pokhrel RM, Chiaro G, Katagiri T, Sharma K & Wilkinson S (2015). The 2015 Gorkha Nepal earthquake: insights from earthquake damage survey, Frontiers in Built Environment, 1, 1-8. https://doi.org/10.3389/fbuil.2015.00008.

Güllü A, Yüksel E, Yalçın C, Dindar A A, Özkaynak H, Büyüköztürk O (2019). An improved input energy spectrum verified by shake table tests. Earthq. Eng. Struct. Dynam. 48(1), 27-45. doi: 10.1002/eqe.3121

Hadjian A H (2002). Fundamental period and mode shape of layered soil profiles. Soil. Dynam. Earthq. Eng. 22, 885–891. doi: 10.1016/S0267-7261(02)00111-2.

National Research Institute for Earth Science and Disaster (2019). NIED K-NET, KiK-net, National Research Institute for Earth Science and Disaster Resilience. doi:10.17598/NIED.0004.

Madera G A (1970). Fundamental Period and Amplification of Peak Acceleration in Layered Systems. Research Report R70-37, Dept. of Civil Engineering, MJ.T., Cambridge, Mass.

Mathworks Inc, MATLAB available at www.mathworks.com.

Sextos A, De Risi R, Pagliaroli A et al (2018), Local site effects and internal damage of buildings during the 2016 central Italy earthquake sequence, Earthquake Spectra, 34(4), 1639-1669. https://doi.org/10.1193/100317EQS194M.

Urzua A, Dobry R & Christian J (2017). Is harmonic averaging of shear wave velocity or the simplified Rayleigh method appropriate to estimate the period of a soil profile. Earthq. Spectra 33, 895–915. doi:10.1193/101716EQS174M.

Vijayendra K V, Nayak S & Prasad S K (2014). An Alternative Method to Estimate Fundamental Period of Layered Soil Deposit, Indian Geotech J. doi: 10.1007/s40098-014-0121-7

Wang S, Shi Y, Jiang W, Yao E & Miao Y (2018). Estimating Site Fundamental Period from Shear-Wave Velocity Profile. Bulletin of the Seismological Society of America,Vol. 108, No. 6, pp. 3431–3445. doi: 10.1785/0120180103.

Zhao J X (1996). Estimating modal parameters for a simple soft-soil site having a linear distribution of shear wave velocity with depth. Earthq. Eng. Struct. Dynam. 25, 163–178. doi: 10.1002/(SICI)1096-9845(199602) 25:2<163::AID-EQE544>3.0.CO;2-8.

Zhao J X (1997). Modal analysis of soft-soil sites including radiation damping. Earthq. Eng. Struct. Dynam. 26, 93–113. doi: 10.1002/(SICI)1096-9845(199701)26:1<93::AID-EQE625>3.0.CO;2-A

Zhao J X, Zhang J, Asano A, Ohno Y, Oouchi T, Takahashi T, Ogawa H, Irikura K, Thio H K & Somerville P G (2006). Attenuation relations of strong ground motion in Japan using site classification based on predominant period. Bull. Seismol. Soc. Am. 96,898–913, doi: 10.1785/0120050122.

Zhao J X & Xu H (2013). A comparison of VS30 and site period as site effect parameters in response spectral ground-motion prediction equations, Bull. Seismol. Soc. Am. 103, 1–18, doi: 10.1785/0120110251.

Zhao J X, Hu J S, Jiang F, Zhou J, Zhang Y B, An X M, Lu M & Rhoades D A (2015). Nonlinear site models derived from 1D analyses for ground-motion prediction equations using site class as the site parameter. Bull. Seismol. Soc. Am. 105, 2010–2022, doi: 10.1785/0120150019.

Turkish Journal of Engineering

https://dergipark.org.tr/en/pub/tuje

e-ISSN 2587-1366

Partial engine fault detection and control of a Quadrotor considering model uncertainty

Davood Asadi[*1]

[1]*Adana Alparslan Türkeş Science and Technology University, Aerospace Engineering Faculty, Adana, Turkey*

Keywords
Fault tolerant Control
Fault detection
Engine Fault
Autonomous Emergency Landing

ABSTRACT

This paper presents a trajectory tracking fault-tolerant control strategy inside an autonomous emergency landing architecture to control a quadrotor in case of partial rotor fault. The proposed architecture, which is composed of required hardware and subsystems, aims to ensure a fully autonomous safe landing of the impaired quadrotor to a suitable landing site. The controller strategy, which is tried to be coincident with the proposed emergency landing architecture and the Pixhawk autopilot contains a cascade three-loop structure of adaptive sliding mode and a modified PID algorithm along with a fault detection algorithm. The adaptive sliding mode and the PID algorithms are applied to the fast dynamics of angular velocity rates and the position control of the quadrotor, respectively. A lightweight fault detection algorithm is developed to detect and identify the partial faults of engine using the controller outputs and the filtered angular rates. The simulation results demonstrate that the proposed fault-tolerant controller can control the multi-rotor in partial engine faults with satisfactory tracking performance. The results also demonstrate the effect of fault detection time delay on the overall control performance.

1. INTRODUCTION

The development of multi-rotor Unmanned Aerial Vehicles (UAVs) is being increased in both military and civil applications due to significant benefits such as compactness, maneuverability, mechanical simplicity, quick deployment time, low cost, and ability to operate in outdoor and indoor environments. This development grows the demand for the vital problem of safety for the UAVs (Chen et al., 2015; Saied et al., 2015; Mazeh et al. 2018). One common problem regarding the safety of multi-rotor UAVs is the occurrence of actuator fault (engine fault or propeller damage). The fault of actuator might lead to a crash and loss of system or might endanger human beings to injury risks in the environment of operation (Giribet et al., 2018, Nguyen et al., 2019, Lopez-Franco et al., 2017). Redundancy is not a logical solution for multi-rotors due to added weight and complexity to the system. Therefore, automation enhancement has attracted the researchers as a viable solution to the challenging problem of flight safety of multi-rotor UAVs in emergency flight conditions [Asadi et al., 2017*a*, *b*; Asadi et al.2013; Asadi et al. 2014]. Fault-Tolerant Control (FTC) and Fault Detection and Identification (FDI) modules are key elements in the Autonomous Emergency Landing Architecture (AELA) for safe landing of UAVs in emergency flight conditions. In addition to the FTC and FDI modules, trajectory planning and landing site detection are other required subsystems in the AELA structure, as proposed in this paper.

Different control algorithms ranging from linear to nonlinear, sliding mode, robust, and adaptive control algorithms have been proposed in the literature to control the faulty aerial vehicles. In (Lanzon et al., 2014), a controller is presented for a quadrotor with single rotor failure applying robust feedback linearization and assuming that the failure is known. In Ref (Milton et al., 2019), a trajectory tracking adaptive dynamic controller was proposed to guide an unmanned aerial vehicle (UAV). Stability and control of quadcopters experiencing one, two, or three rotor failures are presented in (Mueller and Andrea 2014). Several control methods based on L_1 adaptive control (Ahmadi et al. 2017), Robust adaptive Control (Asadi and Ahmadi, 2020), sliding mode control (SMC) (Sharifi et al., 2010), and adaptive SMC techniques (Asadi et al., 2017, Barghandan et al., 2017) are proposed to handle model uncertainties and faults. Considering

* **Corresponding Author**

*(dasadihendoustani@atu.edu.tr) ORCID ID 0000 – 0002 – 2066 – 6016

Cite this article

Asadi D (2022). Partial engine fault detection and control of a Quadrotor considering model Uncertainty, Turkish Journal of Engineering – 2022; 6(2); 106-117

Research Article / DOI: 10.31127/tuje.843607

Received: 19/12/2020; Accepted: 04/03/2021

model-based control, the authors of (Mohammadi and Shahri 2013) proposed a model reference adaptive control (MRAC) technique to control a quadrotor with parametric and non-parametric uncertainties in the model. Supposing loss in the efficiency of a quadrotor's propeller, control algorithms are proposed in (Ranjbaran and Khorasani 2010, Zhang and Chamseddine, 2012) to estimate the aerial vehicle model after the failure, guaranteeing the stability of the platform. A back stepping approach is proposed in (Khebbache, et al., 2012) for the performance loss of the motors. In fault-tolerant control of multi-rotors, the existence of a fast converging algorithm is necessary for fault detection. Fault detection approaches can be categorized into model-based, signal-based, knowledge-based, and active diagnosis techniques (Zhiwei et al. 2015). (Amoozgar, et al. *2013)* proposed a two-stage Kalman filter to detect, isolate, and estimate possible faults in each motor whereas the method was evaluated on a UAV testbed. (Avram, et al., 2017) presented a fault identification scheme for actuator faults using nonlinear adaptive estimation technique. In Ref. (Cen, et al., 2014), an adaptive Thau observer was developed to estimate and detect the actuator faults. An on-line detection algorithm was proposed to detect a single motor failure and a control allocation technique is proposed to control the drone in (Frangenberg, et al., 2015). A parity space method with recursive least squares algorithm was introduced in (Han et al., 2018), for actuator faults detection and identification of a drone.

Landing site detection and trajectory planning modules are other critical issues besides the fault detection and control algorithm for safe landing of an impaired drone. Therefore, an Autonomous Emergency Landing Architecture (AELA) based on the Pixhawk autopilot is proposed for emergency landing of an impaired multi-rotor drone. Moreover, this research presents a fault-tolerant trajectory tracking control strategy, which can be implemented as a subsystem in the AELA. Therefore, this research is innovative in several ways including; 1) suggestion of AELA strategy to enable the faulty drone for a safe landing, 2) development of a complete mathematical nonlinear model considering dynamic uncertainties due to rotors' gyroscopic effects and airframe drag along with partial actuator fault effect, 3) application of a cascade fault-tolerant adaptive sliding model controller integrated with a modified PID algorithm with anti-windup filter, 4) application of a fast converging fault detection algorithm for partial engine fault detection based on the extended Kalman filter estimate of states. In order to be coincident with the Pixhawak software structure and having minimum required changes, a three-loop control algorithm similar to the Pixhawk autopilot is proposed in the controller design section.

In section II the AELA structure and in section III the mathematical modeling is discussed. Section IV introduces the fault tolerant control and fault detection algorithm. Sections V presents the simulation results that validate the proposed approach. Finally, section VI points out the key conclusions.

2. Autonomous Emergency Landing Architecture

In fault scenarios where continuation of flight is not possible or endangers the flight safety, the emergency flight system is triggered to recover the drone's stability and safely guide it toward a suitable landing site (Nguyen et al., 2019). There are several challenges respecting the safe landing of an impaired drone such as obstacle detection, suitable landing site detection/selection, fault detection and identification, characterizing the aircraft's kinematic constraints, trajectory planning to the desired landing area, and control of the faulty drone toward the landing site. To cover these challenges, an Autonomous Emergency Landing Architecture (AELA) is proposed according to Figure 1. The AELA is translated to an architecture consisting of various subsystems that are capable of landing a faulty drone to the desired landing site over a designed trajectory without colliding with human or animal. In the proposed AELA, the fault detection algorithm identifies the fault based on the filtered IMU (Inertial Measurement Unit) and GPS data applying the Kalman filter. In the meanwhile, on-line images in the drone's Field of View (FOV), taken by the onboard camera along with image processing algorithms are implemented for suitable landing site detection as well as obstacles/human detection in the vicinity of the desired landing site. The area that is free from the obstacle and closest to the center of the image is defined as the most immediate and suitable landing zone. After characterizing a suitable landing site, the trajectory generation unit generates a controllable trajectory toward the selected landing site. The controller generates the required total thrust and three-axis torques to track the desired trajectory toward the landing site. A Multi-Criteria Decision-Making (MCDM) algorithm manages the strategic decision and controls the whole architecture. The emergency landing mission continues as long as the number of functioning motors provides controllability of the drone otherwise MCDM switches to a safe crash.

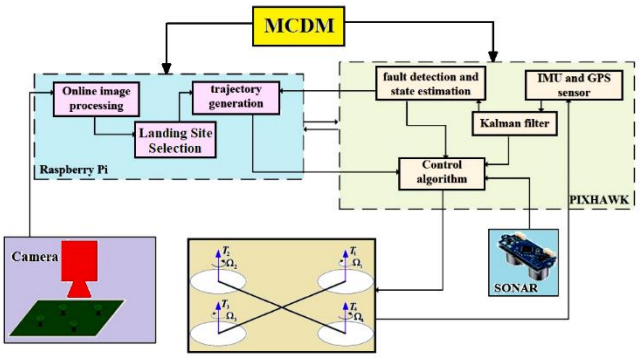

Figure 1. Autonomous Emergency Landing Architecture with Subsystems

The Pixhawk flight controller which is equipped with GPS, IMU, and SONAR is proposed as the autopilot board, which enables the engine control, navigation, and communication with the ground station (Desaraju et al., 2015). The Pixhawk applies an open-source flight control software (Github PX4 Documentation), which can be used as the baseline for the developed algorithms required for emergency landing. The controller

algorithms, the guidance and navigation algorithms, estimators, and filters, can be modified according to the required proposed algorithms for AELA. Image processing and trajectory planning task is executed on the "Raspberry Pie 3" board. A connection between the Raspberry Pie and Pixhawk is required to transmit the position of the landing area and obstacles for guidance and control of the drone.

3. Mathematical Model

In this section, the quadrotor model, the engine model, as well as the motor mixer equations are presented.

3.1. Quadrotor Model

The S500 frame (Fig. 3) with the EMAX MT3506 650KV motors with 11-inch diameter propellers have been selected in this research. The quadrotor parameters which is used in the simulations are given in Table 1.

Table 1. Quadrotor frame Specifications

Quadrotor Parameters	
Mass, *m*	1.6 kg
Thrust Coefficient, *b*	4.068×10^{-7} N/rpm^2
Drag Coefficient, *d*	8.43×10^{-9} Nm/rpm^2
Moment arm, *l*	0.243 m
Moment of Inertia about *x*-axis, Ixx	0.0213 kg.m^2
Moment of Inertia about *y*-axis, Iyy	0.0221 kg.m^2
Moment of Inertia about *z*-axis, Izz	0.028 kg.m2
Total rotational moment of inertia, J_T	6.8×10^{-5} kg.m^2

3.2. Dynamic Equations

The translational and rotational equations of the quadrotor in the body frame are presented in Eq.s (1) and (2), respectively. As depicted in Figure 2, the quadrotor consists of four motors, which motors number one and three rotate clock-wise with velocities Ω_1, Ω_3, respectively, whereas the other two other motors (2, 4) rotate in the opposite (counter-clockwise) direction with velocities Ω_2, Ω_4.

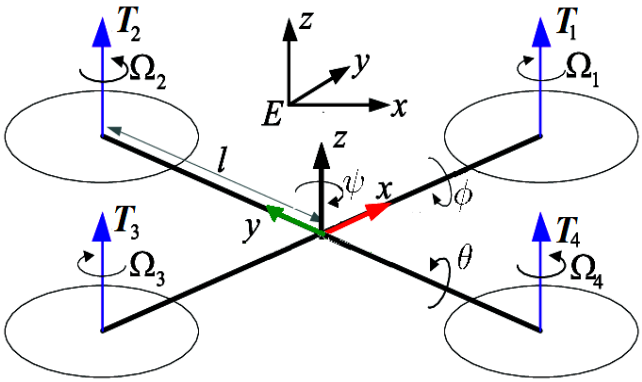

Figure 2. Schematic representation of quadrotor

Applying the rigid-body equations of motion and Euler angle transformation (Eq. (4)), the complete dynamical model of the quadrotor is presented as below:

3.2.1. Translational dynamics

$$\begin{aligned}
\ddot{x} &= (\sin\psi\sin\phi+\cos\psi\sin\theta\cos\phi)\frac{u_z}{m}-\frac{k_x}{m}\dot{x}\\
\ddot{y} &= (-\cos\psi\sin\phi+\sin\psi\sin\theta\cos\phi)\frac{u_z}{m}-\frac{k_y}{m}\dot{y}\\
\ddot{z} &= -g+(\cos\theta\cos\phi)\frac{u_z}{m}-\frac{k_z}{m}\dot{z}
\end{aligned} \tag{1}$$

where *x*, *y*, and *z* are the position of quadrotor center of mass in inertial frame and ψ,θ,φ are the Euler angles, which represent the body-frame rotation with respect to the Inertial frame.

The input u_z is the total lift force (u_z) generated by propellers in *z*-direction. $k_x = k_y = 5.5e-4\,{}^{N}/_{m/s}$, $k_z = 6.3e-4\,{}^{N}/_{m/s}$ are translational drag coefficients. The last terms in the above equation regarding the airframe drag are applied in the equations of motion but is considered as model uncertainty, when designing the controller algorithm.

3.2.2. Rotational dynamics

$$\begin{aligned}
\dot{p} &= \frac{I_{yy}-I_{zz}}{I_{xx}}qr+\frac{u_\varphi}{I_{xx}}+\frac{J_T}{I_{xx}}q\Omega-\frac{k_\varphi}{I_{xx}}p^2\\
\dot{q} &= \frac{I_{zz}-I_{xx}}{I_{yy}}pr+\frac{u_\theta}{I_{yy}}-\frac{J_T}{I_{yy}}p\,\Omega-\frac{k_\theta}{I_{yy}}q^2\\
\dot{r} &= \frac{I_{xx}-I_{yy}}{I_{zz}}pq+\frac{u_\psi}{I_{zz}}-\frac{k_\psi}{I_{zz}}r^2
\end{aligned} \tag{2}$$

where I_{xx}, I_{yy} and I_{zz} are the moment of inertia in *x*, *y* and *z* direction, respectively. The quadrotor inputs are represented by $u_\varphi, u_\theta, u_\psi$, which are moments about *x*, *y*, *z* axes, respectively. $k_\varphi = k_\theta = 5.5e-4\,N/rad/s$, $k_\psi = 6.35e-4\,N/rad/s$ are rotational drag coefficients. J_T is the moment of inertia of each motor and Ω represents the propellers total speed as below:

$$\Omega = -\Omega_1-\Omega_2+\Omega_3+\Omega_4 \tag{3}$$

The drag and gyroscopic terms in the rotational dynamics equations are the unknown terms and are considered as the model uncertainty.

3.2.3. Euler Equations

$$\begin{aligned}
\dot{\varphi} &= p+q\sin\varphi\tan\theta+r\cos\varphi\tan\theta\\
\dot{\theta} &= q\cos\varphi-r\sin\varphi\\
\dot{\psi} &= \frac{1}{\cos\theta}\left[q\sin\varphi+r\cos\varphi\right]
\end{aligned} \tag{4}$$

Where ψ,θ,φ are the Euler angles, which represent the body frame rotation with respect to the inertial frame.

3.3. Rotor Dynamics

The thrust generated by the engines are modeled as a first-order system to account for the engines dynamic for variation of rotational speed:

$$u_{i_c} = K\frac{\omega_0}{S+\omega_0}u_i \tag{5}$$

where u_{i_c} is the i-th engine input which is the PWM reference signal to the engines, K is the motor gain, and ω_0 is the bandwidth of the engines. The engines' thrust force and torque depend on the rotational velocity, propeller diameter, as well as the aerodynamics characteristics of blades as below:

$$\begin{aligned} T_i &= C_t \rho \Omega_i^2 D^4 = b \Omega_i^2 \\ Q_i &= C_d \rho \Omega_i^2 D^5 = k T_i = d \Omega_i^2,\ k = 2.07e-2\ m \end{aligned} \tag{6}$$

where C_t, C_d are thrust and drag coefficients, ρ is air density, Ω_i is the rotational speed of each engine in rpm, and D is the propeller diameter. The numerical values of b and d are introduced in Table 1. Accordingly, the actuation inputs around body-frame are expressed as follows:

$$\begin{aligned} u_z &= T_1 + T_2 + T_3 + T_4 = b(\Omega_1^2 + \Omega_2^2 + \Omega_3^2 + \Omega_4^2) \\ u_\varphi &= l(T_2 - T_4) = b l(\Omega_2^2 - \Omega_4^2) \\ u_\theta &= l(T_3 - T_1) = b l(\Omega_3^2 - \Omega_1^2) \\ u_\psi &= k(T_1 + T_3 - T_2 - T_4) = d(\Omega_1^2 + \Omega_3^2 - \Omega_2^2 - \Omega_4^2) \end{aligned} \tag{7}$$

The autopilot outputs ($u_z\ u_\varphi\ u_\theta\ u_\psi$) must be translated into each motor inputs to send the signal to the quadrotor speed controls then apply the related PWM signal to each quadrotor's engine.

3.4. Motor Mixer

Given that the controller computes the intermediate control inputs ($u_z, u_\varphi, u_\theta, u_\psi$), these are transformed into the engines desired rotational velocities. Typically, this transformation is called motor mixing. By inverting the relationship of Eq. (7), motor mixer expression is derived as below:

$$\begin{bmatrix} \Omega_1^2 \\ \Omega_2^2 \\ \Omega_3^2 \\ \Omega_4^2 \end{bmatrix} = \begin{bmatrix} \frac{1}{4b} & 0 & \frac{-1}{2lb} & \frac{1}{4d} \\ \frac{1}{4b} & \frac{1}{2lb} & 0 & \frac{-1}{4d} \\ \frac{1}{4b} & 0 & \frac{1}{2lb} & \frac{1}{4d} \\ \frac{1}{4b} & \frac{-1}{2lb} & 0 & \frac{-1}{4d} \end{bmatrix} \begin{bmatrix} u_z \\ u_\theta \\ u_\varphi \\ u_\psi \end{bmatrix} \tag{8}$$

3.5. Engine fault modeling

The fault considered in this paper is a sudden partial loss of engine propeller. If damage occurs on the propeller, the thrust and torque of the faulty engine can be expressed as a parametric uncertainty as follows:

$$\begin{aligned} T_{if} &= T_i + \Delta T_i = b\Omega_i^2 + \Delta b \Omega_i^2,\ \Delta b = -f_i b \\ Q_{if} &= Q_i + \Delta Q_i = d\Omega_i^2 + \Delta d\, \Omega_i^2,\ \Delta d = -f_i d \end{aligned} \tag{9}$$

Where $\Delta b, \Delta d$ are bounded variation of propeller effectiveness respecting its nominal values and can be represented as $-b \le \Delta b \le 0$, $-d \le \Delta d \le 0$ and f_i is the i-*th* engine fault. Therefore, the actual signal (U) generated by the faulty actuator (U^f) is as follows:

$$\begin{aligned} U^f(t) &= (1-\Gamma)U(t) \\ \Gamma &= \begin{cases} 0 & t < t_f \\ diag(f_1, f_2, f_3, f_4) & t > t_f \end{cases} \end{aligned} \tag{10}$$

Where $0 \le f_i < 1$ and $f_i = 0$, $f_i = 1$ represent the healthy and the fully damaged rotor, respectively and t_f is the time that fault occurs.

4. Fault Tolerant Control Strategy

In this section, by applying the multiple-timescales approach, the rotational and translational dynamics are separated by assuming that the rotational dynamics is much faster than the translational dynamics. In the PX4 software of the Pixhawk autopilot, a three-loop cascade architecture composed of a rate controller, an attitude controller, and a position controller exists to control the aerial vehicles.

Thus, in order to be coincident and consistent with the Pixhawak software structure and having minimum required changes on the software, a three-loop control algorithm is proposed in this paper. According to Fig. 3, for the fast inner-loop, a nonlinear adaptive sliding mode controller is applied and for the two slow outer-loops of attitude and position, the desired dynamics and PID algorithm similar to the PX4 algorithm with some modifications is proposed.

Based on the rotational dynamics according to Eq. (2), the uncertainty due to engine fault, and the fault model based on Eq. (11), the nonlinear model of quadrotor can be transformed into an affine control model as below:

$$\dot{x} = f(\mathrm{x}) + \Delta f(\mathrm{x}) + [\mathrm{g}(\mathrm{x}) + \Delta g]U \tag{11}$$

where $x \in \Re^3$ is the vector of rotational velocities ($x = [p, q, r]$); $U \in \Re^3$ is the plant control input vector ($U = [u_\theta, u_\varphi, u_\psi]$); $f(\mathrm{x}) \in \Re^3$ and $g(\mathrm{x}) \in \Re^{3\times3}$ are known differentiable vector functions and input matrices, respectively, $\Delta g(\mathrm{x}) \in \Re^{3\times3}$ is the unknown bounded perturbations due to the propeller damage, and $\Delta f(\mathrm{x}) \in \Re^3$ is an unknown bounded uncertainty caused by propellers gyroscopic effects and airframe drag as defined below:

$$f(\mathrm{x}) = \begin{bmatrix} \frac{I_{yy} - I_{zz}}{I_{xx}} qr \\ \frac{I_{zz} - I_{xx}}{I_{yy}} pr \\ \frac{I_{xx} - I_{yy}}{I_{zz}} pq \end{bmatrix},\ \Delta f(\mathrm{x}) = \begin{bmatrix} \frac{J_T}{I_{xx}} q\Omega - \frac{k_\varphi}{I_{xx}} p^2 \\ -\frac{J_T}{I_{yy}} p\,\Omega - \frac{k_\theta}{I_{yy}} q^2 \\ -\frac{k_\psi}{I_{zz}} r^2 \end{bmatrix} \tag{12}$$

$$g(\mathrm{x}) = diag(\frac{l}{I_{xx}}, \frac{l}{I_{yy}}, \frac{l}{I_{zz}}),$$
$$\Delta g(\mathrm{x}) = diag(\frac{-l\, f_1}{I_{xx}}, \frac{-l\, f_2}{I_{yy}}, \frac{-l\, f_3}{I_{zz}}) \quad (13)$$

4.1. Inner-Loop Controller Design

For the inner-loop rotational dynamics an adaptive sliding mode controller is proposed. Accordingly, the sliding function is defined based on the error dynamics as below:

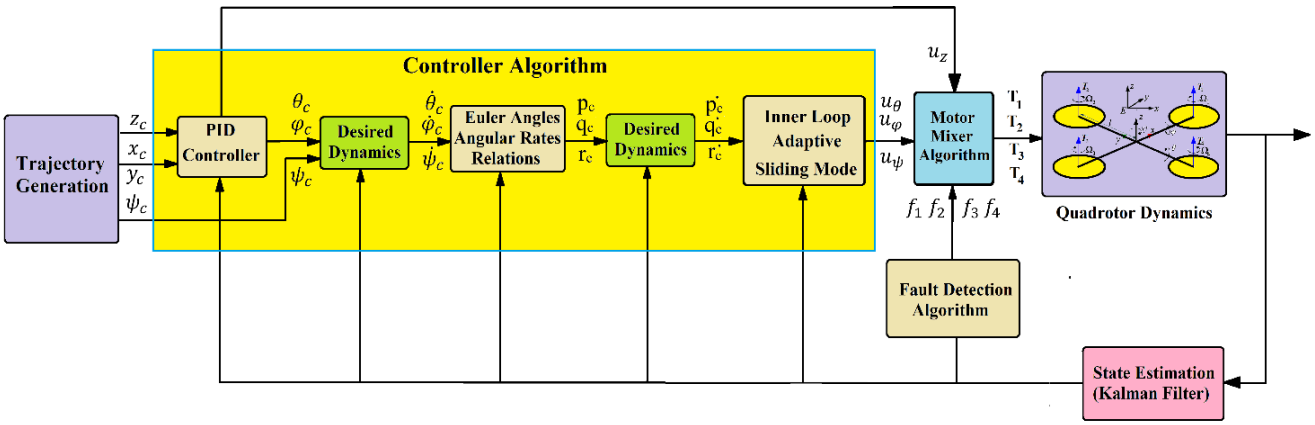

Figure 3. Three-Loop Fault-Tolerant Control Block Diagram

$$S = e + k\int_0^t e\, d\tau,\ S, e \in \Re^3$$
$$S = [s_1, s_2, s_3],\ e = [e_1, e_2, e_3] \quad (14)$$

where e is the error defined as $e_i = x_{c_i} - x_i$, and $k = diag\{k_i\}$, i = 1, 2, 3 is the gain defined to achieve the desired dynamics. Based on the introduced sliding function, a positive definite Lyapunov functional is defined and the sliding mode algorithm is derived based on the time derivation of the Lyapunov function:

$$V = \tfrac{1}{2} S^T S$$
$$\dot{V} = S^T(\dot{\mathrm{x}}_c - f(\mathrm{x}) - \Delta f(\mathrm{x}) - (g(\mathrm{x}) - \Delta g(\mathrm{x}))\delta + k e) \quad (15)$$
$$\dot{V} = S^T(\psi_0 - (g(\mathrm{x}) - \Delta g(\mathrm{x}))\delta),\ \psi_0 = \dot{\mathrm{x}}_c - f - \Delta f + k e$$

By forcing the time derivative of the Lyapunov function to be negative $\dot{V} < 0$, the error dynamics can be reduced. Proper selection of input commands can guarantee the stability of the rotation dynamics as below:

$$\delta_c = \hat{\delta}_{c_{eq}} + diag(\rho_i)\, g^{-1}(\mathrm{x})\, SIGN(\mathrm{S})$$
$$\hat{\delta}_{c_{eq}} = g^{-1}(\mathrm{x})\hat{\psi}_0\ ,\ \hat{\psi}_0 = \dot{\mathrm{x}}_c - f(\mathrm{x}) + k e \quad (16)$$
$$\rho_i = \rho_{b_i} + k_{\rho_i}\int_0^t |s_i|\, d\tau\ ,\ \rho_i > 0$$

where SIGN (S) is the sign function operating on the sliding function and other terms are defined as below:

$$\varphi_0 = \psi_0 - (\mathrm{I} + E_0)\hat{\psi}_0\ ,\ \varphi_0 \in \Re^3,\ \mathrm{I} \in \Re^{3\times 3}$$
$$E_0 = \Delta g_1\, g_1^{-1},\quad E_0 \in \Re^{3\times 3}, \quad (17)$$
$$\tilde{\rho}_i = \rho_{b_i} - \rho_i,\ \rho_{b_i} = \frac{\gamma_i}{1 - L_i}$$

Where $\dot{\gamma}$ and L_i are the logical bounds on the functions φ_0 and E_0, respectively and the ρ_i values are also defined based on the aforementioned bounds as below:

$$|\varphi_{0i}| < \gamma_i < \infty,\ |E_{0ij}| < \sigma_{ij},\ \sum_{j=1}^{3}\sigma_{ij} < L_i < 1,\ \rho_i > \frac{\gamma_i}{1 - L_i}$$
$$\forall i = 1,2,3\ ,\ \forall j = 1,2,3 \quad (18)$$

The output commands of the sliding mode controller in Eq. (16) has undesirable chattering problem during the system operation on the sliding function and therefore must be removed. Thus, a continuous standard saturation function, *sat ()*, is defined and replaced instead of SIGN(S) function to avoid this problem as below:

$$sat(s_i/\varepsilon_i) = \begin{cases} 1 & if\ \ s_i > \varepsilon_i \\ s_i/\varepsilon_i & if\ \ |s_i| \le \varepsilon_i \\ -1 & if\ \ s_i < \varepsilon_i \end{cases} \quad (19)$$

Where ε_i is a constant value defined by the designer to avoid the chattering problem. Applying the adaptive sliding controller in Eq. (18), the asymptotically tracking of the inner-loop desired inputs $x = \{p_c, q_c, r_c\}$ can be ensured by demonstrating that the Lyapunov function is negative. The details of the stability proof and adaptive sliding mode control algorithm has been presented in our previous research (Asadi et al., 2017)

A proportional-integral (PI) feedback controller is applied to track the reference model and generating the pseudo input $\dot{x}_c$ (Asadi et al., 2017) according to Fig. 4.

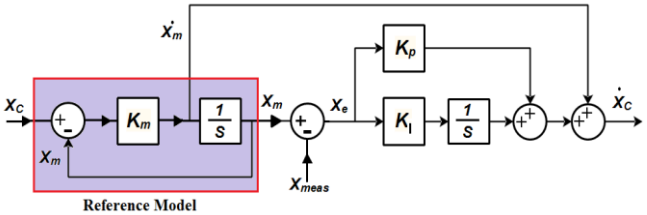

Figure 4. Desired Dynamics Block Diagram

4.2. Outer Loop Controller Design

For the outer-loop position control, a modified PID control algorithm is applied. Based on the desired trajectory and their first and second derivatives, the dynamics of the position error can be derived as:

$$\begin{aligned} &\ddot{P}_e + K_d \dot{P}_e + K_p P_e + K_i \int P_e \, dt = 0 \\ &P_d = [x_d, y_d, z_d], \; P_e = P_d - P \end{aligned} \tag{20}$$

Where P_d is the desired position with bounded first and second derivatives, P_e is the positions error, and the PID gains (K_p, K_d, K_i) are derived based on the conditions of Routh-Hurwitz to exponentially converge the error to zero. Based on the error dynamics, the following equation can be derived:

$$\ddot{P} = \ddot{P}_d + K_d \dot{P}_e + K_p P_e + K_i \int P_e \, dt = 0 \tag{21}$$

Based on the desired positions and translational dynamics of Eq. (1), the desired Euler angles can be derived as below:

$$\begin{cases} \theta_c = \arcsin\left(\dfrac{m\ddot{x}}{\cos\psi_d \, u_z} \right) \\ \varphi_c = -\arcsin\left(\dfrac{m\ddot{y}}{\cos\psi_d \, u_z} \right) \end{cases} \tag{22}$$

where in the above equation $u_z = m\sqrt{\ddot{x} + \ddot{y} + (\ddot{z} + g)}$ and the desire heading angle (ψ_d) is imposed by the trajectory generation module.

4.3. State Estimation

The extended Kalman filter is applied for the quadrotor state estimation using the GPS, IMU, magnetometer, SONAR, and accelerometers data in the presence of sensor noise and system disturbance. IMU measures the angular rates, magnetometer, and accelerometer data are applied to estimate the Euler angles (based on Eq. (22)), and SONAR and GPS are used to measure the altitude and position. Extended Kalman filters apply a two-step recursive process, which predicts the estimates, by applying prior knowledge of the states and then correct the states by using the current measurements. The nonlinear dynamics of quadrotor can be shown as below:

$$\begin{aligned} x_k &= f(x_{k-1}, u_k) + w_k \\ z_k &= h(x_k) + v_k \end{aligned} \tag{23}$$

where u_k is the control input and w_k and v_k are the process and output noises with assumed zero mean and with covariances Q_k and R_k, respectively. By linearizing the nonlinear system about each trim condition, the linear state equation and the error covariance matrix is derived as:

$$\begin{aligned} \hat{x}_{k|k-1} &= F_k \hat{x}_{k-1|k-1} + B_{k-1} u_{k-1} \\ P_{k|k-1} &= F_k P_{k-1|k-1} F_k^{\,T} + Q_{k-1} \end{aligned} \tag{24}$$

Where $\hat{x}_{k|k-1}$ is the state estimation, F_k is the transition matrix, u_{k-1} is the control input, B_{k-1} is the control input matrix, and $P_{k|k-1}$ is the error covariance matrix. The readers are referred to Ref (Tarhan and Altug, 2011, Merheb 2016) for more details about the Extended Kalman filter and the linearization of state.

4.4. Fault detection and Identification

The relationship between the controller output and each engine thrust considering the effect of fault is as follows:

$$\begin{bmatrix} T_1 \\ T_2 \\ T_3 \\ T_4 \end{bmatrix} = \begin{bmatrix} \frac{1}{4(1-f_1)} & 0 & \frac{-1}{2l(1-f_1)} & \frac{1}{4(1-f_1)} \\ \frac{1}{4(1-f_2)} & \frac{1}{2l(1-f_2)} & 0 & \frac{-1}{4(1-f_2)} \\ \frac{1}{4(1-f_3)} & 0 & \frac{1}{2l(1-f_3)} & \frac{1}{4(1-f_3)} \\ \frac{1}{4(1-f_4)} & \frac{-1}{2l(1-f_4)} & 0 & \frac{-1}{4(1-f_4)} \end{bmatrix} \begin{bmatrix} u_z \\ u_\theta \\ u_\varphi \\ u_\psi \end{bmatrix} \tag{25}$$

Since there is no sensor to measure the engine thrust, estimated states by Kalman filter and the controller outputs are used to detect and identify the partial propeller fault. In the case of propeller damage, the objective is to detect the faulty engine and identify the magnitude of fault f_i.

The differences between the controller outputs and the angular rates after one sample time (T_s) are used for fault detection. The criteria for the occurrence of partial damage to each engine is as follows:

- If $\Delta u_\theta < u_{threshold}$ and $\Delta q > q_{threshold}$, number **one** engine is faulty.
- If $\Delta u_\theta < u_{threshold}$ and $\Delta q > q_{threshold}$, number **two** engine is faulty.
- If $\Delta u_\varphi < u_{threshold}$ and $\Delta p > p_{threshold}$, number **three** engine is faulty.
- If $\Delta u_\varphi < u_{threshold}$ and $\Delta p > p_{threshold}$, number **four** engine is faulty.

where $\Delta u_\varphi, \Delta u_\theta$ are the input change one step time before the fault time as $\Delta u_\varphi = u_\varphi(t_f - T_s) - u_\varphi(t_f - 2T_s)$ and Δp and Δq are the change of angular velocity at the time of fault as $\Delta p = p(t_f) - p(t_f - T_s)$. The angular rates are measured using the extended Kalman filter. The presented control architecture is able to effectively track the desired trajectory considering uncertainty and limited amounts of propeller damage but is not able to control the system in the presence of severe faults. Therefore, the threshold values are determined based on the performance of the controller without fault detection algorithm.

Table 2 presents a lookup table which is prepared by injecting different magnitudes of the fault and measuring the filtered variation of angular rotations ($\Delta p, \Delta q$) in the simulation. A fixed time-step of $T_s = 0.01$ has been applied in the simulation. Based on the quadrotor rotational equations the rotational rates can be estimated as below:

$$\frac{(p_k - p_{k+1})}{T_s} \cong \frac{l}{I_x}(T_4 k_4 - T_2 k_2) \tag{26}$$

Where $k_i = 1 - f_i$ in the above equation. Considering each engine thrust force equal to $T_4 = T_2 = W/4$ in hover trim condition and considering that damage occurs on one of the engines, $\Delta k_p = k_4 - k_2$ can be estimated as below:

$$\Delta k_p \cong \frac{4I_x}{lW}(\frac{\Delta p}{T_s}) \tag{27}$$

Therefore, if $\Delta p < 0$, then $\Delta k_p < 0$ meaning that engine number four is faulty otherwise if $\Delta p > 0$, then $\Delta k_p > 0$ and therefore number two engine is faulty. Since it is assumed that only one engine is faulty, the percentage of fault magnitude is equal to $f = 1 - \Delta k_p$.

Table 2. Look up table for engine fault estimation, values in deg/s

Engine	10%	20%	30%	40%	50%
No.1	$\Delta q = -2.55$ $\lvert\Delta p\rvert < p_{threshold}$	$\Delta q = -5.1$ $\lvert\Delta p\rvert < p_{threshold}$	$\Delta q = -7.66$ $\lvert\Delta p\rvert < p_{threshold}$	$\Delta q = -9.87$ $\lvert\Delta p\rvert < p_{threshold}$	$\Delta q = -12.62$ $\lvert\Delta p\rvert < p_{threshold}$
No.2	$\Delta p = 2.55$ $\lvert\Delta q\rvert < q_{threshold}$	$\Delta p = 5.1$ $\lvert\Delta q\rvert < q_{threshold}$	$\Delta p = 7.66$ $\lvert\Delta q\rvert < q_{threshold}$	$\Delta p = 9.87$ $\lvert\Delta q\rvert < q_{threshold}$	$\Delta p = 12.62$ $\lvert\Delta q\rvert < q_{threshold}$
No.3	$\Delta q = 2.55$ $\lvert\Delta p\rvert < p_{threshold}$	$\Delta q = 5.1$ $\lvert\Delta p\rvert < p_{threshold}$	$\Delta q = 7.66$ $\lvert\Delta p\rvert < p_{threshold}$	$\Delta q = 9.87$ $\lvert\Delta p\rvert < p_{threshold}$	$\Delta q = 12.62$ $\lvert\Delta p\rvert < p_{threshold}$
No.4	$\Delta p = -2.55$ $\lvert\Delta q\rvert < q_{threshold}$	$\Delta p = -5.1$ $\lvert\Delta q\rvert < q_{threshold}$	$\Delta p = -7.66$ $\lvert\Delta q\rvert < q_{threshold}$	$\Delta p = -9.87$ $\lvert\Delta q\rvert < q_{threshold}$	$\Delta p = -12.62$ $\lvert\Delta q\rvert < q_{threshold}$

The same formulation and results can be derived for the pitch dynamics respecting the percentage of fault regarding number one and three engines. Table 2 shows the signs and magnitudes of rotational angular velocity variation in different percentages of propeller fault where the maximum fault is considered to be 50% of partial damage on one of the quadrotor engine's propeller.

The magnitude of thresholds in **Table 2** is determined based on the magnitudes of Δp and Δq for 5% of propeller damage. It will be shown that the proposed adaptive sliding mode controller is robust and has desirable performance for 5% of damage to any one of the engine's propeller.

5. Simulation results

Several numerical simulations are considered in the presence of partial loss of rotor effectiveness to verify the performance of the proposed three-loop fault-tolerant controller. First, the robustness of the controller is investigated without applying the fault detection algorithm. Next, the performance of the fault-tolerant control is examined for different percentages of fault on different engines.

5.1. Controller without fault detection algorithm

The robustness of the proposed adaptive sliding mode controller is examined in the presence of 5% and 10% of the propeller fault of number one engine. Fig. 5 illustrates the controller performance for the above cases. The fault is introduced to the quadrotor model at *t=10s* while the control algorithm tries to recover the quadrotor stability and tracking the desired inputs of position (*x*, *y*, *h*) and a constant heading rate (ψ). Accordingly, the proposed controller performance is satisfactory for 5% of the fault but is not desirable in 10% of fault. Based on the simulations it can be inferred that the proposed controller is robust for 10% of the engine fault but does not have a good tracking performance. Therefore, the fault detection algorithm will be applied for the faults bigger than 5%.

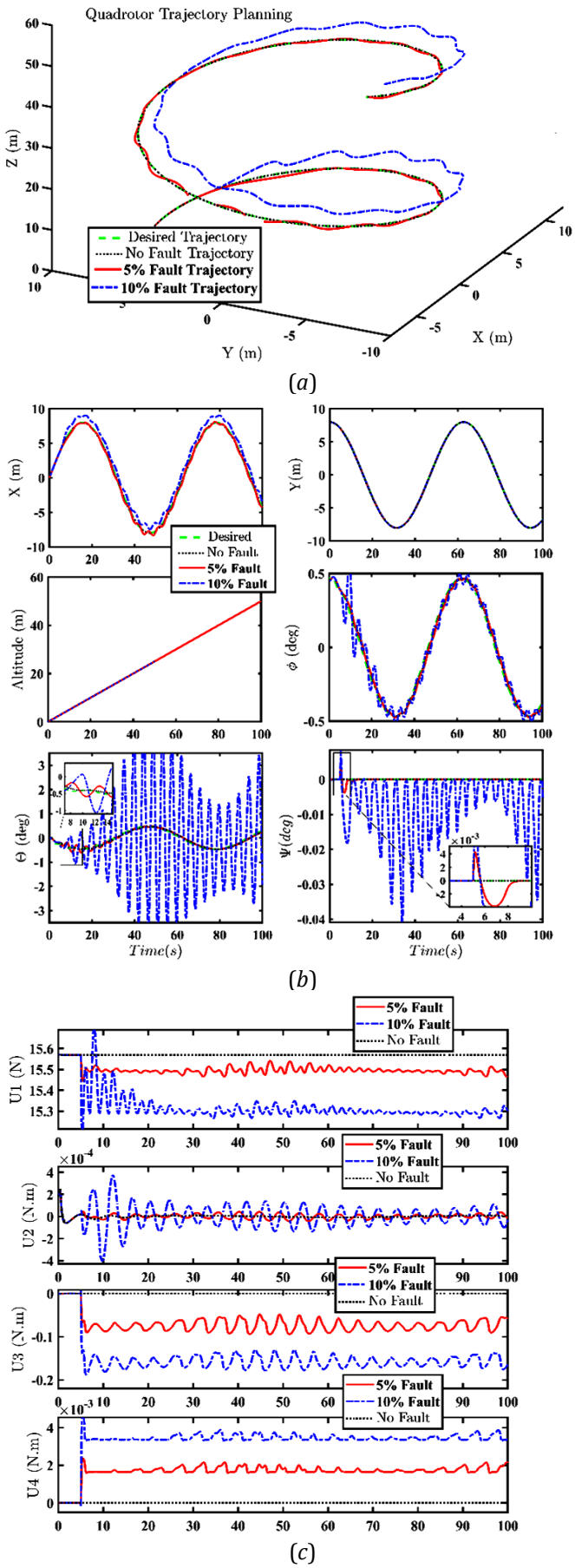

Fig. 5 Controller performance without fault detection algorithm for: no fault, 5% propeller fault, and 10% of fault, (a) 3-D trajectory, (b) Position and Euler angles, (c) Controller outputs

5.2. Fault-tolerant Controller performance

The proposed controller must recover the stability of quadrotor and track the desired trajectory in the presence of abrupt propeller effectiveness up to 50% of damage. For the propeller faults more than 50% the faulty engine will be saturated and cannot generate enough thrust to control all three rotations of quadrotor around x, y, and z axes. For more severe faults or complete loss of one engine, which is not the case of analysis in this paper, the control of one axis (around z) is neglected and the other two axes (roll and pitch) are controlled. According to the lookup table of Table 2, the variation of pitch and roll rates is used to detect and identify the partial rotor damage. For this purpose, the Extended Kalman Filter (EKF) is applied to minimize the effect of noise.

The performance of the proposed fault-tolerant controller is examined in two separate fault scenarios. 40% of fault is introduced to the engine number 2, in the first scenario. Fig. 6 illustrates the tracking performance of the controller in the first scenario. Fig10*a* represents the position and Euler angles tracking. A sudden increase in roll angle and yaw angle is experienced due to the propeller damage at t=10s but the controller satisfactorily recovers the roll and yaw angles and tracks the desired input values. Fig.6 (*b*, *c*) illustrates the controller outputs and each engine rotational velocity that affect the thrust force, respectively. Accordingly, the rotational speed of the faulty engine suddenly increases to compensate for the thrust reduction of the due to 40% of propeller damage.

Fig.6*d* illustrate the variation of estimated pitch rate, which is used for fault estimation. At time t_f =10s, the pitch rate suddenly changes from around zero to 12 *deg/s* which indicates 50% of fault in the second engine as described in Table 2. In fact, the fault of number 2 engine induces an abrupt positive roll rate and consequently positive roll angle. Fig.6*e* depicts the estimated percentage of fault which occurs one time-step ahead at t = 10.01s. According to the described fault detection logic, the value of fault will be determined based on the initial jump of the angular rates bigger than a threshold value, which is considered as 2 *deg/s*. In fact, this value is less than the effect of 5% damage, which can be tackled by the controller without fault detection and is bigger than the effect of state and output noises.

Scenario 2, investigates the control algorithm performance for the partial damage to the propeller of engine number one. The fault to engine one induces a sudden negative pitch rate according to Eq. (1). Simulation results of different fault cases of 30%, 40%, and 50% demonstrate the acceptable performance of the proposed strategy in controlling the drone in the presence of noise and engine fault. Fig. 7*a* and Fig 7*b* illustrates the Euler angles and the rotational speeds of each engine, respectively. Accordingly, a sudden increase in the rotational speed of engine number one is obvious. Fig. 7(*c*, *d*) illustrate the fault detection procedure based on the variations of angular rates and the values presented in Table 2 for the 40% of the fault to engine number 1. At t_f =10 s, the pitch rate suddenly changes from zero to -10 deg/s.

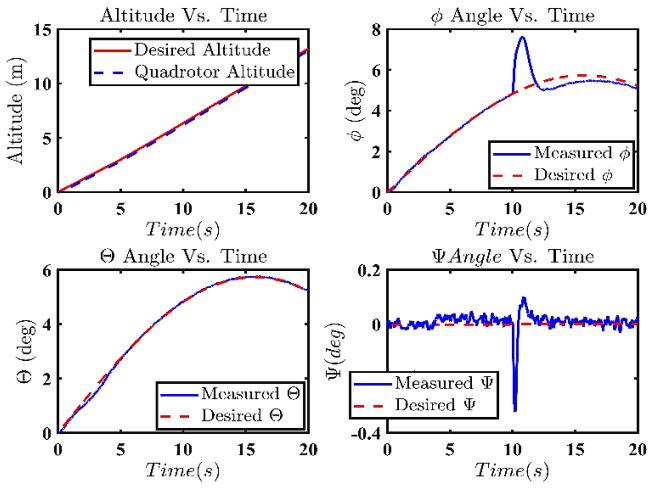

(a)

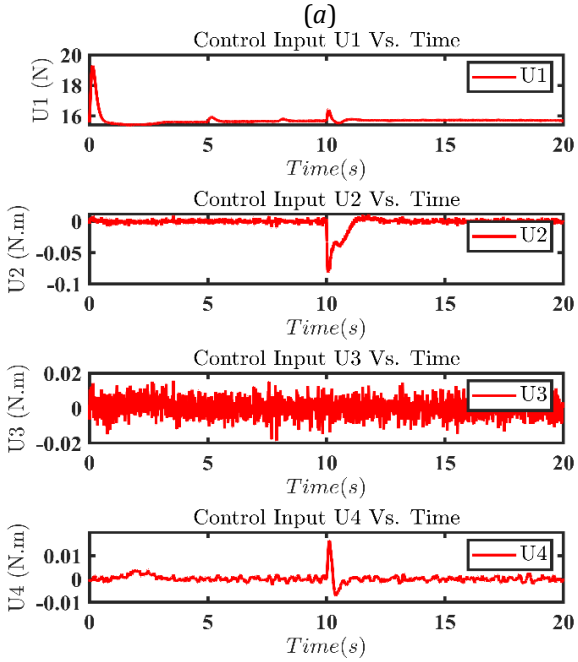

(b)

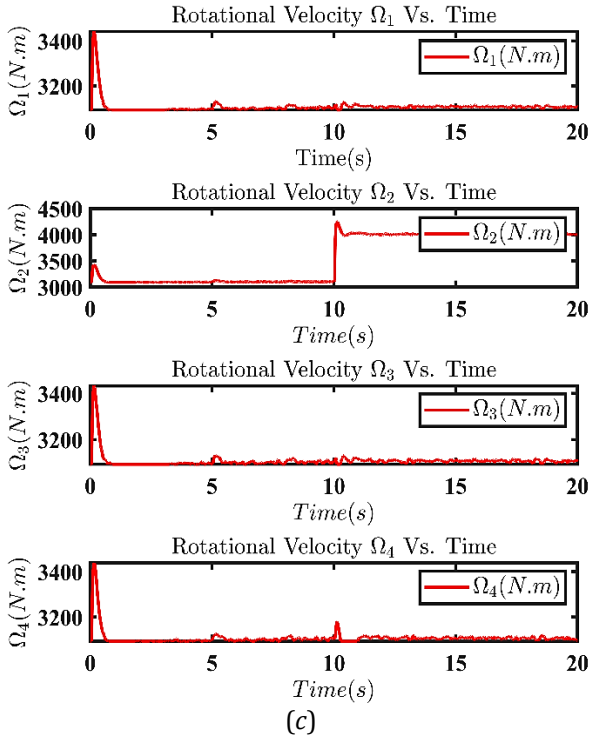

(c)

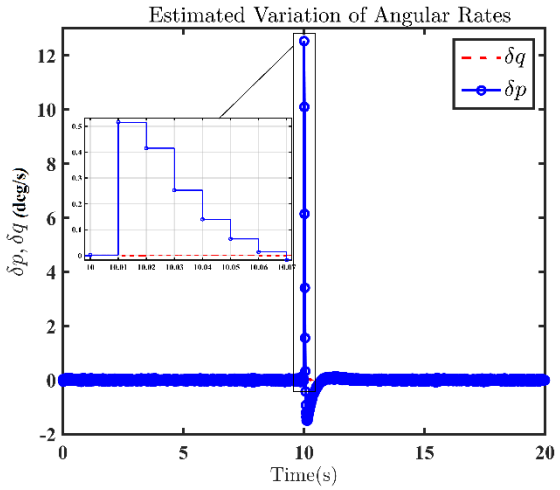

(d)

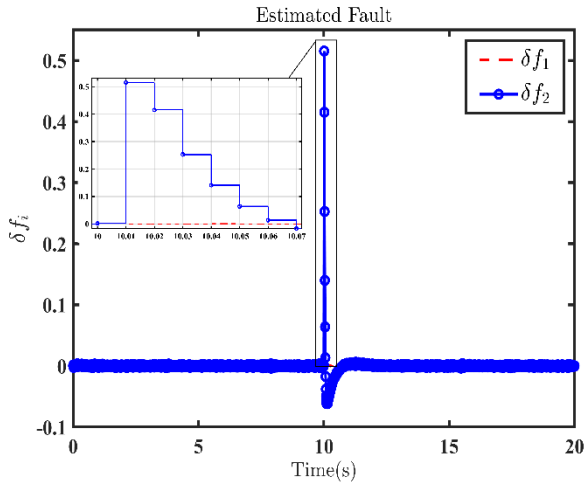

(e)

Fig. 6 Simulation of fault scenario 1, (a) quadrotor states, (b) controller outputs, (c) rotational speeds of the propellers (d) variation of quadrotor angular speeds, (e) fault estimation

In fact, a negative pitch rate indicates the fault of engine one and the positive value determines the fault in engine number 4. One of the main properties of the fault detection algorithm is being able to quickly detect and identify the fault before the system stability is lost. Fig. 8 illustrates the effect of time delay in fault detection on the performance of the controller. The Euler angles variation are illustrated for a delay time of 0.01s, 0.05s (five time-steps (T_s) ahead of t_f), and 0.1s (10 time-steps ahead) after the occurrence of fault (t_f=10s). The performance of the controller degrades as the time delay increases whereas it can lead to the quadrotor instability for bigger values of time delay. In fact, fast identification of fault is an important property of the introduced fault-tolerant controller.

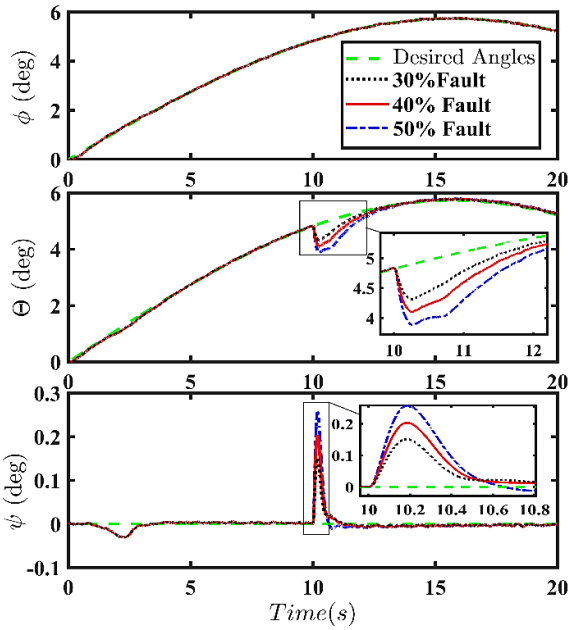

(a)

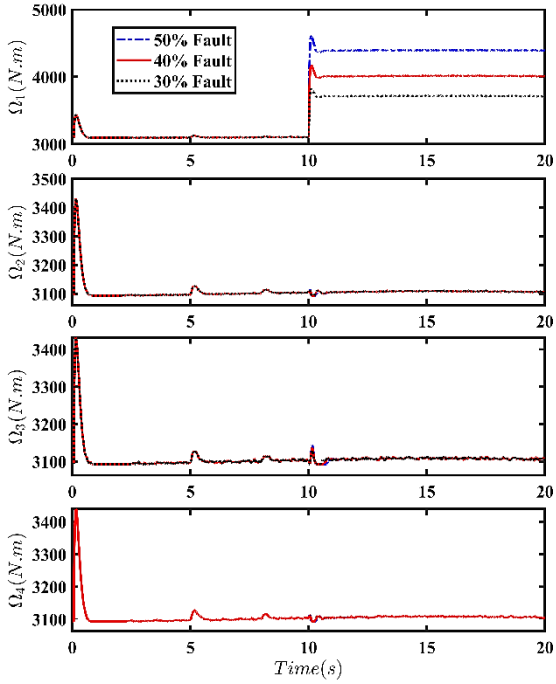

(b)

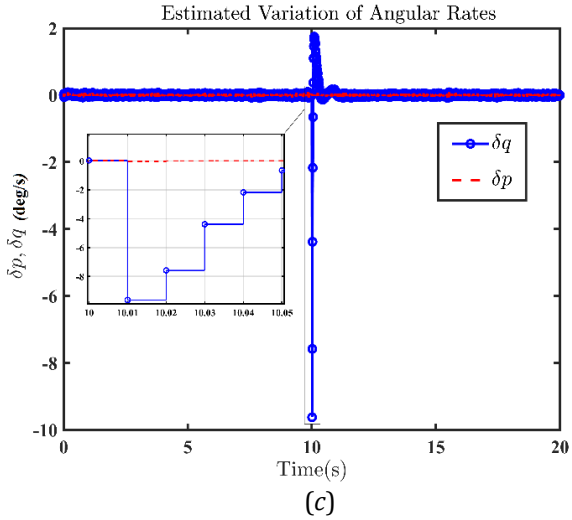

(c)

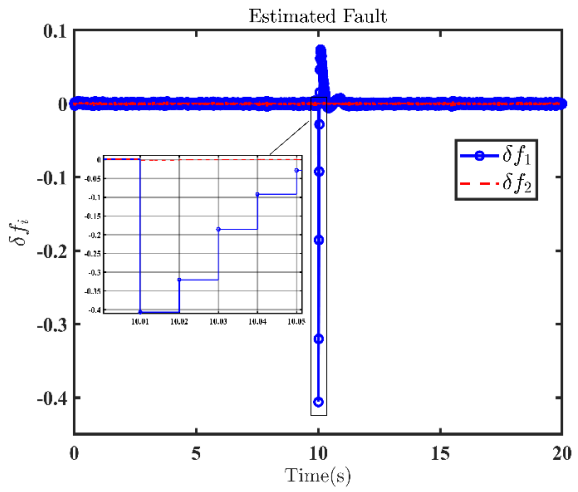

(d)

Fig. 7 Simulation of fault scenario 2, (a) quadrotor Euler angles, (b) rotational speeds of the propellers (c) variation of quadrotor angular speeds, (d) fault estimation

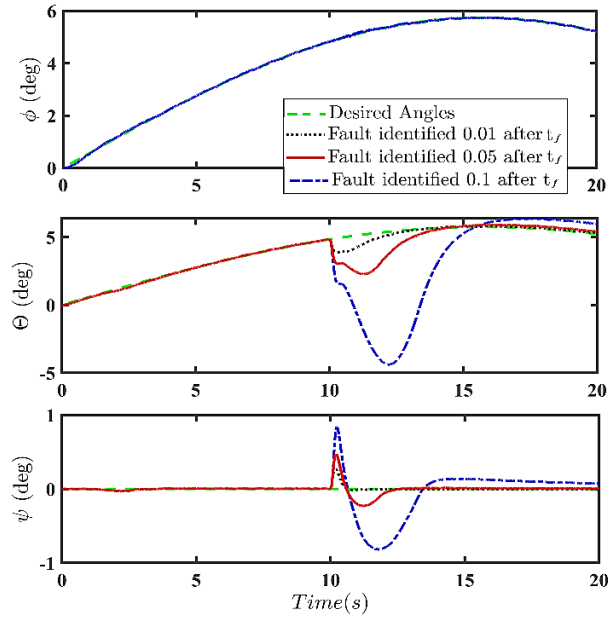

Fig. 8 Effect of fault detection time delay on the performance of the controller

6. CONCLUSION

This paper presents an autonomous emergency landing architecture (AELA) for the recovery and safe landing of a drone in presence of the engine fault. Inside the AELA, a fault-tolerant trajectory tracking controller including a fault detection algorithm and a three-loop adaptive sliding mode controller is proposed. The fault detection algorithm uses the filtered angular rates based on the extended Kalman filter and the autopilot commands to detect and identify the magnitude of partial loss of propeller effectiveness. The simulation results demonstrate that the adaptive controller without fault detection algorithm is robust to 10% of propeller damage but with considerable degradation of performance. Therefore, the threshold values which determine the occurrence of a fault is defined based on 5% of damage in which the controller performance without fault detection

algorithm is satisfactory. The simulation results demonstrate that the proposed controller has satisfactory performance considering rotor damages up to 50%. For more severe damages, the engine thrust saturates and trajectory tracking control cannot be achieved. In addition, the simulation results demonstrate the effect of time-delay in the fault detection process on the overall controller performance and therefore the effectiveness of the proposed fast converging fault detection algorithm. In future research, the proposed effective algorithm and AELA structure will be implemented on the drone in flight tests to verify the performance of the algorithms in different fault scenarios.

ACKNOWLEDGEMENT

This research was supported by Scientific Research Project Unit (BAP) of Adana Alparslan Türkeş Science and Technology University with the project number of 19119002.

Conflicts of interest

The authors declare no conflicts of interest.

REFERENCES

Ahmadi K, Asadi D, Pazooki F (2017). Nonlinear L1 adaptive control of an airplane with structural damage, Proceedings of the Institution of Mechanical Engineers, Part G: Journal of Aerospace Engineering, 233(1), 341-353: 0954410017730088.

Amoozgar M H, Chamseddine A & Zhang Y (2013). 'Experimental test of a two-stage Kalman filter for actuator fault detection and diagnosis of an unmanned quadrotor helicopter. J. Intell. Robot. Syst., vol. 70, pp. 107–117, Apr. 2013.

Asadi D & Ahmadi K (2020). Nonlinear Robust adaptive control of an airplane with structural damage, Proceedings of the Institution of Mechanical Engineers, Part G: Journal of Aerospace Engineering.

Asadi D & Bagherzadeh S (2017a). Nonlinear adaptive sliding mode tracking control of an airplane with wing damage, Proceedings of the Institution of Mechanical Eng., Part G: Journal of Aerospace Engineering, 232 (8), 1405-1420.

Asadi D, Atkins E M (2017b). Multi-Objective Weight Optimization for Trajectory Planning of an Airplane with Structural Damage. Journal of Intelligent & Robotic Systems.

Asadi D, Sabzehparvar M & Talebi H A (2013). Damaged airplane flight envelope and stability evaluation. Aircraft Engineering and Aerospace Technology, Vol. 85, No. 3, pp. 186-198. Doi: 10.1108/00022661311313623.

Asadi D, Sabzehparvar M, Atkins E M & Talebi H A (2014). Damaged Airplane Trajectory Planning based on Flight Envelope and Stability of Motion Primitives. Journal of Aircraft, Vol. 51, No. 6, pp. 1740-1757. doi: 10.2514/1.C032422.

Avram R C, Zhang X & Muse J (2017). 'Quadrotor actuator fault diagnosis and accommodation using nonlinear adaptive estimators. IEEE Trans. Control Syst. Technol., 25(6), 2219–2226.

Barghandan S, Badamchizadeh M A & Jahed-Motlagh, M R (2017). Improve Adaptive Fuzzy Sliding Mode Controller for Robust Fault-tolerant of a Quadrotor. Int. J. Control Autom. Syst., 15, 427–441.

Cen Z, Noura H, Susilo B T & Younes Y A (2014). Robust fault diagnosis for quadrotor UAVs using adaptive Thau observer,'' J. Intell. Robot. Syst., 73(1), 573–588.

Chen F, Wu Q, Jiang B & Tao G (2015). A reconfiguration scheme for quadrotor helicopter via simple adaptive control and quantum logic. IEEE Trans. on Industrial Electronics, 62 (7), 4328–4335.

Desaraju V R, Michael N, Humenberger M, Brockers R, Weiss S, Nash J Y (2015). Vision-based landing site evaluation and informed optimal trajectory generation toward autonomous rooftop landing, Auton Robot 39:445–463.

Frangenberg M, Stephan J & Fichter W (2015). Fast Actuator Fault Detection and Reconfiguration for Multicopters (AIAA 2015-1766). In Proceedings of the AIAA Guidance, Navigation, and Control Conference and Exhibit, 2015.

Gao Z, Carlo Cecati & Steven X D (2015). A Survey of Fault Diagnosis and Fault-Tolerant Techniques Part I: IEEE Transactions on Industrial Electronics, 62, 6.

Giribet J I, Pose C D, Ghersin A S & Mas I (2018) Experimental Validation of a Fault-tolerant Hexacopter with Tilted Rotors International Journal of Electrical and Electronic Engineering & Telecommunications, 7(2), 58-65.

Github PX4 Documentation, https://github.com/kylemanna/px4firmware/tree/master/Documentation.

Han W, Wang Z & Yi S (2018). Fault estimation for a quadrotor unmanned aerial vehicle by integrating the parity space approach with recursive least squares. Proc. Inst. Mech. Eng. G, J. Aerosp. Eng., 232(4) 783–796.

Khebbache H, Sait B, Yacef F & Soukkou Y (2012). Robust stabilization of a quadrotor aerial vehicle in presence of actuator faults. International Journal of Information Technology, Control and Automation, 2(2), 1–13.

Lanzon A, Freddi A & Longhi S (2014). Flight Control of a Quadrotor Vehicle Subsequent to a Rotor Failure. Journal of Guidance, Control, and Dynamics, 37:580-591.

Lopez-Franco C, Gomez-Avila J, Alanis A Y, Arana-Daniel, N & Villasenor C (2017). Visual Servoing for an autonomous Hexarotor Using a Neural Network Based PID Controller, Sensors, 17, 1865; doi:10.3390/s17081865.

Mazeh H, Saied M, Shraim H & Francis C (2018). Fault-tolerant control of an hexarotor unmanned aerial vehicle applying outdoor tests and experiments. Int. Fed. Autom. Control, 51, 312–317.

Merheb A R (2016). Diagnostic and Fault-Tolerant Control Applied to an Unmanned Aerial Vehicle, AIX Marseille University, Ph.D. Thesis.

Milton C P S, Claudio R, Jorge S, Mario S-F & Ricardo C, (2019) An Adaptive Dynamic Controller for

Quadrotor to Perform Trajectory Tracking Tasks, J. of Intel. Robotic Systems, 93, 5–16.

Mohammadi M & Shahri A M (2013). Adaptive nonlinear stabilization control for a quadrotor UAV: theory, simulation and experimentation. J. Intell. Robot. Syst. 72(1), 105–122.

Mueller, M W & Andrea R D (2014). Stability and control of a quadcopter despite the complete loss of one, two, or three propellers. IEEE International Conference on Robotics and Automation (ICRA), pp. 45–52

Nguyen N P, Xuan Mung N & Hong S K (2019). Actuator Fault Detection and Fault-Tolerant Control for Hexacopter. Sensors, 19, 4721; doi: 10.3390/s19214721.

Ranjbaran M, Khorasani K (2010). Fault recovery of an under-actuated quadrotor aerial vehicle. 49th IEEE Conference on Decision and Control, Atlanta, GA, 4385–4392.

Saied M, Lussier B, Fantoni I, Francis C, Shraim H & Sanahuja G (2015) "Fault diagnosis and fault-tolerant control strategy for rotor failure in an octarotor," in Proc. IEEE ICRA.

Sharifi F, Mirzaei M, Gordon, B W & Zhang Y M (2010). Fault-tolerant control of a quadrotor UAV using sliding mode control. Proceedings of the Conference on Control and Fault-tolerant Systems, Nice, France, 6–7 October 2010; pp. 239–244.

Tarhan M & Altug E (2011). EKF Based Attitude Estimation and Stabilization of a Quadrotor UAV Using Vanishing Points in Catadioptic images. J. Intell Syst, Vol. 62, 2011, pp. 587-607DOI 10.1007/s10846-010-9459-y.

Zhang Y & Chamseddine A (2012). Fault-tolerant flight control techniques with application to a quadrotor UAV testbed. Automatic Flight Control Systems - Latest Developments, T. Lombaerts, Ed. InTech, 2012, pp. 119–150.

Turkish Journal of Engineering

https://dergipark.org.tr/en/pub/tuje

e-ISSN 2587-1366

Aluminum in food and potential role on Alzheimer's disease of aluminum

Günseli BOBUŞ ALKAYA*[1], Çağatay DEMİRCİ [2], Hüseyin ŞEVİK [3]

[1]*Mersin University, Institute of Science, Food Engineer, Mersin, Turkey*
[2]*Mersin City Training and Research Hospital General Surgery Department, Mersin, Turkey*
[3]*Mersin University, Engineering Faculty, Metallurgy and Materials Engineering, Mersin, Turkey*

Keywords
Food
Aluminum
Toxicology
Alzheimer's

ABSTRACT

Several studies have shown the relationship between the aluminum exposure and the Alzheimer's disease. The gastrointestinal absorption of Aluminum (Al) is low. Also, If the renal filtering system works as needed, generally urine can be enough to eliminate overdose (rational over concentrations) of Al. But Al can be found in kinds of foods and drinks such as processed foods (because of additives, packaging materials, utensils…), fresh vegetables and fruits (because of soil) and even in drinking water therefore, in some cases, the Al level may pose a health risk. Chronic high concentration to Al exposure preferably intakes by oral, intravascular ways with also not having a good condition of Glomerular Filtering System of Kidneys (GFR). Nowadays, although mankind is having more Al by oral ways than past and many studies have been conducted to determine whether there is a relationship between aluminum and Alzheimer's disease(AD) or not. Therefore, this review is intended to provide a short summary of the works done in the past and it may warn people about Al intake in the next decade, therefore human can change their life to be more natural less industrial.

1. INTRODUCTION

Aluminum is the third most common element in the Earth's crust with about 8%. Pure aluminum has not been existing in nature, therefore it has mainly oxide, hydroxide and silicate compounds (Chappard 2016, EFSA 2011, Krewski et al. 2007, Stahl et al. 2017, Yokel 2016). Aluminum is used in many areas of the industry due to its advantages such as low density, good thermal conductivity, ductility and corrosion resistance. These areas can be listed as transportation (automobiles, aircraft, ships), construction (windows, doors, railing, profiles), packaging (cans, soft packaging, foils, cooking utensils), machine construction, electrical engineering (cable, distributing, dispensing bar), cosmetics, personal care industry and food additives (Chappard 2016, Krewski et al. 2007). Today, the fastest increase in the use of aluminum and its alloys is seen in the transportation industry. It is also used in forms of powders, dyes and pigments, gasoline and diesel additives, explosives, and propellant gases. The oxidized components of aluminum are often used as food additives, abrasive material, refractory, electrical insulators and ceramic (Krewski et al. 2007). Aluminum hydroxide is usually used in personal care products and pharmaceuticals. Also, various aluminum components are used in food such as preservatives, fillers, colorants, emulsifiers and baking powder; soy-based baby food. Furthermore, natural aluminum minerals, especially zeolite and bentonite are used in water treatment, sugar treatment, paper and beer industries (Becker et al. 2016, Krewski et al. 2007). As a result, we can say that aluminum is widely used in many industries. This study is compiled to compare the levels of aluminium content in different types of food then Al effects are viewed on human body. Finally, discussions on the relationship between Al and Alzheimer's are presented.

2. ALUMINUM CONTENT IN FOOD PRODUCTS

It is well-known that some metals such as magnesium, iron and zinc are necessary for body activities and they must intake via nutrition, while aluminum is unnecessary for body (Stahl et al. 2017). People can intake aluminum from two main sources; through food and dermal contact (Al-based

* **Corresponding Author**

*(gbobus@mersin.edu.tr) ORCID ID 0000 – 0003 – 1732 – 9163
(cagataydemirci@gmail.com) ORCID ID 0000 - 0002 – 6482 - 5007
(sevik@mersin.edu.tr) ORCID ID 0000 – 0002 – 2065 – 412X

Cite this article

Alkaya G B, Demirci Ç & Şevik H (2022). Aluminum in food and potential role on Alzheimer's disease of aluminum. Turkish Journal of Engineering, 6(2), 118-127

Review Article / DOI: 10.31127/tuje.846455

Received: 24/12/2020; Accepted: 14/02/2021

antiperspirant salts are widely used to reduce perspiration in the armpit area) (Chappard et al. 2016, Dabre 2016, Stahl et al. 2011). When considered Table 1, it is possible to classify these sources as "external sources" and "dietary sources". Humans exposure to aluminum more dietary then external contact (Chappard et al. 2016, Stahl et al. 2017).

Table 1. Aluminum- external and dietary contact

Examples of external contact	Examples of dietary contact
Construction materials including aluminum alloys (e.g. facades, suitcases, tent construction)	Packaging and containers (beverage and food cans, coffee pots, outdoor cutlery and dishes, coffee capsules, household aluminum foil)
Vehicles, aerospace components including aluminum alloys (e.g. gearbox, seat frame, dashboard)	Nanoparticles in sunscreens
Electrotechnology, including alloys (e.g., electrical conductors)	Foodstuffs
Pigments for paints (e.g., "silver" bronze paints)	Toothpaste (e.g. Aluminum hydroxide, AlF_3)
Metal polish (Al_2O_3: paste, suspension in MeOH or H_2O)	Pharmaceuticals (e.g., heartburn medicines—pH-regulation; vaccine adjuvants)
Organic syntheses (e.g., $LiAlH_4$: reducing agent)	Cosmetics (e.g., deodorants–antitranspirants)
Jewelry and ornaments	Vaccine adjuvant (increases the immune reaction)
Fuel for solid-fuel rockets (up to 30% Al) and pyrotechnics	Food additives (e.g., as colorants or stabilizers)

Source: Chappard et al. 2016, Stahl et al. 2017

Aluminum is one of the most common elements in nature and therefore, it is a natural component of drinking water and foodstuffs (Stalh 2011). Natural puddles such as rivers, lakes, groundwater, coastal sea water and open ocean water (their aluminum concentration are approximately 0.15, 0.4, 0.1, 0.001–0.007, and 0.001 mg/l, respectively.) contain low aluminum concentration. However, the aluminum concentration can change based on acidic and organic matters. As a consequence, people can intake aluminum by having toxic effects via drinking water or foods (Barabasz et al. 2002, FIRA 2007, Flaten 2001, Yokel 2016, Wang et al. 2010, Wills and Savory 1985). The World Health Organization (WHO) has stated that several methods exist to minimize residual aluminum concentrations in filtered water. These involve the use of optimum pH in coagulation, avoiding extreme aluminum dosing, good mixing of the clumping agent (flocculants such as aluminum sulfate ($Al_2(SO_4)_3$) or poly-aluminum chloride (PACI) are commonly used in drinking water treatment to improve the removal of colloidal, particulate and dissolved substances via coagulation process), optimum paddle speeds for flocculation (water treatment process by precipitation), and the filtration of clumped aluminum (Bakar et al. 2010, Rondeau et al. 2008, Othman et al. 2010). In the case of good working circumstances, it can be obtained from those aluminum concentrations of 0.1 mg/l or less in large water treatment facilities. For small facilities (e.g. those serving fewer than 10 000 people), 0.2 mg/l or less is a practicable level for aluminum in finished water (they have some difficulty might experience in attaining this level, because the small size of the plant implements little buffering for fluctuation in operation). According to the U.S. Environmental Protection Agency (U.S. EPA), the European Union (EU) and the TC Ministry of Health have stated that the maximum Aluminum concentration in the drinking water should be lower than 0.2 ppm (Yokel 2016, Bakar et al. 2010, Rubinos et al. 2005).

Aluminum in foods is attributed to the two sources called primary and secondary causes. The primary cause is the natural content of foods taken from the geologic surrounding during growth. The secondary cause is intaking it in the additives, food processing, preparing and storage as well as from veterinary drugs, fertilizers and the air (Stalh 2011, Yokel 2016). Therefore, aluminum concentration in food is very changeable. Some of the negative consequences of rapid industrialization, such as acid rain, lead to an increase in the concentration of aluminum in natural waters and biological systems (Ranau et al. 2001). Ranau and friends had been researching the aluminum content of the edible part of sea food. Most of the fillets of fatty and lean fish species aluminum contents were found lower than 0.2 mg Al/kg wet weight. In the same research they indicated that the fish collected near the smelting plant had 1 mg Al/kg wet weight aluminum content. This was explained because of the aluminum content of the sea water (Ranau et al. 2001). Table 2 summarizes the allowable secondary aluminum sources that may lead to aluminum accumulation in food (Stalh 2011, WHO 1998).

Table 3 shows the concentration range of aluminum in foodstuffs (it was obtained from the European food safety authority (EFSA) (Stalh et al. 2017). The concentration values of aluminum in unprocessed foods at Table 3 are below 5 mg/kg, the concentration values of Al in animal products (milk, sausage, seafood), bakery products and vegetables are between 5 and 10 mg/kg, the concentration values of Al in coffee, tea, spices and cocoa products is above 10 mg (Stalh et al. 2017). Table 4 contains more details about Al concentration values in some beverages and foodstuffs (Yokel 2016). As it can be seen from Table 4, the Al concentration values of most unprocessed foods are below 5 mg. Furthermore, Al concentration values in spices especially paprika and pepper, based on their wet weight, have much higher compared with other unprocessed foods, based on the dry weight.

Aluminum is not an easily absorbable element, but if vegetables such as spinach and lettuce grow in soil containing approximately 5-10% aluminum, they can have high aluminum content. Plant-eating animal products such as eggs and milk contain very little aluminum due to their low bioavailability and limited transport . However, some plants, such as black or green tea, concentrate aluminum in their leaves and accounting for the higher Aluminum concentration than other beverages by brewing method (Street et al. 2007, Yokel 2016).

Table 2. Allowable secondary aluminum sources. (Approved food additives are written with the ”E" prefix.)

Regulation	Designation	Permitted concentration	Admitted for
Feedstuffs Regulation	E 561 Vermiculi Mg Al Fe silicate		All feedstuffs
	E 554 Na-Al-silicate		All feedstuffs
	E 559 Kaolinite clay containing Al silicate		All feedstuffs
	E 599 Perlite Na Al silicate	50,000mg/kg	In mineral feedstuffs only
Drug colouring Regulation	E 173 Aluminum		
	Aluminum salts of all other colors		
Animal drug residues Regulation	Aluminum distereate		All animals for food production
	Aluminum hydroxyl acetate		
	Aluminum phosphate		
	Aluminum tristereate		
	Aluminum trisalicylate		
	Magnesium aluminum silicate		
	Aluminum hydroxide		
Cosmetics Regulation	Some particular aluminum compounds only are forbidden or subject to limited admission		
Ecology Regulation	Aluminum calcium phosphate		As fertilizer/soil improvement agent
Tobacco regulation	Aluminum hydroxide		White burning agent
	Aluminum oxide		Materials for filters
	Aluminium sulphate		Materials for filters
	Aluminum		Materials for filters
	Aluminum potassium sulphate		Chewing tobacco
Drinking water Regulation	Aluminum	0,2 mg/l	
Wine Regulation	Aluminum	8 mg/l	Wine and other products
Food additives admission	E 173 Aluminum		Covering of sugar confectionery for cake decoration, pastries
	E 520 Aluminum sulphate	30 mg/kg	Egg white
	E 521 Aluminum sodium sulphate		
	E 523 Aluminum ammonium sulphate	200 mg/kg expressed as aluminum	Candied, crystallized crystalized and glazed fruit and vegetables
	E 541 Sodium aluminum phosphate, acidic	1,000 mg/kg expressed as aluminum	Fine bakery wares (scones and sponge wares only
	E 554 Sodium aluminum silicate	10 g/kg	Sliced or grated hard, semi-hard and processed cheese
	E 556 Calcium aluminum silicate	30 g/kg	Spices
	E 556 Calcium aluminum silicate	30 g/kg	Products for the greasing of baking trays
	E 559 Aluminum silicate	As required	Confectionery excluding chocolate (surface treatment only)
	E 555 Aluminum potassium silicate	As required	Dye for coloring Easter eggs

Source: Stalh 2011, WHO 1998

Table 3. Concentration range of aluminum in foodstuffs

Concentration range (aluminum in mg/kg foodstuff)	Foodstuff
≤ 5.00	Most unprocessed foods
5.00 – 10.0	Bread, cake, pastries, baking mixes, flour, vegetables: mushrooms, spinach, radishes, chard, lettuce
	Candied fruits
	Animal products: milk products, sausage, offal, sea foods
> 10.0	Tea leaves
	Cocoa and cocoa products
	Spices, herbs
	Coffee

Source: Stalh et al. 2017

Table 4. Median Al concentration in some representative beverages and foodstuffs

Beverage or foodstuff	Median Al concentration (mg/l or mg/kg)
Cow milk	0.070
Human milk	0.043
Apple	0.72
Banana	0.55
Grape	0.82
Orange	1.5
Peach	2.6
Pear	0.64
Plum	1.1
Raisin (sultana)	10
Strawberry	1.0
Watermelon	0.28
Apple juice	0.44
Orange juice	0.18
Pineapple juice	0.35
Tomato juice	0.67
Bean	4.0
Broccoli	1.3
Cabbage	0.31
Carrot	0.57
Cauliflower	0.80
Celery	0.90
Corn	1.5
Cucumber	2.2
Lettuce	5.5
Mushroom	2.9
Onion	0.30
Pea	2.1
Pepper (green)	0.94
Potato	2.5
Soybean	7.8
Spinach	24
Tomato	0.74
Corn flour	5.3
Oats	4.0
Rice	3.3
Wheat flour	5.6
Eggs	0.27
Beef	1.2
Chicken	1.2
Pork	2.2
Fish	0.15
Almonds	3.0
Cashews	4.6
Chestnuts	3.8
Peanuts	2.0
Pine nuts	38
Walnuts	2.3
Paprika	92
Pepper	31

Source: Yokel 2016

Table 5 exhibits the aluminum concentration in some processed foods and beverages (Stahl et al. 2017, Yokel 2016). When we compare Tables 4 and 5, it can be seen that the aluminum concentration in the soy-based infant formula is higher than cow milk-based infant formula. Predictably, the main source for this is the use of soybeans with higher aluminum content. Among the food additives, the sodium aluminum phosphate (SALP), American Food and Drug Administration (FDA) approved, is the most widely used as a food additive (FAO/WHO 2011, Paiva et al. 2020, Stahl et al. 2011, Yokel et al. 2009, Yokel 2012).

Table 5. The aluminum concentration in some processed foods and beverages

Beverage or food	Median Al concentration (mg/l or mg/kg)
Tap water	0.04
Mineral water	0.016
Cow milk – based infant formula	0.19
Soy - based infant formula	3.9
Infant foods (>50 foods, many commercial, from 15 reports)	10
Infant foods (strained) (>30 commercially purchased foods from 2 reports)	0.41
Cola	0.25
Noncola soft drinks	0.40
Beer	0.16
Wine	0.90
Butter	1.4
Cheese (non goat)	3.8
Cheese (processed)	15
Cheese (goat)	15
Cheese (on restaurant pizza)	2.9
Cheese (on frozen pizza)	415
Yogurt	0.28
Yogurt (goat)	2.8
Margarine	1.7
Olive oil	0.043
Vinegar	0.21
Peanut butter	1.9
Bacon	2.4
Luncheon meat	3.2
Sausage	6.2
Soup	1.2
Chocolate	9.4
Honey	0.050
Sugar	1.7
Jelly and jam	4.1
Biscuit	22
Bread (white)	3.6
Bread (wheat)	4.5
Cake mix	445
Cake (not stated to contain SALP)	6.3
Cake (containing acidic SALP)	190
Cereal	1.0
Cookie	6.9
Baking power	69
Pancake mix	100
Pancake	85
Pasta	5.5
Nondairy creamer powder (multiple-serving container)	38
Nondairy creamer (single-serving packet)	170
Salt (single-serving packet)	180
Fine pastries in aluminum trays	3.0
Salt pretzels and similar savory biscuits	4.0
Evaporated milk	0.205
Soft cheese	1.37
Harz cheese	0.438
Milk curd	0.109
Ready-cooked meals in aluminum trays	1.0
Pork (canned)	1.08
Beef (canned)	0.669
Herring (canned)	1.60
Crustaceans	2.54

Source: Stahl et al. 2017, Yokel 2016

When acidic SALP, which acts as acidifying and leavening agent, is used as a food additive, processed food will contain high amounts of aluminum. For example, SALP added to processed cheeses or cream cheeses, easy melting and soft texture give the property. The use of acidic SALP in foodstuffs such as biscuits, cake mix, pan cakes, baking powder causes these foods to contain high aluminum. Table 5 can be evaluated and many examples can be given like this.

2.1. Migration of Aluminum and Alloys Used in Storage and Packaging

Metal packaging provides advantages as high mechanical and thermal stability for food industry. Metals used are generally tin, aluminium, certain steel grades (Bott et al. 2018). Pure aluminum and its alloys have low density, low melting temperature, excellent formability because of surface-centered cubic crystal, good corrosion resistance good thermal conductivity and recyclable, therefore they are intensively used for food processing, packaging and storage operations by many countries without any restrictions (Aguilar at el. 2008, Carrasco et al. 2014, Chappard 2016, Filippini et al. 2019, Jabeen et al. 2016, NSCFE 2013, Seruga et al. 1994, Seruga et al. 1997, Soares et al. 2019, Verissimo and Gomes 2008, Yokel 2016,). While pure or near-pure aluminum is widely used for foil production, 3xxx (usually 3104) and 5xxx (usually 5182) series aluminum alloys are used for food and beverages packaging (Soares et al. 2019). In beverage industry over 95% of carbonated drinks and beer are preferred to be packaged in aluminium cans due to their lightness and recyclability (Krewski et al. 2007). When pure aluminum or its alloys contact with oxygen in the air, a very thin aluminum oxide (Al_2O_3) layer forms on the aluminum surface, this has provided excellent corrosion resistance between pH 4.5 to 8.5 medium. The layer is colorless, tough and non-flaking and few chemicals are able to dissolve it. Especially in cases where the pH is below 4.5, it occurs very quickly on the surface of the aluminum to a layer of corrosion. For this reason, lacquer (polymeric) coating is applied to the contact surface of the alloy to prevent food contact with aluminum alloys. Food content (acidity, high salt concentration…) can cause to increase the migration. (Chappard 2016, Krewski et al. 2007, Mannheim and Passy 2009, Yokel 2016). Different variations of lacquer are applied due to the food in the cans. So that the coating protects the food from free metal ions which may cause sensory deterioration or even health related concerns (Bott et al. 2018). Table 6 displays examples of food contact materials made of aluminum (Stahl et al. 2017).

Many studies have shown that the migration of aluminum into food occurs over time as a result of food contact with aluminum and the values for each food vary (Yokel 2016, Seruga et al. 1994, Seruga et al.1997, Verissimo and Gomes 2008). For instance, it was determined that when tap water (pH 8.2) was kept in a new aluminum bottle for 32 hours, the amount of aluminum increased from 0.053 to 0.16 mg/l. It was

Table 6. Examples of food contact materials made of Al

Food packaging	Aerosol cans (e.g., canned whipped cream) Aluminum foil Containers for convenience foods Lids for yogurt containers Beverage cans Coffee capsules Tubes for mustard, mayonnaise Packaging for candy Composite materials for beverage cartons and packaged coffee
Food manufacturing	Aluminum tanks for wine, juices, oil, milk Baking trays Meat and sausage hooks Machine parts
Cooking and kitchen utensils	Baking sheets Bread boxes Lids Coffee pots Cooking utensils (cooking spoons, ladles) Pans Pots
Household equipment	Ice cream makers Juicers Moka pots Coffee percolators

Source: Stahl et al. 2017

observed that the amount of aluminum increased by 31 times as a result of keeping the tomato puree in the aluminum pan for 72 hours, and it was determined that this value increased by 10% with the addition of salt. The concentration of aluminum was observed to increase 14-fold by coke and lemonade at the end of 12 weeks. At the end of 12 months, there was a 26-fold increase in orange soda and a 9-fold increase in lime (lime) soda (Yokel 2016).

Another study done by Seruga et al. was stated that analyzed seven soft drink aluminum cans (two arms, two oranges, two lemons, one tonic) had found that the aluminum content increased throughout the storage period of 12 months. The obtained result was attributed to the low pH value of these drinks by the authors (pH = 2.80 to 3.20) (Seruga et al. 1994). Another study conducted by Seruga et al. related to beer drinks belonging to different brands, found that the amount of aluminum in expired cans was higher than in bottles of beer. In contrast, they found the amount of aluminum in both cans and bottles below 1 mg/l (Seruga et al. 1997).

A study performed by Verrisimo and Gomes on aluminum cans of beer and tea, measured the aluminum migration values at the end of seven months. According to the measurements, they calculated an increase of 0.14 mg/l in beer and 0.6 mg/l in tea drink compared with their initial values. Also, in this study included dented cans and found that there was a significant increase by measuring the aluminum value of 9.6 mg/l, especially in tea. Also, they observed an increase of 0.17 mg/l in beer. The reason for the higher amount of aluminum in tea than in beer is due to the difference in pH values (tea pH 3.0, beer pH 4.2) (Verrisimo and Gomes 2008).

2.2. Tolerable Weekly Intake of Aluminum

People are exposed to a considerable amount of aluminum because they consume foods, water, drugs, the air they breathe (flying powders), the anti-perspiration deodorants. Food and drink are the most effective ones. Food additives used especially in food and beverages make up a significant proportion of the percentage of aluminum taken daily (Aguilar et al. 2008, NSCFE 2013, Stahl et al. 2017, Yokel 2016). In 1990, depending on the results obtained from animal experiments studying the toxicology of aluminum in dogs, mice and rats, The World Health Organization (WHO), The Food and Agriculture Organization (FAO), and The Scientific Food Committee (SCF) announced a provisional tolerable weekly intake (PTWI) for aluminum of 7.00 mg/kg body weight (BW) per week (Aguilar et al. 2008, NSCFE 2013, Stahl et al. 2017). The same committee revised this value to 1 mg/kg body weight as a result of several meetings held in 2008 (new data are taken into account), which is 7 times lower than the first (Aguilar et al. 2008). According to the obtained data, an adult weighing an average of 70 kg may be allowed to take 70 mg of aluminum per week, while a child weighing an average of 30 kg has 30 mg (Stahl et al. 2017, Stahl et al. 2011).

People's weekly intake of aluminum from foods varies according to the food consumption habits of countries. For example, studies in America have shown that men intake more aluminum than women. The average daily intake of aluminum was 4.8 mg/day in adults, 8.6 in teens, 6 in children and 0.7 mg/day in infants under two years of age. The highest values were determined for people living in China, Japan and Taiwan (approximately 9 mg/day). Besides, adults in the United States and Canada have been reported to intake more aluminum than adults in Europe, which is mainly since they have placed more restrictions on the use of aluminum additives. Also, the main reason for the higher daily intake of aluminum in young people is the higher consumption of prepared meals (Yokel 2016).

3. ALUMINUM IN THE BODY AND ALZHEIMER'S DISEASE (AD)

Aluminum taken either way (external or nutritional sources) can be eliminated by excretion via intestines and normal, healthy kidneys (Krewski et al. 2007, Stahl et al. 2011). However, various studies have shown that the daily amount of aluminum increases in the kidneys of dialysis patients having kidney failure (Krueger et al. 1984, Krewski et al. 2007, Stahl et al. 2011). Aluminum has not been considered in the healthcare field up to 1965 because of its low bioavailability. But in 1965 a study related to aluminum salts injected directly into the rabbit brain was carried out and it was observed that these salts caused tissue alterations. Obtained results from this study suggested a possible connection between aluminum and Alzheimer's disease (Stahl et al. 2011). However, recent studies have shown that there is no conclusive evidence to support or disprove the existence of a relationship between Alzheimer's disease and aluminum (Campbell 2002, Gupta et al. 2005, Rogers and Simon 1999, Tomljenovic 2011, Wang et al. 2016).

Alzheimer's disease (AD) was first defined by German neurologist Alois Alzheimer in 1906 as language problems, short-term memory loss, slow memory loss and unpredictable behavior (Yang et al. 2019). Many studies extensively were carried out related to the absorption, elimination and distribution properties of aluminum and its compounds in humans and experimental animals. Previous biochemical and toxicological studies in animals related to Food additives, flavorings, processing aids and food contact materials (AFC) did not measure the "normal" aluminum content of the main diet fed to the animals, and thus the stated dose in such studies is likely to be an underestimate of the total aluminum exposure (EFSA 2011). However, it is well-known that aluminum has long been toxic (Crepeaux et al. 2017, Domingo 1995, Exley 1998, Mailloux et al. 2011, Meyer-Baron et al. 2007, Rensburg et al. 2001, Stahl et al. 2017, Walton 2006, Walton 2007). In a study conducted by Crapper et al. in both human and animal subjects in 1973, they identified neurofibrillary degeneration of aluminum concentration in the brain and considered its possible role in the etiology of AD (Meyer-Baron et al. 2007). Although morphological changes are not defined as those seen in AD, great efforts are being made to decipher the relationship between aluminum exposure and neurodegenerative sequels (Gupta et al. 2005, Mailloux et al. 2011). Aluminum toxicity, depending on the amount of intake of food sources (such as food, cooking utensils, aluminum content storage and packaging products, drinking water) into the body, has been related to various pathological conditions such as Alzheimer's, Parkinson's disease, osteomalacia, anemia and obesity (Mailloux et al. 2011).

The amount of aluminum in the brain increases from birth to old age, even in patients without dementia. Aluminum has irregular distribution in the brain (Walton 2006), it is known to accumulate higher concentrations in brain regions including the entorhinal cortex, hippocampus, lower lateral lobe (inferior parietal lobule) and amygdala region (a region that shows the earliest pathological changes in ad) (Campbell 2002, Kasbe et al. 2005, Tair et al. 2016, Tomljenovic 2011, Walton 2007, Walton 2009). Pyramidal cells in the Cortex and hippocampus, basal forebrain cholinergic neurons, and upper brainstem Catecholaminergic neurons associated with higher cognitive functions are the neuronal populations most susceptible to aluminum-induced neurofibrillary degeneration and also most affected in AD (Tomljenovic 2011). Around 50 million people worldwide (about 60% of that number are in low-and middle-income countries) have Alzheimer's and other dementia patients, according to 2019 World Health Organization data. This number is expected to increase by about 10 million each year. The incidence of Alzheimer's disease is highest in Latin American and Asian countries (Bostancıklıoğlu 2019). In 2019, the number of Alzheimer's patients in America (AAR 2019) and Germany (AA 2020) were approximately 5.8 and 1.5 million, respectively while

this number is around 600 thousand in Turkey (Özbabalık and Hussein 2017).

As mentioned before, the one of ways of intaking aluminum into the body is oral. In general, people are exposed to aluminum during the day from drinking water, unprocessed or processed foods, beverages, foods that come in contact with aluminum (packaging, storage). The sources of intaking aluminum vary in each country. For instance, the main source in the United States is foods and beverages (unprocessed meat, fruit, fish, coffee, wine, black tea, green tea, and tap water) (Mathiyazahan et al. 2015, Paolo et al. 2014, Yokel and Florence 2008, Walton 2009). Most adult Americans intake between 1-10 mg Al/day of aluminum, especially from fruit, fish and unprocessed meat foods. In addition to this, it is estimated that 50% of Americans are exposed to less than 0.34 mg/kg (body weight-Day), 45% to 0.34-1.36 mg/kg, and the rest to more than 1.36 mg/kg of aluminum (Walton 2009). In another study conducted in France, it was reported that adults who are living in the country exposure hot beverages except of coffee (13%) and vegetables containing potatoes (11%). The French adults and children exposure to aluminum are estimated at 40.3 µg/kg bw/day and 62.2 µg/kg bw/day, respectively (Arnich et al. 2012). In Italy, the amount of exposure to aluminum for adults has been reported as 4.1 mg/day. (Most of the aluminum is taken from legumes, sweets and cereals) (Filippini et al. 2019). In Germany, Stahl et al. estimated Al consumption by German adults (70 kg) and children (30 kg). It was informed within all German foods used in this study, that cocoa powders had the highest mean Al (165 mg/kg) and chocolate had a mean 48 mg Al/kg. According to average annual cocoa consumption, the German adult and child received 2% and 4% of the PTWI, respectively; chocolate provided up to 12% of the adult and 30% of the child's PTWI (Stahl et al. 2011). In 2008, EFSA declared that the daily intake of aluminum in adults living in European countries was between 28.6-214 µg/kg body weight-per day (Bostancıklıoğlu 2019). Finally, a study conducted in Japan in 2019 found that adults were exposed to 41.1 µg/kg of aluminum daily (Hayashi et al. 2019).

Another source of aluminum is drinking water (Kramer and Heath 2014, Krewski et al. 2007, Panhwar et al. 2016). Many people consume water between meals. When water is not taken with food, it reaches directly from the esophagus to the stomach, where it comes into contact with the digestive juice (pH is between 2-3.5 and, as mentioned earlier, Aluminum dissolves more quickly in acidic medium) (Rogers and Simon 1999, Rondeau et al. 2000, Samir and Rashed 2018, Walton 2012). In such cases the free Al^{+3} in the water is more absorbed by the body (Gardner et al. 2003, Klotz et al. 2017, Mendecki et al. 2020, Yang et al. 2019, Zhang et al. 2016, Willhite et al. 2014).

Studies have shown that Alzheimer's patients accumulate 2-3 times more aluminum in their hippocampus and cortices than those who do not have dementia (Samir and Rashed 2018, Yang et al. 2019). Data from another study declared that individuals who consumed foods with high aluminum content had twice the risk of developing Alzheimer's disease (Rogers and Simon 1999). The concentration of aluminum in the brain of deceased Alzheimer's patients has been observed to increase, however, other studies have found no definitive indicators supporting the hypothesis that aluminum plays a causal role in Alzheimer's disease or causes pathological changes in the species studied. Many studies have been performed in the literature, such as the examples given above.

4. CONCLUSION

Even the mechanisms of aluminum on humans are not totally understood, it is certain that exposure to Al at high values or at low values for a long time causes health problems. Also many studies indicate the aluminum content of various foods. The most important effect of Al is on the nervous system. Beside this many studies have been conducted to determine the relationship between aluminum and Alzheimer's disease. Some authorities mention a significant correlation, some authorities declare that there is no meaningful relation between aluminum and Alzheimer's disease. In this review we have tried to mention about all these studies in a wide range, but the conclusion has not yet been reached that there is no definite evidence supporting or refuting the association between aluminum and Alzheimer's disease. As a consequence, the uncertainties in the literature regarding aluminum can be overcome by conducting interdisciplinary studies. As future work, it could be necessary to develop new materials for the food industry to consume healthy foods (no health risks) as an alternative material to aluminum.

Author contributions

Günseli Bobuş Alkaya: Investigation, writing, methodology. **Çağatay Demirci:** Investigation, methodology, writing, reviewing and editing. **Hüseyin Şevik:** Conceptualization, reviewing and editing, supervision.

Conflicts of interest

The authors declare no conflicts of interest.

REFERENCES

Aguilar F, Autrup H, Barlow S, Castle L, Crebelli R, Dekant W, Engel K-H, Gontard N, Gott D, Grilli S, Gürtler R, Larsen J C, Leclercq C, Leblanc J – C, Malcata F - X, Mennes W, Milana M - R, Pratt I, Rietjens I, Tobback P & Toldrá F (2008). Safety of aluminum from dietary intake" The EFSA Journal, 754, 1-34.

Alzheimer's Association (2020). 2020 Alzheimer's Disease Facts and Figures. Alzheimers Dement, 16 (3), 94.

Alzheimer's Association Report (2019). 2019 Alzheimer's disease facts and figures. Alzhemier's and Dementia, 15, 321-387.

Arnich N, Sirot V, Riviere G, Jean J, Noel L, Guerin J & Leblanc T (2012). Dietary exposure to trace

elements and health risk assessment in the 2nd French Total Diet Study. Food and Chemical Toxicology, 50, 2432-2449.

Bakar C, Karaman H, Baba A & Şengünalp F (2010). Effect of high aluminum concentration in water resources on human health, case study: Biga Peninsula, Northwest part of Turkey. Achieve Environmental Contamination Toxicology, 58, 935-944.

Barabasz W, Albinska D, Jaskowska M & Lipiec J (2002). Ecotoxicology of Aluminum. Polish Journal of Environmental Studies, 11, 199-203.

Becker L, Boyer I, Bergfeld W, Belsito D, Hill R, Klaassen C, Liebler D, Marks J, Shank R, Slaga T, Snyder P & Andersen A (2016). Safety Assessment of Alumina and Aluminum Hydroxide as Used in Cosmetics. International Journal of Toxicology, 3, 16-33.

Bostancıklıoğlu M (2019). An update on the interactions between Alzheimer's disease, autophagy and inflammation. Gene, 705, 157-166.

Bott J, Störmer A & Albers P (2018). Investigation into the release of nanomaterials from can coating into food. Food Packaging and Shelf Life, 16, 112-121.

Campbell A (2002). The Potential role of Aluminum in Alzheimer's disease. Nephrology Dialysis Transportation, 17, 17-20.

Carrasco C, Inzunza G, Camurri C, Rodríguez Radovic L, Soldera F, & Suarez S (2014). Optimization of mechanical properties of Al-metal matrix composite produced by direct fusion of beverage cans. Materials Science and Engineering A, 617, 146-155.

Chappard D (2016). Effects of aluminum on cells and tissues. Morphologie, 100, 49-50.

Chappard D, Bizot P, Mabilleau G & Hubert L (2016). Aluminum and bone: Review of new clinical circumstances associated with Al^{3+} deposition in the calcified matrix of bone. Morphologie 100, 95-105.

Crepeaux G, Eidi H, David M, Amer Y, Giros B, Authier F, Exley C, Shaw C, Cadusseau J & Gherardi R (2017). Non-linear dose-response of aluminum hydroxide adjuvant particles: Selective low dose neurotoxicity. Toxicology, 375, 48-57.

Dabre P D (2016). Aluminum and the human breast. Morphologie, 100, 65-74.

Domingo J (1995). Reproductive and Developmental Toxicity of Aluminum: A Review. Neurotoxicology and Teratology, 17, 515-521.

European Food Safety Authority (2011), On the Evaluation of a new study related to the bioavailability of aluminum in food. EFSA Journal, 9 (5), 2157.

Exley C (1998). Does antiperspirant use increase the risk of aluminum-related disease, including Alzheimer's disease? Molecular Medicine Today, 107-109.

FAO/WHO (2011). Evaluation of certain food additives and contaminants. Seventy-fourth report of the joint FAO/WHO Expert Committee on Food Additives. ISBN: 9789241209663

Federal Institute for Risk Assessment (2007), No risk of Alzheimer's disease from aluminium in consumer products. BfR Health Assessment No. 033/2007.

Filippini T, Tancredi S, Malagoli C, Cilloni S, Malavolti M, Violi F, Vescovi L, Bargellini A & Vinceti M (2019). Aluminum and tin: Food contamination and dietary intake in an Italian population. Journal of Trace Elements in Medicine and Biology, 52, 293-301.

Flaten T P (2001). Aluminium as a risk factor in Alzheimer's disease, with emphasis on drinking water. Brain Research Bulletin, 55, 187-196.

Gardner J D, Sloan S, Miner P & Robinson M (2003). Meal-stimulated gastric acid secretion and integrated gastric acidity in gastro-oesophageal reflux disease. Aliment Pharmacology Therapy, 17, 945-953.

Gupta V B, Anitha S, Hegde M L, Zecca L, Garruto R M, Ravid R, Shankar S, Stein R, Shanmugavelu Pm& Rao K (2005). Aluminum in Alzheimer's disease: are we still at a crossroad?. Cellular and Molecular Life Sciences, 62, 143-158.

Hayashi A, Sato F, Imai T & Yoshinaga J (2019). Daily intake of total and inorganic arsenic, lead, and aluminum of the Japanese: Duplicate diet study. Journal of Food Composition and Analysis, 77, 77-83.

Jabeen S, Ali B, Khan M A, Khan M B & Hasan S A (2016). Aluminum Intoxication Through Leaching in Food Preparation. Alexandria Science Exchange Journal, 37, 618-626.

Kasbe P, Jangra A & Lahkar M (2005). Mangiferin ameliorates aluminum chloride-induced cognitive dysfunction via alleviation of hippocampal oxido-nitrosative stress, proinflammatory cytokines and acetylcholinesterase level. Journal of Trace Elements in Medicine and Biology, 31, 107-112.

Klotz K, Weistenhöfer W, Neff F, Hartwig A, Thriel C & Drexler H (2017). The health effect of Aluminum Exposure. Deutsches Ärzteblatt International, 114, 653–659.

Kramer M & Heath M (2014). Aluminum in allergen-specific subcutaneous immunotherapy- A German perspective. Vaccine, 32, 4140-4148.

Krewski D, Yokel R, Nieboer E, Borchelt D, Cohen J, Harry J, Kacew S, Lindsay J, Mahfouz A & Rondeau V (2007). Human Health Risk Assessment for Aluminum, Aluminum Oxide, And Aluminum Hydroxide. Journal Toxicology Environmental Health B Critical Review, 10(1), 1–269.

Krueger G, Morris T, Suskind R & Widner, E (1984). The Health Effect of Aluminum compounds in mammals. Critical Review in Toxicology 13, 1-25.

Mailloux R, Lemire J & Appanna V (2011). Hepatic response to aluminum toxicity: Dyslipidemia and liver diseases. Experimental Cell Research, 317, 2231-2238.

Mannheim C & Passy N (2009). Internal corrosion and shelf-life of food cans and methods of evaluation. Critical reviews in food science and Nutrition, 17, 371-407.

Mathiyazahan D B, Thenmozhi A J, Manivasagam T (2015). Protective effect of black tea extract against aluminium chloride-induced Alzheimer's disease in rats: A behavioral, biochemical and molecular approach. Journal of Functional Foods, 16, 423-435.

Mendecki L, Granados-Focil S, Jendrlin M, Mold M & Radu A (2020). Self-plasticized, lumogallion-based

fluorescent optical sensor for the determination of aluminum (III) with ultra-low detection limits. Analytica Chemical Acta, 1101, 141-148.

Meyer-Baron M, Schaper M, Knapp G & Thriel C (2007). Occupational aluminum exposure: Evidence in support of its neurobehavioral impact Neuro Toxicology, 28, 1068-1078.

Othman M, Abdullah P & Aziz Y F (2010). Removal of aluminium from drinking water. Sains Malaysiana, 39, 51-55.

Özbabalık D & Hussein S (2017). Demans Bakım Modeli Raporu. Ankara: Aile ve Sosyal Politikalar Bakanlığı Sosyal İçerme Politikaları alanında Kurumsal Kapasitenin Artırılması Projesi.

Paiva E, Medeiros C, Milani R, Morgano M, Pallone J & Bragotto A (2020). Aluminum content and effect of in vitro digestion on bio accessible fraction in cereal-based baby foods. Food Research International, 131, 1-6.

Panhwar A, Kazi T, Afridi H I, Shah F, Arain M B & Arain S A (2016). Evaluated the adverse effects of cadmium and aluminum via drinking water to kidney disease patients: Application of a novel solid phase micro-extraction method. Environmental Toxicology and Pharmacology, 43, 242-247.

Paolo C, Reverte I, Colomina M, Domingo J, Gomez M (2014). Chronic exposure to aluminum and melatonin through the diet: Neurobehavioral effects in a transgenic mouse model of Alzheimer disease. Food and Chemical Toxicology, 69, 320-329.

Ranau R, Oehlenschlager J & Steinhart H (2001). Aluminum content in edible parts of seafood. Europe Food Research Technology, 212, 431-438.

Rensburg S J, Potocnik F C V, Kiss T, Hugo F, Zijl P, Mansvelt E, Carstens M E, Theodorou P, Hurly P, Emsley R & Taljaard J (2001). Serum concentrations of some metals and steroids in patients with chronic fatigue syndrome with reference to neurological and cognitive abnormalities Brain Research Bulletin, 55, 319-325.

Rogers M & Simon D (1999). A Preliminary study of dietary Aluminum intake and risk of Alzheimer's Disease. Age and Ageing, 28, 205-209.

Rondeau V, Commenges D, Gadda H & Dartigues J (2000). Relation between aluminum concentrations in drinking water and Alzheimer's disease: an 8-year follow-up study. American Journal of Epidimiol, 152, 59-66.

Rondeau V, Gadda H J, Commenges D, Helmer C & Dartigues J F (2008). Aluminum and silica in drinking water and the risk of Alzheimer's disease or cognitive decline: Findings from 15-year follow-up of the PAQUID Cohort. American J. of Epidemiology, 169, 489-496.

Rubinos D A, Arias M, Aymerich C & Fierros F (2005). Aluminum contents in drinking water from public water supplies of Galicia. The Fourth Inter-Celtic Colloquium on Hydrology and Management of Water Resources, 1-10, Guimaraes, Portugal.

Samir A M & Rashed L A (2018). Effect of occupational exposure to aluminum on some oxidative stress and DNA damage parameters. Human and Experimental Toxicology, 37, 901-908.

Seruga M, Grgic J & Mandic M (1994). Aluminum content of soft drinks from aluminum cans. Z. Lebensm Unters Forsch, 198, 313-316.

Seruga M, Grgic J, Gtgic Z & Seruga B (1997). Aluminum content of beers. Z. Lebensm Unters Forsch, 204, 221-226.

Soares D, Bolgar G, Dantas S, Augusto P & Soares B (2019). Interaction between aluminum cans and beverages: Influence of catalytic ions, alloy and coating in the corrosion process. Food Packaging and Shelf Life, 19, 56-65.

Stahl T, Falk S, Rohrbec A, Georgii S, Herzog C, Wiegand A, Hort S, Boschek B, Zorn H & Brunn H (2017). Migration of aluminum from food contact materials to food- a health risk for consumers? Part I of III: exposure to aluminum, release of aluminum, tolerable weekly intake (TWI), toxicological effects of aluminum, study design, and methods. Environmental Science Europe, 29, 19-27.

Stahl T, Taschan H & Brunn H (2011). Aluminum content of selected foods and food products. Environmental Science Europe, 23, 37- 43.

Street R, Drabek O, Szakova J & Mladkova L (2007). Total content and speciation of aluminum in tea leaves and tea infusions. Food Chemistry, 104, 1662-1669.

Tair K, Kharoubi O, Tair O A, Hellal N, Benyettou I & Aoues A (2016). Aluminum-induced acute neurotoxicity in rats: Treatment with aqueous extract of Arthrophytum. Journal of Acute Disease, 5, 470-482.

The Norwegian Scientific Committee for Food and Environment (2013). Risk assessment of the exposure to aluminum through food and the use of cosmetic products in the Norwegian population. Norwegian Scientific Committee for Food Safety, Report No: 2013:20.

Tomljenovic L (2011). Aluminum and Alzheimer's Disease: After a Century of Controversy, Is there a Plausible Link?. Journal of Alzhemier's Disease, 23, 567-598.

Verissimo M I S & Gomes M T S R (2008). Aluminum migration into beverages: Are dented cans safe?. Science of the Total Environmental, 405, 385-388.

Walton J (2012). Evidence that Ingested Aluminum Additives Contained in Processed Foods and Alum-Treated Drinking Water are a Major Risk Factor for Alzheimer's Disease. Current Inorganic Chemistry, 2, 19-39.

Walton J R (2006). Aluminum in hippocampal neurons from humans with Alzheimer's disease. Neuro Toxicology, 27, 385-394.

Walton J R (2007). An aluminum-based rat model for Alzheimer's disease exhibits oxidative damage, inhibition of PP2A activity, hyperphosphorylated tau, and granulovacuolar degeneration. Journal of Inorganic Biochemistry, 101, 1275-1284.

Walton J R (2009). Functional impairment in aged rats chronically exposed to human range dietary aluminum equivalents. Neuro Toxicology, 30, 182-193.

Wang W, Yang H, Wang X, Jiang J & Zhu W (2010). Factors effecting aluminium speciation in drinking

water by laboratory research. Journal of Environmental Science, 22, 47-55.

Wang Z, Wei X, Yang J, Suo J, Chen J, Liu X & Zhao X (2016). Chronic exposure to aluminium and risk of Alzheimer's disease: A meta-analysis. Neuroscience Letters, 610, 200-206.

Willhite C, Karyakina N, Yokel R, Yenugadhati N, Wisniewski T, Arnold I, Momoli F & Krewski D (2014). Systematic review of potential health risks posed by pharmaceutical, occupational and consumer exposures to metallic and nanoscale aluminum, aluminum oxides, aluminum hydroxide and its soluble salts. Critical Review in Toxic, 44, 1-80.

Wills M & Savory J (1985). Water content of aluminium, dialysis, dementia, and osteomalacia. Environmental Health Perspective, 63, 141-147.

World Health Organization (1998). Guidelines for drinking-water quality, 2nd ed. Addendum to Vol. 2. Health criteria and other supporting information. World Health Organization, Geneva.

Yang M, Chen S, Lin Y, Lee Y, Huang M, Chen K, Wu H, Lin P, Gozes I & Tyan Y (2019). Reduction of aluminum ion neurotoxicity through a small peptide application- NAP treatment of Alzheimer's disease. Journal of Food and Drug analysis, 27, 551-564.

Yokel R & Florence R (2008). Aluminum bioavailability from tea infusion. Food and Chemical Toxicology, 46, 3659-3663.

Yokel R (2016) Aluminum: Properties, Presence in Food and Beverages, Fate in Humans, and Determination. Encyclopedia of Food and Health. ISBN: 978-0-12-384953-3.

Yokel R A (2012). Aluminum in Food- The nature and contribution of food additives. Food Additives, Yehia El-Samragy, IntechOpen, 203-228.

Yokel R, Hicks C & Florence R (2009). Aluminum bio availability from basic sodium aluminum phosphate, an approved food additive emulsifying agent, incorporated in cheese. Food Chemical Toxicology, 46, 2261-2266.

Zhang Y, Shi B, Zhao Y, Yan M, Lytle D & Wang D (2016). Deposition behavior of residual aluminum in drinking water distribution system: Effect of aluminum speciation. Journal of Environmental Science, 42, 142-151.

Turkish Journal of Engineering

https://dergipark.org.tr/en/pub/tuje

e-ISSN 2587-1366

Valorization of banana pseudostem: endoxylanase production by *Streptomyces* sp. SH5027 using statistical approaches and its characterization and application in bread making

Ali Osman Adıgüzel*

Ondokuz Mayıs University, Faculty of Science and Letters, Department of Molecular Biology and Genetics, Samsun, Turkey

Keywords
Banana pseudostem
Endoxylanase
Streptomyces
RSM
Bread making

ABSTRACT

The present study aimed to achieve a cost-effective production of endoxylanase by *Streptomyces* sp. SH5027 using banana pseudostem with the combination of conventional and statistical optimization and to determine the biochemical properties of the enzyme and its effect on bread making. Enzyme production increased from 7.25 U/mL to 50.21 U/mL as a result of the optimization studies. The enzyme was stable at 50-75 °C and also retained more than 50% of its activity at pH 5.0-9.0 for an hour at optimum temperature. The calculated K_m value for the purified enzyme was 1.689 mg/mL.min, while the V_{max} value was 23.17 µmol/min.mg. The specific volume of the bread increased 9.6%, 12.8%, and 16.8% when 200 U, 300 U, and 400 U endoxylanase was added to the flour per kg, respectively. This study is the first to be conducted on the statistical optimization of endoxylanase production using banana pseudostem.

1. INTRODUCTION

In the last decade, agricultural wastes have increased day by day as a result of the agricultural economy developed in parallel to unrelenting population growth. Landfilling and burning, which are commonly used processes for the disposal of agricultural wastes, result in environmental and economic damages as they release toxic and/or hazardous compounds into the environment. Therefore, the interest in the conversion of agricultural wastes including wheat straw, corn stover, rice husk, sugar cane bagasse, and banana pseudostem, into value-added products has increased considerably due to the need to ensure sustainability in environmental management, bio-economy, and crops and food security (Adıgüzel and Tunçer 2017a; Adıgüzel 2020).

Bananas are one of the most important agro-industrial crops worldwide with about 114 million tons of production and 18.1 million tons of export volume in 2017 according to the Food and Agriculture Organization (FAO) (Fao 2017). Although bananas are mainly cultivated in the tropical and sub-tropical regions of Latin America, Asia and Africa, they can be produced all over the world. In the Mediterranean region of Turkey, approximately 200-300 thousand tons of bananas are produced every year. With the harvest of each ton of banana, approximately 3 tons of pseudostems, 0.16 tons of stems, 0.48 tons of leaves and 0.44 tons of skin residues are generated (Padam et al. 2014). These wastes, which are either discharged, left to dry on fields or burned by farmers, pollute the atmosphere, contaminate groundwater and cause the spread of plant pathogens such as *Thielaviopsis paradoxa*, *Colletotrichum musae* and *Fusarium verticillioides* (Alvindia and Natsuaki 2009). Furthermore, banana wastes mostly end up in the sea due to extreme winds and rain in winter since, in Turkey, most of the areas cultivated with banana are sloping lands. Thus, due to the pollution of the sea, economic loss occurs in these regions which have a significant tourism potential.

Banana pseudostems consist of 25-30% cellulose, 20-25% hemicelluloses, and 10-15% lignin (Gabhane et al. 2014). On account of its relatively low lignin content, it is considered as a potential feedstock in green chemistry

* **Corresponding Author**

*(adiguzel.ali.osman@ gmail.com) ORCID ID 0000-0002-5602-5886

Cite this article

Adıgüzel A O (2022). Valorization of banana pseudostem: endoxylanase production by *Streptomyces* sp. SH5027 using statistical approaches and its characterization and application in bread making. Turkish Journal of Engineering, 6(2), 128-139

Research Article / DOI: 10.31127/tuje.847736

Received: 27/12/2020; Accepted: 21/03/2021

applications such as the production of bioethanol, carboxymethylcellulose (CMC), bioactive compounds, and the absorbent of xenobiotics (Padam et al. 2014). Furthermore, banana pseudostems can be used as a cheap and efficient inducer for the production of lignocellulolytic enzymes such as cellulases and xylanases with microbial fermentation methods. Xylanases are a group of enzymes that catalyze the hydrolysis of xylan, which is the second most abundant polysaccharide, after the cellulose of lignocellulosic biomass. The endo-1,4-β-xylanase (1,4-β-D-xylan xylohydrolases, EC 3.2.1.8) otherwise known as endoxylanase, releases xylooligosaccharides, xylobiose, and xylose by random breakage of the β-1,4 glycosidic bonds in the xylan chain. They have a huge commercial potential as they can be used in various industrial applications such as the bleaching of kraft pulps, deinking of paper, clarification of fruit juices and wines, saccharification of hemicelluloses, improvement of animal feed digestibility, and extraction of oils from plants or vegetables. They are also used for improving the rheological properties and machinability of dough as well as the shelf life and nutritional quality of bread (Walia et al. 2017). Until today, very few studies have been conducted on xylanase production using banana pseudostems. Vieira et al. (2007) reported that *Clostridium thermocellum* produced from 5.14 U/mL xylanase after being grown in a medium containing 2% banana pseudostem. In their study, Shah et al. (2005) reported that *Phylosticta* spp. MPS-001 could produce using laccase, lignin peroxidase, xylanase and cellulase on banana pseudostem through solid-state fermentation.

One of the most significant challenges in green chemistry applications is the high process cost. It is seen that the use of cheap inducers alone is not sufficient to reduce the cost of value-added products such as endoxylanase. However, this can be reduced with process optimization through conventional and/or model-based statistical approaches. One-factor-at-time (OFAT), a conventional method in which only one independent variable is tested in each step, is time-consuming, especially in evaluating the effect of a large number of variables on enzyme production (Yabalak et al. 2017). Alternatively, Placket Burman Design (PBD) and Response Surface Methodology-Central Composite Design (RSM-CCD) provide a rapid selection of the most significant independent variables and an evaluation of the combined effect of the selected variables on the result, respectively. Su et al. (2011) reported that the xylanase yield of *Thermomyces lanuginosus* SDYKY-1 increased approximately 2.4-fold through PBD and RSM-CCD in a fermentation medium prepared using corncobs and soybeans as carbon sources. Kumar and Satyanarayana (2012) reported that *Bacillus halodurans* produced 7.35-fold more xylanase using wheat bran as the carbon source after the optimization of the process by the same approach. Sharma and Bajaj (2018) achieved a 1.92-fold enhancement in xylanase production from *Aspergillus terreus* S9 using model-based statistical approaches. To our knowledge, endoxylanase production using banana pseudostem has not yet been studied through model-based statistical approaches.

In the present study, actinobacterial strains were selectively isolated from soil contaminated with banana plant wastes and screened by quantitative and qualitative analysis for endoxylanase production using banana pseudostem as the carbon source. The process conditions were optimized by (One Factor at Time) OFAT while PBD and RSM-CCD were used for the optimization of the composition of the medium. Endoxylanase produced under optimum condition was purified by ion exchange and gel filtration chromatography methods. Subsequently, its biochemical properties were detected. Finally, potential application of enzyme in bread making were studied.

2. METHOD

2.1. Isolation and Identification of Microorganisms

A total of 10 soil samples were collected from different areas contaminated with banana wastes in Erdemli (Mersin/Turkey) and stored at 4 °C. The analysis of the soils and the isolation of bacteria were initiated within 12 h (hours) after sampling. The air-dried soil samples were suspended in distilled water at 1:2.5 and 1:5 (w/v, soil/water) ratios for pH and conductivity analysis. After the suspensions were agitated at 150 rpm for 30 min, their pH and conductivity were measured by pH/Conductivity Meter (Hanna HI-2300) (Houfani et al. 2017). Gravimetric water and organic matter contents were determined by measuring weight loss in crude soils incubated at 105 °C for 48 h in an oven and water-free soils incubated at 550 °C for 16 h in a muffle furnace, respectively (Houfani et al. 2017).

Before bacterial isolation, the soil samples were pretreated with incubation at 50 °C for 1 h and serially diluted in ¼ ringer solutions (10^{-2}-10^{-7}). 100 µL of the diluted solution (10^{-4}-10^{-6}) was spread on a modified (International Streptomyces Project 4) ISP4 medium containing birchwood xylan instead of soluble starch (pH 7.0 ± 0.2). The colonies that had different structures, shapes, and colors were picked and purified on a (International Streptomyces Project 2) ISP2 medium. All isolates were maintained on an ISP2 medium slant at +4 °C and in 20% glycerol at -20 °C, respectively.

2.2. Screening of Xylanolytic Isolates

For the selection of the most efficient endoxylanase producers, the isolates were screened by quantitative and qualitative analysis. The pure isolates were spot inoculated on a modified ISP4 medium and then incubated at 30 °C for 4 days for quantitative analysis. At the end of the incubation period, the surface of the plates was coated with 1% (w/v) Congo red solution for 15 min and then washed using 1M NaCl three times to remove any excess and unbound dye. A slight yellow hydrolysis zone around the colony indicates that the isolate produces xylanolytic enzymes. Subsequently, the extracellular endoxylanase production in 50 mL un-optimized fermentation medium (UFM: 10 g/L banana pseudostem, 1 g/L peptone, 1 g/L yeast extract, 1 g/L KNO_3, 0.5 g/L KH_2PO_4, 0.5 g/L $MgSO_4$, 0.3 g/L $CaCl_2$, 3 g/L NaCl and 0.6 g/L tween 80) was assessed. Endoxylanase production was performed in a 250 mL Erlenmeyer flask

under shaking condition at 160 rpm and 30 °C for 4 days after inoculation of strain.

2.3. Identification of Strain

The strain used for endoxylanase production was identified based on 16S rRNA gene sequences. The strain was grown in an ISP2-liquid medium at 30 °C and 160 rpm for 3 days. The cells were recovered by centrifugation (10000 *g*, 5 min). DNA isolation was carried out using the AMBRD DNA isolation kit as described by the manufacturer. The 16S rRNA gene was amplified using 27 forward (5'-AGA GTT TGA TCA TCA TGG CTC AG) and 1492 reverse (5'-TAC GGC TAC CTT GTT ACG ACT T) primers according to Adigüzel and Tunçer (2016). Subsequently, the sequences data of the 16S rRNA gene were compared with the sequences in the National Center for Biotechnology Information (NCBI) database by BLAST to construct a phylogenetic tree using MEGA 6 software.

2.4. Preparation of Inoculums

One mL of ¼ ringer solution was poured on a 15-day-old culture grown on an ISP2 medium. Subsequently, spore suspension was prepared by gently shaking the culture plate for 1 min (minute). After counting, 200 µL of diluted spore suspension containing approximately 10^6 spore/mL was used as inoculum.

2.5. Estimation of Extracellular Total Protein and Endoxylanase Activity

The supernatant obtained with the centrifugation of the culture (10000 *g*, 5 min) was used as a crude enzyme. The total protein in the crude enzyme was estimated using bovine serum albumin as standard (Bradford 1976). Endoxylanase activity was determined by the dinitrosalicylic acid (DNS) method of Miller with slight modification (Miller 1959). The reaction mixture consisting of supernatant and 1% birchwood xylan solution prepared in a phosphate buffer (100 mM, pH 7.0) was incubated at 30 °C for 10 min. The reaction was terminated with the addition of the DNS solution. The mixture was kept in boiling water for 10 min. Subsequently, the amount of reducing sugar released was calculated by measuring the absorbance at 540 nm. A unit (U) of enzyme activity is defined as the amount of endoxylanase required to catalyze the release of 1 µmol of xylose equivalent per min at 30°C (Adıgüzel and Tunçer 2017b).

2.6. Estimation of Extracellular Total Protein and Endoxylanase Activity Selection of Cultural Conditions by OFAT for Endoxylanase Production

The Placket Burman matrix was developed using Design Expert 7.0. software (Stat-Ease, Minneapolis, MN, USA) to determine the most important variables on endoxylanase production. As shown in table 1, 9 independent variables including banana pseudostem (A), peptone (B), yeast extract (C), KNO_3 (D), $MgSO_4$ (E), KH_2PO_4 (F), $CaCl_2$ (G), NaCl (H) and Tween 80 (J) were tested in two levels: +1 for high level and -1 for low level. A total of 12 experimental runs were conducted in triplicate and the average endoxylanase activities were taken as responses. The significance of the statistical model was determined using ANOVA. The effects of each independent variable were calculated according to the Equation 1.

$$Ex_i = \left(\sum M_i^+ - \sum M_i^-\right)/ N \quad (1)$$

where, Ex_i is the effect of a variable, M_i^+ and M_i^- are the responses of the experimental runs at the high and low levels of each variable, respectively, and N is the total number of runs.

2.7. Optimization of Parameters by RSM-CCD

RSM-CCD was employed to optimize the three most important variables identified by PB design, and to elucidate the relationship between these variables for enhancing endoxylanase production. The construction of the design matrix was carried out using Design Expert 7.0 software (Stat-Easy). The variables denoted (banana pseudostem), (yeast extract) and (tween 80) were analyzed at 5 coded levels (-α, -1, 0, +1, +α) as shown in table 2. Based on the design matrix, a total of 20

Table 1. Levels of variables in Plackett Burman design matrix along with experimental and predicted endoxylanase production

Run	Variables (g/L)									Endoxylanase production (U/mL)	
	A	B	C	D	E	F	G	H	J	Experimental	Predicted
1	20	0.5	0.5	3	1	0.2	0.4	5	0.1	14.20	14.08
2	20	3	3	1	0.2	1	0.4	5	0.1	19.36	19.21
3	4	0.5	0.5	3	0.2	1	0.4	1	0.5	10.04	9.89
4	4	3	3	3	0.2	0.2	0.1	5	0.1	12.14	12.26
5	20	0.5	0.5	1	1	1	0.1	1	0.1	16.46	16.61
6	4	3	0.5	1	0.2	0.2	0.1	1	0.1	9.30	9.42
7	4	0.5	3	3	1	0.2	0.4	1	0.1	13.24	13.12
8	20	3	3	1	0.2	1	0.4	1	0.5	24.94	24.81
9	4	0.5	0.5	1	1	0.2	0.4	5	0.5	11.32	13.31
10	4	3	3	1	1	1	0.1	5	0.5	13.16	13
11	20	0.5	3	3	1	0.2	0.1	1	0.5	23.84	23.99
12	20	3	0.5	3	0.2	0.2	0.1	5	0.5	16.60	16.72

experimental runs involving 6 centers, 6 axials, and 8 factorial points were performed in triplicate. Average endoxylanase production was taken as a response. To predict endoxylanase production, results from each experimental run in the design matrix were fitted to the following second order polynomial Equation 2.

$$Y_{\text{i}} = b_0 + b_1X_1 + b_2X_2 + b_3X_3 + b_{11}X_1^2 + b_{22}X_2^2 + b_{33}X_3^2 + b_{12}X_1X_2 + b_{23}X_2X_3 + b_{13}X_1X_3 \quad (2)$$

where, Y_{i} is the predicted endoxylanase production by *Streptomyces* sp. SH5027, X_1, X_2, X_3 are the independent variables, b_0 is the offset term, b_1, b_2, b_3 are the linear effects, b_{11}, b_{22}, b_{33} are the squared effects and b_{12}, b_{23}, b_{13} are the interaction terms.

Table 2 Levels of variables tested in RSM-CCD

Variables	Coded levels				
	- α	-1	0	+1	+ α
X_1 (g/L)	4.00	7.24	12.00	16.76	20.00
X_2 (g/L)	1.00	2.01	3.50	4.99	6.00
X_3(g/L)	0.20	0.36	0.60	0.84	1.00

2.8. Purification of Endoxylanase for Characterization

Streptomyces sp. SH5027 was cultivated in the optimized fermentation medium under optimum cultural conditions. All purification steps were carried out at approximately 4 °C. The culture supernatant was used as the crude enzyme after centrifugation at 10000 *g* for 5 min. The crude enzyme was both concentrated and fractionated with a 30 kDa molecular weight cut-off membrane using pressure based Amicon stirred ultrafiltration cells. Proteins higher than 50 kDa in fraction were separated with 50 kDa molecular weight cut-off membrane using the same method. Subsequently, a partially purified enzyme was dialyzed against 20 mM Tris-HCl (pH 8.0) and then loaded onto DEAE Sephadex A-50 anion-exchange column (2.6 X 10 cm) equilibrated with 20 mM Tris-HCl (pH 8.0). The elution of the bound proteins was performed with a linear gradient of 0-1 M NaCl in the same buffer containing a flow rate of 0.75 mL/min. The endoxylanase activity and protein concentration of each fraction (5 mL) were estimated by the DNS method and measuring absorbance at 280 nm, respectively. The fractions showing high endoxylanase activity were pooled, concentrated and dialyzed for further studies. The purity of the enzyme was shown on acrylamide gel by sodium dodecyl sulfate polyacrylamide gel electrophoresis (SDS-PAGE) (Adıgüzel and Tunçer, 2016).

2.9. Characterization of Endoxylanase and Its Application in Baking

The enzyme assay was carried out by varying only one factor at a time to determine the biochemical properties of endoxylanase from *Streptomyces* sp. SH5027. The reaction was carried out at different temperatures (20-80 °C) in a 50 mM phosphate buffer (pH 7.0) to determine the optimum temperature for endoxylanase activity. The optimum pH was detected by assaying the endoxylanase activity in the various buffers (50 mM) including a citrate buffer (pH 4.0–6.0), a phosphate buffer (pH 6.0–7.5), and a Tris-HCl buffer (pH 7.5–9.0) at 45 °C. The measured maximum activity was found to be 100%. The thermostability of the enzyme was evaluated by the pre-incubation of the enzyme (1-12 h) in a 50 mM phosphate buffer (pH 6.5) at various temperatures ranging from 40 to 80 °C. The stability of endoxylanase at different pH values ranging from 4.5 to 10.0 was investigated by the pre-incubation of the enzyme in various buffers (50 mM) described above at 45 °C. To investigate the storage time of the enzyme, the endoxylanase solution prepared in a 50 mM phosphate buffer (pH 6.5) was the kept at -20 and +4 °C for 180 days. The initial enzyme activity was accepted as 100%.

The endoxylanase was pre-incubated with 5 mM metal ions (Mn^{+2}, Mg^{+2}, Ca^{+2}, Hg^{+2}, Zn^{+2}, and Cu^{+2}), 10% organic solvents (ethanol, methanol, isopropanol, dimethyl sulfoxide, ethyl acetate, and dimethylformamide) and 5 mM inhibitors (ethylenediaminetetraacetic acid, sodium dodecyl sulfate, 1,4-dithiothreitol, and mercaptoethanol,) in a phosphate buffer (50 mM, pH 6.5) for 30, 60 and 120 min, respectively. Subsequently, residual endoxylanase activity was measured at 45 °C. The activity of endoxylanase pre-incubated in an additive-free buffer under the same condition was accepted to be 100%.

To investigate the substrate specificity of the enzyme, various substrates (beechwood xylan, oat spelt xylan, carboxymethyl cellulose, filter paper, soluble starch, and citrus pectin) were used instead of birchwood xylan in the activity assay performed under optimum temperature and pH. The activity against birchwood xylan was found to be 100%. The kinetic study was performing the assaying the enzyme using a range of birchwood xylan concentration from 0.5 to 20 mg/mL under optimum condition. A Linewaever–Burk plot illustrating the Michaelis constant (K_m) and the specific activity (V_{max}) was generated using Hyper32 software.

Within the scope of the present study, breads were produced at a local bakery (Karadeniz Bakery) in Adana, Turkey. The dough was prepared conventionally by adding 20 g NaCl (w/w), 40 g yeast (w/w), and 1200 mL tap water supplemented with endoxylanase (100-400 U) for 1 kg flour. After the dough was mixed at room temperature for 120 min, it was divided into pieces of 200 g, hand-rounded and left to rest on a tray for 120 min. Subsequently, the dough was baked at 300 °C for 15 min. The breads were cooled for 2 h before determining their specific volumes. The specific volume of the dough prepared without the enzyme was accepted as 100%.

3. RESULTS and DISCUSION

3.1. Isolation and Selection of Xylanolytic Strains

There were no significant differences in the pH, conductivity, gravimetric water content, or organic matter content of the soil samples collected from 10 different locations (data was not shown). The appropriate dilutions of the soil samples, contaminated with banana wastes, were plated on a modified ISP-4 medium. Out of approximately 180 bacterial colonies that could grow on the medium, 48 were isolated

considering the morphological differences (shape and color). Their ability to produce xylanolytic enzymes on the same medium was screened by Congo red staining which is a low cost and practical method. A total of 28 strains showed xylanolytic activity which was indicated by the appearance of a slight yellow zone of hydrolysis around the colonies (figure 1). Among them, the isolate SH5027 exhibited the highest endoxylanase production (7.25 U/mL) with 30.16 U/mg specific activity in un-optimized fermentation medium. Therefore, the isolate SH5027 was selected for further studies.

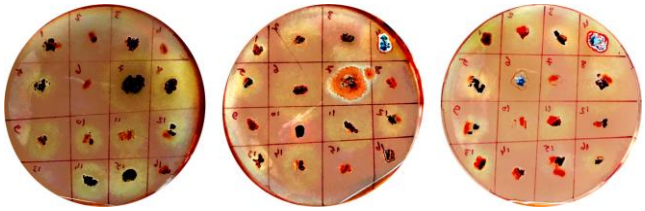

Figure 1. Screening of xylan production on agar plates. The slight yellow zone around the colony indicates that the strain can produce xylanolytic enzymes

3.2. Molecular identification

The partial 16S rRNA gene sequence (1210 bp) of the isolate SH5027 was analyzed by BLAST in NCBI. The sequence showed a 96.07% identity to those of *Streptomyces almquistii* NRRL B-1685, *Streptomyces althioticus* strain 12740, *Streptomyces griseoincarnatus* NBRC 12871, *Streptomyces labedae* NBRC 15864 and *Streptomyces variabilis* NRRL B-3984. The 16S rRNA gene sequences from the other related type strains, which were shown in the phylogenetic tree, exhibited less than 96% sequence identity to the isolate SH5027 (figure 2). It was revealed that the isolate was closely related to the genus *Streptomyces*. Therefore, the isolate was classified into the *Streptomyces* genus and expressed as *Streptomyces* sp. SH5027. The polyphasic approach including chemotaxonomic, phenotypic, and genotypic characterizations of the isolate is required for a more detailed explanation of its taxonomic position.

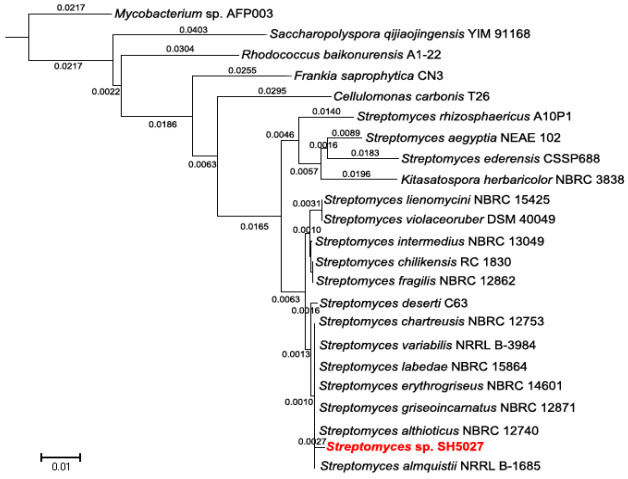

Figure 2. Phylogenetic tree showing the relationship between the isolate SH5027 and strain types. The tree was constructed based on their 16S rRNA gene sequences by MEGA6 software using neighbor-joining

3.3. Selection of cultural conditions for endoxylanase production

Cultural conditions such as temperature, initial pH of the medium and agitation speed highly influence enzyme production (Figure 3). The maximum endoxylanase production (7.77 U/mL) by *Streptomyces* sp. SH5027 was observed at 35 °C. A relatively high enzyme titer was also detected at 25 °C (6.15 U/mL), 30 °C (7.28 U/mL) and 40 °C (6.60 U/mL). However, significant decreases in enzyme production were detected at 20 °C (2.64 U/mL) and 45 °C (1.05 U/mL). The results of this study were in accordance with previous studies conducted on endoxylanase production by *Streptomyces cuspidosporus* (Maheswari and Chandra 2000), *Streptomyces* sp. isolated in India (Thomas et al. 2013) and *Streptomyces* sp. RCK-2010 (Kumar et al. 2012), which exhibited high endoxylanase production at 25-40 °C. The effect of the initial pH of the medium on endoxylanase production was investigated at 35 °C and under a shaking condition of 160 rpm. The endoxylanase titer was found to be maximum when the initial pH of the medium was adjusted to 6.0 (8.01 U/mL). Enzyme production decreased slightly when the initial pH of the medium was increased to 7.0 (7.59 U U/mL) and 8.0 (6.46 U/mL). At pH 5.0, enzyme production decreased in half (4.36 U/mL). The findings were in line with a previous study conducted by Porsuk et al. (2013). The test performed to determine the influence of agitation speed on endoxylanase production showed that high xylanase production occurred at 120-220 rpm. Any agitation speed beyond this range was not suitable for endoxylanase production. In addition, maximum endoxylanase production was recorded at 180 rpm with 8.26 U/mL. The decrease in endoxylanase production under lower agitation speeds may be due to weak oxygen transfer, insufficient distribution of oxygen in Erlenmeyer flask and interaction between bacteria and banana pseudostem used as inducer.

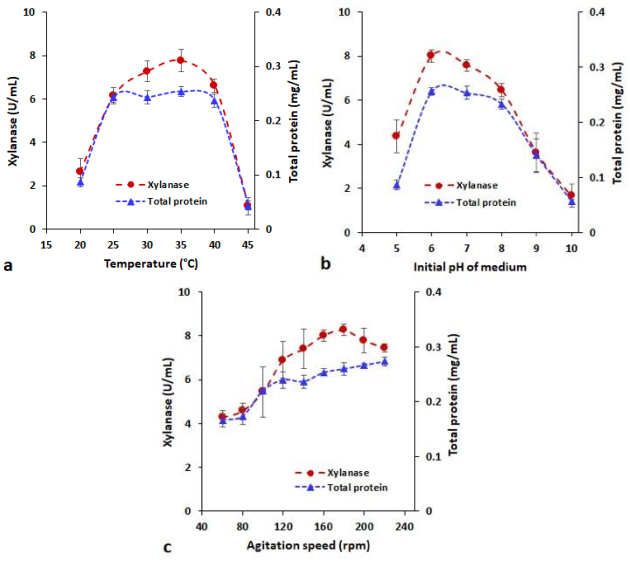

Figure 3. The effect of temperature **(a)**, initial pH of the medium **(b)**, and agitation speed **(c)** on endoxylanase production by *Streptomyces* sp. SH5027 as well as extracellular protein secretion

3.4. Selection Selection of the most important variables affecting endoxylanase production by PBD

All experimental runs were performed at 35 °C and under a shaking condition of 180 rpm. The initial pH of the medium was adjusted to 6.0 before the experiments. The experimental results showed significant variation in endoxylanase production from 9.30 U/mL to 24.96 U/mL. The significance and adequacy of the model were analyzed using Fischer's test for analysis of variance (ANOVA). The calculated *F*-value (286.04) showed that the applied model was statistically significant. The *p*-value of 0.0035 was found to be at a 95% confidence interval. The variability in endoxylanase production was detected to be 99.92% according to the determination coefficient (R^2) value. Furthermore, the values of the adjusted coefficient (Adj-R^2) and the predicted coefficient (Pred-R^2) were calculated to be 0.9957 and 0.9721, respectively, and were in reasonable agreement. The adequate precision values (Adeq-Precision) of 50.671, which give the signal to noise ratio, also indicated that the model generated strong signals to design space. The model was fitted for endoxylanase production with the Equation 3.

$$Y = +7.83694 + 0.48146A + 0.16067B + 0.95933C - 0.14167D - 0.22500E - 0.1277778F - 0.75000G - 0.46083H + 3.17083J \quad (3)$$

where Y is the predicted endoxylanase activity and A, B, C, D, E, F, G, H, and J are the coded values of the independent variables.

The regression analysis coefficient and the *t*-values of the variables, which are shown in table 3, revealed that banana pseudostem, yeast extract, tween 80, peptone, and $CaCl_2$ had a positive effect on endoxylanase production by *Streptomyces* sp. SH5027, whereas NaCl, KH_2PO_4, KNO_3, and $MgSO_4$ had a negative effect. Among the variables, banana pseudostem, yeast extract, tween 80 and NaCl were significant due to their confidence level which was above 95% ($p<0.05$). Furthermore, a Pareto chart was drawn to illustrate the order of importance of the variables and which variables are the most important for endoxylanase production (figure 4). The chart revealed that banana pseudostem was above the Bonferroni limit, which is almost certainly important, while those above the *t*-value limit, namely, yeast extract, tween 80 and NaCl, are possibly important. Considering the previous studies which focused on the induction of enzyme secretion by lignocellulosic agricultural wastes, it is not surprising that banana pseudostem showed a strong effect (Sharma and Bajaj 2018). The second important variable was found to be yeast extract used as a nitrogen source. This may be due to the effects of various growth factors and essential amino acids in yeast extract on the growth of the *Streptomyces* sp. SH5027. Another very significant variable, tween 80, may provide the rapid transportation of compounds such as enzymes and soluble inducers across the cell membrane (Ahamed and Vermette 2008). In conclusion, banana pseudostem, yeast extract and tween 80 were selected for further optimization studies by RSM-CCD.

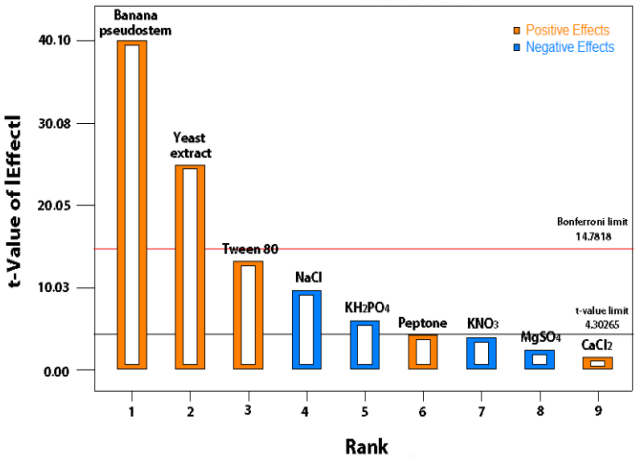

Figure 4. The Pareto chart illustrates the effects of independent variables on endoxylanase production by Streptomyces sp. SH5027

3.5. RSM-CCD

RSM-CCD was used to evaluate the interaction of the variables, selected based on the results from PBD, and to determine their optimal levels for endoxylanase production. The design matrix and experimental results, fitted with the second-order polynomial Equation 4, are presented in table 4.

$$Xylanase\ activity\ \left(\frac{U}{mL}\right) = +3.10988 + 4.73488X_1 - 2.56680X_2 - 15.16615X_3 - 0.70039X_1X_2 + 0.32704X_1X_3 + 11.80161X_2X_3 - 0.040353X_1^2 + 0.62678X_2^2 - -29.79754X_3^2 \quad (4)$$

where, X_1, X_2, X_3 are independent variables.

The highest and lowest experimental results were obtained from Run 20 (45.75 U/mL) and Run 11 (10.16 U/mL), respectively. The model fit was statistically assessed by ANOVA. It was revealed that the model with an *F*-value of 210.22 and *p*-value of < 0.0001 was adequate and significant. Furthermore, the R^2-value calculated as 0.9947 proved the adequacy of the model

Table 3. ANOVA results of the model constructed by Plackett Burman

Variables (g/L)	Effect	Coefficient estimate	Standard error	Sum of square	F-value	p-value prob >F
A	7.70	3.85	0.096	178.02	1608.7	0.0006*
B	0.80	0.40	0.096	1.94	17.49	0.0527
C	4.80	2.40	0.096	69.02	623.52	0.0016*
D	0.28	0.14	0.096	0.24	2.18	0.2782
E	-0.45	-0.22	0.096	0.61	5.49	0.1438
F	-1.15	-0.57	0.096	3.97	35.84	0.0268*
G	-0.75	-0.38	0.096	1.69	15.24	0.0598
H	-1.84	-0.46	0.048	10.19	92.08	0.0107*
J	2.54	1.27	0.096	19.30	174.38	0.0057*

and indicated that variability up to 99.47% in endoxylanase production could be explained by the model. The reasonable agreement between pred-R^2 (0.9712) and Adj-R^2 (0.9900) indicated a strong relationship between the experimental and predicted results. It was also determined that the signal was adequate and the model adapted to the results in a good methodology considering the Adeq-precision value of 63.754 and lack of fit *F*-value of 1.65, respectively.

The ANOVA results of the terms are listed in table 5. Among the linear terms, banana pseudostem, yeast extract, and tween 80 were statistically significant. The quadratic effects of all the variables were also found to be significant. A strong interaction between banana pseudostem and yeast extract was found. Another strong interaction was also observed between yeast extract and tween 80. Furthermore, the results indicated that the banana pseudostem with the lowest *p*-value was the most important variable for endoxylanase production.

Three-dimensional (3D) response surface plots were generated to evaluate the influence of the variables on endoxylanase production by *Streptomyces* sp. SH5027. An evaluation of the two variables was performed while the other variable was kept at the middle level. The plots illustrated in figure 5a indicate that endoxylanase production enhanced with the increase in banana waste concentration at the low and middle levels of yeast extract. On the other hand, endoxylanse production decreased with the increase in banana pseudostem concentration at the high level of yeast extract. The increase in yeast extract levels resulted in the enhancement in enzyme production at the low level banana pseudostem. However, the fact that the yeast extract increased from the middle level to the high level showed a negative effect on endoxylanase production when the banana pseudostem was kept at the high level. This may be due to the *Streptomyces* sp. SH5027 preferred to use some degradation products of banana pseudostem as nitrogen sources during fermentation. Figure 5b illustrates the increase in endoxylanase yield with an increasing level of banana pseudostem at all levels of tween 80. An increase or decrease in tween 80 concentration resulted in a decrease in endoxylanase production at all levels of the banana pseudostem. Enzyme production increased gradually with the increase in yeast extract concentration at the high level of tween 80 (figure 5c). At the low level of yeast extract, the increase of tween 80

Table 4. Design matrix constructed by RSM-CCD, experimental and predicted results

Run	Variables (g/L)			Endoxylanase production (U/mL)		Run	Variables (g/L)			Endoxylanase production (U/mL)	
	X_1	X_2	X_3	Experimental	Predicted		X_1	X_2	X_3	Experimental	Predicted
1	12	3.5	0.6	30.41	30.71	11	7.24	2.01	0.84	10.16	10.72
2	12	3.5	0.6	30.62	30.71	12	16.76	4.99	0.36	30.04	29.28
3	12	3.5	0.6	30.33	30.71	13	12	3.5	0.6	32.09	30.71
4	7.24	4.99	0.6	30.04	29.28	14	12	3.5	0.2	27.41	28.22
5	12	3.5	0.6	30.42	30.71	15	16.76	2.01	0.84	19.05	18.90
6	4	3.5	0.6	15.53	16.03	16	12	1	0.6	33.74	33.38
7	7.24	2.01	0.36	23.15	22.51	17	12	6	0.6	35.22	35.87
8	16.76	4.99	0.84	35.22	35.66	18	12	3.5	1	24.18	23.66
9	7.24	4.99	0.84	30.95	30.44	19	12	3.5	0.6	30.42	30.71
10	20	3.5	0.6	40.43	40.21	20	16.76	2.01	0.36	45.75	46.05

Table 5. The ANOVA results of the terms used in construction of response surface by CCD

Model terms	Coefficient estimate	Sum of square	Mean Square	*F*-value	*p*-value prob >F
Model		1162.40	129.16	210.22	< 0.0001*
$\boldsymbol{X_1}$	7.19	705.77	705.77	1148.75	<0.0001*
$\boldsymbol{X_2}$	0.74	7.45	7.45	12.13	0.0059*
$\boldsymbol{X_3}$	-1.35	25.04	25.04	40.76	< 0.0001*
$\boldsymbol{X_1X_2}$	-4.95	196.22	196.22	319.37	< 0.0001*
$\boldsymbol{X_1X_3}$	4.17	1.10	1.10	1.78	0.2114
$\boldsymbol{X_2X_3}$	0.40	139.28	139.28	226.70	< 0.0001*
$\boldsymbol{X_1^2}$	-0.91	12.02	12.02	19.56	0.0013*
$\boldsymbol{X_2^2}$	1.39	27.64	27.64	45.00	< 0.0001*
$\boldsymbol{X_3^2}$	-1.69	40.95	40.95	66.65	< 0.0001*
Residual		6.14	0.61		
Total		1168.54			

concentration caused a significant decrease in enzyme production.

The optimum levels of the variables within the tested ranges for endoxylanase production were determined by using the numerical optimization panel of Design Expert software with the desirability approach. The desired goal for banana pseudostem, yeast extract and tween 80 was adjusted to the "in range" mode, while, as a response, endoxylanase production was adjusted to the "maximize" mode. Solutions were generated with desirability values that varied from 0 (undesirable response value) to 1 (completely desired response value). This suggests that the maximum endoxylanase production (49.42 U/mL) with a desirability value of 1.0 could occur with 15.27 g/L banana pseudostem, 1.30 g/L yeast extract and 0.24 g/L tween 80. To verify the predicted result, endoxylanase production was experimentally carried out in triplicate under optimum conditions. It was determined that the experimental value of 50.21 U/mL was very close to the predicted value. Over the last few years, various studies were performed to demonstrate the feasibility of statistical optimization methods for the enhancement of enzyme production. However, no statistical optimization studies for endoxylanase production using banana pseudostem have yet been reported.

3.6. Purification of Endoxylanase

In the first step, the crude enzyme (750 mL) containing a total of 212 mg protein and 12145 U/mL endoxylanase activity was filtered through a 30 kDa cut-off ultrafiltration membrane to remove the lower proteins as well as increase the concentration of the others. This resulted in a yield of 93.4% and purification of 1.5-fold. No endoxylanase activity was detected in the ultrafiltrate. The retentate was further fractionized by a 50 kDa cut-off ultrafiltration membrane, resulting in a yield of 88.4% and purification of 3.4-fold. Finally, the dialyzed ultrafiltrate was loaded onto a DEAE Sephadex A-50 column and then eluted with NaCl. It was determined that the enzyme was 11.2-fold purified with a 32.3% yield after the fractions (182-202), corresponding to the endoxylanase peak on the chromatogram (figure 6a), were pooled and concentrated for further SDS-PAGE and zymogram analyses. The homogeneity of the purified endoxylanase was confirmed by the visualization of a single band on the acrylamide gels through SDS-PAGE analysis. The molecular mass of the enzyme was calculated to be approximately 38 kDa (figure 6b), which was similar to the endoxylanase from *Streptomyces* sp. CS428 (37 kDa) (Pradeep et al. 2013), *Streptomyces*

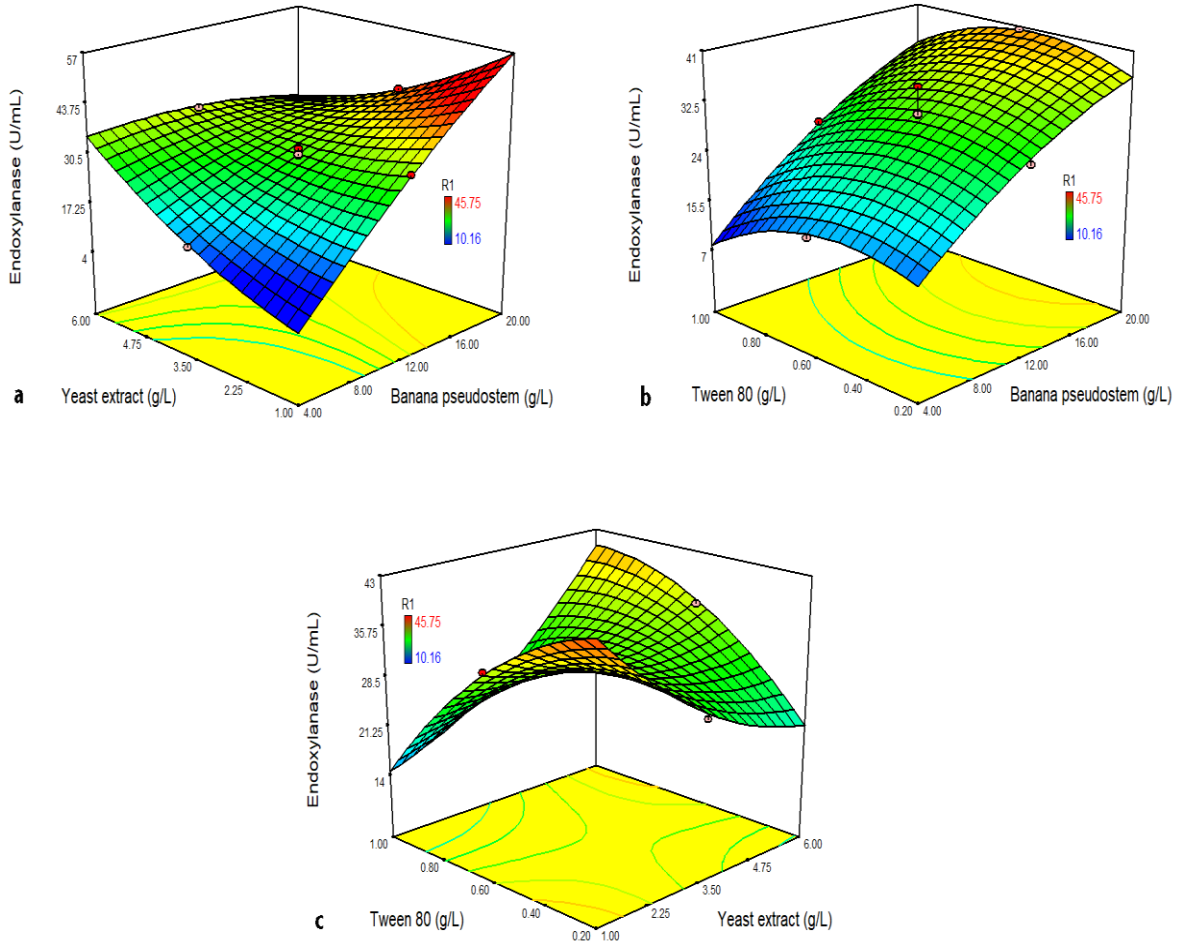

Figure 5. Response surface plots of endoxylanase production show interaction between (a) yeast extract and banana pseudostem, (b) banana pseudostem and tween 80, (c) yeast extract and banana pseudostem

thermocyaneociolaceu (35 kDa) (Shin et al. 2009), *Streptomyces* sp. TN119 (35.9 kDa) (Zhou et al. 2011), *Streptomyces olivaceus* (42 kDa) (Sanjivkumar et al. 2017), *Streptomyces* sp. S9 (46 kDa) (Li et al. 2008), and *Streptomyces* sp. CS624 (40 kDa) (Mander et al. 2014).

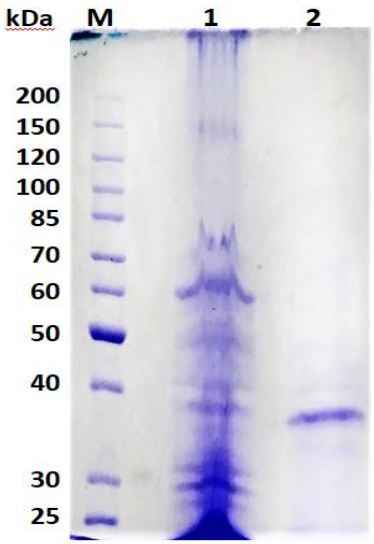

Figure 6. SDS-PAGE analysis; Lane 1: protein molecular weight marker, Lane 2: crude enzyme, Lane 3: purified endoxylanase

3.7. Characterization of Endoxylanase

The optimal temperature was found to be 60 °C which was similar to that of the xylanases obtained from other *Streptomyces* (Wang et al. 2007; Li et al. 2008; Shin et al. 2009). However, the relative activity of the endoxylanase in the present study was over 80% at 25-60 °C (figure 7a) unlike the other xylanase from *Streptomyces* sp. CS428 (Pradeep et al. 2013), *Streptomyces megasporus* DSM 41476 (Qiu et al. 2010), and *Streptomyces rochei* L10904 (Li et al. 2018). A significant decrease in enzyme activity was observed when the reaction temperature was decreased below 20 °C or increased to 70 °C. However, an endoxylanase activity over 60% was recorded in both cases. The results showed that the enzyme can be used in a wide variety of biotechnological applications carried out at different temperatures. The highest enzyme activity was attained at pH 6.5 in a 50 mM phosphate buffer (figure 7b). However, the enzyme showed a high relative activity (>75%) in a wide pH value range (5.0-10.0). The relative endoxylanase activities at pH 4.5 and 4.0 were 55.1% and 26.7%, respectively. Similar pH optima (pH 6.0-7.0) were previously reported for xylanases obtained from other strains such as *Streptomyces* sp. RCK-2010 (Kumar et al. 2012), *Streptomyces flavogriseus* (Pennacchio et al. 2018), and *Streptomyces* matensis (Yan et al. 2009).

The stability of endoxylanase at different temperatures is illustrated in Figure 8a, which reveals that the enzyme was highly stable at 40 °C and 45 °C while the moderate stability was observed at 50 °C for 12h. Furthermore, the half-life of the enzyme was calculated as approximately 450 min, 360 min, 180 min, 60 min, 30 min and 20 min for 55 °C, 60 °C, 65 °C, 70 °C, 75 °C and 80 °C, respectively. Although the reported

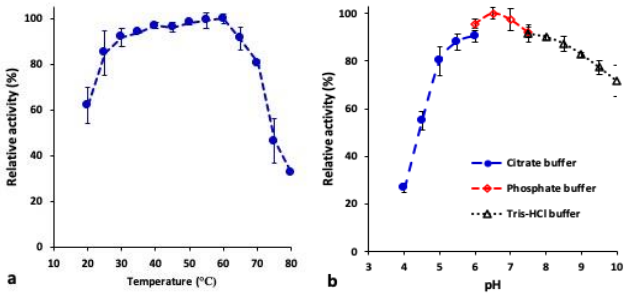

Figure 7 The effect of temperature **(a)** and pH **(b)** on the endoxylanase activity. Relative activities were expressed as a percentage of the xylanase activity and data are presented as means of three replicates with standard error (SE) bars

thermo-tolerant or thermophilic xylanase from other *Streptomyces* showed maximum activity at 60-65 °C, the endoxylanase present in this study was more stable at 30-70 °C (Nascimento et al. 2002; Yan et al. 2009; Qiu et al. 2010; Liu et al. 2013). Similar to the endoxylanase results previously reported from other *Streptomyces*, the results of this study showed that endoxylanase was more stable at pH 6.0-7.5 for 12 h at 60 °C (figure 8b). The enzyme retained active more than 50% of its activity at pH 5.0-9.0 for an hour. Therefore, the enzyme has a huge potential for various industrial applications such as the enhancement of dough, hydrolysis of lignocelluloses and deinking.

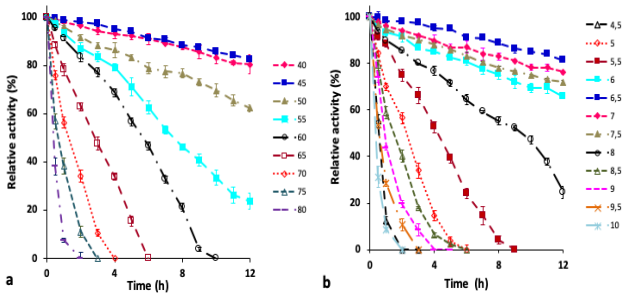

Figure 8 The stability of the enzyme in different temperatures **(a)** and pH **(b)** for 12 h

Storage stability, which is one of the most important properties of an enzyme for industrial applications, was investigated at -20 and +4 °C. The results showed that the enzyme could be stored at -20 °C for more than 180 days. On the other hand, the relative activity of the enzyme decreased to approximately 50% within the first 30 days.

Among the investigated metal ions, Mg^{+2} and Ca^{+2} caused slight enhancement in endoxylanase activity while a significant decrease was observed by the pre-incubation of the enzyme with Cu^{+2} and Hg^{+2} for 120 min. Considering the results of the structural xylanase studies previously reported, the activation of the enzyme by Ca^{+2} may be due to glutamate residues at the active site (Li et al. 2008; Kui et al. 2010) and strong inactivation by Hg^{+2} may be due to the oxidation of the indole ring of tryptophan amino acid present in the catalytic domain close the active site (Kui et al. 2010). A significant enhancement in enzyme activity was observed with the pre-incubation of the enzyme with methanol for 60 min. Furthermore, the relative activity of the enzyme slightly increased with ethanol, isopropanol, and ethyl acetate.

However, dimethyl sulfoxide (DMSO) and dimethylformamide (DMF) exhibited a slight inhibitory effect on the enzyme while sodium dodecyl sulfate (SDS) and 1,4-dithiothreitol (DTT) significantly inhibited endoxylanase activity in a time-dependent manner. A very low inhibitory effect of ethylenediaminetetraacetic acid (EDTA) on endoxylanase activity showed that the enzyme did not need metal ions for activity (Gilead and Shoham 1995). Surprisingly, complete inhibition in the enzyme activity was detected by 2-mercaptoethanol at the end of the 120 min incubation period unlike most of the other reported studies (Carvalho et al. 2017; Kumar and Shukla 2018).

The endoxylanase showed the highest specificity towards oat spelt xylan (115.70%). The hydrolytic activity of the enzyme on beechwood xylan with 98.87% relative activity was very close to birchwood xylan. However, the enzyme did not show any activity towards CMC, filter paper, soluble starch, or citrus pectin. The kinetic parameters K_m and V_{max} of the endoxylanase were studied using various concentrations of birchwood xylan (0.5-20 mg/mL). The K_m and V_{max} values estimated by the Lineweaver–Burk reciprocal plot were 1.689 mg/mL.min and 23.17 µmol/min.mg, respectively. The lower K_m value of the endoxylanase present in this study suggested that it had much more affinity on birchwood xylan than xylanases produced by other *Streptomyces* species (Pradeep et al. 2013; Zhou et al. 2011; Mander et al. 2014; Qiu et al. 2010; Ninawe et al. 2008; Li et al. 2012; Adıgüzel and Tunçer 2016;). This property of the enzyme indicates that endoxylanase from *Streptomyces* sp. SH5027 is exceptional for many industrial applications.

3.8. Application of Endoxylanase in Bread Making

The results presented in Figure 9 showed that the endoxynalase from *Streptomyces* sp. SH5027 improved the specific volume of bread. Increases in the specific volumes were 9.6%, 12.8%, and 16.8% when 200 U, 300 U, and 400 U endoxylanase was added to the flour per kg. An increase in the bread's specific volume may be due to the decrease in un-extractable xylan which can hold water 10-fold than its mass as reported earlier (Courtin and Delcour 2002).

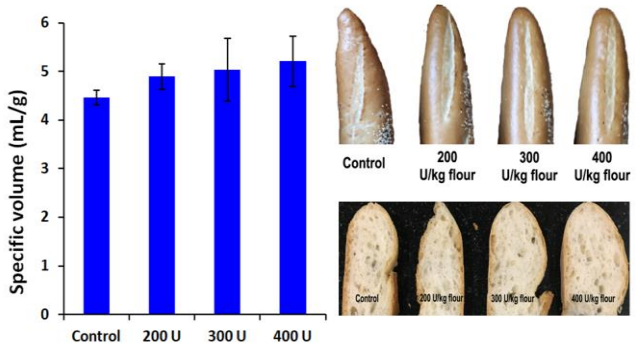

Figure 9. The specific volumes of breads prepared with and without endoxylanase

4. CONCLUSION

The present study showed that *Streptomyces* sp. SH5027, which was newly isolated from soil contaminated with banana wastes and identified based on 16S rRNA gene sequences, can produce endoxylanase by using banana pseudostem as the carbon source. The optimization studies on endoxylanase production by *Streptomyces* sp. SH5027, conducted using the OFAT and RSM approaches, were found to be an effective tool to increase the yield approximately 7-fold and decrease the production cost. This study also presents a sustainable solution for the disposal problems of banana wastes. The superior biochemical features of the enzyme, such as thermostability, wide pH stability range, organic solvent stability, and high affinity to substrate make it a promising candidate for many biotechnological applications. In conclusion, the use of endoxylanase in bread making increased the specific volume of bread.

Conflicts of interest

The authors declare no conflicts of interest.

REFERENCES

Adıgüzel A O (2020). Production and characterization of thermo-, halo-and solvent-stable esterase from *Bacillus mojavensis* TH309. Biocatalysis and Biotransformation, 38(3), 210-226.

Adigüzel A O & Tunçer M (2016). Production, characterization and application of a xylanase from *Streptomyces* sp. AOA40 in fruit juice and bakery industries. Food Biotechnol, 30(3), 189-218.

Adıgüzel A O & Tunçer M (2017a). Production, purification, characterization and usage of a detergent additive of endoglucanase from isolated halotolerant *Amycolatopsis cihanbeyliensis* mutated strain Mut43. Biocatalysis and Biotransformation, 35(3), 197-204.

Adıgüzel A O & Tunçer M (2017b). Production and characterization of partially purified thermostable endoxylanase and endoglucanase from novel Actinomadura geliboluensis and the biotechnological applications in the saccharification of lignocellulosic biomass. BioResources, 12(2), 2528-2547.

Ahamed A & Vermette P (2008). Culture-based strategies to enhance cellulase enzyme production from Trichoderma reesei RUT-C30 in bioreactor culture conditions. Biochem Eng J, 40(3), 399-407.

Alvindia D G & Natsuaki K T (2009). Biocontrol activities of *Bacillus amyloliquefaciens* DGA14 isolated from banana fruit surface against banana crown rot-causing pathogens. Crop Prot, 28(3), 236-242.

Bradford M M (1976). A rapid and sensitive method for the quantitation of microgram quantities of protein utilizing the, principle of protein-dye binding. Anal Biochem, 72, 248-254.

Carvalho E A, dos Santos Góes L M, Uetanabaro A P T, da Silva E G P, Rodrigues L B, Pirovani C P & da Costa A M (2017). Thermoresistant xylanases from Trichoderma stromaticum: Application in bread making and manufacturing xylo-oligosaccharides. Food Chem, 221, 1499-1506.

Courtin C M & Delcour J A (2002). Arabinoxylans and endoxylanases in wheat flour bread-making. J Cereal Sci, 35(3), 225-243.

Food and Agriculture Organization. (2017). Banana statistical compendium. FAO, http://www.fao.org/fileadmin/templates/est/COMM_MARKETS_MONITORING/Bananas/Documents/Banana_Statistical_Compendium_2017.pdf

Gabhane J, William S P, Gadhe A, Rath R, Vaidya A N & Wate S (2014). Pretreatment of banana agricultural waste for bio-ethanol production: Individual and interactive effects of acid and alkali pretreatments with autoclaving, microwave heating and ultrasonication. Waste Manage, 34(2), 498-503.

Gilead S & Shoham Y (1995). Purification and characterization of alpha-L-arabinofuranosidase from *Bacillus stearothermophilus* T-6. Appl Environ Microbiol, 61(1), 170-174.

Houfani A A, Větrovský T, Baldrian P & Benallaoua S (2017). Efficient screening of potential cellulases and hemicellulases produced by *Bosea* sp. FBZP-16 using the combination of enzyme assays and genome analysis. World J Microbiol Biotechnol, 33(29), 1-14.

Kui H, Luo H, Shi P, Bai Y, Yuan T, Wang Y, Yang P, Dong S & Yao B (2010). Gene cloning, expression, and characterization of a thermostable xylanase from *Nesterenkonia xinjiangensis* CCTCC AA001025. Appl Biochem Biotechnol, 162(4), 953-965.

Kumar A, Gupta R, Shrivastava B, Khasa Y P & Kuhad R C (2012). Xylanase production from an alkalophilic actinomycete isolate *Streptomyces* sp. RCK-2010, its characterization and application in saccharification of second generation biomass. J Mol Catal B: Enzym, 74(3-4), 170-177.

Kumar V & Satyanarayana T (2012). Thermo-alkali-stable xylanase of a novel polyextremophilic *Bacillus halodurans* TSEV1 and its application in biobleaching. Int Biodeterior Biodegradation 75:138-145.

Kumar V & Shukla P (2018). Extracellular xylanase production from *T. lanuginosus* VAPS24 at pilot scale and thermostability enhancement by immobilization. Process Biochem, 71, 53-60.

Li N, Meng K, Wang Y, Shi P, Luo H, Bai Y, Yang P & Yao B (2008). Cloning, expression, and characterization of a new xylanase with broad temperature adaptability from *Streptomyces* sp. S9. Appl Microbiol Biotechnol, 80(2), 231.

Li Q, Sun B, Li X, Xiong K, Xu Y, Yang R, Hou J & Teng C (2018). Improvement of the catalytic characteristics of a salt-tolerant GH10 xylanase from *Streptomyces rochei* L10904. Int J Biol Macromol, 107, 1447-1455.

Li X, Li E, Zhu Y, Teng C, Sun B, Song H & Yang R (2012). A typical endo-xylanase from *Streptomyces rameus* L2001 and its unique characteristics in xylooligosaccharide production. Carbohydr Res, 359, 30-36.

Liu Z, Zhao X & Bai F (2013). Production of xylanase by an alkaline-tolerant marine-derived *Streptomyces viridochromogenes* strain and improvement by ribosome engineering. Appl Microbiol Biotechnol, 97(10), 4361-4368.

Maheswari M U & Chandra T S (2000). Production and potential applications of a xylanase from a new strain of *Streptomyces cuspidosporus*. World J Microbiol Biotechnol, 16(3), 257-263.

Mander P, Choi Y H, Pradeep G C, Choi Y S, Hong J H, Cho S & Yoo J C (2014). Biochemical characterization of xylanase produced from *Streptomyces* sp. CS624 using an agro residue substrate. Process Biochem 49(3), 451-456.

Miller GL (1959) Use of dinitrosalisylic acid reagent for determination of reducing sugar. Anal Chem, 31, 426-428.

Nascimento R P, Coelho R R R, Marques S, Alves L, Gırio F M, Bon E P S & Amaral-Collaço M T (2002). Production and partial characterisation of xylanase from *Streptomyces* sp. strain AMT-3 isolated from Brazilian cerrado soil. Enzyme Microb Technol, 31(4), 549-555.

Ninawe S, Kapoor M & Kuhad R C (2008). Purification and characterization of extracellular xylanase from *Streptomyces cyaneus* SN32. Bioresour Technol, 99(5), 1252-1258.

Padam B S, Tin H S, Chye F Y & Abdullah M I (2014). Banana by-products: an under-utilized renewable food biomass with great potential. J Food Sci Technol, 51(12), 3527-3545.

Pennacchio A, Ventorino V, Cimini D, Pepe O, Schiraldi C, Inverso M & Faraco V (2018). Isolation of new cellulase and xylanase producing strains and application to lignocellulosic biomasses hydrolysis and succinic acid production. Bioresour Technol 259, 325-333.

Porsuk I, Özakın S, Bali B & Yilmaz E I (2013). A cellulase-free, thermoactive, and alkali xylanase production by terrestrial *Streptomyces* sp. CA24. Turkish J Biol 37(3):370-375.

Pradeep G C, Choi Y H, Choi Y S, Seong C N, Cho S S, Lee H J & Yoo J C (2013). A novel thermostable cellulase free xylanase stable in broad range of pH from *Streptomyces* sp. CS428. Process Biochem, 48(8), 1188-1196.

Qiu Z, Shi P, Luo H, Bai Y, Yuan T, Yang P, Liu S & Yao B (2010). A xylanase with broad pH and temperature adaptability from *Streptomyces megasporus* DSM 41476, and its potential application in brewing industry. Enzyme Microb Technol, 46(6), 506-512.

Sanjivkumar M, Silambarasan T, Palavesam A, Immanuel G (2017). Biosynthesis, purification and characterization of β-1, 4-xylanase from a novel mangrove associated actinobacterium *Streptomyces olivaceus* (MSU3) and its applications. Protein Expr Purif, 130, 1-12.

Shah M P, Reddy G V, Banerjee R, Babu P R & Kothari I L (2005). Microbial degradation of banana waste under solid state bioprocessing using two lignocellulolytic fungi (*Phylosticta* spp. MPS-001 and *Aspergillus* spp. MPS-002). Process Biochem, 40(1), 445-451.

Sharma S & Bajaj B K (2018). Xylanase production from a new strain of *Aspergillus terreus* S9 and its application for saccharification of rice straw using combinatorial approach. Environ Prog Sustain, 37(3), 1210-1219.

Shin J H, Choi J H, Lee O S, Kim Y M, Lee D S, Kwak Y Y, Kim W C & Rhee I K (2009). Thermostable xylanase from *Streptomyces thermocyaneoviolaceus* for optimal production of xylooligosaccharides. Biotechnol Bioprocess Eng, 14(4), 391-399.

Su Y, Zhang X, Hou Z, Zhu X, Guo X & Ling P (2011). Improvement of xylanase production by thermophilic

fungus *Thermomyces lanuginosus* SDYKY-1 using response surface methodology. N Biotechnol, 28(1), 40-46.

Thomas L, Sindhu R & Pandey A (2013). Identification and characterization of a highly alkaline and thermotolerant novel xylanase from *Streptomyces* sp. Biologia, 68(6), 1022-1027.

Vieira W B, Moreira L R S, Neto A M & Filh E X F (2007). Production and characterization of an enzyme complex from a new strain of *Clostridium thermocellum* with emphasis on its xylanase activity. Braz J Microbiol, 38, 237-242.

Walia A, Guleria S, Mehta P, Chauhan A & Parkash J (2017). Microbial xylanases and their industrial application in pulp and paper biobleaching: a review. 3 Biotech, 7(1), 11.

Wang Y, Zhang H, He Y, Luo H & Yao B (2007). Characterization, gene cloning, and expression of a novel xylanase XYNB from *Streptomyces olivaceoviridis* A1. Aquaculture 1(267), 328-334.

Yabalak E, Adigüzel S K, Adıgüzel A O, Ergene R S, Tuncer, M & Gizir A M (2017). Application of response surface methodology for the optimization of oxacillin degradation by subcritical water oxidation using H_2O_2: genotoxicity and antimicrobial activity analysis of treated samples. Desalination and Water Treatment, *81*, 186-198.

Yan Q, Hao S, Jiang Z, Zhai Q & Chen W (2009). Properties of a xylanase from *Streptomyces matensis* being suitable for xylooligosaccharides production. J Mol Catal B: Enzym, 58(1-4), 72-77.

Zhou J, Shi P, Zhang R, Huang H, Meng K, Yang P & Yao B (2011). Symbiotic *Streptomyces* sp. TN119 GH 11 xylanase: a new pH-stable, protease-and SDS-resistant xylanase. J. Ind. Microbiol Biotechnol, 38(4), 523-530.

Turkish Journal of Engineering

https://dergipark.org.tr/en/pub/tuje

e-ISSN 2587-1366

Cantilever piles or well foundations in supporting temporary deep excavations: comparison of performance, safety and cost

Cihan Öser*[1], Sinan Sarğın [2]

[1]*Istanbul University, Cerrahpaşa Faculty of Engineering, Department of Civil Engineering, Istanbul, Turkey*

Keywords
Deep excavation
Cantilever piles
Well foundation
Finite element method
Cost-Safety-Performance

ABSTRACT

Due to the increasing population in the metropolitans, the construction of the high-rise buildings and shopping malls etc. has rapidly increased for last three decades. Therefore, especially in the city centers, the area of the construction sites has become very limited. Moreover, the requirements such as high bearing capacity of the soils beneath the skyscrapers and the parking area for the vehicles makes the application of the deep excavations essential. It is well-known that designing both safe and economical retaining structures in cohessionless soils such as sands and gravels or silty-clayey mixtures of them is still a challenging issue in geotechnical engineering discipline. Under that circumstances, the construction of two types of the retaining structures frequently comes into the minds: cantilever piles and well foundations. These retaining systems should be designed not only to be resist against failure but also to meet safety requirements for existing buildings and infrastructures near the site until the active forces, which are induced by the soil mass, are supported by the structural elements of the superstructures. In addition to this, the horizontal deformations along the retaining structures should be less than the limits defined by the specifications and the structural codes. In this study, the performances and costs of the both cantilever piles and well foundations in different excavation heights are compared parametrically. For this purpose, a benchmark sandy soil profile given in the literature and the retaining systems are modeled in 2D by using finite elements method. Furthermore, in order to determine the internal forces based reinforced concrete design and the unit costs; a well-known commercial software is used. The promising results of this study could guide to the design engineers in practice for selecting safer and more economical systems within engineering judgment.

1. INTRODUCTION

Population growth in urban areas cause requirement of new housing, working places, parking lots, etc. construction. The mentioned new construction works cause many problems. Especially during the construction of new buildings in a limited number of empty spaces in big cities, collapses can be occurred due to deep excavations. Due to these collapses, major damages may occur in the surrounding buildings and infrastructure facilities as well as loss of life and property (Bian and Huang 2006; Boone 1996; Laefer et al. 2009; Leisenring 2012; Liu and Wang 2009; Wang and Xu 2010).

Deep excavations are made to go down to the required foundation level in case of encountering thick fill layers near to surface or soils with low bearing capacity. Deep excavations are also made to construct underground parking lots and basement floors for buildings. For this reason, retaining structures are constructed in order to preserve the stability of excavation surfaces and to prevent the lateral ground displacements

The most important factors in the design of retaining structures, which are designed to be temporary or permanent according to the serviceability time, are defining the soil profile as representing the whole construction site, determining the soil parameters in accordance with the design criteria and determining the ground water level correctly. In temporary retaining structures which are designed to hold the excavation until the basement curtain walls of the superstructure

* **Corresponding Author**

*(oser@istanbul.edu.tr) ORCID ID 0000-0002-5057-0920
(ssargin@istanbul.edu.tr) ORCID ID 0000-0001-9275-6531

Cite this article

Oser C & Sargın S (2022). Cantilever piles or well foundations in supporting temporary deep excavations: comparison of performance, safety and cost. Turkish Journal of Engineering, 6(2), 140-148

Research Article / DOI: 10.31127/tuje.861268

Received: 14/01/2021; Accepted: 26/02/2021

are constructed, it is aimed to finish the construction of superstructure in a short period of time. In this case, effect of dynamic loads (i.e. earthquake) are not taken into account in the design of retaining structures. However, in projects where the excavation surfaces will remain open for a long time, additional dynamic effects will be carried by the retaining structures in case of possible earthquakes. In such projects, retaining structures are designed permanently and earthquake forces are also taken into account.

Retaining structures may be exposed to excessive displacements due to reasons such as incorrect determination of soil parameters, not modelling of the soil environment properly, not designing the structures with sufficient strength. As a result, general or partial collapse may occur in the retaining structures. For this reason, retaining structures should be designed to be safe against collapse, as well as to make displacements within the permissible limits specified in the regulations not to cause damage at the surrounding structures, roads and infrastructure systems.

Locally in Turkey, cantilever bored piles, ground anchors and well foundations are frequently preferred as retaining systems to support deep excavations in recent years. Within the scope of this study, the advantages and disadvantages of cantilever bored piles and well foundations were revealed, and retaining structures were designed to ensure safety and performance against collapse in a certain sandy soil profile for various excavation depths. In addition, costs have been calculated for the design sections of retaining structures. In this way, comparisons were made in terms of safety-performance-cost for the two different retaining systems, and it is aimed to guide engineers in their design to choose a safe and economical retaining system.

In this study, three different excavation heights (H=8, 9 and 10 m.) and three different bored pile diameters (D=0.65, 0.80 and 1.00 m.) were selected. Plaxis 2D finite element analysis software was used for the displacement calculations of the piles and well foundations. IstCAD software, which is frequently used for the design of retaining structures in our country, was preferred by the authors for the reinforced calculations and cost calculations of the bored piles and well foundations.

Within the scope of this parametric study, Costs for constructing bored piles and well foundations were considered depending on the unit costs list announced by Republic of Turkey, Ministry of Environment and Urbanization.

2. METHOD

Cantilever bored piles and well foundations were selected by the authors as temporary retaining structures to compare the systems in terms of safety-performance and cost. In the analysis, 8, 9 and 10 meters of excavation heights were selected. The reason for limiting the excavation height to 10 meters is that, construction of cantilever piles for higher excavations would not be applicable for engineering criteria. Also three different diameters for bored piles are used (D=0.65, 0.80 and 1.00 m.). Smaller diameters (D<0.65 m.) for piles are described as mini-piles and they are not suitable for deep excavations. Moreover, bigger and stronger drilling machines are required for greater diameters (D>1.00 m.) and this is not economical and suitable in city centers.

2.1. Determination of the dimensions

Required embedded lengths of bored piles are calculated by using Eq. 1 depending on excavation height and shear strength angle (ϕ) as given in Gajan (2011).

$$\frac{d}{H} = \left(FS\right)^{0.25} \cdot \left[\left(\frac{K_p{}^2}{FS}\right)^{0.17} - 1\right]^{-1} \quad (1)$$

In Eq. 1, dimensional properties of piles are not taken into consideration and only excavation height (H), factor of safety (FS) and passive earth pressure coefficient (K_p) are used. Passive earth pressure coefficient (K_p) for the selected soil profile is calculated by using Eq. 2 (Bowles, 1997).

$$K_p = \frac{\sin^2\left(\alpha - \phi\right)}{\sin^2\alpha \cdot \sin\left(\alpha + \delta\right)\left[1 - \sqrt{\frac{\sin\left(\phi + \delta\right)\cdot\sin\left(\phi + \beta\right)}{\sin\left(\alpha + \delta\right)\cdot\sin\left(\alpha + \beta\right)}}\right]^2} \quad (2)$$

In Eq. 2:

α: the angle between the wall back surface and the base of the wall (α=90° in this problem)
δ: friction angle between the soil and the wall (δ=3/4 ϕ)
β: the angle of inclination of the ground surface behind the wall relative to the horizontal plane (β=0°)

The passive earth pressure coefficient was calculated as K_p=8.952 for the soil profile selected within the scope of the study and whose features are given in Section 2.3.

The dimensional properties of cantilever bored piles and well foundations were determined according to the passive earth pressure coefficient (K_p) value, excavation heights ($H_{excavation}$) and factor of safety (FS) values as described in the following sections.

2.1.1. Bored piles

The diameters of the bored piles were selected as ϕ65cm, ϕ80cm and ϕ100cm in the study. Embedded lengths of piles were calculated as given in Table 1 by using Eq. 1 for various factor of safety values (with an increase of 0.1 between FS=1 and FS=2).

In the design of the retaining system with cantilever bored piles, it has been accepted that the piles will be constructed adjacent and there is no gap between the piles in order to prevent the soil flowing through piles for sandy soil profile. Another reason for the contiguous design of the piles is that the piles will displaced like a wall similar to the well foundations and with this similarity a suitable comparison can be done.

Table 1. Embedded length of piles

Factor of Safety (FS)	Socket length of piles (L_{socket}) (m)		
	$H_{excavation}$ 8 m	$H_{excavation}$ 9 m	$H_{excavation}$ 10 m
1.0	7.2	8.1	9.0
1.1	7.6	8.6	9.5
1.2	8.0	9.0	10.0
1.3	8.4	9.5	10.5
1.4	8.8	9.9	11.1
1.5	9.2	10.3	11.4
1.6	9.5	10.7	11.9
1.7	9.9	11.1	12.3
1.8	10.2	11.5	12.8
1.9	10.6	11.9	13.2
2.0	10.9	12.3	13.6

2.1.2. Well foundations

Well foundations are constructed in slabs and within the scope of this study, only a single slab with 3 meters length and 2 meters width was taken into consideration. Foundation width for the well foundations was used as 2 meters that is the width of the slab. In cantilever retaining structures, the critical issue is to satisfy the safety requirements for overturning. For this purpose, foundation depths for well foundations ($H_{founadtion}$) were optimized by following the instructions predefined in iSTCAD (2020) software and dimensional properties of well foundations are given in Table 2, depending on the excavation heights and the factor of safety against overturning ($FS_{overturning}$).

Table 2. Dimensional properties of well foundations

Factor of Safety against overturning ($FS_{overturning}$)	Foundation Width (m)	$H_{excavation}$=8 m		$H_{excavation}$=9 m		$H_{excavation}$=10 m	
		Wall Thickness D_{wall} (m)	Foundation Depth $H_{foundation}$ (m)	Wall Thickness D_{wall} (m)	Foundation Depth $H_{foundation}$ (m)	Wall Thickness D_{wall} (m)	Foundation Depth $H_{foundation}$ (m)
1.0	2.0	0.5	3.50	0.6	4.50	0.6	5.45
1.2	2.0	0.5	4.40	0.6	5.40	0.6	6.45
1.4	2.0	0.5	5.20	0.6	6.30	0.65	7.35
1.5	2.0	0.5	5.60	0.6	6.70	0.65	7.80
1.6	2.0	0.5	6.00	0.6	7.10	0.7	8.25
1.8	2.0	0.5	6.60	0.8	7.85	0.7	9.15
2.0	2.0	0.5	7.30	0.8	8.70	0.8	10.00

2.2. Implemented software

Two different software were used within the scope of this study for the numerical design and reinforced concrete calculations of bored piles and well foundations. Plaxis 2D (Brinkgreve et al., 2019) software was used for the FEM analysis (finite element method) and displacement calculations of retaining structures. Also iSTCAD (2020) retaining wall software (Göksa, 2020) was used for the reinforced concrete calculations of retaining systems (Figure 1).

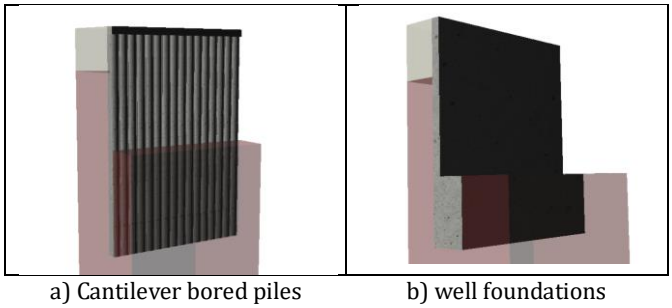

a) Cantilever bored piles b) well foundations

Figure 1. Screenshots of istCAD software

2.3. Numerical Modeling with Finite Element Methods

2.3.1. Model mesh and boundary condition

One of the main aims of this study is comparing the performance and cost-efficiency of bored pile and well foundations under the same soil conditions. For this purpose, a benchmark soil stratum is selected. A medium-dense sandy soil has a thickness of 27 m. is underlying 3-m-thick silty soil from ground surface. In addition to this, the groundwater level is not defined in the model due to considering the difficulties of excavation of the well foundation under groundwater level in real practice. The soil profile with finite element meshing is shown in Figure 2. There are no interface elements among the periphery, the pile or well foundation and the surrounding soils because the shear strength at the interface between the structural elements and the surrounding soil is higher that of the surrounding sand and silt formation. To ensure that the boundary effect will be minimized, the finite element mesh is extend to a depth of 30 m. and a horizontal length of 100 m. The displacement and rotations in the two directions are restricted at the bottom of the finite element mesh. Furthermore, the displacements in the x direction of the horizontal boundaries of the model are set zero. The stages of the construction of the both pile and well foundations are followed in the finite-element calculation as tabulated in Table 3.

2.3.2. Constitutive models and determined parameters

The silt and medium dense sand soil layers are modeled as linearly elastic to perfectly plastic materials with the Mohr-Coulomb model (MC). The constitutive models controlling the stress-strain behavior of the soil

and regarding stiffness and strength parameters are summarized in Table 4.

The bored piles and the well foundation are modeled as linear elastic (LE) model with structural elements which allows to users determine internal forces and displacements of a pile or wall. The properties of structural elements are given in Table 5.

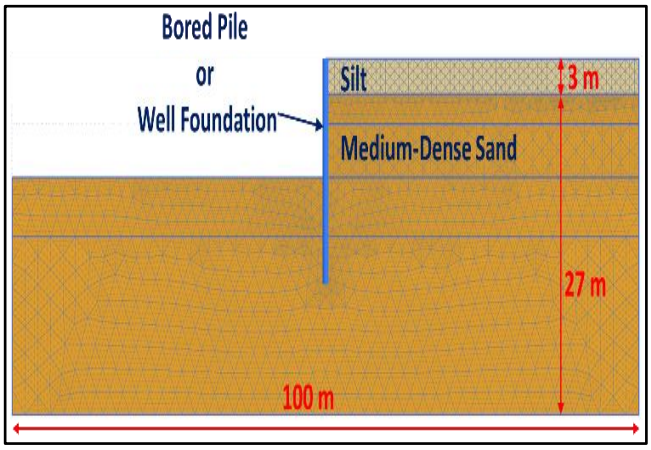

Figure 2. Finite element model of the problem

Table 3. Construction stages in the FEM calculation

Stages	Explanation
0	Generation of the initial stresses (Gravity loading)
1	Installation of the pile or well foundation
2	Excavation of a 3.0-m-high soil
3	Excavation of a 3.0-m-high soil
4	Excavation of the soil until required depth

Table 4. Parameters used in MC model

Parameters	Silt	Medium Dense Sand
Unit weight, γ (kN/m^3)	16	18
Elastic modulus, E' (MPa)	90	135
Poisson's ratio, ν'	0.3	0.3
Cohesion, c (kPa)	5	-
Friction angle, ϕ (°)	30	34
Dilatancy angle, ψ (°)	-	3
Permeability Coeff., k (m/day)	0.59	0.98
Material behavior	Drained	Drained

Table 5. Parameters used in LE model

Parameters	Cross-sections width of the walls in well foundation, H (cm)						Diameters of the bored piles, D (cm)		
	50	60	65	70	80	Base (H=200 cm)	65	80	100
Unit weight, γ (kN/m^3)	24	24	24	24	24	24	24	24	24
Axial stiffness, EA (kN/m)	14x10^6	16.8x10^6	18.2x10^6	19.6x10^6	22.4x10^6	56x10^6	14.3x10^6	17x10^6	21.9x10^6
Bending stiffness, EI (kNm^2/m)	292x10^3	504x10^3	605x10^3	800.3x10^3	1195x10^3	1867x10^3	377x10^3	703x10^3	1375x10^3
Poisson's ratio, ν'	0.2	0.2	0.2	0.2	0.2	0.2	0.2	0.2	0.2

2.4. Determination of the modulus of subgrade reaction for deeper soil

In general, finite elements and finite differences, numerical methods have solutions considering the stiffness of both soil and structural members. On the other hand, early methods are based on the numerical solution of the forth order differential equation. The foundation of any buildings is considered as a linear elastic structural element whose soil reaction is replaced by an infinite number of independent linear elastic springs following the Winkler (1867) hypothesis. The mechanical constant of these springs represents the modulus of subgrade reaction for soils can be defined, as the pressure required producing a unit settlement (Figure 3a).

The numerical model developed in IstCAD software to determine the design requirements of the reinforced concrete bored piles needs subgrade modulus of the soil in order to take into account effect of the soil that the piles are socketed. The subgrade modulus could be defined in the software by a constant value and found in the literature for a granular soils. Although, there are lots of references (Biot, 1937; Terzaghi, 1955; Vesic, 1961; Meyerhoff and Baike, 1963; Selvadurai, and Gladwell 1980; Bowles, 1997) which are useful for determining the subgrade modulus, these values given in Table 6 belong to the specific soils and the range of them are doubtfully wide.

Table 6. Modulus of subgrade reaction for specific soil types (Bowles, 1997)

Soil Type		Modulus of Subgrade Reaction, k_s (kN/m^3)
Loose sand		4.8x10^3 – 16x10^3
Medium dense sand		9.6x10^3 – 80x10^3
Dense sand		64x10^3 – 128x10^3
Clayey medium dense sand		32x10^3 – 80x10^3
Silty medium dense sand		24x10^3 – 48x10^3
Clayey soil		
	qa ≤ 200 kPa	12x10^3 – 24x10^3
200 <	qa ≤ 800 kPa	24x10^3 – 48x10^3
	qa > 800 kPa	> 48x10^3

For this purpose, the single pile and surrounding soil stratum is modeled numerically in PLAXIS 2D V20 software (Brinkgreve et al., 2019). The details of the soil properties and constitutive models are given in previous section.

In PLAXIS 2D, the load (stress)-displacement history of any FEM points could be saved for both construction and loading stages of any geotechnical structures.

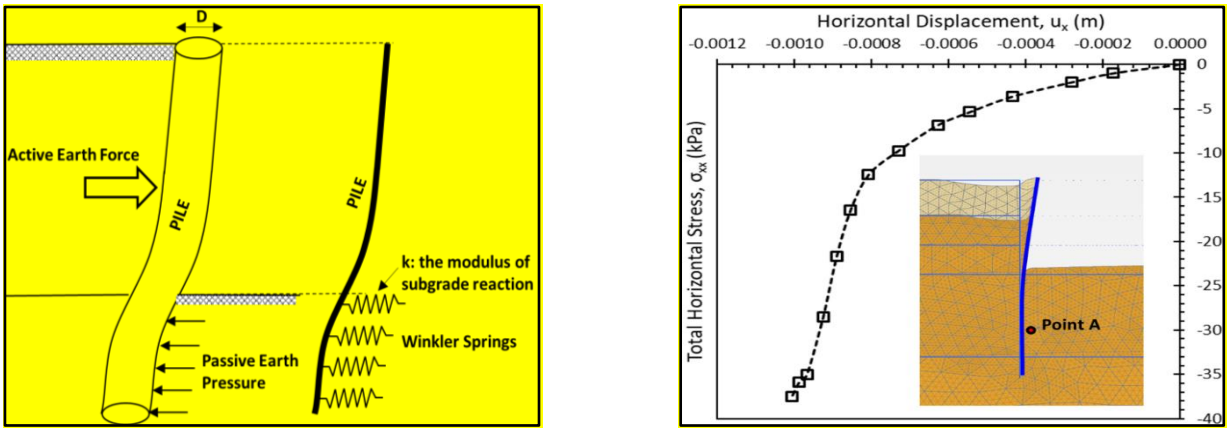

a) Schematic explanation of modulus of subgrade reaction b) Determining the modulus of subgrade reaction

Figure 3. Schematic explanation of modulus of subgrade reaction and determining the modulus of subgrade reaction for the selected soil profile

In this study, a stress point (Point A) is selected and its stress-displacement history is plotted as given in Figure 3b. The modulus of subgrade reaction could be estimated from stress-displacement curve as k_x= 15500 kN/m^3 for deeper soils that the bored pile is socketed. The modulus of subgrade reaction has been determined only for cantilever bored piles, because this parameter is only used as an input data for pile design in iSTCAD (2020).

3. COST CALCULATIONS

"2019 Construction and Installation Unit Prices" announced by the Republic of Turkey, Ministry of Environment and Urbanization was used for the cost calculations of bored piles and well foundations (T.C Çevre ve Şehircilik Bakanlığı, 2019).

In the design, C25/30 concrete class was preferred both for piles and well foundations. Unit prices of reinforced concrete bored piles are given in Table 7. Unit prices of excavation, formwork and concrete pouring were used in the cost calculations of well foundations. The price list of these installations are given in Table 8. It must be noted that, prices of the steel reinforcements are not included in these tables and they are given in Table 9 separately.

Table 7. Unit prices list of bored piles (T.C Çevre ve Şehircilik Bakanlığı, 2019)

Pose No	Previous Pose No	Type of Construction/Installation	Unit	Unit Cost (TL)
15.140.1103	Y.16.061/04	Constructing cast-in-place reinforced concrete bored piles with a diameter of ϕ65cm, with C25/30 compression strength (length between 0.0-18.0m, 18.0 m included)	m	242.63
15.140.1104	Y.16.061/05	Constructing cast-in-place reinforced concrete bored piles with a diameter of ϕ65cm, with C25/30 compression strength (length between 18.01-36.0 m, 36 m included)	m	262.78
15.140.1105	Y.16.061/06	Constructing cast-in-place reinforced concrete bored piles with a diameter of ϕ80cm, with C25/30 compression strength (length between 0.0-18.0m, 18.0 m included)	m	316.61
15.140.1106	Y.16.061/07	Constructing cast-in-place reinforced concrete bored piles with a diameter of ϕ80cm, with C25/30 compression strength (length between 18.01-36.0 m, 36 m included)	m	350.20
15.140.1107	Y.16.061/08	Constructing cast-in-place reinforced concrete bored piles with a diameter of ϕ100cm, with C25/30 compression strength (length between 0.0-18.0m, 18.0 m included)	m	474.54
15.140.1108	Y.16.061/09	Constructing cast-in-place reinforced concrete bored piles with a diameter of ϕ100cm, with C25/30 compression strength (length between 18.01-36.0 m, 36 m included)	m	534.55

Table 8. Unit prices list of well foundations (T.C Çevre ve Şehircilik Bakanlığı, 2019)

Pose No	Previous Pose No	Type of Construction/Installation	Unit	Unit Cost (TL)
15.150.1005	Y.16.050/15	Pouring mixed concrete with C25/30 compression strength, in gray color, produced or purchased in the concrete plant and poured with concrete pump (transportation is included)	m^3	220.11
15.180.1002	Y.21.001/02	Manufacturing reinforced concrete form from wood	m^2	54.95
15.115.1202	14.012/2	Narrow deep excavation by hand in soft and hard soil at any depth (loose and organic soils, loose silt, sand, clay, silty, sand and soft clay, clayey sand and gravel, and similar soils that can be shoveled)	m^3	59.31

Table 9. Unit prices list of steel reinforcement bars (T.C Çevre ve Şehircilik Bakanlığı, 2019)

Pose No	Previous Pose No	Type of Construction/Installation	Unit	Unit Cost (TL)
15.160.1003	Y.23.014	ϕ8-ϕ12 mm ribbed concrete steel bar (cutting, bending and placing are included)	ton	4029.78
15.160.1004	Y.23.015	ϕ14-ϕ28 mm ribbed concrete steel bar (cutting, bending and placing are included)	ton	3965.28
15.160.1005	Y.23.015	Ribbed concrete steel bar thicker than ϕ28 mm (cutting, bending and placing are included)	ton	3916.65

4. RESULTS

The results of the safety-performance and cost comparison, in which the embedded lengths of bored piles with diameter of D=65 cm., 80 cm. and 100 cm. are taken into account for the excavation heights of H=8 m., 9 m. and 10 m., are presented in Figure 4 (a)-(c) respectively.

The maximum displacement values at the end of excavation were calculated between 1.25 cm. and 3.0 cm. for the excavation with a height of 8 m. These results appear to be within the permissible displacement limits given in the related deep excavation codes and regulations (Sabatini et al., 1999; BS-EN 1997-1, 2004). Although the number of safety increases, the decrement in the wall displacements are limited as seen in Figure 4 (a). On the other hand, when the safety-cost curve examined, it can be seen that the costs increase rapidly if a safer design is made. In addition, considering the minimum amount of reinforcement to be used depending on the constructive rules, it is seen that the costs increase when using bored piles with larger diameters in excavations with relatively low heights. According to Figure 4 (b)-(c), in case the excavation height increases and the diameter of the bored pile decreases, it has been calculated that the predicted horizontal displacements increase considerably. In the same manner, it was concluded that, the costs increased considerably and became uneconomical in order to make safe excavation using bored piles with small diameters. This is because, in piles with small diameters, the cost of reinforcement to be used to compensate the bending moments and shear forces increases approximately 1.5 times.

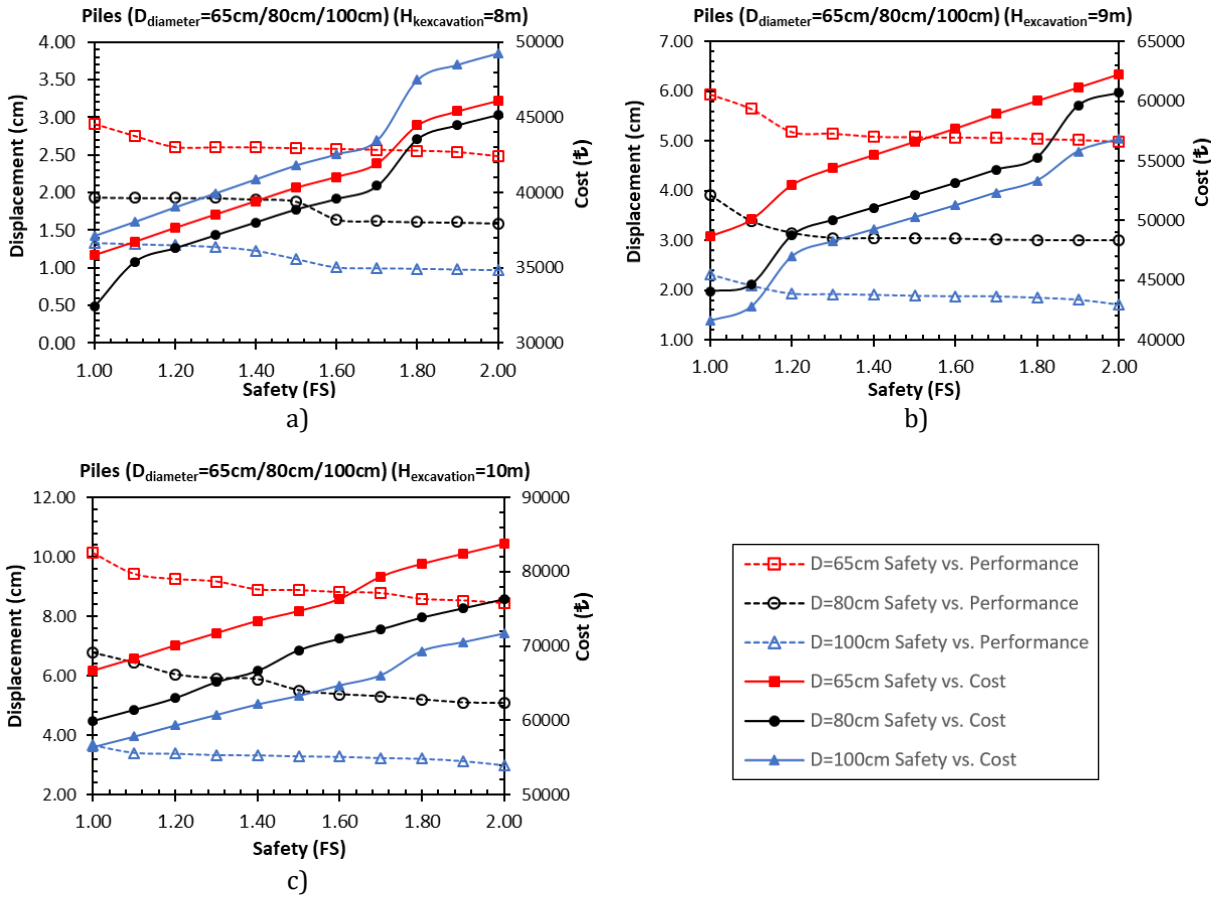

Figure 4. Comparison of the safety-performance-cost efficiency of the cantilever-bored piles for various excavation heights; a) 8 m, b) 9 m, c) 10 m

The performance of the well foundations are more sensitive than cantilever bored piles according to the required safety. In Figure 5 (a), the horizontal displacement estimated by FEM analysis rapidly decrease when the factor of safety is slightly increased from 1.0 to 1.2. If the safety requirements is increased up to FS=2.0, the determined displacement, which is initially (FS=1.0) about 5.2 cm can be less than 1.0 cm.

On the other hand, the majority of the decrease in horizontal deformation is seen in the range of factor of safety between 1.0 and 1.4. Although the decrease of the horizontal displacement is limited, the costs increase rapidly after that level of the safety. Thus, the wall with the selected thickness seems to be overdesigned if the factor of safety is greater than 1.4.

The similar trend of both in the horizontal displacements and the costs can be observed for the excavation depth of 9 m. and 10 m. of well foundations in Figure 5 (b) and (c), respectively.

In the analysis of the well foundations, while the height of the excavation remains at the same level (i.e. $H_{excavation}$=8 m., 9 m. or 10 m.), the foundation depth is increased in order to raise the factor of safety against overturning ($FS_{overturning}$). In the presented study, 2 meters wide rigid foundations are used in well foundations. For this reason, deeper foundations are excavated to raise the factor of safety against overturning. Correspondingly, the active earth pressures acting on the wall increase and the displacement values in the cantilever section of the wall increase sensitively. Moreover, structural elements used in Plaxis 2D models have different rigidity properties as seen in Table 2.

Comparison of the unit costs and horizontal displacements, which are in terms of the performance of both cantilever bored piles and well foundations in excavation depth of 8 m., is presented in Figure 6 (a). Under limit equilibrium condition (FS=1.0) the displacements of cantilever bored piles and well foundations differs significantly. For instance, while the horizontal displacement of the bored pile (D=100 cm.) is 1.3 cm, the displacement of the well foundation is about four times greater than the displacement estimated in related bored pile. Furthermore, the displacements calculated from numerical analysis modeled for bored piles with diameters of 80 cm. and 65 cm. are 40% and 60% of the displacement belongs to well foundations in the same depth under limit equilibrium condition. However, as the factor of safety rise, the horizontal displacements obtained for the well foundation decrease sharply, the displacements determined for the bored piles remain constant vice versa.

In Figure 6 (b)-(c), the cantilever–bored pile with a diameter of 65 cm. can be evaluated as the most unsafe design in terms of the displacement for 9 m. and 10 m. excavation depth. As the height of excavation increases, the piles with smaller cross sectional area becomes insufficient.

On the other hand, although the displacements calculated for well foundations are approximately same as the predicted displacement of the piles has a diameter of 80 cm., the displacements of the piles has a diameter of 100 cm were determined smaller.

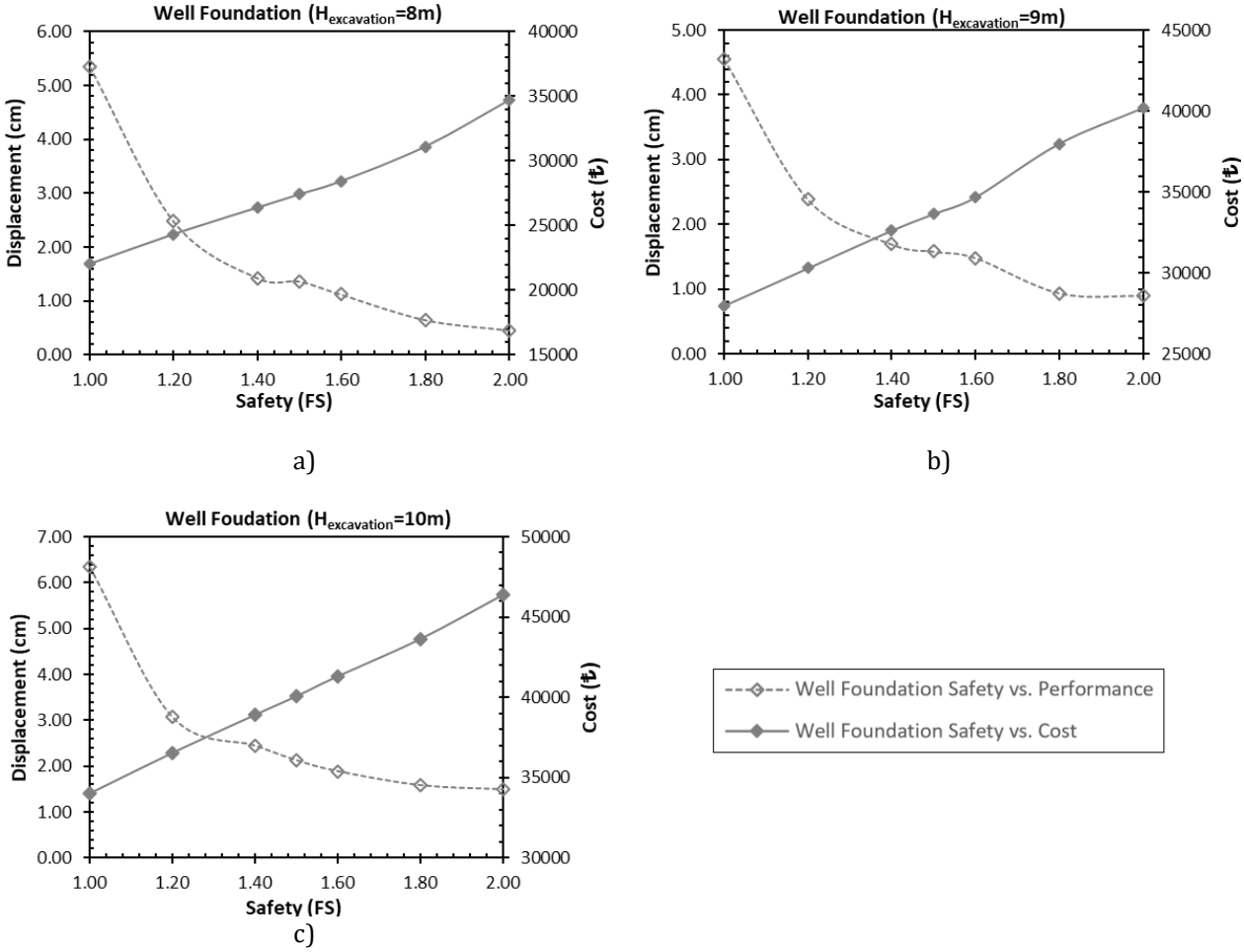

Figure 5. Comparison of the performance/cost efficiency of the well foundations

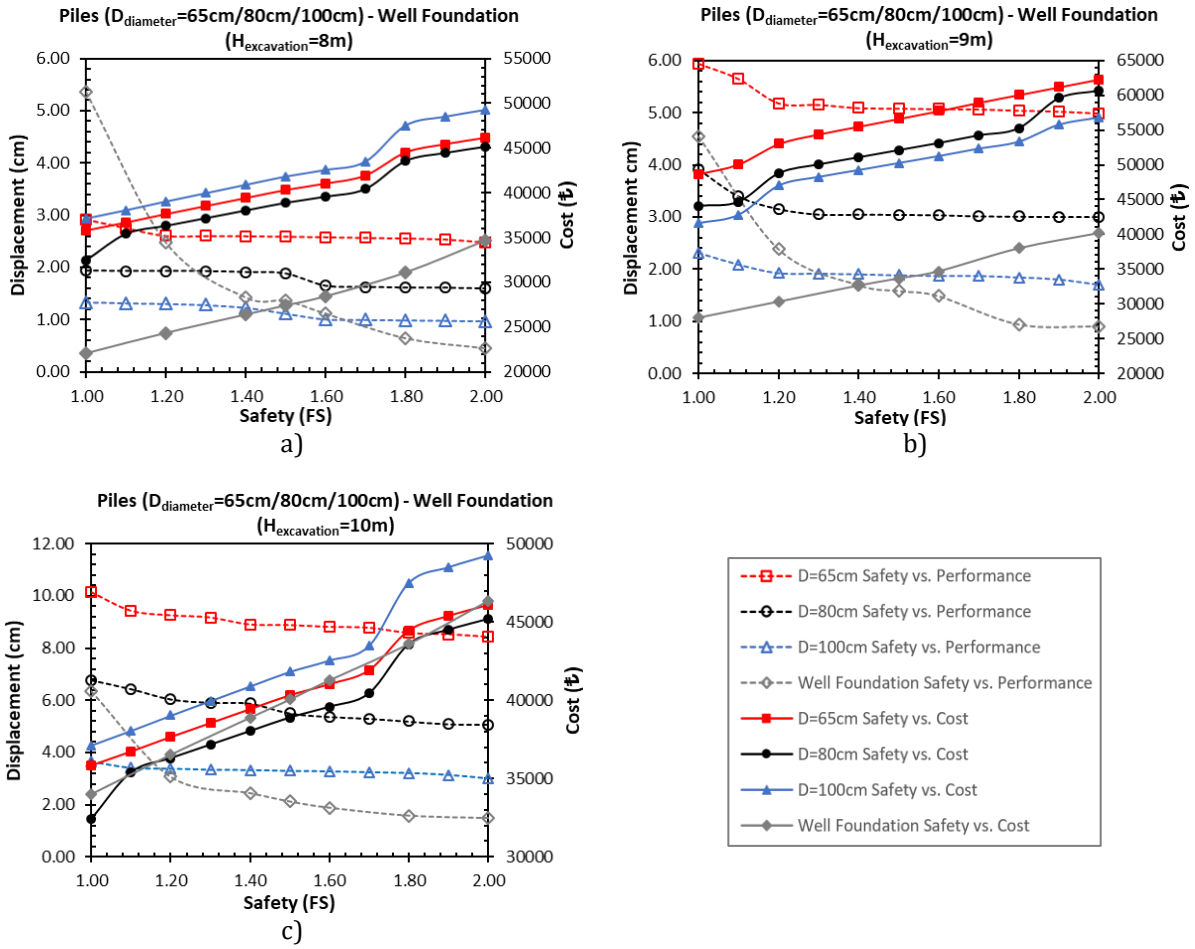

Figure 6. Comparison of the performance/cost efficiency of the well foundation

The costs of the retaining structures analyzed in this study are also compared in Figure 7. It can be easily observed that the costs of well foundations with selected cross sections remain less than the cost of the application of the cantilever-bored piles for 8 and 9 meters excavation height. However, in the 10-meter high excavations; well foundation depth should be increased as shown in Table 2 for safe design. It can be said that this situation increases the well foundation costs significantly and brings them to the same level with the piles (D=65 cm. and D= 80 cm.).

5. RECOMMENDATIONS FOR FURTHER STUDIES

This study is a preliminary study aiming to compare well foundations and cantilever bored piles, which are retaining structures, in terms of performance and cost. It is clear that factors such as the presence of the groundwater, variability of the spacing between bored piles, installation of the anchors or soil nails etc. effect the performance, safety and cost of the design. Further studies in which these factors are also taken into consideration are ongoing.

6. CONCLUSION

Within the scope of this study, two different retaining structures, cantilever bored piles and well foundations, are compared in terms of "performance-safety" and "cost-safety" in deep excavations with different heights. For this purpose, a series of numerical analyses based on finite element (FEM) and limit equilibrium (LE) methods conducted.

In order to compare the efficiency of the cantilever bored piles with different diameters (D = 65, 80 and 100 cm.) for various excavation heights (H = 8, 9 and 10 m.) the horizontal displacements and the costs are calculated. According to the results, the retaining system constructed with piles has smaller diameter deflects more than the systems including piles with larger diameters. In point of view from cost analysis, in the cantilever piles constructed in the sandy soil profile where the excavation height is 8 meters, it has been observed that the optimum solution is piles has 80 cm. in diameter. As the excavation height rises, the internal forces (especially the bending moment) and accordingly the pile diameters increase, so it can be concluded that the more economical solution is piles has 100 cm. in diameter.

In retaining systems where well foundations are used, the factor of safety for overall stability is determined and the height of the foundations should be increased for safer designs. Accordingly, when the factor of safety increases, the calculated displacements decrease rapidly, in contrast the costs are getting more expensive

Finally, "performance-safety" and "cost-safety" of the two different retaining structure systems are compared. It can be concluded that, by the increment of the factor of safety numbers, performance of the well foundations improves, thus the horizontal displacements rapidly reduce. On the other hand, the reduction of the

displacements at the bored piles are negligible. Even though, the costs of the well foundation reach almost the same level with cantilever bored piles at 10 meters excavation height in sandy soil profile, it can be said that well foundations are generally more economical than cantilever bored piles.

Author contributions

Cihan Öser: conceived of the presented idea, developed the theory, write and edit the manuscript; **Sinan Sarğın**: performed the computations and verified both the analytical and numerical methods.

Conflicts of interest

The authors declare no conflicts of interest.

7. REFERENCES

Bian Y H & Huang H W (2006). Fuzzy fault tree analysis of failure probability of SMW retaining structures in deep excavations. GeoShanghai International Conference 2006, 312-319. doi: 10.1061/40867(199)38

Biot M (1937). Bending of an infinite beam on an elastic foundation. Journal of Applied Mechanics, 203, 1-7.

Boone S J (1996). Ground-Movement-Related Building Damage. Journal of Geotechnical Engineering, 122, (11), 886-896, doi: 10.1061/(asce)0733-9410(1996)122:11(886)

Bowles J E (1997). Foundation Analysis and Design. The McGraw-Hill Companies, Inc., ISBN: 0-07-912247-7

Brinkgreve R B J, Kumarswamy S, Swolfs W M, Zampich L & Manoj N R (2019). PLAXIS 2D Tutorial Manual CONNECT Edition V20. Plaxis.

BS EN 1997-1:2004 British Standard. (2004). Eurocode 7: Geotechnical design - Part 1: General rules. In Journal of Constructional Steel Research.

Gajan S (2011). Normalized relationships for depth of embedment of sheet pile walls and soldier pile walls in cohesionless soils. Soils and Foundations, 51(3), 559-564. doi:10.3208/sandf.51.559

Göksa Mühendislik Yazılım Ltd. Şti. (2020, Aralık 22). istCAD Yeni Deprem Yönetmeliğine Tam Uyumlu Duvar Analiz, Tasarım ve Çizim Programı . www.göksa.com.tr.

Laefer D F, Ceribasi S, Long J H & Cording E J (2009). Predicting RC Frame Response to Excavation-Induced Settlement. Journal of Geotechnical and Geoenvironmental Engineering, 135(11), 1605-1619. doi:10.1061/(asce)gt.1943-5606.0000128

Leisenring B R (2012). Damage to adjacent building during construction-Expert investigation. Lanchester: Robson Forensic.

Meyerhoff G G & Baike L D (1963). Strength of steel culverts sheets bearing against compacted sand backfill. Highway Research Board Proceedings, pp. 1-19

Sabatini P J, Pass D G & Bachus R (1999). Ground Anchors and Anchored Systems. Geotechnical Engineering Circular No.4, Federal Highway Administration, Publication No. FWA-IF-99-015

Selvadurai, A. P. S., & Gladwell, G. M. L. (1980). Elastic Analysis of Soil-Foundation Interaction. Journal of Applied Mechanics, 47(1), 219 doi:10.1115/1.3153622

T.C. Çevre ve Şehircilik Bakanlığı (2019). 2019 yılı İnşaat ve Tesisat Birim Fiyatları. Ankara, Turkiye: Yüksek Fen Kurulu Başkanlığı.

Terzaghi K (1955). Evaluation of coefficients of subgrade reaction. Geotechnique, 5(4), 297-326, doi:10.1680/geot.1955.5.4.297

Wang X & Liu Y (2009). Overview of the assessment on the damage from underground excavating on adjacent buildings. Chinese J. Underground Space Eng., 4, 841-847

Wang W D & Xu Z H (2010). Simplified analysis method for evaluating excavation-induced damage of adjacent buildings. Journal of Geotechnical Engineering, 32(1), 32-38.

Winkler E (1867). Die Lehre von Elastizat and Festigkeit (on Elasticity and fixity), 182, Prague

Turkish Journal of Engineering

https://dergipark.org.tr/en/pub/tuje

e-ISSN 2587-1366

Repairing of damaged composite materials and self-healing composites

Yusuf KEPIR*[1], Alper GUNOZ [1], Memduh KARA [1]

[1]*Mersin University, Department of Mechanical Engineering, Mersin, Turkey*

Keywords
Self-healing composites
Microcapsule
Repair of composites
Patch
Intelligent materials

ABSTRACT

Repairing any damage in composite materials is very important in terms of the mechanical strength of the structure in which they are used. Therefore, the damage needs to be detected and repaired quickly. The increasing use of composite materials in various industries makes it more important to repair damage in composites both quickly and cost effectively. Patch repair method is one of the most preferred methods for repairing damaged composites because it does not create a new tension on the structure it is applied, does not damage the damaged area and is light. In addition, thanks to the embedded microcapsules placed in its matrix, self-healing composites have been studied in recent years. In this study, both the repair of composite materials and self-healing composites are discussed.

1. INTRODUCTION

The use of polymers and polymer-based composites in structural applications in aircraft, cars, ships, defense and construction industries is increasing day by day. Despite their superior properties, composite materials used in many areas today can be damaged over time due to the stresses and loads they are exposed to. Replacing the damaged item is both costly and time consuming in terms of procuring the material. Instead, repairing the damage to the material is the most reasonable solution in terms of both cost and time. Various techniques have been developed and adopted to repair visible or detectable damage on polymeric structures (Wu et al. 2008). Damaged composite structures can be repaired by methods such as patching and bonding. The repaired material is in many cases stronger than before it was damaged. Considering the spare part supply time, labor, part and replacement costs, it is often preferred to repair damaged composite materials because it is very advantageous (Adin 2018).

There are three types of repairs, depending on the size of the damage area (Abrate 1998). These are superficial repair, temporary repair and structural repair. Superficial repair methods are used in cases where damage to the material does not affect the structural integrity of the material. Temporary repair methods are used in cases where the damage does not threaten the structural integrity and mechanical properties of the material itself. Simple patch repairs can be given as an example of the temporary repair method. For example, screwed aluminum plate or riveted fiber-reinforced patches are some of the temporary repair methods. The large damage area in the material can only be repaired by structural repair. Among the structural repair applications, the patch repair method is widely used.

Repair of the damaged sample is usually carried out with external reinforcement parts. With the development of technology in recent years, the focus of scientific studies has been directed to micro and nano-scale studies. Scientists have focused their studies on composite materials that can repair themselves. These materials can repair themselves in case of damage thanks to the micro and nanoscale capsules placed inside while they are being produced. In case of damage, certain triggering conditions are provided, allowing the capsules to break down and thus the repair process to begin. When the trigger condition is realized, the alkyd resin that comes out with the breakdown of the capsules penetrates the damaged area and performs the repair.

In this study, information about repair of damaged composites and self-healing composites are discussed.

2. REPAIR OF DAMAGED COMPOSITES

It is a common problem that composites exposed to mechanical, chemical, thermal, etc. stresses are damaged over time. There are various types of damage such as

* **Corresponding Author**

*(ykepir@mersin.edu.tr) ORCID ID 0000-0002-3536-3931
(alpergunoz@mersin.edu.tr) ORCID ID 0000-0001-7978-6306
(memduhkara@mersin.edu.tr) ORCID ID 0000-0002-5201-5453

Cite this article

Kepir Y, Gunoz A & Kara M (2022). Repairing of damaged composite materials and self-healing composites, Turkish Journal of Engineering, 6(2), 149-155

Review Article / DOI: 10.31127/tuje.866955

Received: 16/03/2021; Accepted: 18/04/2021

matrix damage, delamination, and fiber damage. These damage types are shown in Figure 1.

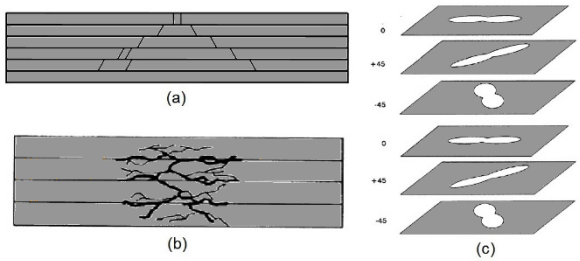

Figure 1. (a)Matrix damage (b)Fiber damage (c) Delamination (Kara 2012)

Damage to the material can be visible or detected by non-destructive testing methods. All types of damage that occur reduce the strength of the material and pose a threat to the security of the building to which it belongs.

Repair methods are used to extend the life of damaged or manufacturing defective components of various structures. Fatigue recovery, crack closure and corrosion repair are among the main objectives of repair (Dağdelen 2010).

The repair of the damaged composite structure takes place in three stages: structural damage assessment, repair design and analysis. If these three stages are successfully overcome, the composite structure becomes ready for long-term use (Kara 2012).

There are some basic repair methods used during the repair of a damaged composite structure. These methods are classified as superficial repair, temporary repair and structural repair. As superficial and temporary repair methods; Protective tape method, resin sealing method, filling repair method, repair method with bolted pairs can be given as examples. Hand lay-up method, pre-preg repair method and patch repair method can be given as examples of structural repair methods (Kılınç 2019).

It is the most preferred patch repair method among the above mentioned repair methods. The patch repair method can be used in two ways, as filling and stepped patch repair. Filling patches are a method of patch repair that requires good bonding strength and is used on flat parts. Figure 2 shows a schematic representation of the filling patch method.

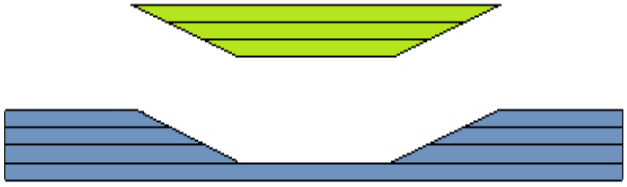

Figure 2. Filling patch method (Dağdelen 2010)

The other method of patch repair, stepped patch repair, is used in applications where it is necessary to minimize composite layers that take up extra space. It has two different types as single-sided and double-sided step patch. A schematic representation of the single-sided stepped patch repair method is presented in Figure 3.

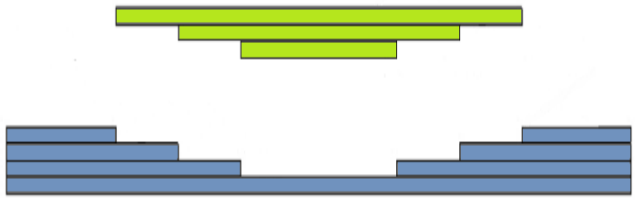

Figure 3. Single-sided step patch method (Dağdelen 2010)

The most preferred of the repair methods that can be made to the damaged area of the material is to create double-sided overlapping joints with a fiber-reinforced composite patch. The material is repaired by applying the adhesively bonded patch to the damaged area. The double-sided stepped patch repair method is given in Figure 4.

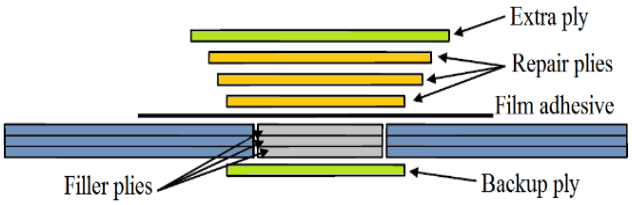

Figure 4. Patch repair application for layered composites (Kara 2012)

The advantages of adhesive bonds can be listed as follows;

- It can be easily applied to materials of different thicknesses.
- These connections also act as seals.
- Good insulation and damping abilities.
- They are easy and cheap connection forms.
- No stress accumulation since they do not damage the structure of the elements to be connected to each other (Erkek 2019).

There are studies in the literature on the repair of damaged composites and various patch methods.

Li et al. (2019) in their study, produced many carbon fiber / epoxy composite plates with holes of the same size and repaired these plates with patches in various geometries. They subjected the patch repaired samples and the undamaged base sample to tensile testing. As a result of the study, it was concluded that the tensile strength of the samples repaired with patches improved between 5% and 16% compared to the non-damaged sample, depending on the patch shape.

He et al. (2019), in their study, repaired the damaged aluminum alloy plates using carbon fiber reinforced epoxy resin composite patches. As a result of their performance evaluation of the mechanical properties of damaged sheets repaired with a two-layer carbon fiber/epoxy composite patch, they concluded that the repair efficiency of repaired aluminum alloys increased to 160% compared to undamaged aluminum alloys.

Kim et al. (2020) produced polyvinyl chloride (PVC) sandwich composites with the resin transfer method in their study. They subjected these samples they produced to bending and fatigue tests. They repaired the damaged samples with 3 different patch types: scarf patch, step patch and external patch. They subjected the repaired specimens to re-bending and buckling tests. As a result of

the tests performed, they showed that the sample repaired with the scarf patch had a recovery rate of approximately 92%.

Moreira et al. (2020) investigated the repair efficiency of 5 different patch types, namely Single-Strap, Double-Strap, Scarf, One-Stepped and Two-Stepped, on the damaged carbon-epoxy composite plate in their numerical study. They performed numerical fatigue and 3 point bending experiments by modeling the samples separately with different patch types. As a result of the study, they observed the bending and fatigue strength of the repaired samples with two stepped patch as 141% and 94%, respectively.

Psarras et al. (2020) investigated the effect of repair of carbon fiber reinforced polymer composites (CFRP) with scarf patch on the mechanical properties of the sample. They subjected the CFRP sample to tensile testing. They repaired the damaged sample with a scarf patch. They observed the tensile strength recovered in the repaired sample as 67% and the hardness as 95%.

3. SELF-HEALING COMPOSITES

Self-healing composites have become an increasingly important subject of research since the early 1980s, as they make it possible to ensure the safety of building components that are loaded or exposed to various stresses by repairing the damage that occurs in polymer-based composites (Brown 2011).

Self-repairing smart materials are developed by taking inspiration from biological systems such as repair of bleeding areas through vessels. Polymers and polymer-based structural composites are highly susceptible to damage caused by mechanical, chemical, thermal, UV radiation, or a combination of these factors, and can undergo various damages under these effects. This may lead to the formation of deep micro cracks in the structure where detection and external intervention is difficult or impossible. The presence of microcracks in the polymer matrix can affect the dominant properties of both the fiber and matrix of a composite (Wu et al. 2008).

Depending on the active substance placed in the matrix during the production phase of the composite, the time and conditions for the material to self-repair in case of damage vary. The beginning of the repair process can take two forms. One is that the active substance starts with external intervention such as exposure to heat, light, mechanical action and chemicals. The other can be autonomously, without any external effects, by breaking the microcapsule containing the restorative agent as the crack progresses (Algaifi et al. 2021). The classification of the self-healing process of materials according to external effect is shown in Figure 5.

3.1. Autonomous Healing

Self-repair of a material whose internal structure is damaged is a common situation in nature. As an imitation of the system in nature, the self-repair of composite materials can be achieved with micro capsules or micro veins placed in them. (Cao et al. 2020).

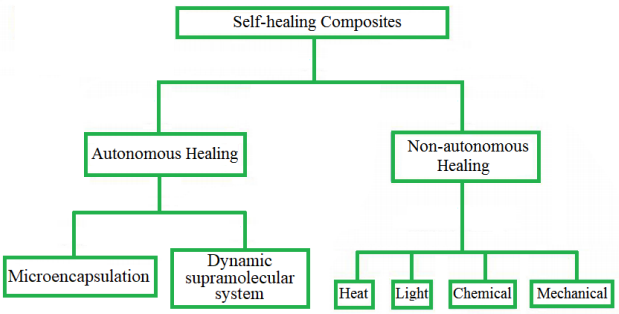

Figure 5. Classification of self-healing processes

3.1.1. Microencapsulation

In autonomous repair, microcapsules break down with the effect of breaking and the active substance inside penetrates into capillary cracks. The material interacts with the catalyst embedded in the matrix and the polymerization process takes place. Thus, the autonomous self-repair process of the damaged material begins (Pittala 2021). The autonomous self-healing process of damaged composite materials is shown schematically in Figure 6.

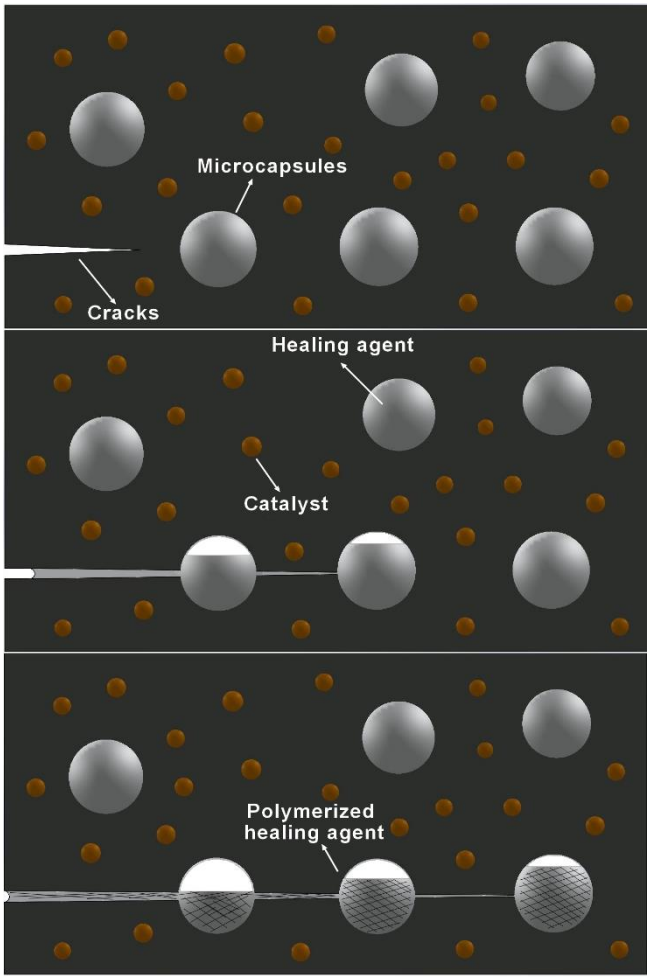

Figure 6. Schematic representation of the autonomous self-repair method

3.1.2. Dynamic supramolecular system

With the dynamic supramolecular system, its self-healing takes place by combining two different types of polymers with a macro-scale interface interaction. The basic concept of this self-healing variant is based on cross-linking processes that enable the repair of mechanically induced damage with subsequent networking (Zheng et al. 2021). The self-healing mechanism realized with the dynamic supramolecular system is shown in Figure 7.

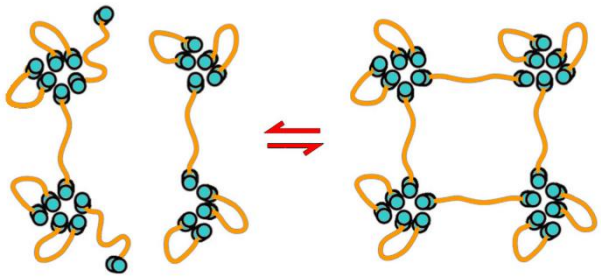

Figure 7. Dynamic supramolecular system

3.2. Non-autonomous healing

An external trigger is needed for the non-autonomous healing process to begin. This trigger can be heat, light, mechanical force, or a chemical.

3.2.1. Heat

Heat is the trigger currently used in most self-healing composite materials. Most of the studies on self-healing materials in the literature use heat as a trigger [Fang et al. 2017; Wu et al. 2018; Le et al. 2017]. Compared to other non-autonomic self-healing systems, these mechanisms are most applicable to polymer matrix composites due to their relatively easy thermal control.

3.2.2. Light

Light can be used in the initiation of the chemical-based improvement process due to the rapidity of photo reactions. Using light as a trigger provides the advantage of choosing the most suitable wavelength (visible light or UV light) for the material. Since the light can also be placed in the desired area, it provides more control of local damage during the healing process. There are studies in the literature that use light as a trigger in self-healing materials. [Amamoto et al., 2011; Telitel et al. 2014; Meng et al. 2016; Michal et al. 2013].

3.2.3. Mechanical

Biological systems can actively and functionally respond to mechanical triggers. However, in polymers, in case of mechanical loading, the covalent bonds of material can break. This causes the material to be damaged. Intelligent molecular design developed as an alternative to bulk polymers has a positive effect on the mechanical force applied to synthetic materials [Liu et al. 2015; Piermattei et al. 2009; Watuthanthrige et al. 2020]. When these materials are damaged, thanks to the mechanophore compounds placed in them, they can repair themselves with a triggering force. Depending on the direction of the force, covalent bonds can be broken and reattached.

3.2.4. Chemical

Another trigger used in self-healing composite materials is chemical triggers. Chemical triggers activate the self-healing system by providing the appropriate conditions such as increasing the pH value or decreasing the chloride ion concentration. When the appropriate conditions are met, the healing agent is released from microcapsules and the healing process begins. There are studies in the literature on self-healing composite materials activated by chemical triggers [Wang et al. 2018; Yang and Urban 2018; Li et al. 2018].

3.3. Experimental Studies on Self-healing Composites

Various studies have been done on self-healing composite materials in the literature. The efficiency of the method was observed by comparing the results of the tests applied to the samples that were not damaged and the self-healed samples.

Everitt et al. (2015) added carboxyl-finite liquid butadiene-acrylonitrile as a healing microcapsule to glass fiber reinforced epoxy matrix composite plates. They subjected the samples to fracture and release tests. As a result of the study, they observed that the self-healing samples showed an improvement of 139% and 269% in shear strength and fracture toughness, respectively, compared to the non-damaged samples.

He et al. (2019) added microcapsules with isocyanate active ingredient to epoxy and polyurethane resins. They subjected the samples to the fracture toughness test. They observed that the fracture toughness values of self-healing samples increased by 105% compared to undamaged samples.

Do Nascimento et al. (2020) in their study, they added poly (ethylene-co-methacrylic acid) (EMAA) to carbon-epoxy composites as a self-healing agent. Dynamic mechanical analysis and interlayer shear strength test were applied to the unmodified sample and the samples with added EMAA. As a result of the study, they observed that the addition of EMAA to carbon epoxy composites prevented visible delaminations in the materials after damage, and increased the interlayer shear strength and storage modulus.

Feng et al. (2020) placed healing agents and fluorescent secret curing agents (FLCA) into epoxy resin in their study. They investigated the self-healing of polymer composites that were damaged underwater. The optimum microcapsule content of the epoxy resin was determined as 15% and the optimum FLCA content as 6%. They also conducted experiments at different temperatures and times. When the material was damaged by an external force, it could be repaired

underwater at 60 °C for 4 hours, and the self-healing efficiency reached 85.6%.

In their study, Ebrahimnezhad-Khaljiri and Eslami-Farsani (2020) added 3 different microcapsules, 7%, 14% and 21%, into the glass fiber-epoxy composite. They applied tensile and interlayer shear strength (ILSS) tests to the samples. The damaged samples were placed in the oven and kept at 130 C for 60 minutes for the healing process. They then applied the tensile and ILSS tests to the samples a second time. As a result of the study, they observed the self-healing rate of samples in terms of tensile and ILSS strengths as 97% and 144%, respectively.

In their study, Kumar et al. (2020) placed healing agents into the hybrid resin (vinyl ester / epoxy) composite samples produced by vacuum assisted resin transfer molding (VARTM) method. They applied a low speed impact test to the samples. As a result of the experiments, they reported that the impact resistance of the samples reinforced with healing agents was 177% higher than the pure samples.

In their study, Wertz et al. (2014) performed a break test on polylactic acid samples in which microcapsules were placed. As a result of the study, they observed that samples kept at room temperature for 24 hours after being damaged regained fracture toughness by 84% compared to virgin samples.

3.4. Self-healing efficiency of composites

Self-healing efficiency is defined as the ability of the material to regain fracture toughness after the fracture test (Aïssa et al. 2012). The fracture test is applied to the sample gradually, ensuring that the sample is damaged in a controlled manner. The crack in the sample is then allowed to close and heal at room temperature. After this healing process, the same sample is retested to measure the healing efficiency and to determine its ability to regain fracture toughness. The healing efficiency results of the previous studies in the literature are gathered together in Table 1.

Table 1. Self-repair efficiency results of studies in the literature

Matrix material	Experimental conditions	Healing efficiency	Reference
Thermoset	25°C – 24 h	72%	Souzandeh and Netravali 2019
	25°C – 24 h	80%	Ahangaran et al. 2019
	120°C – 24 h	79%	Rodriguez et al. 2020
	60°C – 4 h	86%	Feng et al. 2020
	25°C – 24 h	60%	Radovic et al. 2020
Thermoplastic	IR Light – 3 min	76%	Du et al. 2020
	25°C – 6 h	93%	Ying et al. 2020
	25°C – 3 h	104%	Zhu et al. 2015
	80°C – 7 min	87%	Jin et al. 2020
	IR Light – 3 min	96%	Xu et al. 2018
Elastomer	100°C – 24 h	80%	Imato et al. 2020
	135°C – 15 min	90%	Zhao et al. 2020
	25°C – 3 h	92%	Cai et al. 2020
	25°C – 48 h	75%	Keller et al. 2007
	25°C – 2 h	88%	Pignanelli et al. 2020

4. CONCLUSION

In this study, information has been given by researching the repair of composite materials damaged by various stresses and loads. Self-healing composite materials, which are a type of material developed to repair composites with adhesive bonded patches and to repair themselves when damaged, have been investigated. As a result of the study, it was concluded that both the adhesive bonding method of repair and producing the material as a self-repairing smart material from the very beginning would be much more advantageous in terms of both cost and time compared to replacing parts.

Author contributions

Yusuf KEPİR: Conceptualization; Investigation; Resources; Manuscript writing; Review & editing. **Alper GÜNÖZ:** Investigation; Methodology; Visualization; Manuscript writing. **Memduh KARA:** Supervision; Validation; Review & editing.

Conflict of Interest: The authors have no conflicts of interest to declare.

REFERENCES

Abrate S (1998). The Dynamics of Impact on Composite Structure, Impact Response and Dynamic Failure of Composites and Laminate Materials, Part 2, editors JK Kim and T., X., Yu. Trans Tech Publications, Switzerland.

Adin H (2018). Numerical analysis of bending behavior of elliptical perforated aluminum plates repaired with composite patch. DÜMF Journal of Engineering 9(2), 713-725.

Ahangaran F, Hayaty M, Navarchian A H, Pei Y & Picchioni F (2019). Development of self-healing epoxy composites via incorporation of microencapsulated epoxy and mercaptan in poly (methyl methacrylate) shell. Polymer Testing, 73, 395-403.

Aïssa B, Therriault D, Haddad E & Jamroz W (2012). Self-healing materials systems: overview of major approaches and recent developed technologies. Advances in Materials Science and Engineering, 2012.

Algaifi H A, Bakar S A, Alyousef R, Sam A R M, Ibrahim M W, Shahidan S, ... & Salami B A (2021). Bio-inspired self-healing of concrete cracks using new B. pseudomycoides species. Journal of Materials Research and Technology.

Amamoto Y, Kamada J, Otsuka H, Takahara A & Matyjaszewski K (2011). Repeatable photoinduced self-healing of covalently cross-linked polymers through reshuffling of trithiocarbonate units. Angewandte Chemie, 123(7), 1698-1701.

Brown E N (2011). Use of the tapered double-cantilever beam geometry for fracture toughness measurements and its application to the quantification of self-healing. The Journal of Strain Analysis for Engineering Design, 46(3), 167-186.

Cai Y, Zou H, Zhou S, Chen Y & Liang M (2020). Room-Temperature Self-Healing Ablative Composites via Dynamic Covalent Bonds for High-Performance Applications. ACS Applied Polymer Materials, 2(9), 3977-3987.

Cao S, Zhu W & Liu T (2020). Bio-inspired self-healing polymer foams with bilayered capsule systems. Composites Science and Technology, 195, 108189.

Dağdelen O (2010). Repair optimization for damaged composite plates. Doctoral dissertation, DEÜ Institute of science, İzmir (in Turkish).

Do Nascimento A A, Fernandez F, da Silva F S, Ferreira E P, Melo J D D & Barbosa A P C (2020). Addition of poly (ethylene-co-methacrylic acid) (EMAA) as self-healing agent to carbon-epoxy composites. Composites Part A: Applied Science and Manufacturing, 137, 106016.

Du W, Jin Y, Lai S, Shi L, Shen Y & Yang H (2020). Multifunctional light-responsive graphene-based polyurethane composites with shape memory, self-healing, and flame retardancy properties. Composites Part A: Applied Science and Manufacturing, 128, 105686.

Ebrahimnezhad-Khaljiri H & Eslami-Farsani R (2020). The tensile properties and interlaminar shear strength of microcapsules-glass fibers/epoxy self-healable composites. Engineering Fracture Mechanics, 106937.

Erkek B (2019). Investigation of the effects of thermal aging on the buckling behavior of composite boards repaired using patches and adhesives. Master's Thesis, Dicle University Institute of Science, Diyarbakır (in Turkish).

Everitt D T, Luterbacher R, Coope T S, Trask R S, Wass D F & Bond I P (2015). Optimisation of epoxy blends for use in extrinsic self-healing fibre-reinforced composites. Polymer, 69, 283-292.

Fang Y, Du X, Du Z, Wang H & Cheng X (2017). Light-and heat-triggered polyurethane based on dihydroxyl anthracene derivatives for self-healing applications. Journal of Materials Chemistry A, 5(17), 8010-8017.

Feng H, Yu F, Zhou Y, Li M, Xiao L & Ao Y (2020). Fabrication of microcapsule-type composites with the capability of underwater self-healing and damage visualization. RSC Advances, 10(56), 33675-33682.

He Y, Liu X & Yu Z (2019). Mechanical properties of UV-curable carbon fiber-reinforced polymer composite patch: Repair evaluation of damaged aluminum alloy. Polymers for Advanced Technologies, 30(8), 2034-2044.

He Z, Jiang S, An N, Li X, Li Q, Wang J, ... & Kang M (2019). Self-healing isocyanate microcapsules for efficient restoration of fracture damage of polyurethane and epoxy resins. Journal of Materials Science, 54(11), 8262-8275.

Imato K, Nakajima H, Yamanaka R & Takeda N (2020). Self-healing polyurethane elastomers based on charge-transfer interactions for biomedical applications. Polymer Journal, 1-8.

Jin C, Sinawang G, Osaki M, Zheng Y, Yamaguchi H, Harada A & Takashima Y (2020). Self-healing thermoplastic polyurethane linked via host-guest interactions. Polymers, 12(6), 1393.

Kara M (2012). Damage behavior under internal pressure of filament wound GRP pipes repaired with patch after low speed impact. Doctoral Thesis, Selçuk University Institute of Science, Konya (in Turkish).

Keller M W, White S R & Sottos N R (2007). A self-healing poly (dimethyl siloxane) elastomer. Advanced Functional Materials, 17(14), 2399-2404.

Kilinc İ M (2019). Experimental investigation of bonding parameters in aluminum foam sandwich structures. Master's thesis, Bursa Uludağ University Institute of Science, Bursa (in Turkish).

Kim S, Ha J, Yoon S & Kim M (2020). A study on mechanical properties after bonded repair of sandwich composite materials. Modern Physics Letters B, 34(07n09), 2040033.

Kumar R, Hynes N R J, Saravanakumar S S, Senthamaraikannan P, Khan A, Asiri A M, ... & Nagarajan S (2020). Concept of self-repair and efficiency measurement in polymer matrix composites. In Self-Healing Composite Materials (pp. 375-391). Woodhead Publishing.

Le H H, Böhme F, Sallat A, Wießner S, auf der Landwehr M, Reuter U, ... & Das A (2017). Triggering the Self-Healing Properties of Modified Bromobutyl Rubber

by Intrinsically Electrical Heating. Macromolecular Materials and Engineering, 302(4), 1600385.

Li Z, Davidson-Rozenfeld G, Vázquez-González M, Fadeev M, Zhang J, Tian H & Willner I (2018). Multi-triggered supramolecular DNA/bipyridinium dithienylethene hydrogels driven by light, redox, and chemical stimuli for shape-memory and self-healing applications. Journal of the American Chemical Society, 140(50), 17691-17701.

Li C, Zhao Q, Yuan J, Hou Y & Tie Y (2019). Simulation and experiment on the effect of patch shape on adhesive repair of composite structures. Journal of Composite Materials, 53(28-30), 4125-4135.

Liu Y, Liu Y, Hu H, Liu Z, Pei X, Yu B, ... & Zhou F (2015). Mechanically induced self-healing superhydrophobicity. The Journal of Physical Chemistry C, 119(13), 7109-7114.

Meng Y, Yang J C, Lewis C L, Jiang J & Anthamatten M (2016). Photoinscription of chain anisotropy into polymer networks. Macromolecules, 49(23), 9100-9107.

Michal B T, Jaye C A, Spencer E J & Rowan S J (2013). Inherently photohealable and thermal shape-memory polydisulfide networks. ACS Macro Letters, 2(8), 694-699.

Moreira R D F, de Moura M F S F, Silva F G A, Ramírez F M G & Silva F D R (2020). Numerical comparison of several composite bonded repairs under fatigue loading. Composite Structures, 112250.

Piermattei A, Karthikeyan S & Sijbesma R P (2009). Activating catalysts with mechanical force. Nature chemistry, 1(2), 133-137.

Pignanelli J, Qian Z, Gu X, Ahamed M J & Rondeau-Gagné S (2020). Modulating the thermomechanical properties and self-healing efficiency of siloxane-based soft polymers through metal–ligand coordination. New Journal of Chemistry, 44(21), 8977-8985.

Pittala R K (2021). Effect of epoxy resin healing agent viscosity on the self-healing performance of capsules reinforced polymer composite. Journal of Polymer Research, 28(4), 1-19.

Psarras S, Loutas T, Galanopoulos G, Karamadoukis G, Sotiriadis G & Kostopoulos V (2020). Evaluating experimentally and numerically different scarf-repair methodologies of composite structures. International Journal of Adhesion and Adhesives, 97, 102495.

Radovic I, Stajcic A, Radisavljevic A, Veljkovic F, Cebela M, Mitic V V & Radojevic V (2020). Solvent effects on structural changes in self-healing epoxy composites. Materials Chemistry and Physics, 256, 123761.

Rodriguez R, Bekas D G, Flórez S, Kosarli M & Paipetis A S (2020). Development of self-contained microcapsules for optimised catalyst position in self-healing materials. Polymer, 187, 122084.

Souzandeh H & Netravali A N (2019). Self-healing of 'green'thermoset zein resins with irregular shaped waxy maize starch-based/poly (D, L-lactic-co-glycolic acid) microcapsules. Composites Science and Technology, 183, 107831.

Telitel S, Amamoto Y, Poly J, Morlet-Savary F, Soppera O, Lalevée J & Matyjaszewski K (2014). Introduction of self-healing properties into covalent polymer networks via the photodissociation of alkoxyamine junctions. Polymer Chemistry, 5(3), 921-930.

Wang C, Fadeev M, Zhang J, Vázquez-González M, Davidson-Rozenfeld G, Tian H & Willner I (2018). Shape-memory and self-healing functions of DNA-based carboxymethyl cellulose hydrogels driven by chemical or light triggers. Chemical science, 9(35), 7145-7152.

Watuthanthrige N D A, Ahammed B, Dolan M T, Fang Q, Wu J, Sparks J L, ... & Ye Z (2020). Accelerating dynamic exchange and self-healing using mechanical forces in crosslinked polymers. Materials Horizons, 7(6), 1581-1587.

Wertz J T, Mauldin T C & Boday D J (2014). Polylactic acid with improved heat deflection temperatures and self-healing properties for durable goods applications. ACS applied materials & interfaces, 6(21), 18511-18516.

Wu D Y, Meure S & Solomon D (2008). Self-healing polymeric materials: a review of recent developments. Progress in polymer science, 33(5), 479-522.

Wu X, Li J, Li G, Ling L, Zhang G, Sun R & Wong C P (2018). Heat-triggered poly (siloxane-urethane) s based on disulfide bonds for self-healing application. Journal of Applied Polymer Science, 135(31), 46532.

Xu X, Fan P, Ren J, Cheng Y, Ren J, Zhao J & Song R (2018). Self-healing thermoplastic polyurethane (TPU)/polycaprolactone (PCL)/multi-wall carbon nanotubes (MWCNTs) blend as shape-memory composites. Composites Science and Technology, 168, 255-262.

Yang Y & Urban M W (2018). Self-healing of polymers via supramolecular chemistry. Advanced Materials Interfaces, 5(17), 1800384.

Ying W B, Yu Z, Kim D H, Lee K J, Hu H, Liu Y, ... & Zhu J (2020). Waterproof, Highly Tough, and Fast Self-Healing Polyurethane for Durable Electronic Skin. ACS Applied Materials & Interfaces, 12(9), 11072-11083.

Zhao L, Shi X, Yin Y, Jiang B & Huang Y (2020). A self-healing silicone/BN composite with efficient healing property and improved thermal conductivities. Composites Science and Technology, 186, 107919.

Zheng N, Xu Y, Zhao Q & Xie T (2021). Dynamic Covalent Polymer Networks: A Molecular Platform for Designing Functions beyond Chemical Recycling and Self-Healing. Chemical Reviews, 121(3), 1716-1745.

Zhu D Y, Cao G S, Qiu W L, Rong M Z & Zhang M Q (2015). Self-healing polyvinyl chloride (PVC) based on microencapsulated nucleophilic thiol-click chemistry. Polymer, 69, 1-9.

Turkish Journal of Engineering

https://dergipark.org.tr/en/pub/tuje

e-ISSN 2587-1366

Determination to the period of a school building before and after its retrofitting using ambient vibration records

Selcuk Kacin[1], Halil Cagri Yilmaz [1*], Cemil Vedat Caglar[1]

[1]*Iskenderun Technical University, Faculty of Engineering and Natural Sciences, Department of Civil Engineering, Hatay, Turkey*

Keywords
SHMSs
Retrofitting
Dynamic Analysis
Ambient Vibration Records
OMA

ABSTRACT

Determining the dynamic parameters of the structures allows us to obtain a substantial amount of information about the state of the building. Recently, the determination of these parameters were performed through Structural Health Monitoring Systems (SHMSs), which are non-destructive methods. In scope of this study, the period values prior to and following the retrofitting of a school building, which are among the dynamic parameters, were examined. The Operational Modal Analysis (OMA) method, which is based on the principle of measuring the responses of ambient effects in the structure in the experimental study, has been utilized. For this purpose, response records taken from the building under the effect of ambient vibration were used. Before and after retrofitting, the records of the building under the effect of ambient vibration were taken from the same locations. 3 sensors were used to record ambient vibrations. The data from these sensors were transferred to a computer by using a data logger. In order to measure and evaluate the responses Enhanced Frequency Domain Decomposition Method (EFDDM) in the frequency domain and Stochastic Subspace Identification Method (SSIM) in the time domain were used. Following the analysis, a comparison of how the period values had changed was conducted.

1. INTRODUCTION

The structures show many different characteristics under dynamic loads. Besides the uncertainties under dynamic loads, the uncertainties in the parameters affecting the dynamic behavior make it difficult to determine the dynamic behavior of the structures realistically. The identification of the dynamic characteristics of structures is an increasingly used method, especially in existing buildings. These characteristics are of particular importance for historical structures for which we do not have sufficient or precise information and complex and huge systems such as civil engineering structures (Safak 2007). Experimental data can be used to solve the problem of determining dynamic parameters. Experimental Modal Analysis (EMA) is a method adopted to determine dynamic parameters (Maia and Silva 1997; Ewins 1995; Mirtarehi and Salehi 2018). Dynamic parameters usually consist of frequency, damping ratio, mode shape, modal participation factor. In the Experimental Modal Analysis, structures are excited by one or several measured forces, the responses of the structures are recorded. Modal models for the structures are identified from the input–output data. Finally, the modal parameters of the structures are extracted from the identified modal models. However, most civil engineering structures (bridges, buildings, etc.) are under ambient loads such as wind, traffic, and earthquakes. And since these loads are immeasurable, the input force cannot be fully defined. In addition, it is both costly and difficult to vibrate these huge structures with equipment. For these reasons, methods and algorithms that perform modal analysis of structures using only output data have been developed. This method, which is included in the literature as Operational Modal Analysis (OMA) or ambient vibration analysis, is a method based on output responses only (Van Overschee and De Moor 1993 ; Brincker et al. 2000 ; Bayraktar et al. 2009; Zhu et. al 2018; Singh and Grip 2019). It has become a frequently used method in recent years due to the fact that the method uses only output data as well as for, its applicability and low cost.

* **Corresponding Author**

(selcuk.kacin@iste.edu.tr) ORCID ID 0000-0001-5406-5756
*(cagri.yilmaz@iste.edu.tr) ORCID ID 0000-0001-7714-1918
(cemilcaglarr@gmail.com) ORCID ID 0000-0001-5064-8188

Cite this article

Kacin S, Yılmaz H C & Caglar C V (2022). Determination to the period of a school building before and after its retrofitting using ambient vibration records. Turkish Journal of Engineering , 6(2), 156-160

Research Article / DOI: 10.31127/tuje.873050

Received: 02/02/2021; Accepted: 25/02/2021

High sensitivity accelerometers are required to measure vibrations in buildings. With the technology developing from the past to the present, the use of accelerometers that can measure with high sensitivity has gained great speed in vibration analysis. In this way, the predominant period and other dynamic parameters of the building can be determined in a short time with the sensors placed in buildings under ambient vibrations. Many methods with the same mathemetical bases yet different algorithms are used in the analysis of the response records. The main difference between the methods is that the variable is in the time domain or frequency domain. Methods in the frequency domain are based on the analysis of the signal measured at each point and the correlation between the signals (Bru et al. 2015). Methods in the time domain are based on the time history of the signal at each point or fitting a model with correlation functions. Within the scope of the experimental study, in the assessment of ambient vibration records taken before and after reinforcement, two commonly favored approaches were used. These are the Enhanced Frequency Domain Decomposition (EFDD) method, one of the frequency-domain methods, and the Stochastic Subspace Identification (SSI) method, one of the time-domain methods (Gunes and Anil 2017; Diaferio et al. 2007; Shokravi et al. 2020a; Shokravi et al. 2020b).

2. GENERAL DESCRIPTION OF THE BUILDING INVESTIGATED

In the experimental study, the ambient vibration records were taken from the B block of the school building, which is a reinforced concrete structure and consists of two blocks (Fig. 1).

The school building consists of 4 floors, each floor with a height of 2.95 m. The building generally consists of 15 cm thick slab, 25 x 60 cm cross-section beams and 25 x 60 cm or 35 x 60 cm cross-section columns. The compressive strength of the concrete used in the construction of the school building was determined to be 15.41 Mpa average.

Figure 1. View of the school building

The current situation of the building has been analyzed as a result of extensive studies. According to the analysis results, it was decided to add shear walls to the building in two directions. The school building plan before and after retrofitting is shown in figure 2(a) and 2(b).

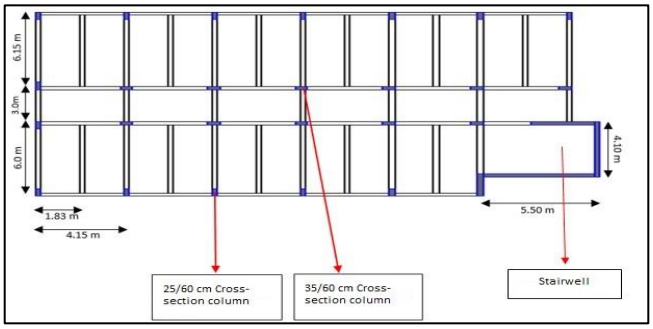

(a)

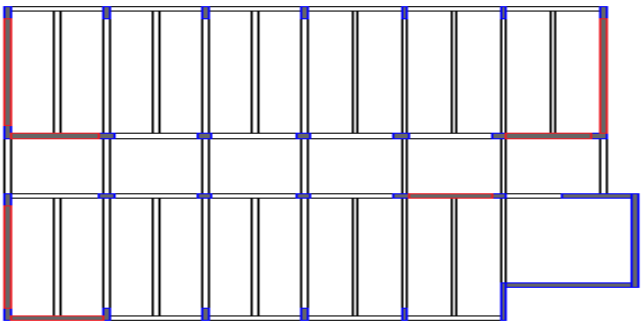

(b)

Figure 2. View of the school building B block plan; (a) before retrofitting (b) after retrofitting

3. METHOD

3.1. Ambient vibration records from school building

In order to determine the dynamic properties of the structures, several different methods are used to obtain the vibration response records of the structures. One of these methods is to wait for an earthquake by placing recording devices and to record the behavior of the building under the effect of earthquakes. In another method, the harmonic external load is given to the structure with a vibration generating device and the reaction of the structure against this load is recorded. In this study, the structure responses were recorded under the influence of ambient vibration, which is another method. There are vibrations that occur and spread due to natural reasons or human activities, which we can also call ambient vibrations in the earth, such as small earthquakes, traffic loads, big engines, etc. These vibrations, which occur due to aforementioned reasons and have amplitudes that are too small to be felt by humans, can be measured with sensitive recording devices.

In this study, structural response values were recorded under the influence of ambient vibration before retrofitting. For this purpose, accelerometer sensors were placed on the building.

In order to measure the response records of the building under the effect of ambient vibration, accelerometers - property of the Department of Civil Engineering of Iskenderun Technical University - with the feature to make 3 dimensional recordings were used. Response records were obtained using the TESTBOX2010 series, which is a 16-channel data acquisition unit (Fig. 3). Approximately 30-minute long response records were taken from the school building. The sampling frequency of the response records of the

building under the effect of ambient vibrations is in the range of 0-100 Hz and the time interval is taken as 0.01 second.

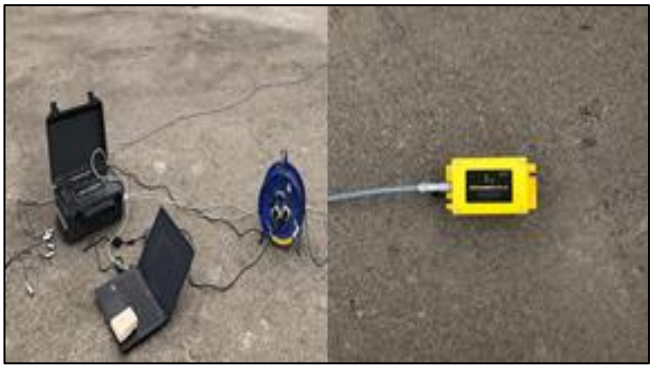

Figure 3. View of data acquisition unit and sensor

With the addition of shear walls to the building during the school building retrofitting, the building's horizontal load capacity was significantly increased (Fig 4.). During the shear wall application, the infill wall materials between the columns and beams were demolished and cleaned. In the reinforcement application, the joints of the floors with the beams were drilled and the longitudinal reinforcements of the additional shear walls were continuously transferred from floor to floor, and the rods were placed with a two-component epoxy-containing chemical anchoring system in the holes where the drilling process was applied to the existing columns and beams. Ambient vibration records were taken from the same points with sensors after retrofitting (Celebi and Liu, 1998 ; Kacin et al. 2011 ; Motosaka et al. 2004 ; Takada et al. 2004).

Figure 4. Adding shear walls

3.2 Numerical values

3.2.1 Calculation of the period with ambient vibration records

ARTeMIS Modal software (SVS, 2010) was used to analyze the vibration data obtained from the data collection system in the experiment. Firstly, a simple model to represent the building was created in the software. Then the vibration data (acceleration-time) obtained was transferred to the program and placed on the relevant floors of the model created as a representation (Fig. 5).

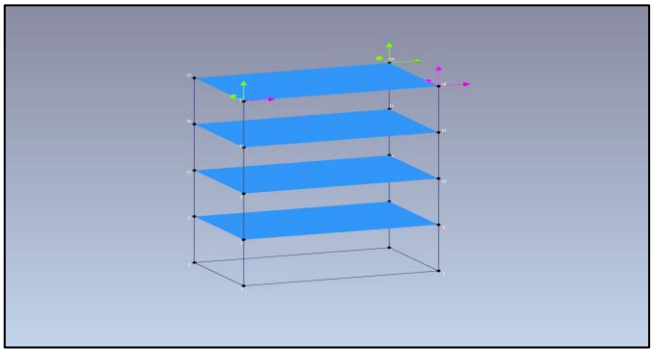

Figure 5. Model of school building and placed sensors

Amplitude-frequency values were obtained by transforming the vibration data from acceleration-time domain to acceleration-frequency domain by Fast Fourier Transformation (FFT) method. After the FFT values were processed, these values were analyzed with both SSI and EFDD aproaches (Fig. 6a and 6b). The predominant period of the school building was calculated after the analysis. The same analyses were done after retrofitting.

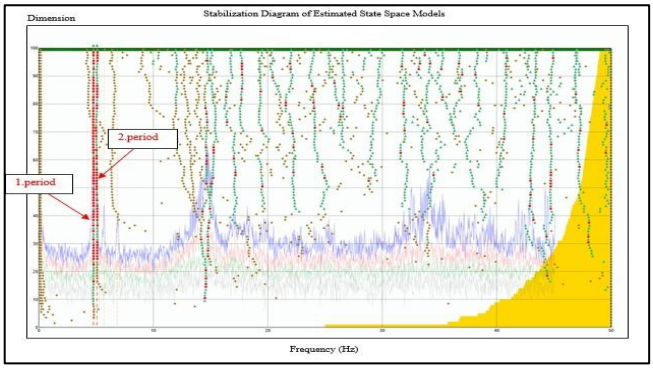

(a)

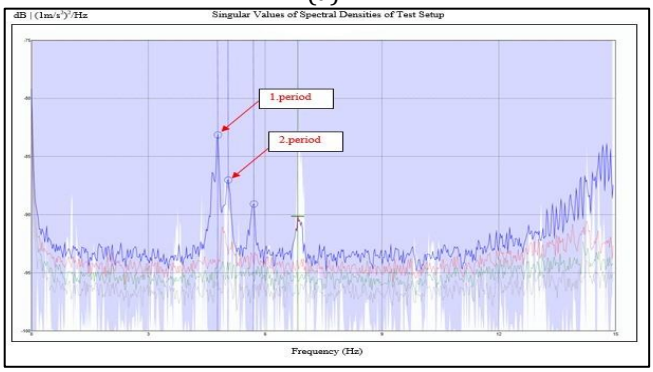

(b)

Figure 6. Analysis results; (a) SSI analysis (b) EFDD analysis

3.2.2 Calculation of the period with structural analsis software

After the results of the experimental study, the building was modeled with a structural analysis program (CSI, SAP2000 2015) for comparison. The concrete compressive strength that makes up the school building was defined as 15.41 Mpa. In retrofitting, C30 (30 N/mm2) grade concrete properties were defined for shear wall. Infill walls were defined based on the cross bar assumption. The school building modeled with the structural analysis program was shown in figures 7a and

7b. In addition, the school building modelled without walls.

Assumptions and formulas related to the modeling of diagonal bars are given below, as defined in Turkish Building Earthquake Code 2018 (TBE) and FEMA 306 (TBEC 2018, FEMA 306 1999). Eqs. (1)-(2) are given for the width of the infill wall by taking the current thickness of the infill wall. After modelling the predominant period of the school building were determined for before and after retrofitting. The school building model with walls was choosen to comparison due to its analysis results.

$$a_{wall} = 0.175(\lambda_{wall} \times h_k)^{-0.4} \times r_{wall} \quad (1)$$

$$\lambda_{wall} = [(E_{wall}*t_{wall}*\text{Sin } 2\theta)/(4*E_c*I_k*h_{wall})^{0.25} \quad (2)$$

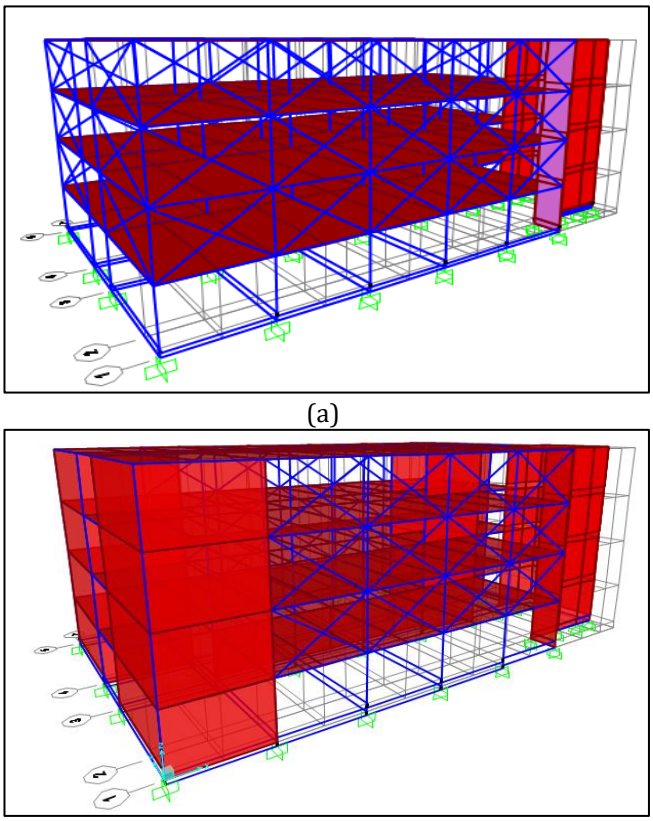

(a)

(b)

Figure 7. General view of school building; (a) before retrofitting (b) after retrofitting

After the analyses, calculated periods were shown as a comparison for both experimental study and structural analysis program (Table 1).

Table 1. Periods before and after retrofitting

	Periods	Before Retrofit-ting(sn)	After Retrofit-ting(sn)	Differ-ence (%)
Experimental results	1.	0.21	0.18	%16.3
	2.	0.20	0.15	%23.1
Sap2000 results with walls	1.	0.29	0.16	%44.8
	2.	0.21	0.13	%38.1
Sap2000 results without walls	1.	0.42	0.16	%61.9
	2.	0.27	0.15	%44.4

4. CONCLUSION

In this study, how to change the periods of reinforced concrete school buildings with retrofitting was studied. For this purpose, measurements were made under ambient vibrations in order to determine before and after retrofitting period values. The school building, which does not provide sufficient performance level, has been strengthened with shear walls. Ambient vibration records were taken by placing high-sensitivity sensors on the top floor of the school building. The determination of the period values with the ambient vibration records obtained was made with two different approaches of the Operational Modal Analysis method. As a result of the analysis, the periods of the school building were obtained as 0.21, 0.20, respectively, as a result of the experimental study before retrofitting. In the experimental study carried out after the strenghtening, the periods of the school building were obtained as 0.18 and 0.15, respectively. The period values obtained show the first and second periods of the school building, respectively. After the retrofitting, the first period and second period are decreased % 16.3 and % 23.1, respectively. As a result of the analysis of the school building modeled with walls with the structural analysis program before retrofitting, the period values were found 0.29 and 0.21, respectively. The period values after retrofitting were found 0.16 and 0.13, respectively. As a result of structure analysis program, after the retrofitting, the first period and second period are decreased % 44.8.3 and % 38.1, respectively. The shear walls added to the school building with the retrofitting provided an increase in the first two natural frequencies of the building, in other words, a decrease in the period of the building. This is to be expected thanks to the increase in the stiffness of the school building with the addition of shear walls.

Author contributions

Selcuk Kacin: Conceptualization, Methodology, Supervision, final revision. **Halil Cagri Yilmaz:** Data curation, Writing-Original draft preparation, Software, Validation. **Cemil Vedat Caglar:** Visualization, Investigation. All authors have read and agreed to the published version of the manuscript.

Conflicts of interest

The authors declare no conflicts of interest.

REFERENCES

Bayraktar A, Turker T, Sevim B, Altunisik A C & Yildirim F (2009) Modal Parameter Identification of Hagia Sophia Bell-tower via Ambient Vibration Test. Journal of Nondestructive Evaluation.

Brincker R, Zhang L & Andersen P (2000). Modal Identification from Ambient Responses using Frequency Domain Decomposition. In Proceedings of the 18th IMAC. San Antonio, Texas.

Bru D, Ivorra S, Baeza F J, Reynau R & Foti D (2015). OMA dynamic identification of a masonry chimney with severe cracking condition. 6th International Operational Modal Analysis Conference (IOMAC15), Gijon, Spain,

Celebi M & Liu H P (1998).Before and after retrofit response of a building during ambient and strong motions. Journal of Wind Engineering and Industrial Aerodynamics, 77&78: 259-268.

Diaferio M, Foti D & Sepe V (2007). Dynamic Identification of the Tower of the Provincial Administration Building, Bari, Italy. Proc. of the Eleventh International Conference on Civil, Structural and Environmental Engineering Computing, Malta,, p. 21. DOI:10.4203/ccp.86.2

Ewins D J (1995) Modal Testing: Theory and Practice. Wiley, NewYork. ISBN : 978-0-863-80218-8

Federal Emergency Management Agency, FEMA, 306 (1999) "Manual, B.P. Evaluation of earthquake damaged concrete and masonary wall buıldings." .

Gunes S & Anil O (2017). Operasyonel Modal Analiz Tekniği ile Yığma Yapıların Dinamik Davranışının Belirlenmesi . 4.UDMSK, 4. Uluslararası Deprem Mühendisliği ve Sismoloji Konferansı.

Kacin S, Bikce M, Genes M C, Doganay Ela & Unlusoy U (2011). Güçlendirme uygulaması yapılan bir binanın güçlendirme öncesi ve sonrasında titreşim ölçümleri ile bazı dinamik parametrelerinin hesaplanması. Yedinci Ulusal Deprem Mühendisliği Konferansı İstanbul: İstanbul Teknik Üniversitesi.

Maia J M & Silva J M (1997). Theoretical and Experimental Modal Analysis. Taunton, Somerset, England: New York: Research Studies Pre.

Mirtaheri M & Salehi F (2018). Ambient vibration testing of existing buildings: experimental, numerical and code provisions. Advances in Mechanical Engineering, 10(4), 1687814018772718.https://doi.org/10.1177/1687814018772718

Motosaka M, Sato T & Yamamoto Y (2004). The amplitude dependent dynamic characteristics of an existing building before and after seismic retrofit. Proc. 13th World Conf. on Earthquake Engineering, Paper No: 1023, August 1-6, Vancouver, Canada.

Safak E (2007). Yapı Titreşimlerinin İzlenmesi: Nedir, Neden Yapılır, Nasıl Yapılır, ve Ne Elde Edilir? Altıncı Ulusal Deprem Mühendisliği Konferansı (ss. 285-293). İstanbul: İstanbul Teknik Üniversitesi

Shokravi H, Shokravi H, Bakhary N, Rahimian Koloor S S, & Petrů M (2020). Health monitoring of civil infrastructures by subspace system identification method: an overview. Applied Sciences, 10(8), 2786. https://doi.org/10.3390/app10082786

Shokravi H, Shokravi H, Bakhary N, Heidarrezaei M, Rahimian Koloor S S & Petrů M (2020). Application of the Subspace-Based Methods in Health Monitoring of Civil Structures: A Systematic Review and Meta-Analysis. Applied Sciences, 10(10),3607.https://doi.org/10.3390/app10103607

Singh H & Grip N (2019). Recent trends in operation modal analysis techniques and its application on a steel truss bridge.

Structural Vibration Solutions (SVS). 2010. ARTeMIS Extractor 2010. Copenhagen, Denmark: Aalborg University/SVS A/S. Available at: http://www.svibs.com

SAP2000. Linear and nonlinear static and dynamic analysis and design of three-dimensional structures. Berkeley (CA), Computers and Struc-tures Inc. (CSI). 2015.

Turkish Building Earthquake Code (TBEC-2018), Afet ve Acil Durum Yönetimi Başkanlığı, Resmi Gazete, Sayı: 30364 (Mükerrer), 18 Mart 2018

Takada T, Iwasaki R, An D D, Itoi T & Nishikawa N (2004). Dynamic Behavior Change of Building Before and After Seismically Retrofitting. Proc. 13th World Conf. on Earthquake Engineering, Paper No: 1237, August 1-6, Vancouver, Canada.

Van Overschee P & De Moor B (1993). Subspace algorithms for the stochastic identification problem. Automatica, 29(3), 649–660.

Zhu Y C, Xie Y L, Au S K (2018). Operational modal analysis of an eight-storey building with asynchronous data ıncorporating multiple setup, Engineering Structures, 165, 50-62

Turkish Journal of Engineering

https://dergipark.org.tr/en/pub/tuje

e-ISSN 2587-1366

An experimental study of the performance of a low-cost paper-based membraneless direct hydrogen peroxide fuel cell

Muhammet ÇELİK *1

[1]*Aksaray University, Engineering Faculty, Department of Mechanical Engineering, Aksaray, Turkey*

Keywords
Hydrogen Peroxide Fuel Cell
DHPFC
Fuel Cell Performance
Membraneless Fuel Cell
Paper-based Fuel Cell

ABSTRACT

A paper-based membraneless direct hydrogen peroxide fuel cell was developed and tested under different potassium hydroxide concentrations (1 to 7 mol lt^{-1}, stepping by 2), different hydrogen peroxide concentrations (1, 2, 3 mol lt^{-1}) and different temperatures (20, 30, 40°C). Moreover, the developed fuel cell was studied for stability under stopped and continuous flow conditions. From the experiments, it was found that the maximum power density of 6.79 mW cm^{-2} and the maximum open circuit voltage of 0.87 V at 40°C were obtained when the anode solution consisted 2 mol lt^{-1} H_2O_2 and 5 mol lt^{-1} potassium hydroxide and cathode solution consisted 2 mol lt^{-1} sulfuric acid and 2 mol lt^{-1} hydrogen peroxide. It was found that if the reactants were supplied constantly into the fuel cell, a current density of 3.12 mA cm^{-2} was obtained. The developed fuel cell produced energy for 91 minutes when the reactant flow was stopped.

1. INTRODUCTION

Membraneless fuel cells (FC) have obtained attention by researchers in recent years due to their simple structure, low cost, and low environmental impact properties. The absence of a membrane in these fuel cells provides some advantages such as avoiding membrane degradation, providing low cost and low internal resistance. Because of the simplicity of membraneless FCs, they can be used to generate power for biological sample analysis (Esquivel et al. 2014), wearable electronics (Valdés-Ramirez et al. 2014, Bandodkar et al. 2015), and supercapacitors (Lu et al. 2014). Moreover, this type of FCs has a wide range of applicability due to the fact that they can produce energy using various solutions such as methanol (Zhang et al. 2019), glucose (Shitanda et al. 2017, Gonzalez-Guerrero et al. 2017), vanadium (Jung and Ahn 2020), human blood (Dector et al. 2017), urea (Chino et al. 2018), formic acid (Copenhaver et al. 2015), hydrogen peroxide (Yang et al. 2019, Ehteshami et al. 2016, Yan et al. 2018), etc. Within this variety of fuels, hydrogen peroxide (H_2O_2) is an attractive fuel because: I) it has a carbon-free structure, II) it can be obtained via using renewable energy sources such as solar energy (Yamada et al. 2010), it can be used both the oxidant and the fuel at the same time in an FC (Yamazaki et al. 2008).

In recent years, employing paper in membraneless FCs has become interesting since the fluids are driven by the capillary effect on the paper. Therefore, any pump for the reactant supplement into the cell is not needed in these FCs. Furthermore, the paper is abundant, light-weight, recyclable, and low-cost material. Arun et al. (2014) developed a formic acid FC which had graphite electrodes stroked with pencil on the paper. The developed FC reached 32 mW cm^{-2} maximum power density (MPD) and 650 mA cm^{-2} maximum current density (MCD). Jung and Ahn (2020) investigated a paper-based vanadium FC consisted of graphene paste electrodes. The FC produced 15.09 mW cm^{-2} MPD and 30 mA cm^{-2} MCD. Shen et al. (2019) built up a paper-based FC that utilizes KCOOH as fuel and air as the oxidant. They tested some operating parameters influences such as textural properties of paper, fuel crossover, or cell resistance. The MPD of 7.10 mW cm^{-2} and the maximum OCV of 0.86 V were acquired from the FC. Zhang et al.

* **Corresponding Author**

*(celik@aksaray.edu.tr) ORCID ID 0000-0001-8978-4814

Cite this article

Celik M (2022). An experimental study of the performance of a low-cost paper-based membraneless direct hydrogen peroxide fuel cell. Turkish Journal of Engineering, 6(2), 161-165

Research Article / DOI: 10.31127/tuje.891626

Received: 05/03/2021; Accepted: 07/04/2021

(2012) demonstrated a biofuel cell on paper that produces energy from some beverages directly. The study showed that the cell could be used as a portable energy provider. Dector et al. (2017) reported paper-based FC that supplies energy for HIV test. The study is so important as it proved that the paper-based FCs could be applied to provide energy from human blood for point-of-care testing.

Studies that use hydrogen peroxide as the fuel or the oxidant inside the FC have been performed by Yang et al. (2019), Ehteshami et al. (2016), Shyu et al. (2012), Han et al. (2015), Shaegh et al. (2014) and Yang et al. (2012). A paper-based hydrogen peroxide FC that utilizes hydrogen peroxide as both the oxidant and the fuel was introduced by Yan et al. (2018). The FC achieved an MPD of 0.88 mW cm^{-2}. The study showed that the hydrogen peroxide can be useable as a sustainable energy carrier. Ehteshami et al. (2016) reported a paper-based FC prepared by micro-fabrication that utilizes hydrogen peroxide both the oxidant and the fuel. The prepared FC produced 0.81 mW cm^{-2} for aluminum anode whereas it produced 0.38 mW cm^{-2} power for nickel anode. By a closer look to the literature, there is a lack of study that emphasizes the economy for the paper-based hydrogen peroxide fuel cell.

Herein, a low-cost, Y-shaped, paper-based direct hydrogen peroxide fuel cell (DHPFC) which uses the hydrogen peroxide as fuel in the alkaline medium and the oxidant in the acidic medium was developed and its performance was investigated. In order to analyze the performance, the voltage-current measurements at different KOH concentrations (1, 3, 5, 7 mol lt^{-1}), different H_2O_2 concentrations (1, 2, 3 mol lt^{-1}) and different temperatures (20, 30, 40°C) were carried out. Moreover, to investigate the stability of the DHPFC chronoamperometry tests under two conditions (continuous flow and stopped flow) were examined.

2. METHOD

A DHPFC is one type of fuel cells that generates electricity from hydrogen peroxide directly. Due to the nature of the hydrogen peroxide, it can be used as the oxidant and the reductant at the same time in a fuel cell. In an acidic medium, the hydrogen peroxide plays a role as oxidant and generates electrons. In an alkaline medium, it serves as a reductant and accepts the electrons. (Hasegawa et al. 2004) Because of this behavior, the hydrogen peroxide becomes usable in the fuel cells. The reactions that occurred in a direct hydrogen peroxide fuel cell (DHPFC) concerning the anode and the cathode are as follows (Ye et al. 2015):

Anode: $H_2O_2 + 2OH^- \rightarrow O_2 + H_2O + 2e^-$	E: 0.146 V	(1)
Cathode: $H_2O_2 + 2H^+ + 2e^- \rightarrow 2H_2O$	E: 1.776 V	(2)
Overall: $2\ H_2O_2 \rightarrow O_2 + 2H_2O$	E: 1.630 V	(3)

With this knowledge, the alkaline medium was provided in the anode by making a solution of H_2O_2 and KOH. On the other hand, the acidic medium was provided in the cathode by making a solution of H_2O_2 and H_2SO_4. The main reason of being the high cost of an FC is the catalyst material and membrane costs. Here, an economic point of view was adopted. Therefore, the DHPFC was considered membraneless for the purpose of eluding membrane cost and energy requirement for pumping reactants. For a paper-based fuel cell, the working principle can be listed as follows:

i) Anode and cathode solutions transport into the fuel cell by capillary action through the flow channels.

ii) The solutions reach the mixing region. The anode and the cathode solution streams meet with each other firmly (diffusion zone in Fig. 1) since the flow of the solutions is in laminar because of the capillary action. Due to the stable streams of the solutions, the demand for separation of membrane disappears (Hasegawa et al. 2004).

iii) The electricity is produced by the anode and the cathode reactions via transporting the electrons from the anode to the cathode with an external circuit. In order to increase the reactions, the appropriate catalyst material is used for the anode and the cathode.

In this work, as the catalyst material, while cheap and abundant nickel was used for the anode electrode, carbon was used for the cathode electrode. All these attempts to reduce the cost will cause an adverse effect on the cell performance. For this reason, the developed DHPFC can be considered to provide power for low-power applications such as medical diagnostic sensors, wearable electronic devices, or drug pumps.

Whatman filter paper (Grade 3) was used as the platform for fluid streams by capillary action. As can be seen from the Fig.1, the paper was cut Y-shape which had 40 mm channel length and 10 mm channel width. Anode and cathode reactants reservoirs were attached to the flow channels. Anode solution (H_2O_2 + KOH) and cathode solution (H_2O_2 + H_2SO_4) were transported via capillary effect from the reservoirs to the channels first and then the mixture region which was 40 mm in length and 20 mm in width.

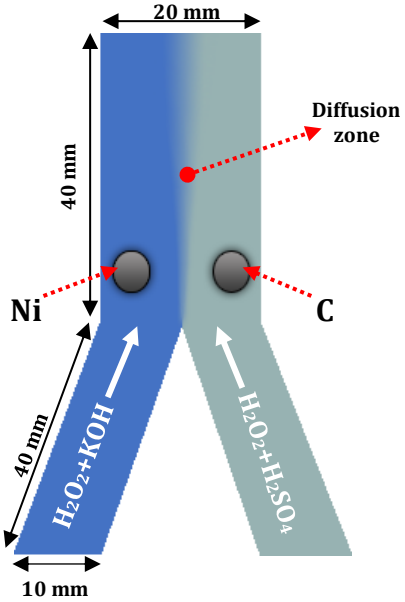

Figure 1. Schematic illustration of the DHPFC.

Catalyst inks were prepared with %4 sol. polyvinyl alcohol (PVA) (0.139 g), water (2.23g), and catalyst (0.947g). PVA was chosen as the catalyst binder instead of a highly expensive Nafion solution. Prepared catalyst

inks (~13 mg) were directly painted on the paper to form a 4 mm diameter circle. After painting and drying the catalyst inks, a steel mesh was attached to each electrode by alligator clips.

The voltage-current and chronoamperometry measurements were taken by using a DC electronic load (Maynuo M9711). Voltage-current measurements were taken with 3-second intervals at 15 steps from the open-circuit voltage (OCV) after the reactants reached the mixing region and OCV was stabilized. According to obtained results from the measurements, power density curves (marked with dashed lines with respect to right y-axis) and polarization curves (marked with solid lines with respect to left y-axis) were created and plotted in the same graph. Constant voltage measurements were taken under two different conditions. Firstly, the current density was measured at 0.4 V constant voltage under continuous flow of reactants. After that, the reactants were removed from the DHPFC and the current density was measured at the same constant voltage value. The experiments were carried out at 20°C unless otherwise stated in the manuscript. In order to make sure the experiment results were accurate; all the experiments were carried out at least 3 times.

3. RESULTS

3.1. Effect of KOH Concentration

In the anode, the OH^- ions in the KOH react with the H_2O_2 with a stoichiometric ratio which dissociates the H_2O_2 and exposes electrons, as given in Eq.1. Besides the other significant role of the KOH in the DHPFC, it serves as the supporting electrolyte by carrying the H_2O_2 into the electrochemical active site. Nevertheless, the KOH concentration should be optimized in the anode solution. At the excess concentrations, the KOH affects the cell performance negatively. Because the viscosity of the anode solution rises at the KOH concentrations (Guo et al. 2016), and the transportation of the H_2O_2 can be limited by the blockage of the OH^- ions in the active sites (Rathoure and Pramanik, 2016). With this consideration, the H_2O_2 concentration was fixed at 2 mol lt^{-1} in anode solution, whereas the KOH concentration was varied from 1 to 7 mol lt^{-1}. As can be seen from the Fig. 2, the performance of the DHPFC was increased by the KOH concentration increment up to 5 mol lt^{-1}. When the concentration of KOH at 7 mol lt^{-1}, the performance significantly dropped. As discussed, the reason for the performance drop was the diffusion losses. The maximum OCV was 0.84 V and the MPD was 5.3 mW cm^{-2} at 5 mol lt^{-1} KOH concentration. The lowest current density (LCD) of 6.56 mA cm^{-2} at 1 mol lt^{-1} KOH and the highest current density (HCD) of 27.36 mA cm^{-2} were found at 5 mol lt^{-1} KOH.

3.2. Effect of H_2O_2 Concentration

Fig. 3 shows the impact of H_2O_2 in the anode solution on the DHPFC performance. The KOH concentration in the anode solution was kept constant at 5 mol lt^{-1} and the H_2O_2 concentration changed from 1 to 3 mol lt^{-1}. It was found that from the experiments, the MPD was 5.31 mW cm^{-2} and the OCV was 0.84 V when the H_2O_2 concentration was 2 mol lt^{-1}. The LCD of 18.16 mA cm^{-2} at 1 mol lt^{-1} and the HCD of 27.36 mA cm^{-2} at 2 mol lt^{-1} were measured. It was observed that the OCV was not strongly dependent on the H_2O_2 concentration in the anode solution. The DHPFC performance increased by increasing the concentration of H_2O_2 from 1 to 2 mol lt^{-1}. After the 2 mol lt^{-1} H_2O_2 concentration, the DHPFC performance was affected negatively. This adverse effect in the performance may be related to the limitation of H_2O_2 transport to the electrocatalytic active site by O_2 molecules generated from the H_2O_2 dissociation (Shyu et al. 2012, Yang et al. 2012), as expressed in Eq.2. The MPDs were obtained as 2.82 mW cm^{-2} at 1 mol lt^{-1} H_2O_2, 5.31 mW cm^{-2} at 2 mol lt^{-1} H_2O_2 and 3.06 mW cm^{-2} at 3 mol lt^{-1} H_2O_2, respectively.

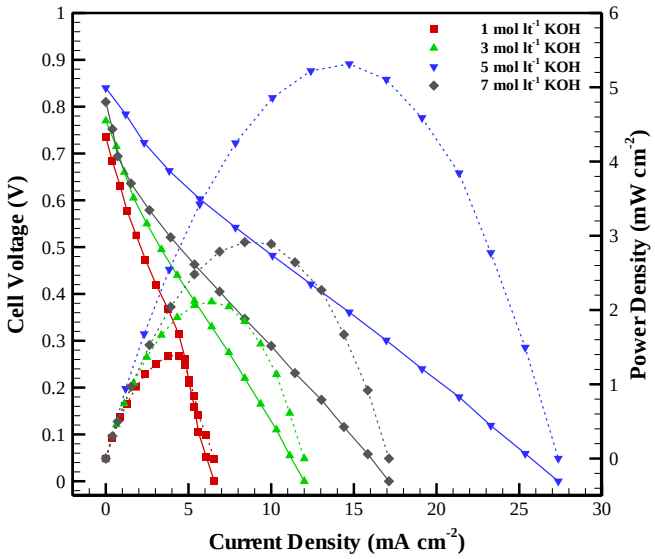

Figure 2. The impact of KOH concentration on the DHPFC performance

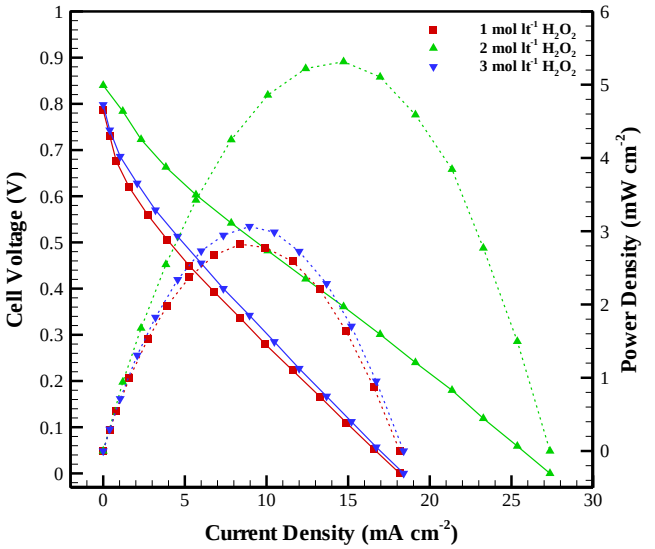

Figure 3. The influence of H_2O_2 concentration on the DHPFC performance

3.3. Effect of Operating Temperature

Fig 4. depicts the polarization curve according to operating temperature. The operating temperature was changed from 20°C to 40°C in order to determine the

effect of the temperature on the DHPFC performance. The OCVs were 0.84 V, 0.86 V and 0.87 V at 20°C, 30°C and 40°C, respectively. As can be seen from the Fig. 4, especially at the ohmic and diffusion overvoltage regions, graphs were escalated with the operating temperature. The reason for this is the electrical conductivity increases as the temperature rises which results the ohmic overpotential drop. Moreover, the diffusion overvoltage occurs when the reactants yielded at the electrochemical active sites. When the temperature rises, the diffusion of the reactants increases. So, the diffusion losses reduce. Consequently, these declines of the ohmic and the diffusion overpotentials conduce to an increase of the DHPFC performance. The experimental results can be given as the MPD was 5.29 mW cm^{-2} at 20°C while it was 6.79 mW cm^{-2} at 40°C. While the LCD was 27.36 mA cm^{-2} at 20°C, the HCD was 33.84 mA cm^{-2} at 40°C.

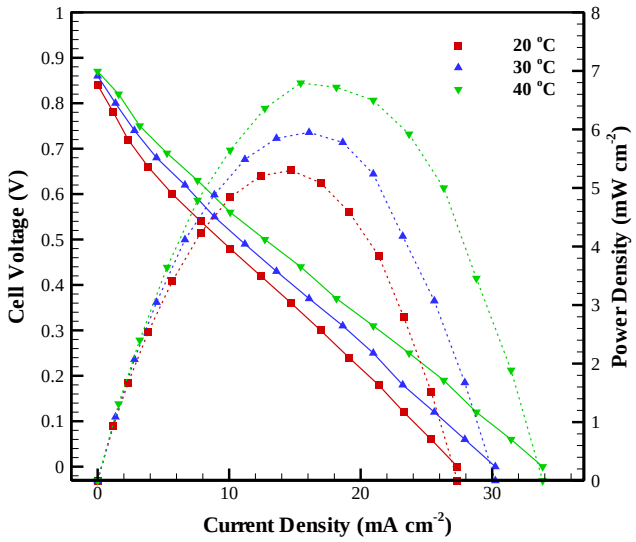

Figure 4. The impact of temperature on the DHPFC performance

3.4. Chronoamperometry Tests

Chronoamperometry tests were carried out to analyze the stability of the developed DHPFC. Tests were examined in two cases: 1) continuous flow condition, 2) stopped flow condition.

Continuous flow condition experiments were carried out when the reactants reached the mixing region, the DHPFC completely saturated with reactants and the OCV was stabilized. While the anode solution was 2 mol lt^{-1} H_2O_2 + 5 mol lt^{-1} KOH, the cathode solution was 2 mol lt^{-1} H_2O_2 + 2 mol lt^{-1} H_2SO_4. The voltage of the DHPFC was fixed at 0.4 V during the experiment. The experiments were carried out under these conditions for 50 min. (3000 seconds).

As can be seen from the Fig. 5, under continuous flow condition, the current density was stabilized near 3.12 mA cm^{-2} of current density. In addition, 1.25 mW cm^{-2} of power density was acquired. Stopped flow condition experiments were carried out by detaching the reactants reservoir from the DHPFC flow channels. The cell voltage was the same as the continuous flow condition. Under the stopped flow condition, the current density dropped from 8.08 to 0.64 mA cm^{-2} until the end of 50 min. After 91 minutes, the reactants in the electrochemical active site were depleted. As a result of this, the current density acquired from the DHPFC dropped to zero.

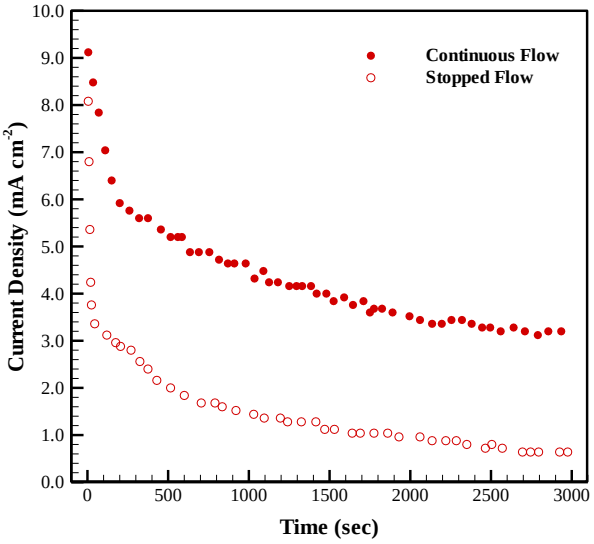

Figure 5. Chronoamperometry tests

4. CONCLUSION

A paper-based membraneless DHPFC was developed and tested in this study. In order to develop a low-cost FC, the nickel for the anode and the carbon powder for the cathode were chosen as catalysts, respectively. As the catalyst binder, PVA was used instead of a highly expensive Nafion binder. The DHPFC was tested for different anode solution compositions and different temperatures. Furthermore, to specify the stability of the developed DHPFC, chronoamperometry tests were examined. The followings can be concluded from the experiments:

- Among all the experiments, the MPD of 6.79 mW cm^{-2} and the maximum OCV of 0.87 V at 40°C is obtained when the anode solution consisted 2 mol lt^{-1} H_2O_2 + 5 mol lt^{-1} KOH with the cathode solution consisted 2 mol lt^{-1} H_2O_2+ 2 mol lt^{-1} H_2SO_4. With the same anode solution and cathode solution components, the DHPFC produces a power density of 5.3 mW cm^{-2} and reached 0.84 V at 20°C.
- The developed DHPFC is tested for stability under stopped and continuous flow conditions. It is seen that if the reactants flowed constantly into the DHPFC, a 3.12 mA cm^{-2} current density and 1.25 mW cm^{-2} power density were obtained.
- When the reactant flow to the cell was stopped, the DHPFC produces energy (although it diminishes) for 91 min.

Consequently, the findings of this study bring out that the paper-based DHPFC could be built at a low-cost and it could be used to provide power for small power requirements.

Conflicts of interest

The authors declare no conflicts of interest.

REFERENCES

Arun R K, Halder S, Chanda N & Chakraborty S (2014). A paper based self-pumping and self-breathing fuel cell

using pencil stroked graphite electrodes. Lab on a Chip, 14(10), 1661-1664.

Bandodkar A J, Jia W, Wang J (2015). Tattoo-Based Wearable Electrochemical Devices: A Review. Electroanalysis. 27, 562–572.

Chino I, Muneeb O, Do E, Ho V & Haan J L (2018). A paper microfluidic fuel cell powered by urea. Journal of Power Sources, 396, 710-714.

Copenhaver T S, Purohit K H, Domalaon K, Pham L, Burgess B J, Manorothkul N, ... & Haan J L (2015). A microfluidic direct formate fuel cell on paper. Electrophoresis, 36(16), 1825-1829.

Dector A, Galindo-De-La-Rosa J, Amaya-Cruz D M, Ortíz-Verdín A, Guerra-Balcázar M, Olivares-Ramírez J M, ... & Ledesma-García J (2017). Towards autonomous lateral flow assays: Paper-based microfluidic fuel cell inside an HIV-test using a blood sample as fuel. International Journal of Hydrogen Energy, 42(46), 27979-27986.

Ehteshami S M M, Asadnia M, Tan S N & Chan S H (2016). Paper-based membraneless hydrogen peroxide fuel cell prepared by micro-fabrication. Journal of Power Sources, 301, 392-395.

Esquivel J P, Del Campo F J, De La Fuente J G, Rojas S & Sabate N (2014). Microfluidic fuel cells on paper: meeting the power needs of next generation lateral flow devices. Energy & Environmental Science, 7(5), 1744-1749.

González-Guerrero M J, Del Campo F J, Esquivel J P, Leech D & Sabaté N (2017). based microfluidic biofuel cell operating under glucose concentrations within physiological range. Biosensors and Bioelectronics, 90, 475-480.

Guo F, Cao D, Du M, Ye K, Wang G, Zhang W, ... & Cheng K (2016). Enhancement of direct urea-hydrogen peroxide fuel cell performance by three-dimensional porous nickel-cobalt anode. Journal of Power Sources, 307, 697-704.

Hasegawa S, Shimotani K, Kishi K & Watanabe H (2004). Electricity generation from decomposition of hydrogen peroxide. Electrochemical and Solid State Letters, 8(2), A119.

Han L, Guo S, Wang P & Dong S (2015). Light-Driven, Membraneless, Hydrogen Peroxide Based Fuel Cells. Advanced Energy Materials, 5(2), 1400424.

Jung D G & Ahn Y (2020). Microfabricated paper-based vanadium co-laminar flow fuel cell. Journal of Power Sources, 451, 227801.

Lu X, Yu M, Wang G, Tong Y & Li Y (2014). Flexible solid-state supercapacitors: design, fabrication and applications. Energy & Environmental Science, 7(7), 2160-2181.

Rathoure A K & Pramanik H (2016). Electrooxidation study of methanol using H2O2 and air as mixed oxidant at cathode in air breathing microfluidic fuel cell. International Journal of Hydrogen Energy, 41(34), 15287-15294.

Shaegh S A M, Ehteshami S M M, Chan S H, Nguyen N T & Tan S N (2014). Membraneless hydrogen peroxide micro semi-fuel cell for portable applications. RSC advances, 4(70), 37284-37287.

Shen L L, Zhang G R, Venter T, Biesalski M & Etzold B J (2019). Towards best practices for improving paper-based microfluidic fuel cells. Electrochimica Acta, 298, 389-399.

Shitanda I, Nohara S, Hoshi Y, Itagaki M & Tsujimura S (2017). A screen-printed circular-type paper-based glucose/O2 biofuel cell. Journal of Power Sources, 360, 516-519.

Shyu J C, Huang C L, Sheu T S & Ay H (2012). Experimental study of direct hydrogen peroxide microfluidic fuel cells. Micro & Nano Letters, 7(8), 740-743.

Valdés-Ramírez G, Li Y C, Kim J, Jia W, Bandodkar A J, Nuñez-Flores R, ... & Wang J (2014). Microneedle-based self-powered glucose sensor. Electrochemistry Communications, 47, 58-62.

Yamada Y, Fukunishi Y, Yamazaki S I & Fukuzumi S (2010). Hydrogen peroxide as sustainable fuel: electrocatalysts for production with a solar cell and decomposition with a fuel cell. Chemical communications, 46(39), 7334-7336.

Yamazaki S I, Siroma Z, Senoh H, Ioroi T, Fujiwara N & Yasuda K (2008). A fuel cell with selective electrocatalysts using hydrogen peroxide as both an electron acceptor and a fuel. Journal of Power Sources, 178(1), 20-25.

Yan X, Xu A, Zeng L, Gao P & Zhao T (2018). A paper-based microfluidic fuel cell with hydrogen peroxide as fuel and oxidant. Energy Technology, 6(1), 140-143.

Yang F, Cheng K, Mo Y, Yu L, Yin J, Wang G & Cao D (2012). Direct peroxide–peroxide fuel cell–Part 1: The anode and cathode catalyst of carbon fiber cloth supported dendritic Pd. Journal of Power Sources, 217, 562-568.

Yang F, Cheng K, Liu X, Chang S, Yin J, Du C, ... & Cao D (2012). Direct peroxide–peroxide fuel cell–Part 2: Effects of conditions on the performance. Journal of Power Sources, 217, 569-573.

Yang Y, Xue Y, Zhang H & Chang H (2019). Flexible H2O2 microfluidic fuel cell using graphene/Prussian blue catalyst for high performance. Chemical Engineering Journal, 369, 813-817.

Ye K, Guo F, Gao Y, Zhang D, Cheng K, Zhang W, ... & Cao D (2015). Three-dimensional carbon-and binder-free nickel nanowire arrays as a high-performance and low-cost anode for direct hydrogen peroxide fuel cell. Journal of Power Sources, 300, 147-156.

Zhang L, Zhou M, Wen D, Bai L, Lou B & Dong S (2012). Small-size biofuel cell on paper. Biosensors and Bioelectronics, 35(1), 155-159.

Zhang Q, Yue F, Xu L, Yao C, Priestley R D & Hou S (2019). Paper based porous graphene/single-walled carbon nanotubes supported Pt nanoparticles as freestanding catalyst for electro-oxidation of methanol. Applied Catalysis B: Environmental, 257, 117886.

Turkish Journal of Engineering

https://dergipark.org.tr/en/pub/tuje

e-ISSN 2587-1366

Design and implementation of a cost effective vacuum cleaner robot

Anıl Eren[1], Hatice Doğan *[1]

[1]Dokuz Eylul U*niversity, Engineering Faculty, Electrical and Electronics Engineering Department, Izmir, Turkey*

Keywords
Vacuum Cleaner Robot
Robot Navigation
Robot Control
Robot Sensing System

ABSTRACT

Robot vacuum cleaners are among the first service robots to enter daily life. However, robot vacuum cleaners are currently inaccessible to many due to their high cost. In order for these robots to become widespread, they must be cheap and functional. In this study, the design and production of a low-cost, high-performance vacuum cleaner robot that can be controlled by smartphones is presented. This autonomous robot moves around the obstacles, vacuums the dust from the floor, performs basic navigation and also it is manually controllable. Designing of a vacuum cleaner robot is divided into three parts which are the mechanical, electrical and software design. In the mechanical design; the robot chassis and cleaning system have been designed and realized. In the electrical design; the electrical components such as batteries, motors, drivers, sensors and microcontroller have been selected and the power system has been designed by considering electrical requirements. In the software design; an easy to use Android application for remote control has been created, autonomous algorithms such as random walk and snake algorithms have been designed. Remote controlling of the robot has been provided by using Bluetooth connection between the Raspberry Pi and Android smartphone.

1. INTRODUCTION

Robot vacuum cleaners are one of the best examples of robotic technology that can be used in homes. The vacuum cleaner robot is a device designed to vacuum all dirt on flat floors without human intervention. In recent years, there have been many advances in vacuum cleaner robot technology to reduce the cost of robots and increase their capabilities. Nowadays, they have gained features such as being autonomous, remote-controlled, lightweight, small space footprint and more.

The vacuum cleaner robot collects external data from sensors mounted on it and uses this data to make various movements according to its navigation algorithm. While navigating and cleaning, the robot avoids obstacles, walls or stairs which are detected by the sensors (Asafa et al. 2018). Simpler vacuum cleaner robots on the market just bump into obstacles, walls and after that randomly change their position. The more complex ones use infrared, ultrasonic, optical and laser sensors to detect and avoid obstacles, walls and stairs. Their navigation models are more accurate due to their ability to create and navigate maps using a camera or laser scanner.

In the literature different types of cleaning robots have been designed (Ulrich et al. 1997; Oh et al. 2002; Dai and Chen 2007; Gao et al. 2007; Liu et al. 2011; Prabakaran et al. 2017; Adithya et al. 2019). The first vacuum cleaner robot called “Trilobite” was developed by James Dizon and manufactured in 1996 by Swedish household company Electrolux. Trilobite is complex and expensive. It creates a map of the room while cleaning and recharges automatically when its battery is low. It uses ultrasonic sensors to avoid obstacles and walls (Maruri et al. 2006). British technology company Dyson designed a vacuum cleaner robot called “DC06” in 2001; but did not go into the mass production because it was too expensive. iRobot company, founded by three robotists from the Massachusetts Institute of Technology, launched the robotic vacuum cleaner robot "Roomba, floor vacuuming robot" in 2002. This robot changes its direction when it counters wall or an object and it could detect dirty places on the floor. Also, the robot could avoid the stairs in order to prevent falling down. The main difference between the vacuum cleaner robots and conventional ones is the autonomy, which means the robots do the cleaning job by moving around without any human intervention. Also, vacuum cleaner

* **Corresponding Author**

(anilerenn@gmail.com) ORCID ID 0000-0001-7340-8590
*(hatice.dogan@deu.edu.tr) ORCID ID 0000-0003-0420-592X

Cite this article

Eren A & Dogan H (2022). Design and implementation of a cost effective vacuum cleaner robot. Turkish Journal of Engineering, 6(2), 166-177

Research Article / DOI: 10.31127/tuje.830282

Received: 23/11/2020; Accepted: 27/04/2021

robots are less noisy and very small in dimension compared to the conventional ones.

The main advantages and disadvantages of using a vacuum cleaner robot can be seen in Table 1.

Table 1. Advantages and disadvantages of vacuum cleaner robots

Advantages	Disadvantages
Save time and energy	Some models can be costly
Lesser noise than standard cleaners	Risk of getting stuck
Scheduling and tracking capabilities	Risk of flipped over
Cleaning by itself	Frequent dust bin changing required
Different cleaning modes	Long cleaning times
Can be remote controlled	Battery life
Lightweight and compact	Ineffective on stairs and thick surfaces
Cordless design	
Automatic Recharge & Docking	
Under furniture cleaning	
Good for people with limited mobility	
Some models have intelligent mapping	
Some models can detect dirt	

In summary, the vacuum cleaner robots do much more than what an ordinary vacuum cleaner offers without requiring human intervention. For widespread use of these robots, they must be functional, cost-effective, and controllable with common devices such as smartphones.

The aim of this study is to design and implement a low-cost, high-performance robot vacuum cleaner that can be controlled by android phones with inexpensive and easily accessible mechanical and electronic components. Most of the low-cost vacuum cleaner robots on the market use only basic switches as sensors for detecting obstacles. The designed robot uses ultrasonic and infrared sensors that enable the robot to detect obstacles before they hit them. In addition, it has a manual control feature and two different autonomous algorithms that are not found in many low-cost vacuum cleaner robots.

2. METHOD

Vacuum cleaner design is divided into three parts: mechanical, electrical and software design.

2.1. Mechanical Design

Mechanical design of the vacuum cleaner robot can be divided into 4 categories. In these categories; how the shape of the robot affects the navigation and cleaning, which driving mechanism used on the robot is suitable, what main materials that can be used as robot chassis and cleaning system design are explained.

2.1.1. The shape of robot body

There are different shapes of vacuum cleaner robots in the market, such as circular, D-shaped and square. If different models of vacuum cleaner robots in the market are examined, it can be appeared that there are few square-shaped vacuum cleaner robots than other circular and D-shaped robots. When different-shaped robots are compared functionally, square vacuum cleaner robots' corners cause them to get stuck in the gaps between obstacles. If these robots get stuck, human intervention is required, which makes the autonomous feature ineffective. Fewer corners the robot has, the lower probability of stuck (Stubbs 2019). D-shaped robots have less stuck probability than the square-shaped robot and the circular-shaped have the least stuck probability than the others. The main purpose of the D-shaped design is to enable the robotic cleaner to clean wall edges and corners more effectively. Circular-shaped robots are less effective about cleaning these wall edges and corners (Stubbs 2019). In order to eliminate this weakness, spinning side cleaning brushes are included. The size of brushes is another factor for the amount of space that the robot can clean in one go. The shape of a vacuum cleaner robot is also an important factor that how much damages it can cause when it collides with other objects. Circular vacuum cleaners have a lower risk to cause damage on the surface of any object they collide due to their soft round edges (Radu 2015). Aesthetics is another factor for vacuum cleaner robots that their shapes affect the sales in the market. Today's buyers largely prefer smooth rounded curves that are more aesthetic in robots (Stubbs 2019).

The shape of the vacuum cleaner robot is selected as circular because of lower risk of getting stuck which ensures the autonomy. Since the corner cleaning performance of circular robots is low, a brush is attached to it to increase performance. One brush is selected instead of two brushes to increase the operating time of the robot since two brushes would have more power consumption than the one brush.

2.1.2. Driving mechanism

Driving mechanism determines how a mobile robot moves from one place to another. There are different types of driving mechanisms that are used on mobile robots such as differential drive, skid steering, synchronous drive, Ackermann steering etc.

Differential drive is the most popular and widely used driving mechanism for mobile robots because it is the simplest and easiest to implement (Dudek and Jenkin 2010; Roh et al. 2013). Also it provides arbitrary motion and in-place rotation (zero radius), however its main disadvantage is the difficulty to maintain straight line motion due to independent motors. To ensure the straight line motion, identical motors should be used and the center of mass should be in the middle of the robot. As the motors deform after a while due to the weight of the robot, their identicality will deteriorate. In order to guarantee straight line motion, open or closed loop control system must be designed. If the system is

open-loop, calibration will be needed to make the robot straight line motion.

As shown in Fig. 1, a differential drive robot has two individually driven wheels mounted in one line which are opposite to each other. Also a castor wheel can be added to balance the robot. Each wheel is controlled by a different motor to make different movements such as forward, reverse, rotating left or right. The speeds of individual motors determine the direction of the motion.

Figure 1. Differential drive robot (Dave 2020)

There are three different cases for the motion of the robot according to the individual motors' speeds (LaValle 2006). In case 1; if the motors have the same speed and rotating at the same direction, the amount of torque produced on both wheels are the same resulting the robot moves forward or backward. In case 2; if the motors have the same speed and rotating at opposite directions, torques are generated on both wheels which are equal in magnitude and opposite in direction resulting the robot rotates around itself left or right. In this case, the center of rotation is equidistant between the motors. In case 3, if the motors rotating at the same direction but have different speeds, the robot starts turning towards to left or right depending the motor that have higher speed. For example, if the left motor has higher speed, then the robot turning towards to right or vice-versa. The motion of the robot depending the individual motors' speed and direction is given in the Fig. 2.

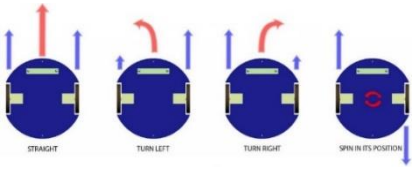

Figure 2. Differential drive robot motions (Ottoviani 2020)

2.1.3. Material and body size

Material is important factor for vacuum cleaner robot chassis that can carry the whole robot components without any deformation.

Base and ceiling of the robot chassis are made of plexiglass because of its durability. PVC foam is used for dust bin of the cleaning system. The diameter of circular base and ceil components of the robot chassis is selected as 33 cm in order to have enough space for electrical components and cleaning system. The ceiling part of the robot has been produced by using the same dimensions as the body plexiglass and it is supported by small plexiglass columns.

2.1.4. Cleaning system design

Vacuum cleaner robots have a cleaning system consist of vacuum motor, dust bin and brush. The vacuum motor cleans the dirt from the floor where the robot moves. Dirt taken from the floor goes to the dust container placed inside the robot. The dust container can be removed easily after it is full. The brush sweeps the floor and pushes the dirt into the area affected by the vacuum motor so the dirt can be vacuumed easily. Since vacuum cleaner robot is circular, the brush also helps the robot sweep dirt near walls or obstacles. In this way, the brush increases the cleaning performance of vacuum cleaner robots. As a vacuum motor, a DC blower can be used.

Figure 3. DC Blower (Blower Documentation, 2020)

While the circular side of the DC blower in Fig. 3 vacuums (sucks) the air, the rectangular side blows to the outside. The material used for dust bin is selected as PVC foam sheet. The dust bin is designed to cover the circular side of the blower completely to increase the air pressure that affects the cleaning performance. It is placed on the middle of the circular body. A plug-in plastic is added to the end of the dust bin space to reduce the distance between the floor and the robot, which improves cleaning performance. The specifications of the selected 12V 1A DC blower are:

- Speed: 3100 RPM
- Air Flow: 36.2 CFM
- Air Pressure (in Water): 1.35 Pa

2.2. Electronic Hardware Design

Electronic hardware design consists of electronic components of the vacuum cleaner robot. It can be divided into 4 categories; motors and motor drivers, sensors, microcontroller, power and charging system.

2.2.1 Motors and motor drivers

Different types of electric motors such as DC (Direct Current) motors, AC (Alternating Current) motors, servo motors and stepper motors can be used in robotic applications. For vacuum cleaner robots, DC motors can be used for the movement of the robot, vacuuming, and brushes.

Motors have two important variables that must be considered depending on the application. These variables are the maximum speed and the torque. The speed and the torque of the motor are inversely proportional. Generally, DC motors have high speeds and low torque values. DC motors used on the vacuum cleaner robots must have enough torque to carry the weight of the robot and provide movement.

Motor drivers are used to control the motors in terms of speed, rotation direction, angle etc. DC motor drivers have H-bridge ICs which consist of MOSFETs or BJTs acting as switches. Simple H-Bridge circuit with a DC motor is given in Fig. 4. In this figure, S1, S2, S3 and S4 are the switches. Different states of these switches determine the direction of the DC motor either clockwise or anti-clockwise. They can also be used to brake the motor. In Fig. 4, assuming that the direction of rotation of the DC motor is clockwise when the current flows from the left to the right, the operations of the motor for some different states of the switches are given in Table 2. Switch state "1" meaning the switch is closed (ON) and switch state "0" meaning the switch is opened (OFF).

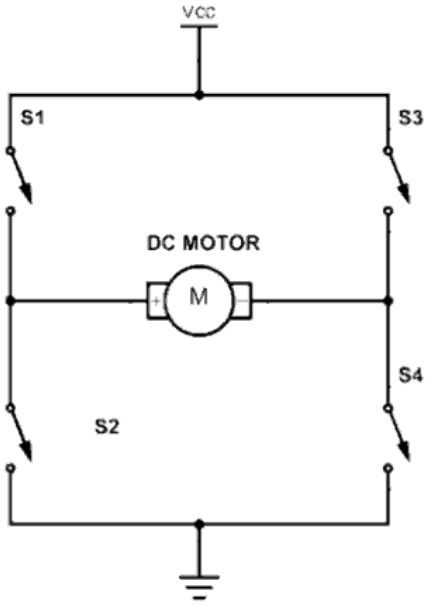

Figure 4. Simple H-Bridge

DC motors attached to wheels have been chosen in gear and micro size to provide sufficient torque for movement and take up small space on the robot body. High torque is required for the robot to move and carry its weight continuously. The voltage for geared DC motors has been selected as 6 V because if the required torque is provided with low voltage, the power consumption will be low. Motor speed has been chosen as 60 RPM that is enough for a vacuum cleaner robot. Also 3-6 V DC motor with gearbox is used for the rotation of the brush.

Table 2. H-bridge motor operations

S1	S2	S3	S4	Operation
1	0	0	1	Clockwise Direction
0	1	1	0	Anti-Clockwise Direction
0	1	0	1	Braking Mode

The motor driver module "L298N" is used to control DC motors. This motor driver has dual H-bridge inside and it can control speed and direction at the same time individually with PWM.

2.2.2 Sensors

Sensors are the most important and essential electrical components of vacuum cleaner robots because robots acquire information about their environment through sensors. They are indispensable for accurate navigation.

The most commonly used sensors are the infrared and ultrasonic sensors for the detection of walls, obstacles or cliffs that are close to robot. Both of the ultrasonic and infrared sensors have the transmitter and receiver parts. The transmitter emits a signal and if there is an object in the way of the signal, the signal reflected back by hitting the object. This signal is detected by the receiver. While the distance is measured according to the intensity of the reflected signal in the infrared sensor, it is measured according to the reflection time in the ultrasonic sensor.

Ultrasonic and infrared sensors are used together on the vacuum cleaner robot. Since the performance of the infrared sensors depends on the lighting conditions and their field of view is very low, ultrasonic sensors have been chosen as the main distance measurement sensors. The infrared sensors are the auxiliary sensors for the distance measurement and they are used for the detection of low density objects. Vacuum cleaner robots in the market have lots of infrared sensors because field of view of one infrared sensor is very low.

The design includes 3 ultrasonic sensors and 2 digital infrared sensors placed 60 degrees apart in front of the vacuum cleaner robot. Ultrasonic sensors are placed at most front-left, most front-right and at the front. Infrared sensors are placed between these ultrasonic sensors. In addition, an ultrasonic sensor is placed under the front of the robot as a cliff sensor to prevent falling from the stairs. This sensor let the vacuum cleaner robot know when it's near a "cliff," such as stairs or a balcony. Placement of the sensors is given in Fig. 5.

The ultrasonic sensor model selected is HC-SR04P with operating voltage between 3V and 5V. The detection range of this ultrasonic sensor is 2 cm to 400 cm. The KY-032 model is used for the infrared sensor. The detection range of this infrared sensor is maximum 10 cm and is sufficient for vacuum cleaner robots. Sensing distance can be adjusted by the potentiometer on the sensor board.

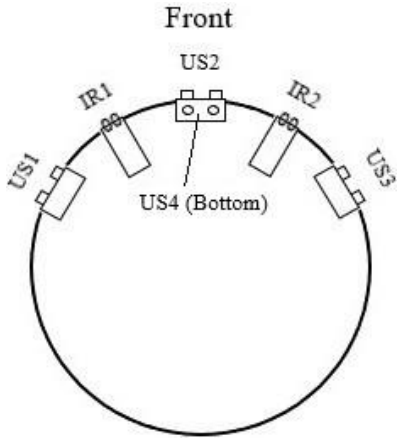

Figure 5. Sensor placement (robot top view)

2.2.3 Microcontroller

The microcontroller is the brain of the vacuum cleaner robot. It controls the robot by sending signals to the motor drivers. These control signals are generated based on the sensor data and the navigation algorithm. There are different types of microcontrollers such as Arduino, Raspberry Pi, BeagleBone. Raspberry Pi and BeagleBone are small computers running Linux OS inside. These microcontrollers can be programmed by using C, C ++ or Python languages.

To choose the microcontroller model; first, the total pin numbers of the sensors and motor drivers are considered. In the design, 4 HC-SR04P ultrasonic sensors, 2 KY-032 infrared sensors and 2 L298N motor drivers are selected. If the supply (Vcc) and ground (GND) pins are not considered, totaly 17 GPIO pins are needed. The Raspberry Pi 3B+ provides this total number of GPIO pins. It is also inexpensive compared to other microcontrollers.

All pins of the Raspberry Pi are digital. It has Wi-Fi and Bluetooth modules that will be useful to control the vacuum cleaner robot remotely. The CPU power and the capacity of RAM are sufficient for the vacuum cleaner robot.

2.2.4 Power and charging system design

Batteries provide energy to keep vacuum cleaner robots running for a specified time. This time should be high enough for the robot to clean a certain area before the battery runs out. These batteries must meet the minimum requirements such as operating voltage and current to supply the electrical components used. The weight of the batteries is also another important factor to consider. Batteries should be as light as possible to reduce the weight of the robot. If the weight is increased, the power consumption will increase and the batteries will drain faster.

Li-ion (lithium ion) batteries are chosen as the main energy source of the robot. Li-ion batteries have high energy, high capacity and low maintenance characteristics. They can be recharged in a short time and are lightweight. However, Li-Ion batteries need protection circuit against over charge and over discharge (Elias et. al 2003; Chen et. al 2019).

Since one Li-on battery is not enough for the robot, 4 li-on batteries that connected series (4S1P) are used. If the nominal voltage of one battery is used (INR18650-30Q Li-on Battery Datasheet, 2014), the maximum voltage can be calculated as

$$Maximum\ Voltage = 3.61 * 4 = 14.44\ V \quad (1)$$

Since the batteries are connected series, the current and capacity are not changed, only the total voltage is increased.

For the 4S1P battery system, the 4S1P BMS (Battery Management System) charging and protection circuit is chosen to prevent the batteries from overcharging and deep discharging because overcharging and deep discharging may damage li-on batteries. The BMS circuit also provides balanced charging and discharging for 4 batteries, which means that 4 batteries are simultaneously charged and discharged.

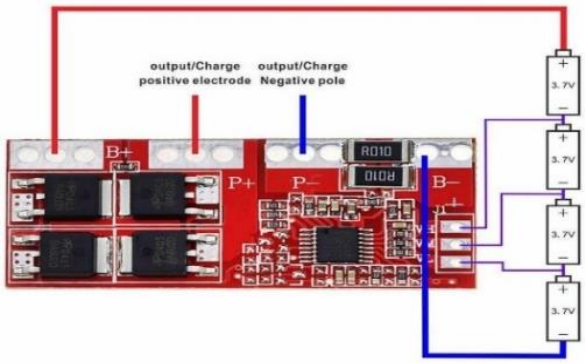

Figure 6. YH11047A4S1P (BMS protection board, 2020)

In the BMS protection board given in the Fig. 6, the anode and cathode of every battery is connected to the board to provide balanced charge and discharge. The batteries can be charged by connecting the charger to the output of the board. Since 4 li-on batteries have total voltage 14.44 V, 15 V charging adapter can be used to charge the batteries.

The total voltage of the batteries connected series cannot be used directly. This voltage is high for the other components such as motors, motor drivers and Raspberry Pi so that this voltage must be reduced to appropriate levels. For this purpose, DC – DC step-down voltage converters can be used.

2.3 Component Placement and Electrical System Layout

The component placement of the prototype vacuum cleaner robot is given in Fig. 7 and the layout of the electrical system is given in Fig. 9. The components in the figure marked with letters are:

A: Raspberry Pi 3B+ Microcontroller
B: Vacuum Motor (12 V 1 A DC Blower) And Dust Bin
C: 18650 4S1P Li-on Battery
D: YH11047A 4S1P BMS Protection Board
E: LM2596-ADJ DC-DC Step Down Voltage Regulator 3A
F: 6 V 60 RPM Micro DC Reducer Motor
G: L298N Dual Channel Motor Driver
H: HC-SR04P Ultrasonic Sensor
I: KY-032 Digital Infrared Sensor
J: 3-6 V DC Geared Motor For Brush

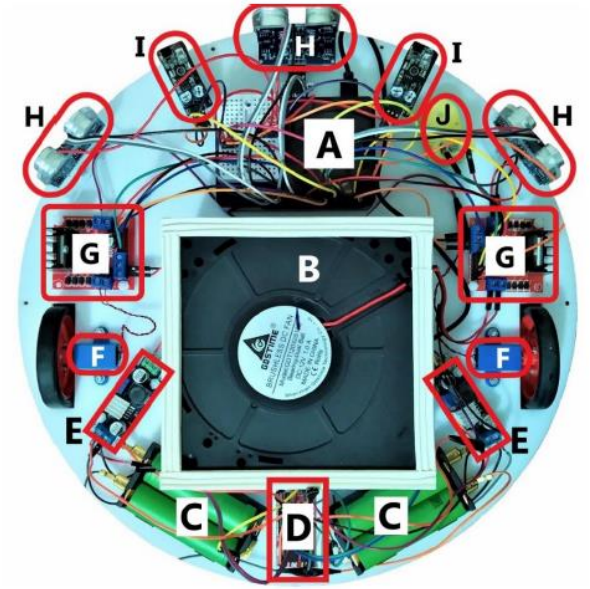

Figure 7. Robot top view and component placement

2.4 Software Design

The robot needs remote control software to be controlled by a smartphone and navigation software to prevent it from hitting the obstacles it encounters and to clean a room efficiently.

2.4.1 Remote control software

In order to control the robot by using Android smartphone, an Android application is needed. With this remote control application, the movement of the robot, the speed of the brush and the vacuum motor can be controlled, and the navigation algorithm can be selected. This Android application have been created by using MIT App Inventor.

MIT App Inventor is a programming environment that is used for building functional applications for Android and iOS. It has a GUI (graphical user interface) to develop applications by using visual functional blocks. Simple and complex applications can be created in a short time. Bluetooth communication has been used to send commands from the smartphone to the Raspberry Pi. The GUI of the developed application is given in the Fig. 8.

In Fig. 8a; buttons, switches and slider are invisible. After the Bluetooth image has been clicked, the Bluetooth connection selection page appears. In this page, the MAC address and the name of the Raspberry Pi mounted on the cleaning robot can be seen. After selecting the Raspberry Pi and the Bluetooth connection is made, the screen given in the Fig. 8b appears. The buttons “Forward”, “Left”, “Right” and “Backward” are used to move the robot manually. Vacuum motor and the brush motor can be activated or deactivated by using ON/OFF switch on the GUI.

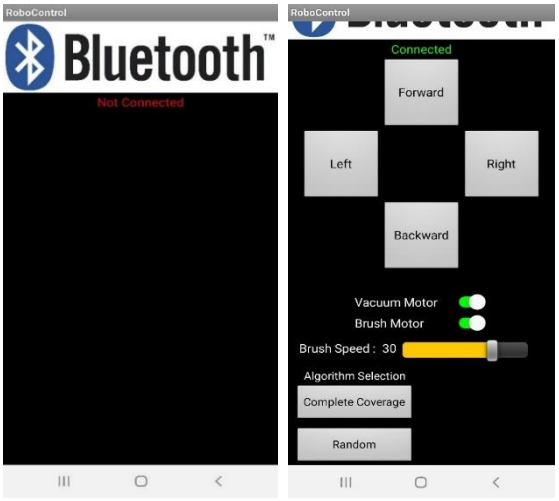

(a) (b)

Figure 8. Android application (a) without Bluetooth connection, (b) with Bluetooth connection

The brush speed slider only visible if the brush motor is activated. This slider can be used to adjust the speed of the rotating brush. The speed of the robot can be adjusted by adding a slider to the application since the motor speed can be controlled by PWM signals. Also the buttons under the algorithm selection are used to change current autonomous algorithm. Robot operates in autonomous mode without Bluetooth connection. When the Bluetooth connection is made, the robot stops and waits for commands from the smartphone. Closing the application will make the robot works in autonomous mode again.

2.4.2 Navigation software

Path planning for autonomous vacuum cleaner robots is very important as the efficiency of the robot depends on it (Hasan and Reza 2014). Path planning or navigation algorithms decide how and where the vacuum cleaner robot will move in an environment. The problem for this type of robots is to decide how to cover a room completely in a shortest possible time with efficient cleaning. The most efficient navigation algorithm is the one that has the mapping ability. The algorithms that create a map of the environment around the robot and try to position it on the map are called SLAM algorithms. In order to use SLAM algorithms, expensive sensors such as RPLIDAR must be used.

Since designing a cost effective robot is one of the main goals, expensive sensors such as LiDAR are not used in the design and simple navigation algorithms are preferred.

In accordance to the robot design, random walk and snake algorithms are designed. The random walk algorithm is widely used in most low-cost vacuum cleaner robots that do not have expensive sensors like RPLIDAR. The snake algorithm can be used to clean all the free space the robot can move in.

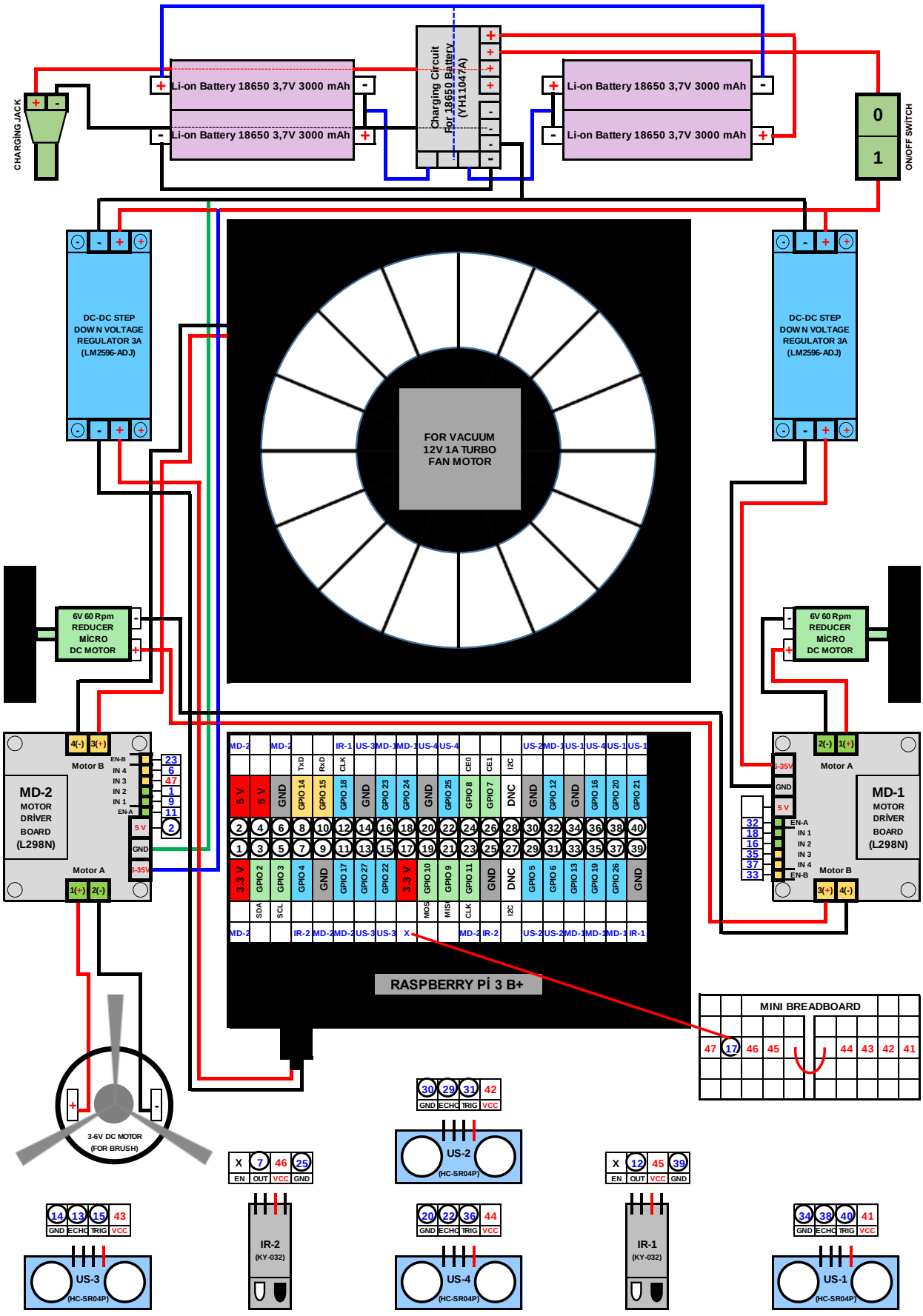

Figure 9. The layout of the electrical system

This algorithm has been designed considering the open-loop system and dimensions of the robot. Algorithms to be run on the robot can be selected from the mobile application. The algorithm selection process is done using multithreading to immediately change the running algorithm.

2.4.2.1 Random walk algorithm

The random walk algorithm is based on the random motion of the vacuum cleaner robot. The main aspect of this algorithm is that it does not require a precise route plan. The disadvantage of the random walk algorithm is that the robot passes the same area several times.

In random walk based algorithm, the vacuum cleaner robot moves in forward direction until an obstacle or wall is detected by the sensors. Then the robot stops, and turns arounds depending the random number generated by microprocessor. Block diagram of the random walk algorithm is given in the Fig. 10.

The random number determines the rotation time. Random rotation time (RRT) is adjusted as

$$RRT = 1\ sec + \ random\ time\ [0 - 1.5\ sec] \qquad (2)$$

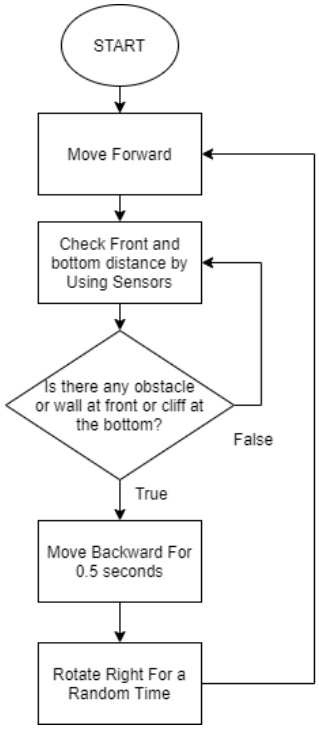

Figure 10. Block diagram of random walk algorithm

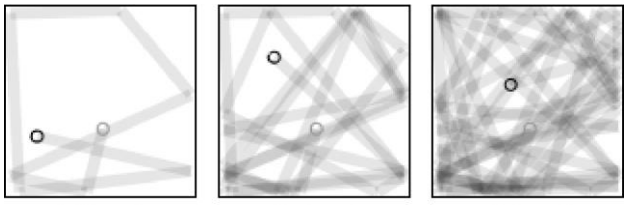

Figure 11. Random walk based algorithm (Edwards and Sörme 2018)

Random walk based algorithm in a square room without any obstacle is given in the Fig. 11 at different times. The black circle in the square indicates the vacuum cleaner robot, the gray circle indicates the starting point of the robot and gray paths indicate the way that the robot has passed. Darker gray path means more times the robot passed the same area. Notice that, in this random walk based algorithm; the robot passes the same area several times which increases the time to clean the entire room completely. Also, in stage 3 in Fig. 11, there are some small areas that have not been cleaned.

2.4.2.2 Snake algorithm

In this algorithm, the vacuum cleaner robot makes S – shaped motion which is snake-like movement. This is the fastest algorithm to cover the entire room area in a certain time. However, snake algorithm has a disadvantage that; in the realization of this pattern, there may many errors occur due to the lots of stopping and rotating motion of the robot. Consider the case that the wheels are not aligned and the sensors are not accurate. The summation of small errors will create bigger errors. Due to this disadvantage, the snake pattern is preferred only in local and small areas in order to prevent positional errors accumulation (Edwards and Sörme 2018).

The snake algorithm is improved for the case when obstacles exist in a room. An algorithm has been designed and implemented based on the region filling navigation using specific templates (Oh et. al 2004). Block diagram of the improved snake algorithm is given in the Fig. 12.

At first, the robot moves forward if no obstacle detected by the sensors. According to the block diagram in Fig. 12, this algorithm has 4 different conditions based on detected obstacle or wall direction. These are;

- Condition 1: Obstacles at front and right directions
- Condition 2: Obstacles at front and left directions
- Condition 3: Obstacles at only front direction
- Condition 4: Obstacles at front, right and left directions

Height from robot body to the floor is measured by the ultrasonic cliff sensor. When height exceeds 6 cm, height flag is set. If the height flag is set, the robot assumes there is a cliff in front of it. The robot moves back 0.5 seconds per cycle until the sensor does not detect the cliff. The height flag resets after the measured height is smaller than 6 cm.

A moving direction flag is used to enable the robot cleans the room from left to right or right to left. Initially, the moving direction is set as “right”. This means, the cleaning robot starts to clean the room from where it is, to the right until it reaches a wall or an unpassable obstacle.

After reaching a wall or an unpassable obstacle, cleaning direction becomes left. The movements of the robot according to the conditions can be exlained as follows:

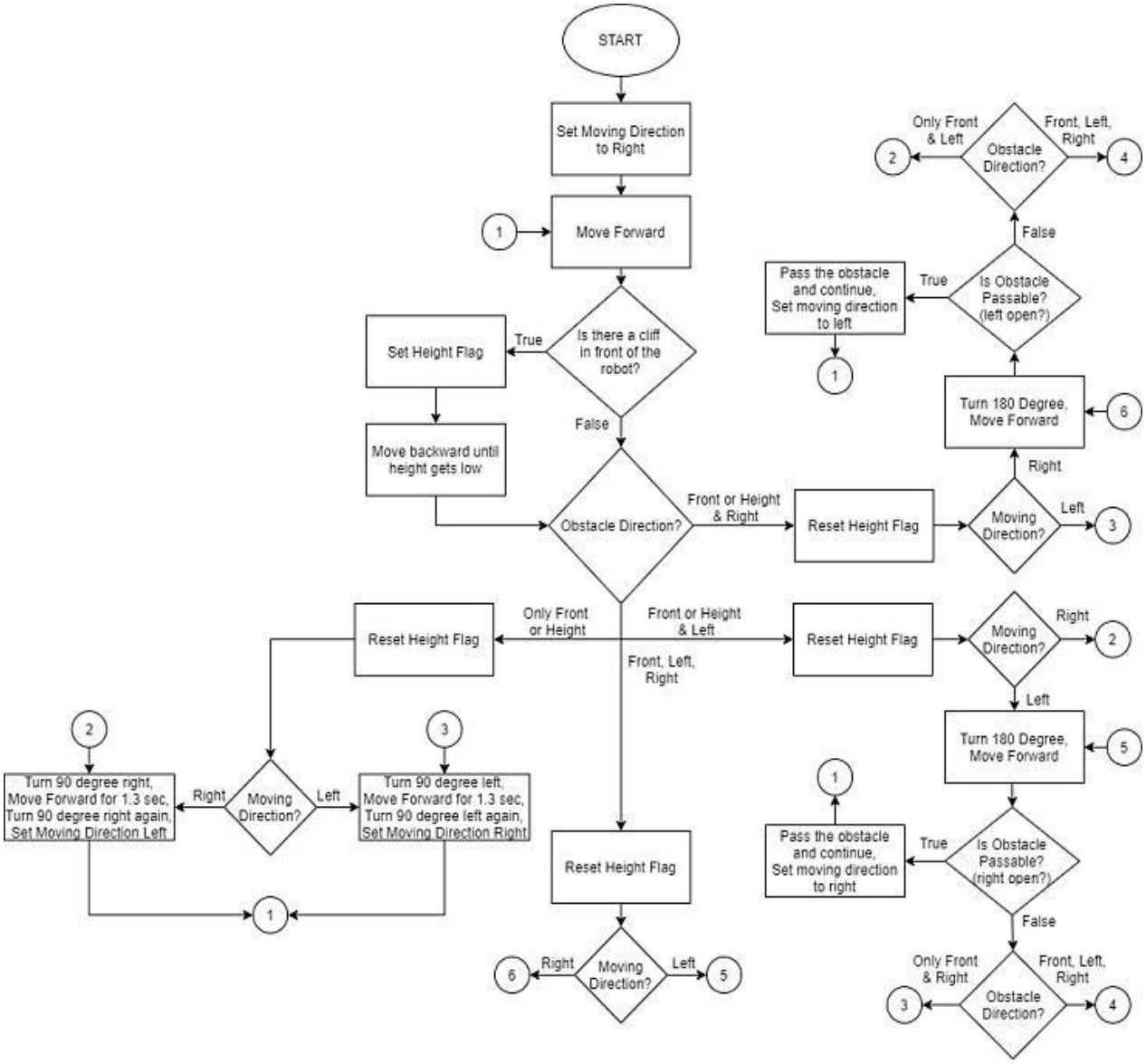

Figure 12. Improved snake algorithm block diagram

Condition-1: The robot moves according to the moving direction. If the moving direction is right, the robot cannot directly move to the right since there is an obstacle at the right side. In this case robot rotates 180 degree. After rotating 180 degrees, it moves forward until it passes the obstacle. When the obstacle is passed, the robot moves next to the obstacle and continues to clean the room by making snake movement again. If the obstacle next to the robot is an unpassable obstacle or a wall, the robot will move forward until an obstacle or wall is detected in front of it. Then it reverses the cleaning direction according to the obstacle direction and continues cleaning. If the moving direction is left, the robot can directly move to the left as there is no obstacle at the left side. Movement patterns of the robot for the condition-1 are given in Fig. 13. The dotted lines and the arrows in the figure represent the past movement of the robot until the condition satisfies.

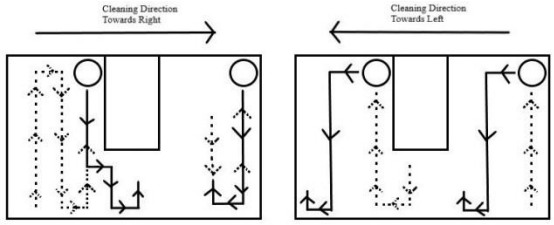

Figure 13. Condition-1 movement patterns

Condition-2: Robot acts similar to the movement given in the condition 1. The only difference in this condition is the obstacle direction (Fig. 14).

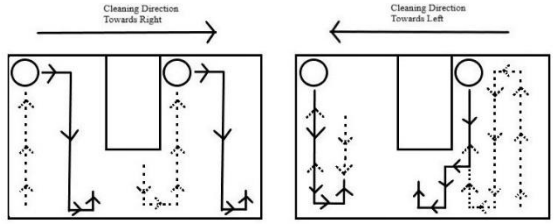

Figure 14. Condition-2 movement patterns

Condition-3: Since there is no obstacle at robot's left and right sides, the robot moves left or right according to the moving direction flag. After it turns left or right, the robot moves forward for 1.3 seconds (moving distance equals to the robot's diameter) and turns left or right again according to the moving direction flag. Then the robot moves forward and reverses the flag.

In summary, the robot makes S-shaped movement when there is no obstacles and walls at the left and right side of the robot (Fig. 15).

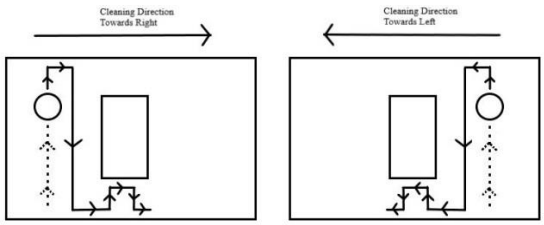

Figure 15. Condition-3 movement patterns

Condition-4: The robot rotates 180 degree and moves forward until it passes the obstacle according to the moving direction and continues to clean. If the obstacle is unpassable or there is a wall, the robot will reverse the direction of cleaning (Fig. 16).

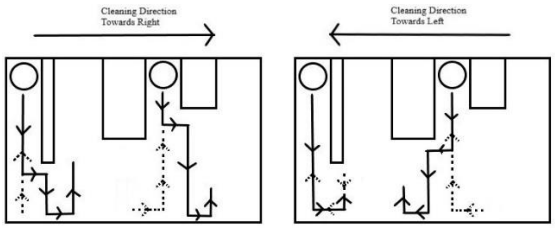

Figure 16. Condition-4 movement patterns

2.4.3 Switching Between Remote Control and Autonomous Modes

Switching between the remote control and autonomous mode needs to be as fast as possible because the user does not want to wait for the switching time. The Bluetooth connection must be checked every time to switch modes. Switching delay is not a problem for switching from remote control mode to the autonomous mode. When the Android application is closed or the Bluetooth connection is disabled, the robot switches from remote control mode to autonomous mode immediately. Since the code execution process is a serial process normally, there will be delay occurred for switching from autonomous mode to the remote control mode. In order to eliminate this delay, multithreading can be used.

Multithreading is the ability of a CPU (Central Processing Unit) to executes a process in multiple threads in parallel. It provides execution of the parts of a process independently. The speed of the computation can be significantly increased by using multithreading. In multithreading, threads share the same memory, meaning they can use the same variables defined in a process.

Two threads are used: One thread is used to check the Bluetooth connection every time while the other thread is used for the execution of autonomous algorithms. When the Bluetooth connection is requested from the smartphone and is accepted by the Raspberry Pi, the thread used for autonomous algorithm is killed. After the Bluetooth connection disabled (switching to autonomous mode), thread for autonomous algorithm starts again and other thread starts to check Bluetooth connection.

3. RESULTS

After the mechanical and electrical parts have been combined, the robot chassis has carried all the electrical components without any deformation. Implemented robot can be seen in the Fig. 17 and 18.

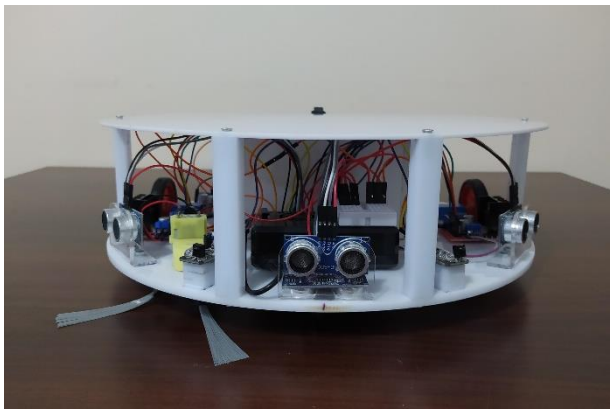

Figure 17. Front view of the robot

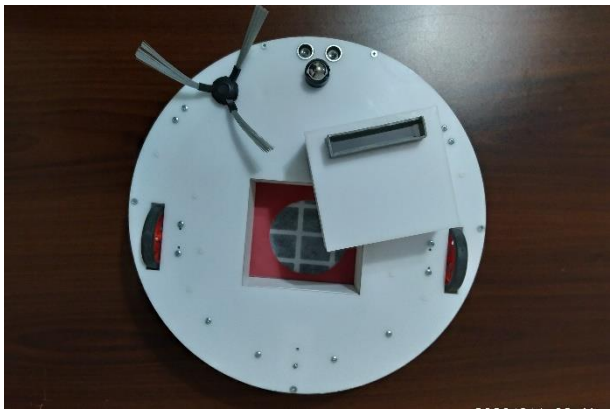

Figure 18. Bottom view of the robot

When the electricity system is energized; all electrical components operated smoothly. The short circuit test showed that the power and charging system automatically cut off the power from the batteries. In addition, a charge test has been carried out to check whether the batteries can be charged or not. As a result, the batteries have been charged from its barrel jack. The robot operated for about 1.5 hours with fully charged batteries.

The remote control mode has been tested using the designed Android application. As a result, this mode has been worked as expected. The robot has executed every given command without delay. Remote control mode has also be used for testing and calibration of the robot movement. At the end of the calibration, straight line motion has been guaranteed. The software code for the autonomous mode was tested and the results were satisfactory. The vacuum cleaner robot has successfully collected the crumbs on the ground.

The voltage across four series batteries has been measured when they are fully charged and found as 16.51 V. The current measurement has been done when the robot is working in autonomous mode and found as 0.76 A. The power consumption (PC) of the designed robot has been calculated by using the measured voltage and current:

$$PC = 16.51\,V\ x\ 0.76\,A = 12.38\,W \quad (3)$$

Table 3 shows the specifications of the implemented robot with the specifications of two low-cost models on the market, Ecovacs Deebot N79S and Roomba 675.

Table 3. Specifications of vacuum cleaner robots

	Implemented Robot	Ecovacs Deebot N79S	Roomba 675
Dimensions (Diameter x Height) in cm	33 x 12	35.3 x 8.4	33 x 9.4
Weight (kg)	3.5	4.3	3.5
Battery Life (mins)	150	95	104
Power (W)	12.38	25	33
Remote Control	No	Yes	No
Phone Control	Yes	Yes	Yes
Noise Level (dB)	52	67	65
Brush Number	One	Two	One
Navigation Algorithm	Random, Snake	Auto (Random), Edge, Spot	Random, Spot

4. DISCUSSION

Ecovacs Deebot N79S and Roomba 675 have similar specifications with the other low-cost vacuum cleaner robots in the market. If the specifications of the implemented robot and the other two robots are compared; their dimensions are almost equal but the height of the implemented robot is higher due to the placement of the dust bin and components.

The weight of the implemented robot is lighter than the Ecovacs Deebot and is equal to Roomba 675. Implemented robot consumes much less power than its counterparts. Since the robot can be controlled by smartphones, there is no need for remote control, which leads to a reduction of production costs. It's the same for the Roomba 675. Ecovacs Deebot has both remote and phone controls. The noise level of the implemented robot is lower than the others. The implemented robot and Roomba 675 have one brush while the Ecovacs Deebot has two brushes. Two brushes need more power consumption and one brush is enough for cleaning.

Three of the robots have their own random algorithms. The implemented robot has a snake algorithm that allows it to clean the entire room in a short time. The snake algorithm is superior to the random algorithm as it saves time and leaves no uncleaned space. Ecovacs Deebot and Roomba 675 have a spot algorithm that can be used to clean a specific area in a spiral motion, but the snake algorithm is also sufficient to clean certain spots. Therefore, there is no need for a spot navigation algorithm.

5. CONCLUSION

Robots are widely used in industry for the mass production of consumer and industrial goods. In order for the use of robots to become widespread in household chores as well as industry, robots must fully perform their functions, be easy to use and most importantly, must be low-cost.

In this paper, the design and implementation of a cost-effective fully functional vacuum cleaner robot is given. Inexpensive, functional and easily accessible components and materials have been selected in the mechanical and electrical design of the robot. The prototype robot can act autonomously and manually. In autonomous mode, the robot cleans the room by going around the obstacles according to the selected algorithm. With the cliff sensor, the robot has been prevented from falling through spaces such as stairs. In remote control mode, navigation can be controlled by a smartphone. A user-friendly android application has been developed where the user can control the brush and vacuum motors and select the navigation algorithm.

Random walk and snake algorithms have been used as the navigation algorithm. Since the robot does not know its exact position and cannot plan the navigation, it has to pass through the same place several times while cleaning a room. This increases the cleaning time. With the use of expensive and advanced sensors such as lidar and camera, it is possible to know the exact position of the robot in the room and plan the navigation accordingly. In order to process the information coming from the sensors, a more advanced microcontroller with more pins is also needed. That means addition of these sensors will increase the cost and the power consumption of the robot.

Author contributions

Anıl Eren: Designed the study, took the measurements, and wrote the manuscript. **Hatice Doğan:** provided the idea, supervised the study, and contributed to the manuscript.

Conflicts of interest

The authors declare no conflicts of interest.

REFERENCES

Adithya P S, Tejas R, Varun V S, & Prashanth B N (2019). Design and Development of Automatic Cleaning and Mopping Robot. IOP Conference Series: Materials Science and Engineering 577, 012126.

Asafa T B, Afonja T M, Olaniyan E A, & Alade H O (2018). Development of a vacuum cleaner robot. Alexandria engineering journal, 57(4), 2911-2920.

Blower Documentation,

https://corporate.usacanadashop.com/item/B00ZL99AFQ/Gdstime-Centrifugal-Brushless-Cooler-Blower, (Access Date: 20.06.2020)

BMS protection board YH11047A, https://tr.aliexpress.com/item/32719942192.html (Access Date:20. 06. 2020)

Chen W, Liang J, Yang Z & Li G (2019). A review of lithium-ion battery for electric vehicle applications and beyond. Energy Procedia, 158, 4363-4368

Dai G T & Chen T (2007). Design on measurement and control system of cleaning robot based on sensor array detection. IEEE International conference on control automation, 2007, 1319-1322, Guangzhou, China.

Dave M (2020). Differential Drive Mechanism, https://sites.google.com/site/mleesrobotronics/home/robotics/differential-drive-mechanism (Access Date: 01.08.2020)

Dudek G, & Jenkin M (2010). Computational principles of mobile robotics. Cambridge university press. ISBN-13: 978-0521692120.

Edwards T, & Sörme J (2018). A Comparison of Path Planning Algorithms for Robotic Vacuum Cleaners, Doctoral dissertation, Bachelor's Thesis, KTH Royal Institute of Technology, Stockholm, Sweden.

Elias M F M, Nor K M, Rahim N A, & Arof A K (2003). Lithium-ion battery charger for high energy application. National Power Engineering Conference, (PECon 2003), 283-288, Bangi, Malaysia.

Gao X, Li K, Wang Y, Men G, Zhou D & Kikuchi K (2007). A floor cleaner robot using Swedish wheels. IEEE international conference on robotics and biomimetics (ROBIO), 2007, 2069-2073, Sanya, China.

Hasan K M & Reza K J (2014). Path planning algorithm development for autonomous vacuum cleaner robots. 2014 International Conference on Informatics, Electronics & Vision (ICIEV), 1-6, Dhaka, Bangladesh.

INR18650-30Q (2014). Li-on Battery Datasheet, Samsung SDI, August 2014.

LaValle S M (2006). Planning Algorithms. Cambridge University Press. ISBN-13: 978051124133-8.

Liu C, Kang L, & Yu S-N (2011). Hardware and software integration for domestic stairs cleaning robot. SICE Annual Conference 2011, 663-670, Tokyo, Japan.

Maruri L, Martinez-Esnaola A, Landaluze J, Casas S & Fernández M (2006). Design of a prototype robot vacuum cleaner-from virtual prototyping to real development. International Conference on Informatics in Control, Automation and Robotics (ICINCO-RA), 461-468, Setúbal, Portugal.

Oh J S, Choi Y H, Park J B, & Zheng Y F (2004). Complete coverage navigation of cleaning robots using triangular-cell-based map. IEEE Transactions on Industrial Electronics, 51(3), 718-726.

Oh Y-J & Watanabe Y (2002). Development of the small robot for home floor cleaning. Proceedings of the 41st SICE Annual Conference, 2002, 3222-3223, Osaka, Japan.

Ottoviani G (2020). Differential Drive Motions, https://guiott.com/Cleaning Robot/C-Motion/C0Theory/differential-drive.jpg (Access Date: 01.08.2020)

Prabakaran V, Elara M R, Pathmakumar T & Nansai S (2017). hTetro: A Tetris inspired shape-shifting floor cleaning robot. IEEE International Conference on Robotics and Automation (ICRA), 2017, 6105-6112, Singapore.

Radu Ş (2015). Relation Between Function and Form in Vacuum Cleaners Design. Journal of Industrial Design & Engineering Graphics 10(2), 37-42.

Roh S G, Lim B, Moon H, Lee J S, Park J H, Koo J C, & Choi H R (2013). Flexible suspension mechanism for stable driving of a differential drive mobile robot, 2013 IEEE/RSJ International Conference on Intelligent Robots and Systems, 5518-5523, Tokyo, Japan.

Stubbs L (2019). D-Shaped vs Round Shaped Vacum Cleaners,https://bestrobotvacuumforyou.com/d-shaped-vs-round-shaped-robot-vacuum-cleaners (Access Date: 27.02.2021).

Ulrich I, Mondada F & Nicoud J D (1997). Autonomous vacuum cleaner. Robotics and Autonomous Systems 19(3-4), 233-245.

Turkish Journal of Engineering

https://dergipark.org.tr/en/pub/tuje

e-ISSN 2587-1366

A novel artificial neural network model for forecasting electricity demand enhanced with population-weighted temperature mean and the unemployment rate

Mustafa Comert[1], **Ali Yildiz** *[1]

[1]*Mersin University, Engineering Faculty, Department of Electrical & Electronics Engineering, Mersin, Turkey*

Keywords
Monthly electricity demand
Balance point temperature
Unemployment Rate
Artificial neural network

ABSTRACT

Precise electricity demand forecasting has principal significance in the energy production planning of the developing countries. Especially during the last decade, numerous recent methods have been utilized to predict the forthcoming electricity demand in different time resolutions accurately. This contribution presents a novel approach, which improves the forecasting of Turkey's electricity demand in monthly time resolution. An artificial neural network model has been proposed with appropriate input features. Yearly-based gross demand shows approximately linear increment due to population increase and economic growth, while monthly-based gross demand indicates an oscillation due to the effect of seasonal temperature fluctuations. However, there is no clear linear relation between electricity demand and temperature; for the ideal case, it is the V-shaped curve around balance point temperature. Since temperature levels in each region of the country demonstrate a high variance even in the same time period, weighted average temperature point was calculated with respect to the population weights of the selected regions of Turkey. In order to fit a function for monthly oscillations, a linear function according to weighted average temperature point was created. Unemployment data was added to the training data set as an indicator of economic fluctuations. The mean absolute percentage errors of the model were calculated for training, validation, and testing as 3.77 %, 2.02 %, and 1.95 % respectively.

1. INTRODUCTION

In today's world, electricity consumption has an influential role in the growth of economies. Therefore, it has been one of the most significant energy types of end-users. As can be observed in many countries, the increase in electricity demand on the industrial side is considered to be a precursor to the development of the technology and the economy. Each country has its own particular electricity consumption behavior, which is directly affected by numerous factors such as population size, meteorological conditions, social, and economic parameters. Researchers have been broadly using various emerging techniques such as fuzzy logic, particle swarm optimization, ant colony optimization, genetic algorithm, artificial neural network, and support vector regression in the modeling of electricity demand. The studies have been shaped as the estimation of electricity demand with several distinct time resolutions in almost all developing countries.

This paper is organized as follows: Section 2 presents a brief historical background both in the world and in Turkey. In Section 3, how the data obtained, analyzed, and preprocessed before modeling is presented. Section 4 provides outcomes of presented model and gives a comparison with previous similar studies. Lastly, Section 5 summarizes the key results.

2. LITERATURE REVIEW

A survey of the studies reported in the literature on electricity demand prediction for the last decade reveals that researchers utilized many different techniques and data for various time resolutions. A study for India has been proposed, which can estimate the monthly peak demand with a multiplicative seasonal autoregressive integrated moving average (MSARIMA) method (Rallapalli and Ghosh, 2012). The time span was very narrow (April 2011 – July 2011) for the study and it

* **Corresponding Author**

(mcomert@mersin.edu.tr) ORCID ID 0000-0001-7566-9794
*(yildiz@mersin.edu.tr) ORCID ID 0000-0003-3904-6017

Research Article / DOI: 10.31127/tuje.903876

Cite this article

Comert M & Yıldız A (2022). A novel artificial neural network model for forecasting electricity demand enhanced with population-weighted temperature mean and the unemployment rate. Turkish Journal of Engineering, 6(2), 178-189

Received: 29/03/2021; Accepted: 27/04/2021

cannot be applied to predict the demand for longer periods. Another model for the electricity demand prediction for India, the deep learning framework was presented in 2019 (Bedi and Toshniwal, 2019). In 2013, the least square - support vector machine (LS-SVM) method was shown to be more successful in predicting the hourly electricity load for Portugal over the 48-hour period when compared with the previous studies (Ferreira, et al., 2013). For the same year, a genetic algorithm (GA) model has been suggested in order to estimate the annual electricity demand of Thailand by using economic parameters such as gross domestic product (GDP) and total income as input features (Mostafavi, et al., 2013). Also, it was shown in the same year for Canada that neural-fuzzy logic network models could be employed to predict the demand for a 5-year period (Zahedi, et al., 2013). Then, hourly effects of weather variables were examined in an another study (Nick MacMackin, et al., 2019). Comprehensive studies were presented for Australia on a monthly estimation of electricity demand by using balance temperature point with utilizing multi-collinearity analyses (Ahmed, et al. 2012; Ahmed, et al. 2018). In 2015, electricity demand data with the 30-minute resolution had been trained with simply using time series as an input feature and had a 0.62% mean absolute percentage error (MAPE) (Vu, et al., 2017). In 2018, it was also shown that the atmospheric variables have effects on both monthly and annual electricity demands (Ahmed et al., 2018). Numerous studies have been published for Australia in 2019 (AL-Musaylh, et al. 2019; Singh, et al., 2019; Wu, et al., 2019; Xu et al., 2019; Yang, et al., 2019). A new model has been presented for the effects of temperature fluctuations for Korea on monthly electricity demand (Chang, et al., 2016). In another study for Korea, the monthly electricity demand has been estimated by the support vector regression SVR technique for the residential sector using social and weather variables for a 2-year range. The study has yielded exclusively training MAPE as 2.13% (Son and Kim, 2017). Also, a forecasting model was developed for institutional buildings in 2019 (Kim, et al., 2019). In 2016, a deep belief network, which has been one of the favorite methods in machine learning, was used to estimate the hourly electricity demand of Macedonia. To train the algorithm, the calendar and temperature information were used as model features. Estimated values generated a MAPE between 3.3% and 7.2% (Dedinec, et al., 2016). For Brazil, forecasting annual electricity demand was proposed using a fuzzy logic method with the help of GDP and population for 10-year period (Torrini, et al., 2016). Another study for Brazil, using similar input features, has demonstrated regional monthly electricity demand prediction with the help of spatial autoregressive integrated moving average (ARIMA) model (Cabral et al., 2017). The hourly and daily peak electricity demand in commercial buildings for Great Britain was estimated by using the triad demand predictive model with a 2.4% MAPE for training data only (Marmaras, et al., 2017). Also for Great Britain, time series analysis has been studied for electricity load forecasting in 2019 (Maldonado, et al., 2019). In 2015, self-adaptive particle swarm optimization (PSO), GA, and radial basis function (RBF) were used in a hybrid model, which presented to estimate annual electricity demand for China (Yu, et al., 2015). After three years, in 2018, electricity demands of two different regions in China were estimated by two different studies using similar Grey models without any economic parameters (Ding, et al., 2018; Wu, et al., 2018). In the same year, echo state network, which has been improved with differential evolution algorithm, was again presented to estimate monthly electricity demand for China (Wang, et al., 2018). A study on hourly peak demand of households in Denmark has been investigated with statistical data in 2017 (Andersen, et al., 2017). Other two studies using similar statistical techniques attempted to determine the factors affecting electricity demand for Israel (Damari and Kissinger, 2018) and Jordan (Al-Bajjali and Shamayleh, 2018). In South Africa, the demand-intensive hours were modeled with partially linear additive quantile regression between 18:00 and 20:00, for a 6-month time interval. The model was created by implementing hours of the day, date, and temperature as input features (Lebotsa, et al., 2018). In 2018, the hourly model of electricity demand in both commercial and residential areas of the USA was suggested to estimate for 250 hours by deep recurrent neural networks which is another recent popular method in machine learning. The model included all atmospheric events and calendar information (Rahman, et al., 2018). A summary of selected studies which fulfilled over the last decade can be seen in Table 1.

Electricity demand estimation of Turkey has also been studied by many researchers with different time resolutions and input parameters so far. The first studies were initiated at the beginning of the 2000s. In the study, they employed an exponential regression from 30-year (1970-2000) demand data to estimate the annual electricity demand for the next 50-year (2000-2050) time span (Yumurtaci and Asmaz, 2004).

Table 1. Summary of the electricity demand prediction studies in world.

Study	Methodology	Features	Forecast Span	MAPE validation	MAPE train
(Rallapalli and Ghosh, 2012)	MSARIMA	Time series	May-July 2011	0.93 – 0.94	1.60 – 2.05
(Ferreira et al., 2013)	LS-SVM	Time series	48 Hours	-	1.90 – 4.00
(Mostafavi et al., 2013)	Genetic programming and simulated annealing (GSA)	Time series, GDP, stock index, total revenue	2003 – 2009	0.50	2.30
(Vu, et al., 2015)	Multi-collinearity	Cooling degree days, heating degree days, number of rainy days in a month of interest, humidity percentage average	2006 – 2010	1.02	1.00 – 4.00
(Vu et al., 2017)	Autoregressive based time varying (ARTV) model	Time series	2015	-	0.62
(Son and Kim, 2017)	SVR and fuzzy-rough feature selection	20 variables are considered including 14 weather variables, 5 social variables, and monthly electricity consumption	2011 – 2012	-	2.13
(Dedinec et al., 2016)	Deep belief networks	Holiday flag, cheap tariff flag, hour of day, day of week, previous day's average load, load for the same hour of the previous day, temperature, load for the same hour - day combination of the previous week	2013 – 2014	-	3.30 – 7.20
(Torrini et al., 2016)	Fuzzy logic	Time series, GDP, population	2003 – 2013	-	0.93 – 2.38
(Cabral et al., 2017)	Spatial ARIMA model	Time series, average tariff in each region, number of residences served in each region, regional economic activity index adjusted seasonally	2013	1.85	-
(Marmaras et al., 2017)	Triad demand predictive model	Cloud base, cloud total amount, wind mean speed, rainfall, hourly global radiation, max gust, air temp deg., rh., hourly sun	2014 – 2015	-	2.40
(Yu et al., 2015)	PSO – GA – RBF	Population, GDP, energy intensity of industry	2014 – 2020	1.31	2.89
(Ding et al., 2018)	Modified grey prediction model	Time series	2012 – 2014	2.86 – 3.38	2.86 – 3.38
(Wu et al., 2018)	Multi-variable grey model	GDP, income, population, gross industrial output, fixed investment assets,	2013 – 2015	3.16	2.61
(Wang et al., 2018)	Echo state network	Time series	10/2008 – 05/2009	0.05	2.16
(Lebotsa et al., 2018)	Partially linear additive quantile regression	Temperature variables, calendar variables	January – June 2012	-	0.77 – 0.97
(Rahman et al., 2018)	Deep recurrent neural networks	Dry bulb, temperature, relative humidity, wind speed, solar irradiation, etc.	250 hours	-	5.46

In 2005, two different studies by the same group presented estimations for different time periods with the help of GA based on yearly resolutions (Ozturk and Ceylan, 2005; Ozturk, et al., 2005). The electricity generation and demand were compared between Turkey and European countries in 2006 (Tunç, et al., 2006). Annual electricity demand and production were modeled with two different methods based on the same learning set in 2007. The Grey prediction model was studied in the first method, and simply time series was chosen as the input feature of the model (Akay and Atak, 2007). In the second study, the annual electricity demand was modeled by a quadratic function, and its parameters were found with the help of ant colony optimization (ACO) (Duran Toksari, 2007). In 2009, economic parameters were included in the artificial neural network (ANN) model, and electricity demands between 2001 and 2006 were estimated with a 0.51 root mean square error (RMSE) per TWh (Kavaklioglu, et al., 2009). The support vector machine (SVM) method was employed to estimate for the same time period by using the same data in 2011 (Kavaklioglu, 2011). A fuzzy logic model was also applied to estimate the total electricity generation in 2010 with the help of total domestic product as an input feature (Kucukali and Baris, 2010). Another study in 2011 established an electricity demand model of residential buildings and exhibited the factors which are effective on the model (Dilaver and Hunt, 2011). By the year of 2012, both training and validation metrics have been delivered in research studies which performed to predict Turkey's electricity demand. Before 2012, studies only presented either the training or the validation metrics. In 2012, monthly electricity demand was investigated for the first time for Turkey. SVR algorithm was utilized for the model, and the MAPEs of both training and validation data sets were calculated as 11.00% and 3.30% respectively (Oğcu, et al., 2012). In another study, a quadratic second order function was fitted with the help of PSO, and the error was decreased down to 3.99% (Kiran, et al., 2012). In 2014, three different studies with three characteristic methods were presented. The first one has been demonstrated that the electricity demand in both industrial and residential buildings could be modeled by using merely time-series (Arisoy and Ozturk, 2014). In the second study, the optimized Grey model was presented to estimate input features for the singular value decomposition (SVD) method from 1970 to 2010 (Kavaklioglu, 2014). In 2015, a model was proposed to estimate the future independent factors using seasonal ARIMA method and non-linear autoregressive ANN method (Tutun, et al., 2015). Hourly electricity demand was estimated with a 1.85% MAPE by using an ANN model (Çevik and Çunkaş, 2015). In the same year, ANN and LS-SVM were compared on annual electricity demand, and LS-SVM has demonstrated better estimation results. (Kaytez, et al., 2015). Similarly, ANN was also compared with multiple linear regression (MLR) model on the annual electricity demand, and it was concluded that the ANN model successfully predicted the electricity energy demand with extreme accuracy, and the forecasts were superior to the official forecasts done by Ministry of Energy and Natural Resources of Turkey. On the other hand, the MLR model was not successful enough to predict the demand within an acceptable accuracy range (Günay, 2016). In 2016, ACO and iterative local search algorithms were used to fit a quadratic function to estimate electricity demand (Toksari, 2016). In 2017, three different studies were performed to estimate daily, monthly, and annual electricity demand. For the estimation of daily electricity demand, sinusoidal oscillations were modeled with temperature data on a linear model that took into account these fluctuations (Yukseltan, et al., 2017). For the estimation of the monthly electricity demand, an ANN with feedback was trained, and MAPE decreased down to 2.28% for the test set (Hamzaçebi, et al., 2017). The yearly prediction demand was linearly modeled with parameters of GDP, population, import and export. The parameter weights of the model were optimized by the help of the PSO algorithm. The model yielded a 2.52% MAPE for the years from 2004 to 2013 (Gulcu and Kodaz, 2017). In 2018, daily electricity demand was estimated with multivariable adaptive splines, and the model has exhibited a 4.00% MAPE on the test set (Nalcaci, et al., 2018). A summary view of selected studies which fulfilled over the last two decades for Turkey can be seen in Table 2.

3. METHOD

In this study, ANN is chosen as a forecasting tool since it can intrinsically model the non-linear behavior in the data. Only time series, temperature data and the unemployment rate were used as input features. In order to keep the model simple, the other economic parameters like GDP, import and export were excluded. Section 3.1 clarifies how population-weighted monthly average temperature point is calculated for Turkey. This function is employed as an additional input feature of the proposed neural network.

Table 2. Summary of the electricity demand prediction studies in Turkey

Study	Methodology	Features	Forecast Span	MAPE validation	MAPE train
(Ozturk et al., 2005)	GA	Time series, gross national product, population, import and export	1996 – 2001	2.29	1.42
(Ozturk and Ceylan, 2005)	GA	Time series, gross national product population,, import and export	1997 – 2003	7.30-16.05	-
(Akay and Atak, 2007)	Grey prediction	Time series	-	3.43-4.36	-
(Duran Toksari, 2007)	ACO	Time series, GDP, import, export and population	-	1.00-3.00	-
(Kavaklioglu et al., 2009)	ANN	Time series, gross national product, population, import and export	2001 – 2006	-	0.51 RMSE per TWh
(Kavaklioglu, 2011)	SVR	Time series, gross national product, population, import and export	2001 – 2006	-	0.76 RMSE per TWh
(Kucukali and Baris, 2010)	Fuzzy logic	GDP	-	4.16	-
(Oğcu et al., 2012)	SVR	Time series	2010 – 2011	11.00	3.30
(Hamzacebi and Es, 2014)	Optimized grey model	Time series	2006 – 2010	-	3.28
(Kavaklioglu, 2014)	SVD	Time series, gross national product, population, import and export	1970 – 2010	-	-
(Tutun et al., 2015)	Ridge-based adaptive evolutionary	Time series, imports, exports, gross generation and transmitted energy	2006 – 2010	0.18	1.60
(Çevik & Çunkaş, 2015)	Adaptive neuro-fuzzy inference system	Load, temperature, season	2012	-	1.85
(Kaytez et al., 2015)	ANN and LS-SVM	Installed capacity, gross electricity generation, population	2010 – 2011	0.88	1.00
(Günay, 2016)	ANN	Population, gross national product, inflation, unemployment, average summer temperature, average winter temperature	2007 – 2013	-	2.52
(Toksari, 2016)	ACO	Time series, gross national product, population, import and export	2004 – 2013	Lin.= 1.15 Qua.=2.16	-
(Yukseltan et al., 2017)	Linear model	Time series, religious holidays	2014	-	2.86
(Hamzaçebi et al., 2017)	ANN	Time series	2014	1.97	2.28
(Gulcu and Kodaz, 2017)	PSO	GDP, population, import, export	2014 – 2030	2.52	-
(Nalcaci et al., 2018)	Multivariate adaptive regression splines	Lags of electricity demand, holidays, temperature date, relative humidity, wind speed	2013 – 2015	3.60	4.00

3.1. Preprocessing

Seven big provinces from each geographical region were selected to represent Turkey. These cities were picked as Istanbul, Ankara, Izmir, Adana, Diyarbakır, Trabzon, and Erzurum. These cities and geographical regions are shown in Figure 1. Monthly mean values of temperature recordings for each region were used as an additional input data from January 2000 up to November 2019 (MGM, 2020).

Figure 1. Selected cities on the geographical region map

The weather data was requested from the Turkish Meteorological Data Information Sales and Presentation System. The most reliable and some of the oldest meteorological stations were preferred in order to have complete temperature information for each city.

Residential populations were used for the year of interest, and the data was downloaded from the Turkish Statistical Institute website (TUIK, 2020). For the year of 2019, the total population of the cities, which is 37.39% of the overall population of Turkey and their population weights were calculated among themselves, can be seen in Table 3.

Table 3. Populations of selected cities and their weights for the year of 2019

Province	Population	Weight
Istanbul	15,029,231	0.498
Ankara	5,445,026	0.180
Izmir	4,279,677	0.142
Adana	2,216,475	0.073
Diyarbakır	1,699,901	0.056
Trabzon	786,326	0.026
Erzurum	760,476	0.025

The electricity demand data was collected from Turkish Electricity Transmission Company (TEIAS) (TEİAŞ, 2020). The monthly gross electricity demand was selected as an input from January 2000 up to November 2019. It can be easily seen in Figure 2 that entire electricity demand data even with short-term variations may fit almost linearly with a reasonable R^2 value of 0.935.

The unemployment rate data was collected from Turkish Statistical Institute (TUIK, 2020). The data was used as an economic indicator of Turkey. It can be clearly seen from Figure 2 that unemployment rate and electricity demand have an inverse correlation.

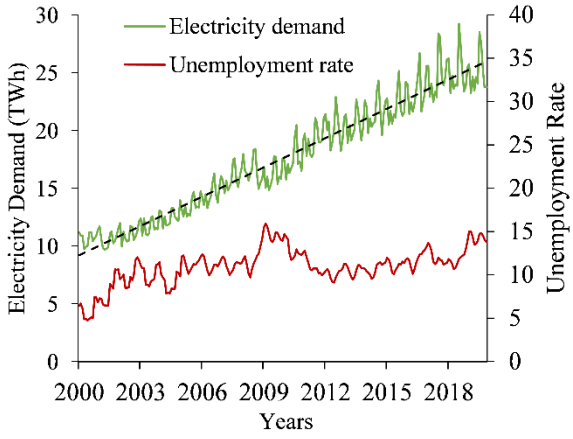

Figure 2. Electricity demand and unemployment rate of Turkey

To clearly observe the oscillations on the monthly electricity demand; the average demands for the same month of all years were calculated (see Figure 3 (right)). Monthly variation of electricity energy demand was observed to be highly correlated with the calculated average temperatures. The square difference of the monthly temperature averages around a fixed BPT is extremely similar to the monthly energy demand (ED) oscillations, as shown in Figure 3 (left) Therefore, it can be eventually determined that monthly electricity demand shows a superposition of a linear increase over the years and intensifying oscillations around the monthly temperature averages. In the light of these observations, a function prototype was proposed as in Equation 1.

$$ED(y,m,T_m) = a\left[12\left(y - y_{offset}\right) + m\right] + b\left[12\left(y - y_{offset}\right) + m\right](T_m - T_b)^2 + D_{offset} \quad (1)$$

The constants were calculated with the help of the "Levenberg-Marquardt" algorithm. They were obtained as demand increase slope a = 6.516e-9, year offset y_{offset} = 1994.937, demand oscillation magnitude b = 1.056e-11, balance point temperature T_b = 15.227, constant electricity consumption D_{offset} = 0.005. Where, the coefficient a represents the slope of linear electricity energy demand increase and the coefficient b represents the amplitude of oscillations on electricity demand over BPT.

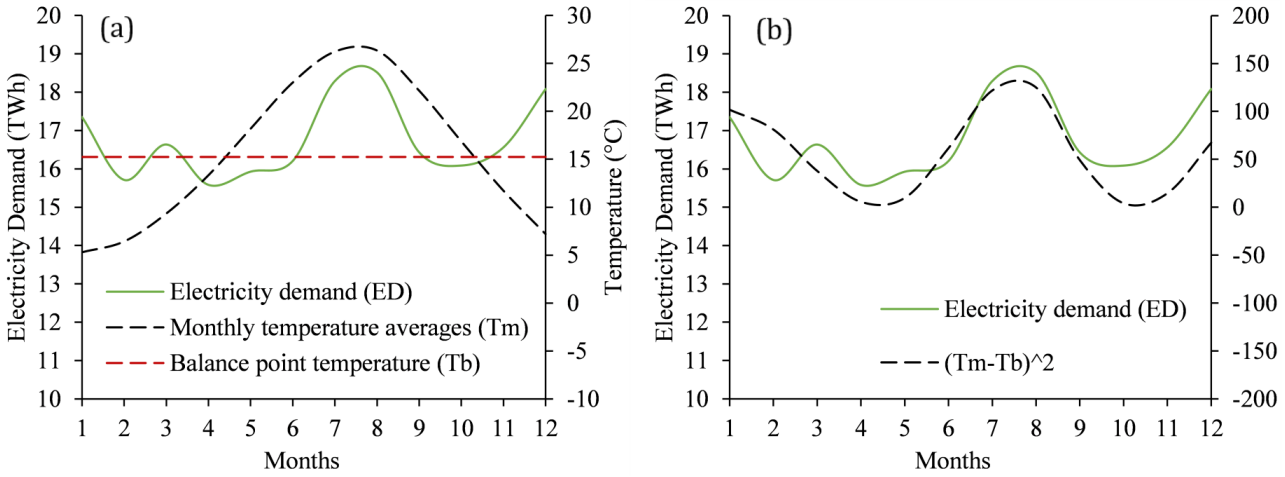

Figure 3. (a) Determining balance point temperature by using averages of temperature variations. (b) Catching similarity between electricity demand fluctuations across months between squared differences of average temperatures with BPT

Electricity energy demand recordings are shared with the function whose constants are calculated. Here D_{offset} shows the constant electricity consumption in PWh, which is not related to oscillations. y_{offset} is the year in which oscillations started. T_m is monthly temperature average and used as an input attribute as $(T_m - T_b)^2$ into the proposed artificial neural network model. This value has helped us to find linear and non-linear relations in the model to predict the temperature-dependent monthly oscillations.

3.2. Multi-layer perceptron networks

An ANN model plainly defines a potential solution space. Neural Network can be defined as seeking for useful mapping of input features to output target within a predefined possibility space of solutions by the help of back-propagation. By picking a model out, one constrains the space of potentiality to specific limits. The field of ANN is often just called multi-layer perceptron since it is the most useful kind of neural network. A multilayer perceptron (MLP) must contain one or more hidden layers besides one input and one output layers. MLP intrinsically possess an ability to learn non-linear functions. Consequently, they own the power to find out the representation in the training data and how to effectively relate it to the output targets that wanted to predict. In this sense, the predictive capability of neural networks comes from the structure of multi-layer. However, the layer could simply learn the linear mapping of the input features without a non-linear activation function since a sequential pile of linear layers would still carry out a linear function. Therefore, contributing more layers would not broaden the potential solution space. In order to have a much extensive potential solution that would profit from multiple mapping, a non-linear activation function is essential between layers.

3.3. Proposed MLP network model

The suggested model consists of an input layer with 15 neurons (1 input for year, 12 inputs for months, 1 input for $(T_m - T_b)^2$, and last input for unemployment rate), 2 hidden layers, and an output layer with one neuron which gives the prediction of energy demand. All neurons are fully connected to the previous and next layers. A model that has less than two hidden layers could not sufficiently learn the pattern in the training data. Therefore, it could not implement a good representation of the input features. Whereas, adding more hidden layers would cause to determine more complicated representations which makes the model computationally expensive and might also contribute to learn undesirable patterns that would improve the performance of the training but not both of the validation and test data sets. A model that does well on the training set is not needfully a model that will performs well on another data set it has never encountered earlier. The fundamental problem in the neural network is the balance between optimization and generalization. Optimization is adjusting a model so that having the most beneficial performance possible on the training data. On the other hand, generalization is indication of how well the model does on the validation data it has never met before. The principal aim is to have good generalization based on training data. Regrettably, there is no known quick process to find the proper number of layers or the correct number of neurons for each layer. In order to determine an appropriate model size in the study, different architectures have been evaluated on training and validation data. Nevertheless, test data has never been used at this stage. Additionally, the training data set has been shuffled to mitigate overfitting. Year and $(T_m - T_b)^2$ values are entered in the model after scaling since feeding relatively large values as input features could incite large gradient modification that will preclude the network from converging. However, the

unemployment rate is fed into the model without scaling because its values are already defined as small numbers. Month values were entered as one-hot encoded value. Therefore, exclusively month of interest is entered as 1 and others are entered as 0. The structure of the proposed model can be seen in Figure 4.

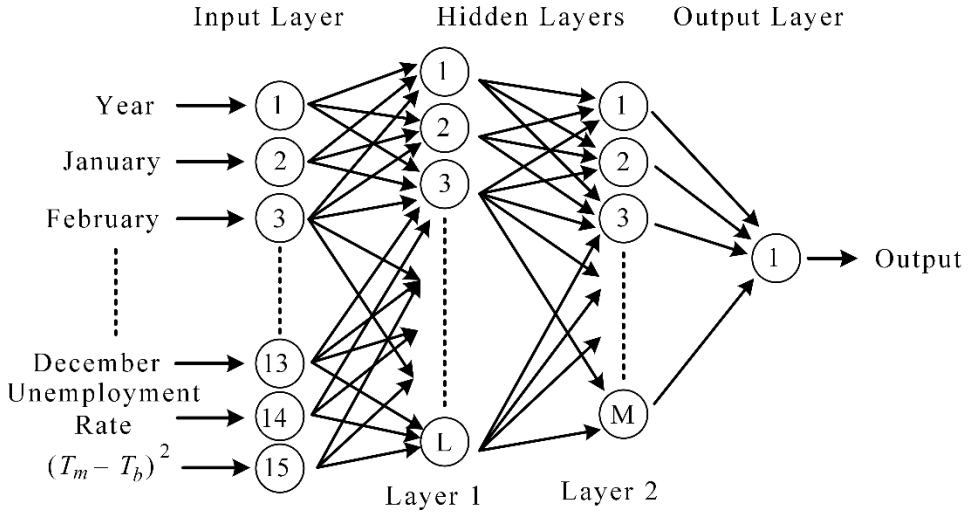

Figure 4. Proposed MLP network scheme

3.4. Evaluation metrics

The performance of the proposed MLP network scheme evaluated using MAPE according to the output of each month with the help of Equation 2. MAPE metric has been chosen as an error metric of the model. The model was created with the help of Sci-kit Learn MLP regressor, and the Limited-memory Broyden Fletcher Goldfarb Shanno algorithm (LBFGS) was chosen as optimizer of the model. As a default value in the MLP regressor, mean square error (MSE) is used as loss function of the back-propagation process.

$$\text{MAPE} = \frac{1}{n}\sum_{i=1}^{n}\left|\frac{e_i}{Y_i}\right| . 100 \qquad (2)$$

Where n is the number of samples, e_i is the error, and Y_i is the real value of the i^{th} element.

4. RESULTS

The hyper-parameter space has been selected as wide as possible in order not to miss any potential solution. In the training phase, 500 best results were chosen as likely solutions candidates. Nevertheless, most of 500 candidates were trained so well with training data so that it has actually memorized the data. Therefore, they have over-fitted the training data; however, fitted very poorly the validation data. In the validation phase, validation data was used to optimize the model parameters. In other words, the ultimate model was selected among these likely solutions by using only validation data. The selected hyper-parameters can be seen in Table 4. It is fundamentally important that test data has not been used during any phase of the training or hyper-parameter selection.

Table 4. Selected hyper-parameter set after validation phase

Name	Values
Activation functions	Rectified linear units (RELU)
Alpha	1e-6
Number of hidden layers	2
Hidden layer sizes	32, 10
Max. iteration count	5000
Solver function	LBGFS
Random seed	870899622

The graphical representations of training can be seen in Figure 5. Actual measurements are given in green, predicted values are shown in red and absolute percentage error (APE) rates for each month dedicated at the bottom of each graph as percentage error with blue bars. The demand data from 2000 up to end of 2017 was chosen as a training set. Neither validation nor test data were used in the training phase.

In order to demonstrate the robustness of the model, a comparison of actual demands and prediction values, which obtained from the proposed model have been made. The real and predicted demand values of validation and test set can be seen in Table 5. The validation data contains all 12 months of 2018, and the test data comprises of 11 months of 2019.

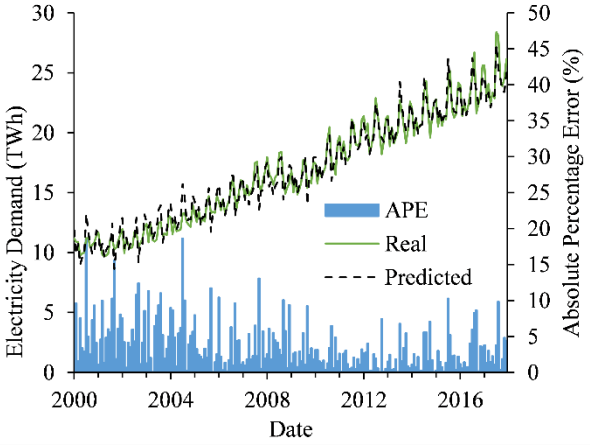

Figure 5. MLP training results with APE

By the help of MAPE metric, the proposed study has also been compared with previous works, which were studied on monthly energy demand for Turkey as can be seen in Table 6. Both the validation and test metrics of the suggested model have been measured more accurately than the metrics of former SVR (Oğcu et al., 2012) and seasonal ANN (Hamzaçebi et al., 2017) models. Only seasonal ANN model performs a better training set over the proposed model. However, their MAPE values of validation and test sets give higher values. In this case, the model shows a little overfitting. On the other hand, the suggested model gives superior results for both validation and test sets without any observable overfitting.

Table 5. Results and comparisons for each month of validation and test data sets

	Date	Real Electricity Demand (TWh)	Predicted Value (TWh)	APE
Validation Set	01/18	26.21	25.01	4.59
	02/18	23.23	23.32	0.36
	03/18	24.73	24.28	1.82
	04/18	23.59	23.04	2.32
	05/18	23.97	23.86	0.44
	06/18	23.86	24.06	0.85
	07/18	29.22	28.57	2.22
	08/18	27.56	26.28	4.63
	09/18	25.05	25.71	2.62
	10/18	23.38	24.16	3.37
	11/18	23.85	23.91	0.24
	12/18	25.48	25.69	0.82
			Validation MAPE :	**2.02**
Test Set	01/19	25.74	25.46	1.09
	02/19	23.20	23.83	2.75
	03/19	24.63	24.74	0.45
	04/19	23.42	23.48	0.24
	05/19	24.60	24.22	1.54
	06/19	24.04	24.68	2.65
	07/19	28.52	28.54	0.09
	08/19	27.51	26.47	3.81
	09/19	25.12	25.41	1.15
	10/19	23.74	24.76	4.31
	11/19	23.74	24.56	3.43
			Test MAPE :	**1.95**

Table 6. Comparison with previous models for Turkey

Study	MAPE		
	Train (Years)	Validation (Years)	Test (Years)
(Hamzaçebi et al., 2017)	**1.97** (2002 – 2012)	2.31 (2013)	2.28 (2014)
(Oğcu et al., 2012)	11.00 (1970 – 2009)	3.30 (2010 – 2011)	-
Proposed study	3.77 (2000 – 2017)	**2.02** (2018)	**1.95** (2019)

5. CONCLUSION

A robust MLP model has been suggested to forecast the monthly electricity demand of Turkey. 500 potential models have been chosen based on training data, then the hyper-parameters of the model were decided to choose the best model based on validationdata. The sucggested MLP model accomplishes exceptional consistency with the data sets of training, validation, and test. Although validation and test data sets were not utilized during the training phase of the model, it achieves relatively low errors for not only training data set but also both validation and test data sets.

Moreover, the studied model is also considerably successful when it is compared with previous models to make a forecast of the electricity demand of Turkey. The substantial prediction of electricity demands with a relatively simple model is the distinctive advantage of the model. As the proposed model incisively estimates the demand for approximately 2 years, governments and decision-makers who decide how much electric power installation will be required, can reliably utilize the model to confirm their ultimate determination with no need any profound mathematics and statistical background.

Proposed model decreases MAPE as low as 3.77%, 2.02%, and 1.95% on training, validation, and test data sets respectively for monthly electricity demand estimations without employing any economic parameters like the gross national product, import or export as an input feature except unemployment rate. The maximum value of the MAPE was observed for the time between 2009 and 2011 in training data set due to the fact of the financial crisis during this period.

As a future research, error rates of electricity demand prediction can also be decreased by applying the recurrent neural network models which are very good in time series inputs.

ACKNOWLEDGEMENT

This document is the results of the research project funded by the BAP Research Fund of Mersin University, under Grant Contract No: 2019-2-TP3-3530.

We would like to thank Turkey electricity transmission corporation for provided electricity demand data, regional directorate of meteorology for provided meteorological data and Turkey statistical agency for provided regional population data and unemployment rates.

DATA AVAILABILITY

The electricity, population, and temperature dataset are hosted on Github (Cömert, 2020) with BPT calculation function script, which was written for Octave software.

Author contributions

Mustafa Cömert: Conceptualization, Visualization, Methodology, Software, Algorithmic Model, Writing-Original Draft Preparation. **Ali Yıldız:** Methodology, Investigation, Algorithmic Model, Model Validation and Test, Writing-Reviewing and Editing.

Conflicts of interest

The authors declare no conflicts of interest.

REFERENCES

Ahmed T, Muttaqi K M & Agalgaonkar A P (2012). Climate change impacts on electricity demand in the State of New South Wales, Australia. *Applied Energy*, *98*, 376–383. https://doi.org/10.1016/j.apenergy.2012.03.059

Ahmed T, Vu D H, Muttaqi K M & Agalgaonkar A P (2018). Load forecasting under changing climatic conditions for the city of Sydney, Australia. *Energy*, *142*, 911–919. https:// doi.org/10.1016/j.energy.2017.10.070

Akay D & Atak M (2007). Grey prediction with rolling mechanism for electricity demand forecasting of Turkey. *Energy*, *32*(9), 1670–1675. https://doi.org/10.1016/j.energy. 2006.11.014

Al-Bajjali S K & Shamayleh A Y (2018). Estimating the determinants of electricity consumption in Jordan. *Energy*, *147*, 1311–1320. https:// doi.org/10.1016/j.energy.2018.01.010

AL-Musaylh M S, Deo R C, Adamowski J F & Li Y (2019). Short-term electricity demand forecasting using machine learning methods enriched with ground-based climate and ECMWF Reanalysis atmospheric predictors in southeast Queensland, Australia. *Renewable and Sustainable Energy Reviews*, *113*. https://doi.org/10.1016/j.rser.2019.109293

Andersen F M, Baldini M, Hansen L G & Jensen C L (2017). Households' hourly electricity consumption and peak demand in Denmark. *Applied Energy*, *208*(May), 607–619. https://doi.org/10.1016/j.apenergy.2017.09.094

Arisoy I & Ozturk I (2014). Estimating industrial and residential electricity demand in Turkey: A time varying parameter approach. *Energy*, *66*, 959–964. https://doi.org/10.1016/j.energy. 2014.01.016

Bedi J & Toshniwal D (2019). Deep learning framework to forecast electricity demand. *Applied Energy*, *238*, 1312–1326. https://doi.org/10.1016/j.apenergy.2019.01.113

Cabral J. de A, Legey L F L & Freitas Cabral M. V. de. (2017). Electricity consumption forecasting in Brazil: A spatial econometrics approach. *Energy*, *126*, 124–131. https://doi.org/ 10.1016/j.energy.2017.03.005

Çevik H H & Çunkaş M (2015). Short-term load forecasting using fuzzy logic and ANFIS. *Neural Computing and Applications*, *26*(6), 1355–1367. https://doi.org/10.1007/s00521-014-1809-4

Chang Y, Kim C S, Miller J I, Park J Y & Park S (2016). A new approach to modeling the effects of temperature fluctuations on monthly electricity demand. *Energy Economics*, *60*, 206–216. https://doi.org/10.1016/j.eneco. 2016.09.016

Cömert M (2020). Project Repository Electiricity Demand Estimatiton With Enhanced ANN Model. Retrieved April 1, 2021, from Forecasting electricity demand by artificial neural network enhanced with population-weighted temperature mean and the unemployment rate website: https:// github.com/mustasyon/electricityDemandEstimationANN

Damari Y & Kissinger M (2018). An integrated analysis of households ' electricity consumption in Israel. *Energy Policy*, *119*(June 2017), 51–58. https://doi.org/10.1016/ j.enpol.2018.04.010

Dedinec A, Filiposka S, Dedinec A & Kocarev L (2016). Deep belief network based electricity load forecasting: An analysis of Macedonian case. *Energy*, *115*, 1688–1700. https:// doi.org/10.1016/j.energy.2016.07.090

Dilaver Z & Hunt L C (2011). Modelling and forecasting Turkish residential electricity demand. *Energy Policy*, *39*(6), 3117–3127.

https://doi.org/10.1016/j.enpol.2011.02.059
Ding S, Hipel K W & Dang Y guo (2018). Forecasting China's electricity consumption using a new grey prediction model. *Energy*, *149*, 314–328. https://doi.org/10.1016/ j.energy.2018.01.169
Duran Toksari M (2007). Ant colony optimization approach to estimate energy demand of Turkey. *Energy Policy*, *35*(8), 3984–3990. https://doi.org/10.1016/j.enpol.2007.01.028
Ferreira P M, Cuambe I D, Ruano A E & Pestana R (2013). Forecasting the Portuguese electricity consumption using least-squares support vector machines. *IFAC Proceedings Volumes (IFAC-PapersOnline)*, *3*(PART 1), 411–416. https://doi.org/10.3182/20130902-3-CN-3020.00138
Gulcu S & Kodaz H (2017). The estimation of the electricity energy demand using particle swarm optimization algorithm: A case study of Turkey. *Procedia Computer Science*, *111*, 64–70. https://doi.org/10.1016/j.procs. 2017.06.011
Günay M E (2016). Forecasting annual gross electricity demand by artificial neural networks using predicted values of socio-economic indicators and climatic conditions: Case of Turkey. *Energy Policy*, *90*, 92–101. https://doi.org/10.1016/j.enpol.2015.12.019
Hamzacebi C & Es H A (2014). Forecasting the annual electricity consumption of Turkey using an optimized grey model. *Energy*, *70*, 165–171. https://doi.org/10.1016/j.energy.2014.03.105
Hamzaçebi C, Es H A & Çakmak R (2017). Forecasting of Turkey's monthly electricity demand by seasonal artificial neural network. *Neural Computing and Applications*, 1–15. https://doi.org/10.1007/s00521-017-3183-5
Kavaklioglu K (2011). Modeling and prediction of Turkey's electricity consumption using Support Vector Regression. *Applied Energy*, *88*(1), 368–375. https://doi.org/10.1016/ j.apenergy.2010.07.021
Kavaklioglu K (2014). Robust electricity consumption modeling of Turkey using Singular Value Decomposition. *International Journal of Electrical Power and Energy Systems*, *54*, 268–276. https://doi.org/10.1016/j.ijepes. 2013.07.020
Kavaklioglu K, Ceylan H, Ozturk H K & Canyurt O E (2009). Modeling and prediction of Turkey's electricity consumption using Artificial Neural Networks. *Energy Conversion and Management*, *50*(11), 2719–2727. https://doi.org/10.1016/ j.enconman.2009.06.016
Kaytez F, Taplamacioglu M C, Cam E & Hardalac F (2015). Forecasting electricity consumption: A comparison of regression analysis, neural networks and least squares support vector machines. *International Journal of Electrical Power and Energy Systems*, *67*, 431–438. https://doi.org/10.1016/j.ijepes.2014.12.036
Kim Y, Son H-G & Kim S (2019). Short term electricity load forecasting for institutional buildings. *Energy Reports*, *5*, 1270–1280. https://doi.org/10.1016/j.egyr.2019.08.086
Kiran M S, Özceylan E, Gündüz M & Paksoy T (2012). Swarm intelligence approaches to estimate electricity energy demand in Turkey. *Knowledge-Based Systems*, *36*, 93–103. https://doi.org/10.1016/j.knosys.2012.06.009
Kucukali S & Baris K (2010). Turkey's short-term gross annual electricity demand forecast by fuzzy logic approach. *Energy Policy*, *38*(5), 2438–2445. https://doi.org/10.1016/j.enpol. 2009.12.037
Lebotsa M E, Sigauke C, Bere A, Fildes R & Boylan J E (2018). Short term electricity demand forecasting using partially linear additive quantile regression with an application to the unit commitment problem. *Applied Energy*, *222*(December 2017), 104–118. https://doi.org/10.1016/j.apenergy. 2018.03.155
Maldonado S, González A & Crone S (2019). Automatic time series analysis for electric load forecasting via support vector regression. *Applied Soft Computing Journal*, *83*, 105616. https://doi.org/10.1016/j.asoc.2019.105616
Marmaras C, Javed A, Cipcigan L & Rana O (2017). Predicting the energy demand of buildings during triad peaks in GB. *Energy and Buildings*, *141*, 262–273. https://doi.org/ 10.1016/j.enbuild.2017.02.046
MGM (2020). MEVBIS. Retrieved April 15, 2020, from https://mevbis.mgm.gov.tr/mevbis/ ui/index.html#/Login
Mostafavi E S, Mostafavi S I, Jaafari A & Hosseinpour F (2013). A novel machine learning approach for estimation of electricity demand: An empirical evidence from Thailand. *Energy Conversion and Management*, *74*, 548–555. https://doi.org/10.1016/j.enconman. 2013.06.031
Nalcaci G, Özmen A & Weber G W (2018). Long-term load forecasting: models based on MARS, ANN and LR methods. *Central European Journal of Operations Research*. https://doi.org/ 10.1007/s10100-018-0531-1
Nick MacMackin, Miller L & Carriveau R (2019). Modeling and disaggregating hourly effects of weather on sectoral electricity demand. *Energy*, *188*, 115956. https://doi.org/10.1016 /j.energy.2019.115956
Oğcu G, Demirel O F & Zaim S (2012). Forecasting Electricity Consumption with Neural Networks and Support Vector Regression. *Procedia - Social and Behavioral Sciences*, *58*, 1576–1585. https://doi.org/10.1016/j.sbspro.2012.09.1144
Ozturk H K & Ceylan H (2005). Forecasting total and industrial sector electricity demand based on genetic algorithm approach: Turkey case study. *International Journal of Energy Research*, *29*(9), 829–840. https://doi.org/ 10.1002/er.1092
Ozturk H K, Ceylan H, Canyurt O E & Hepbasli A (2005). Electricity estimation using genetic algorithm approach: A case study of Turkey.

Energy, *30*(7), 1003–1012. https://doi.org/10.1016/j.energy.2004.08.008

Rahman A, Srikumar V & Smith A D (2018). Predicting electricity consumption for commercial and residential buildings using deep recurrent neural networks. *Applied Energy*, *212*(December 2017), 372–385. https://doi.org/10.1016/j.apenergy.2017.12.051

Rallapalli S R & Ghosh S (2012). Forecasting monthly peak demand of electricity in India-A critique. *Energy Policy*, *45*, 516–520. https://doi.org/10.1016/j.enpol.2012.02.064

Singh P, Dwivedi P & Kant V (2019). A hybrid method based on neural network and improved environmental adaptation method using Controlled Gaussian Mutation with real parameter for short-term load forecasting. *Energy*, *174*, 460–477. https://doi.org/10.1016/j.energy.2019.02.141

Son H & Kim C (2017). Short-term forecasting of electricity demand for the residential sector using weather and social variables. *Resources, Conservation and Recycling*, *123*, 200–207. https://doi.org/10.1016/j.resconrec.2016.01.016

TEİAŞ (2020). ELECTRICAL STATISTICS. Retrieved April 15, 2020, from https://www.teias.gov.tr/tr/elektrik-istatistikleri

Toksari M D (2016). A hybrid algorithm of Ant Colony Optimization (ACO) and Iterated Local Search (ILS) for estimating electricity domestic consumption: Case of Turkey. *International Journal of Electrical Power and Energy Systems*, *78*, 776–782. https://doi.org/10.1016/j.ijepes.2015.12.032

Torrini F C, Souza R C, Cyrino Oliveira F L & Moreira Pessanha J F (2016). Long term electricity consumption forecast in Brazil: A fuzzy logic approach. *Socio-Economic Planning Sciences*, *54*, 18–27. https://doi.org/10.1016/j.seps.2015.12.002

TUIK (2020). Unemplotment Statistics. Retrieved April 15, 2020, from https://biruni.tuik.gov.tr/isgucuapp/isgucu.zul

Tunç M, Çamdali Ü & Parmaksizoglu C (2006). Comparison of Turkey's electrical energy consumption and production with some European countries and optimization of future electrical power supply investments in Turkey. *Energy Policy*, *34*(1), 50–59. https://doi.org/10.1016/j.enpol.2004.04.027

Tutun S, Chou C A & Caniyilmaz E (2015). A new forecasting framework for volatile behavior in net electricity consumption: A case study in Turkey. *Energy*, *93*, 2406–2422. https://doi.org/10.1016/j.energy.2015.10.064

Vu D H, Muttaqi K M & Agalgaonkar A P (2015). A variance inflation factor and backward elimination based robust regression model for forecasting monthly electricity demand using climatic variables. *Applied Energy*, *140*, 385–394. https://doi.org/10.1016/j.apenergy.2014.12.011

Vu D H, Muttaqi K M, Agalgaonkar A P & Bouzerdoum A (2017). Short-term electricity demand forecasting using autoregressive based time varying model incorporating representative data adjustment. *Applied Energy*, *205*(March), 790–801. https://doi.org/10.1016/j.apenergy.2017.08.135

Wang L, Hu H, Ai X Y & Liu H (2018). Effective electricity energy consumption forecasting using echo state network improved by differential evolution algorithm. *Energy*, *153*, 801–815. https://doi.org/10.1016/j.energy .2018.04.078

Wu J, Cui Z, Chen Y, Kong D & Wang Y G (2019). A new hybrid model to predict the electrical load in five states of Australia. *Energy*, *166*, 598–609. https://doi.org/10.1016/j.energy. 2018.10.076

Wu L, Gao X, Xiao Y, Yang Y & Chen X (2018). Using a novel multi-variable grey model to forecast the electricity consumption of Shandong Province in China. *Energy*, *157*, 327–335. https://doi.org/10.1016/j.energy. 2018.05.147

Xu W, Peng H, Zeng X, Zhou F, Tian X & Peng X (2019). Deep belief network-based AR model for nonlinear time series forecasting. *Applied Soft Computing Journal*, *77*, 605–621. https://doi.org/10.1016/j.asoc.2019.02.006

Yang A, Li W & Yang X (2019). Short-term electricity load forecasting based on feature selection and Least Squares Support Vector Machines. *Knowledge-Based Systems*, *163*, 159–173. https://doi.org/10.1016/j.knosys. 2018.08.027

Yu S, Wang K & Wei Y M (2015). A hybrid self-adaptive Particle Swarm Optimization-Genetic Algorithm-Radial Basis Function model for annual electricity demand prediction. *Energy Conversion and Management*, *91*, 176–185. https://doi.org/10.1016/j.enconman.2014.11.059

Yukseltan E, Yucekaya A & Bilge A H (2017). Forecasting electricity demand for Turkey: Modeling periodic variations and demand segregation. *Applied Energy*, *193*, 287–296. https://doi.org/10.1016/j.apenergy.2017.02.054

Yumurtaci Z & Asmaz E (2004). Electric energy demand of Turkey for the year 2050. *Energy Sources*, *26*(12), 1157–1164. https://doi.org/10.1080/00908310490441520

Zahedi G, Azizi S, Bahadori A, Elkamel A & Wan Alwi S R (2013). Electricity demand estimation using an adaptive neuro-fuzzy network: A case study from the Ontario province - Canada. *Energy*, *49*(1), 323–328. https://doi.org/10.1016/j.energy.2012.10.019